UNIVERSIDAD COMPLUTENSE DE MADRID

FACULTAD DE CIENCIAS QUÍMICAS

Departamento de Química Inorgánica I

TESIS DOCTORAL

Pressure-induced phase transitions in $R\mathrm{CrO}_4$ oxides: preparation, magnetic and electronic properties (*R*= rare earth)

Transiciones de fase inducidas por presión en óxidos $R\mathrm{CrO}_4$: preparación, propiedades magnéticas y electrónicas (*R*= tierra rara)

MEMORIA PARA OPTAR AL GRADO DE DOCTOR

PRESENTADA POR

Mahmoud Saleh Mohammed Gamaleldin Abdelkhalek Fahmy
RABIE

Directores

Regino Sáez Puche
Liu Hao Tjeng

Madrid, 2013

© Mahmoud Saleh Mohammed Gamaleldin Abdelkhalek Fahmy Rabie, 2013

UNIVERSIDAD COMPLUTENSE DE MADRID
FACULTAD DE CIENCIAS QUÍMICAS
Departamento de Química Inorgánica I

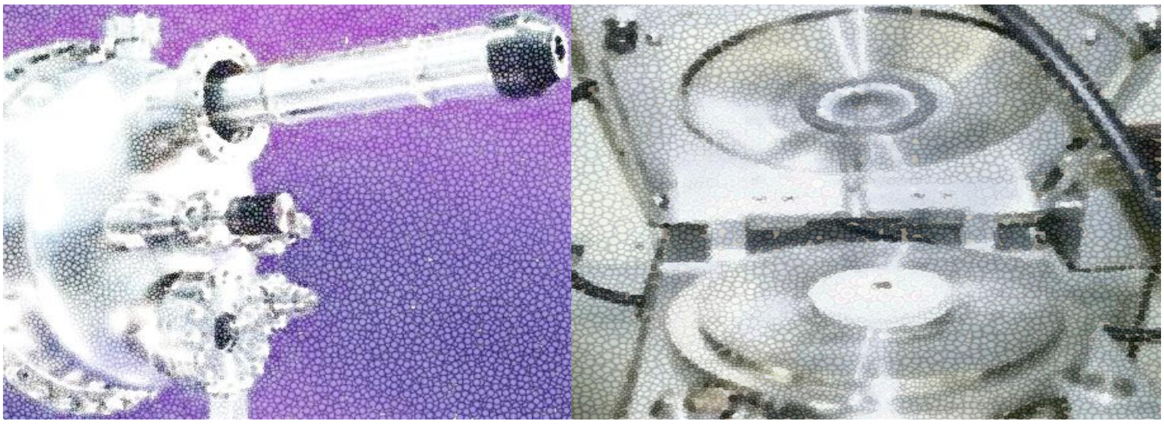

PRESSURE-INDUCED PHASE TRANSITIONS IN $R\text{CrO}_4$ OXIDES: PREPARATION, MAGNETIC AND ELECTRONIC PROPERTIES (*R*= RARE EARTH)

“Transiciones de fase inducidas por presión en óxidos $R\text{CrO}_4$:
preparación, propiedades magnéticas y electrónicas (*R*= tierra rara)”

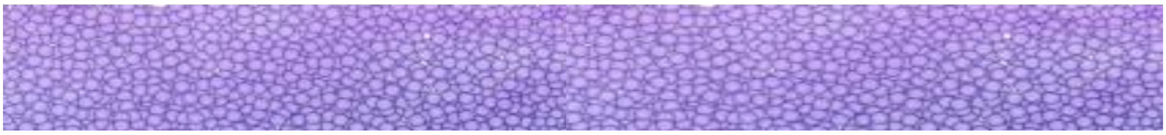

DOCTORAL THESIS

Mahmoud Saleh Mohammed Gamaleldin Abdelkhalek Fahmy RABIE

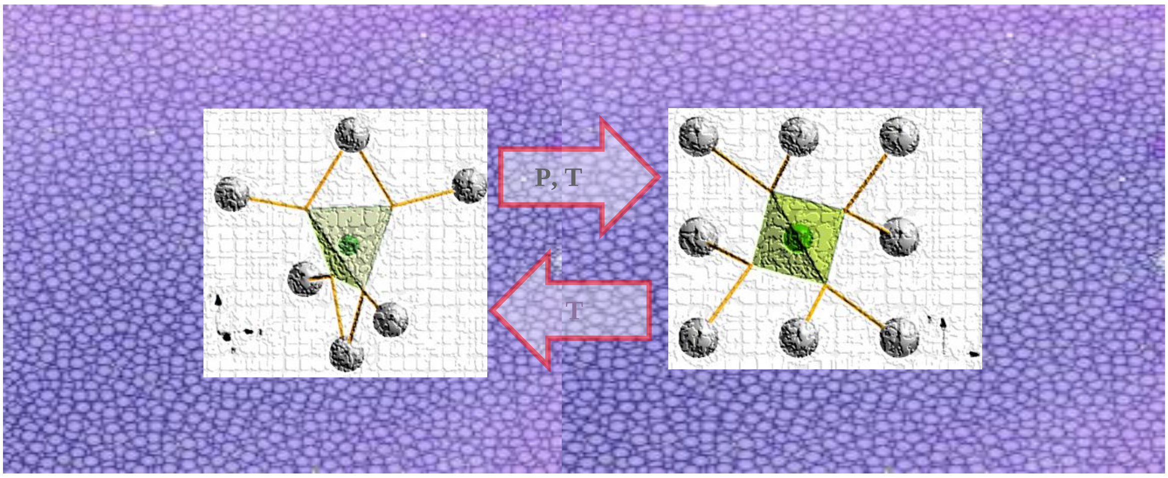

January 2013

MAX-PLANCK-GESELLSCHAFT
SEVENTH FRAMEWORK PROGRAMME
MARIE CURIE ACTIONS

UNIVERSIDAD COMPLUTENSE DE MADRID

FACULTAD DE CIENCIAS QUÍMICAS

Departamento de Química Inorgánica I

PRESSURE-INDUCED PHASE TRANSITIONS IN RCrO$_4$ OXIDES: PREPARATION, MAGNETIC AND ELECTRONIC PROPERTIES (*R*= RARE EARTH)

"Transiciones de fase inducidas por presión en óxidos RCrO$_4$: preparación, propiedades magnéticas y electrónicas (*R*= tierra rara)"

MEMORIA PRESENTADA PARA OPTAR AL GRADO DE

DOCTOR POR

Mahmoud Saleh Mohammed Gamaleldin Abdelkhalek Fahmy RABIE

Con mención de Doctorado Europeo

Bajo la dirección de los Doctores:

Prof. Dr. Regino Sáez Puche

Prof. Dr. Liu Hao Tjeng

Madrid, January 2013

dedicated to the memory of my father

CONTENTS

1. Introduction

1.1 Cr^{5+} Compounds

Chromium occurs in nature as the 21st most abundant element in the Earth's crust, with a concentration of about 100 ppm [1]. The name originates from the Greek word chrōma (χρωμα), which means color and refers to the colors usually coexisting with the chromium compounds and minerals. Chromium has in its 0-oxidation state an electronic configuration of [Ar] $3d^5 4s^1$. Many other states are possible in solid-state materials: the chromium can contain in its compounds a valence state of +1 (like $K_3[Cr(CN)_5NO]^{\cdot}H_2O$) [2], +2 (like Li_2CrCl_4) [3] , +3 (Like $LaCrO_3$) [4], +4 (like $CaCrO_3$) [5], +5 (like $YCrO_4$) [6] or +6 (like $SrCrO_4$) [7]. Although +3 and +6 oxidation states are in a descending order the most stable of all, under certain conditions the other states can also be produced.

Although Cr^{5+} compounds are found less frequently in the literature, one can trace their occurrence to about one century ago. There is little information describing the few Cr^{5+} compounds that have been isolated, as it is generally difficult to produce high-purity polycrystalline samples. It has proven to be an even greater task to grow single crystals of the Cr^{5+} systems. The earliest examples can be found in the work of Meyer and Best in 1899 who synthesized the Oxochlorochromate $A[CrOCl_4]$ [8], where A = H, pyridine or quinoline; followed by Weinland and Fridrich in 1905 who synthesized $A_2[CrOCl_5]$ [9], where A = K, Rb, Cs or NH_4.

The peroxochromate $K_3Cr(O_2)_4$ was studied by Klemm and Werth [10] in 1933. This red salt was proposed to have the structure 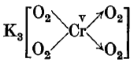 [11] with a tetrahedral coordination for the Cr atom. Of the $ACr(O_2)_4$ series, one can find compounds with A = K, Na, Rb, Cs or NH_4. Another explanation of the anion $[Cr(O_2)_4]^{3-}$ in this later compound was done using x-ray crystal structure analysis considering that the oxygen atoms are in a distorted dodecahedral arrangement around the central chromium atom [12-14]. However, such a coordination for the Cr^{5+} ion is very unusual.

The chromium fluoride, CrF_5, was obtained in 1941 by Wartenberg [15], but it was found to immediately hydrolyze by water to hexavalent and trivalent chromium compounds. Other additional inorganic oxides containing Cr^{5+} are $CrFO_3$ [16] and $A(CrF_6)$ [17], where A = Li, Na, K, Rb or Sc.

Another Series of Cr^{5+} compounds is that with the formula $A_3Cr_2O_8$, where A position can be occupied by Ca [18], Sr [19, 20] or Ba [21, 22]. Furthermore, oxides having the composition of A_3CrO_4 contain Cr^{5+} as well, where A = Li [23], Na, Rb, Cs and K [24, 25].

A possible series that can be added to the families of Cr^{5+} compounds is that with the formula $A_5(CrO_4)_3B$, where A is a divalent cation like Ca^{2+}, Sr^{2+}, Ba^{2+}, Cd^{2+}, Pb^{2+}, Mn^{2+}; while B is a monovalent anion, e.g. F^{-1}, Cl^{-1}, Br^{-1} or OH^{-1}. All these structures presume the apatite-like structure and their lattice constants have been predicted by Wu *et al.*[26] from the elemental ionic radii using pattern recognition and artificial neural networks techniques. Nevertheless, few of these compounds has been already prepared like $Ca_5(CrO_4)_3OH$ [27], $Sr_5(CrO_4)_3OH$ [28], $Ba_5(CrO_4)_3OH$ [29], $Ca_5(CrO_4)_3Cl$ [28], $Sr_5(CrO_4)_3Cl$ [30], $Ba_5(CrO_4)_3Cl$[28], $Ca_5(CrO_4)_3F$ [28], $Sr_5(CrO_4)_3F$ [31] and $Ba_5(CrO4)_3F$ [28]. Table 1.1 lists various Cr^{5+} inorganic compounds found in the literature.

Table 1.1 Cr^{5+} inorganic compounds categorized according to the coordination of the chromium cation.

Cr-stereochemistry	**Cr^{5+} Compounds**	**S.G.**	**Remarks**
Tetrahedral	$A_3(CrO_4)_2$, A = Ca, Sr or Ba [18-22]	$P2_1/c$	black
	$A_5(CrO_4)_3B$ [26-32] $A = Ca^{2+}$, Sr^{2+}, Ba^{2+}, Cd^{2+}, Pb^{2+} or Mn^{2+} $B = F^{-1}$, Cl^{-1}, Br^{-1} or OH^{-1}	$P6_3/m$ $P6_3$	Apatite-type structure
	A_3CrO_4 , A = Li, Na, Rb, Cs or K [23-25, 32]	$I\bar{4}2m$	
	$Ca_2(CrO_4)Cl$ [32, 33]	$Pbcm$	
	$Ba_5(CrN_4)N$ [34]	$C2/m$	
Double tetrahedra	$Li_4Sr_2[Cr_2N_6]$ [35]	$Pbca$	black
Octahedral	$[CrF_5]_\infty$ [15, 32]	Not available	
	$CrFO_3$ [16]	$R\bar{3}h$	
	$A(Cr\ F_6)$ [17], A = Li, Na, K, Rb, Sc	$Pnma$	
	$A_2[CrOCl_5]$ [9, 32], A = K, Rb, Cs or NH_4	Not available	Yellow-brown
Square pyramidal	$A[CrOCl_4]$ [8, 32], A = H	Not available	
	$A[(UO_2)_2Cr_2O_8](H_2O)_n$ [36] $A = K_2$, Rb_2, Cs_2 or Mg n = 0 or 4	($P2_1/c$: for $A = K_2$, Rb_2, Cs_2) ($Pnma$: for A = Mg)	
Dodecahedral	$A_3Cr(O_2)_4$, A = K, Na, Rb, Cs, NH_4 [12-14, 32]	$I\bar{4}2m$	Red brown

1.2 *R*CrO$_4$ Oxides

There is another series of Cr^{5+} compounds of the form *R*CrO$_4$, where *R* is a rare earth cation and corresponds to the series from Lanthanum to Lutetium in addition to Yttrium and Scandium. With an oxidation state for the rare earth R^{3+} cation, the chromium is found in its pentavalent state in this case. These compounds when synthesized at ambient pressure crystallizes in a tetragonal system (Space Group $I4_1/amd$) [37, 38] which represents a structure that is isotypic with the zircon mineral ZrSiO$_4$. Due to the small size of the trivalent La^{3+} and Pr^{3+} cations, an exclusion of this rule applies for the lanthanum and praseodymium chromates. In the first case, the LaCrO$_4$ crystallizes at ambient pressures completely in the monoclinic system (Space Group $P2_1/n$) [39] and is isostructural with the monazite mineral, which is a rare-earth phosphate, e.g. (Ce, La, Nd, Th)PO$_4$, and generally containing concentrations of uranium and thorium [40]. In the second case, the PrCrO$_4$ crystallizes as a dimorphic compound and the standard synthesis conditions yield a mixture of both monazite-like and zircon-like polymorphs [41-42]. On the other hand, in the case of Cerium, the synthesis of CeCrO$_4$ is not possible [41].

The *R*CrO$_4$ compounds are part of a family of a larger series of compounds that are isostructural with the zircon mineral. We would refer to these compounds here as *RX*O$_4$ where *X* is P, V, Cr or As cation. This family of compounds is not only having the same structure but also exhibits similar structural properties and similar behavior during structural transitions, as it will be explained briefly in this chapter and later in details for *R*CrO$_4$ oxides in chapter 3. The YPO$_4$ compound exists naturally and is known as xenotime. While YVO$_4$ and YAsO$_4$ were one of the first compounds in this system to be prepared synthetically [43-44].

The ions of rare-earth elements possess magnetic properties different from each other. The first trial to study the magnetic properties of each type was carried out by J. H. van Vleck [45] in 1965. This difference lies in the electronic configuration $5s^2\ 5p^6\ 4f^n$, in which the filled 5*s* and 5*p* orbitals reduce the possible effects of the other ions in the solid on the innermost 4*f* orbitals. This shielding allows the effect of spin-orbital coupling to be stronger than the effect of inhomogeneous electric fields from the ions of the crystal, leading to the total angular momentum to be considered. The crystal field interaction can be treated therefore as a perturbation of the multiplet with total angular momentum number "*J*" [46]. By contrast, in the case of the transition metals of the first series, the 3*d* orbitals are the most external. Moreover, the 4*s* orbital is empty in the ionized state, or part of the conduction band in the case of electrically conductive material. Consequently, the crystal field effects prevent the spin-orbit coupling effectively and quench most of the orbital angular momentum [47]. Although the molecular field model assumes a net magnetic moment located at each atom, rare-earth elements possess delocalized or itinerant magnetism phenomena in many materials [48-49]. On the other hand, while the magnetic moments in the rare earth ions are localized, the inner 4*f* orbitals do not overlap significantly with the other ions. Therefore, the strong spin-orbit coupling causes strong intrinsic magnetic anisotropy of the rare earth elements, while the transition metals possess relatively high values of the magnetic ordering temperature. These mentioned properties have led the interest in combining both types of elements in different compounds to obtain materials with novel magnetic properties for new applications [49-52].

Inside the crystalline structure of $R\mathrm{CrO}_4$, two ions exist and each of them has an unpaired electron corresponding to Cr^{5+} and R^{3+} ([Xe] $6s^0\ 4f^n$), where n= 0-14 (see table 1.2). Exceptions in this case are when R= Y, La or Lu, in which R^{3+} has no unpaired electron. Therefore, these oxides constitute a very interesting framework to study $3d$–$4f$ magnetic interactions and the predominant role that the rare earth anisotropy could play in the resulting magnetic properties. Moreover, more interesting In case of Gd^{3+}, for example, it represents a fundamental state of $^8S_{7/2}$, which gives it an isotropic symmetry and therefore it is interesting to study how this could affect the electronic and magnetic properties.

Table 1.2 Atomic and R^{3+} electron configuration of the rare-earth elements

R	La	Ce	Pr	Nd	Pm	Sm	Eu	Gd	Tb	Dy	Ho	Er	Tm	Yb	Lu
Atomic number	57	58	59	60	61	62	63	64	65	66	67	68	69	70	71
Free atom [Xe] $6s^2$	$5d^1$	$4f^1\ 5d^1$	$4f^3$	$4f^4$	$4f^5$	$4f^6$	$4f^7$	$4f^7\ 5d^1$	$4f^9$	$4f^{10}$	$4f^{11}$	$4f^{12}$	$4f^{13}$	$4f^{14}$	$4f^{14}5d^1$
R^{3+} [Xe] $6s^0$	$4f^0$	$4f^1$	$4f^2$	$4f^3$	$4f^4$	$4f^5$	$4f^6$	$4f^7$	$4f^8$	$4f^9$	$4f^{10}$	$4f^{11}$	$4f^{12}$	$4f^{13}$	$4f^{14}$

1.3 Motivation and Scheme of this Work

Phase transitions induced by pressure were carried out by Reid and Ringwood [53] for the zircon mineral ZrSiO_4; and by Stubican and Roy [54] for the analogous zircon-types of $RX\mathrm{O}_4$ (X= As and V) which transform from a space group of $I4_1/amd$ into a scheelite-type structure, space group $I4_1/a$. This transition reduces the symmetry of the tetragonal structure and produces a more compact structure. Some $RX\mathrm{O}_4$ compounds containing small radii of R^{3+}, tend to crystallize at ambient pressures as a monazite-type structure (space group $P2_1/n$). In the case of rare earth vanadates and arsenates, quenchable pressure-induced phase transitions take place at 8 GPa and 773 K [54, 56, 57] from monazite to scheelite or from zircon to scheelite, resulting an increase in the density of 6% and 11%, respectively. A similar behavior was observed recently by *in-situ* synchrotron x-ray diffraction experiments for YbPO_4 and LuPO_4 [55], which transform under pressure from zircon to scheelite. However, the pressure-induced transition in these phosphates is reversible, *i.e.* the zircon phase is obtained upon the release of pressure [55].

Regarding the high-pressure phase transitions in RCrO$_4$, in which we are interested, only few studies have been reported [58-60]. This is due to the high instability of Cr^{5+} and its tendency to be reduced to the most stable phase of RCrO$_3$ distorted perovskite. It has been recently reported by our research group that zircon-RCrO$_4$ phases transform to a scheelite polymorph at 4 GPa and 813 K for the HoCrO$_4$ and TbCrO$_4$ compounds [58, 59]. Such a phase transition is quenchable in the case of chromates after releasing the pressure.

Accompanying this structural phase transition from zircon to scheelite the magnetic properties change dramatically. In this sense, most of the zircon-type RCrO$_4$ oxides being ferromagnetic [60] become antiferromagnetic for the corresponding known scheelite polymorph [57, 61]. Detailed structural analyses by x-ray diffraction (XRD) and neutron diffraction (NPD) allow us to establish structure-properties relationships, which represents one of the main interests in the solid-state science.

In this work, we aim to study the RCrO$_4$ oxides through investigating the structural, magnetic and electronic properties. Therefore, the scheelite phase of RCrO$_4$ oxides will be synthesize under pressure for the first time with R= Nd, Sm, Eu, Gd, Er, Tm, Yb and Lu. Other scheelites (with R= Dy and Ho) will be reproduced in this work with higher purity than that previously published in order to study their magnetic and electronic properties.

In this work, we focus first on the structural phase transition from the zircon-type to the scheelite-type structure under pressure and temperature by: optimizing the synthesis parameters for high-purity scheelite phases, studying the transition mechanism and investigating the stability of the zircon and scheelite polymorphs at various temperatures. Second, we study the effect of the Cr^{5+} cation on the magnetic and electronic properties of these materials and the changes occurring in these properties upon the pressure-induced transition.

To achieve these goals, we prepared zircon and scheelite phases of RCrO$_4$ at ambient and high pressures and investigated the structural magnetic and electronic properties with various experimental methodologies, as will be explained in chapter 2. Afterwards, a detailed review of the zircon-to-scheelite transition shall be represented in chapter 3. In addition, we shall carry out various XRD and NPD measurements in chapter 3 to characterize the crystal structure of the synthesized scheelite polymorphs. Moreover, a parallel study of the stability of the scheelite phase is important in order to optimize the synthesis conditions and to understand the factors due to which other secondary phases can form during experiments, as will be explained in chapter 4. Afterwards, we shall discuss in chapter 5 the magnetic properties of the RCrO$_4$-scheelites by studying magnetic susceptibilities, specific heats and neutron diffraction patterns at low temperatures.

Concerning the electronic properties, not much has been done in the literature investigating *R*CrO$_4$ oxides. Only one x-ray photoelectron study of the valence band of LaCrO$_4$ monazite-like structure was done in 1992 by Konno *et al.* [62] without too much interpretation and later a band structure calculation was done in 2006 by Li *et al.* [63] but without any comparison with experimental data. Very recently, Errandonea *et al.* [64] obtained experimentally the band gap of YCrO$_4$ zircon by optical spectroscopy of powder samples. We shall study in this work the electronic structure of *R*CrO$_4$ compounds by x-ray photoelectron spectroscopy (XPS) and band-structure calculations, taking into consideration the comparison between both experimental and calculated values. In addition, we shall carry out soft x-ray absorption spectroscopy (XAS) for the first time for both zircon and scheelite polymorphs. In particular, we would like to verify spectroscopically the valence states of Cr as well as the origin and nature of the states closer to the chemical potential. Specifically, is the system an insulator? and if so, then why?

In chapter 6, we discuss the electronic properties of *R*CrO$_4$ compounds and our XPS measurements for two zircon samples, YCrO$_4$ and GdCrO$_4$. Afterwards we extend our study of the electronic properties in chapter 7 through our XAS measurements for various zircon and scheelite polymorphs of *R*CrO$_4$ oxides.

References

[1] J. Barnhart, *Regulatory Toxicology and Pharmacology* **26**, S3 (1997)

[2] I. Bernal and S. E. Harrison, *Journal of Chemical Physics* **34**, 102 (1961)

[3] H. D. Lutz, M. Schneider and Ch. Wickel, *Zeitschrift fuer Kristallographie* **211**, 8 (1996).

[4] T. Hashimoto, N. Tsuzuki, A. Kishi, K. Takagi, K. Tsuda, M. Tanaka, K. Oikawa, T. Kamiyama, K. Yoshida, H. Tagawa and M. Dokiya, *Solid State Ionics* **132**, 181 (2000)

[5] J. B. Goodenough, J. M. Longo and J. A. Kafalas, *Materials Research Bulletin* **3**, 471 (1968)

[6] H. Schwarz, *Zeitschrift fuer anorganische und allgemeine Chemie* **322**, 137 (1963)

[7] H. Effenberger and F. Pertlik, *Zeitschrift fuer Kristallographie* **-** *Crystalline Materials* **176**, 75 (1986)

[8] E. J. Meyer and H. Best, *Zeitschrift fuer anorganische Chemie* **22**, 192 (1899)

[9] R. F. Weinland and W. Fridrich, *Berichte der Deutschen Chemischen Gesellschaft* **38**, 3784 (1905)

[10] W. Klemm and H. Werth, *Zeitschrift fuer anorganische und allgemeine Chemie* **216**, 127 (1933)

[11] N. V. Sidgwick, The Chemical Elements and their Compounds, Volume II, OXFORD University Press (1950)

[12] R. Stomberg, *Acta Chemica Scandinavica* **17**, 1563 (1963)

[13] J. Fischer, A. Veillard and R. Weiss, *Theoretica Chimica Acta* **24**, 317 (1972)

[14] M. H. Dickman and M. T. Pope, *Chemical Reviews* **94**, 3, 569 (1994)

[15] H. V. Wartenberg, *Zeitschrift fuer anorganische und allgemeine Chemie* **247**, 135 (1941)

[16] M. McHughes, R. D. Willett, H. B. Davis and G. L. Gard, *Inorganic Chemistry* **25**, 426 (1986)

[17] Z. Mazej, E. Goreshnik, *European Journal of Inorganic Chemistry*, 11, 1795 (2008)

[18] I. Arcon, B. Mirtic and A. Kodre, *Journal of the American Ceramic Society* **81**, 222 (1998)

[19] E. Cuno and H. K. Müller-Buschbaum, *Zeitschrift fuer anorganische und allgemeine Chemie* **572**, 95 (1989)

[20] Y. Singh and D.C. Johnston, *Physical Review B* 76 (2007) 012407.

[21] S. Y. Gordeev and V. I. Serdyukov, *Neorganicheskie Materialy* **3**, 1653 (1967) [taken from Ref. 20]

[22] A. A. Aczela, H. A. Dabkowska, P. R. Provencher and G. M. Luke, *Journal of Crystal Growth* **310**, 870 (2008)

[23] M. A. K. L. Dissanayake, S. Garcia-Martin, R. Sáez-Puche, H. H. Sumathipala and A. R. West, *Journal of Materials Chemistry* **4**, 1307 (1994)

[24] R. Olazcuaga, J. M. Reau, G. LeFlem and P. Hagenmuller, *Zeitschrift fuer anorganische und allgemeine Chemie* **412**, 271 (1975)

[25] R. Scholder, E. F. Schwochow, H. Schwarz, *Zeitschrift fuer anorganische und allgemeine Chemie* **363**, 10 (1968)

[26] P. Wu, Y. Z. Zeng and C. M. Wang, *Biomaterials* **25**, 1123 (2004)

[27] K. A. Wilhelmi, O. Jonsson, *Acta Chemica Scandinavica* **19**, 177 (1965)

[28] E. Banks and K. L. Jaunarajs, Inorganic Chemistry **4** (1), 78 (1965)

[29] H. J. Mattausch and H. Müller Buschbaum, *Zeitschrift fuer Anorganische und Allgemeine Chemie* **400**, 1 (1973)

[30] H. Mueller Buschbaum and K. Sander, *Zeitschrift fuer Naturforschung, Teil B. Anorganische Chemie, Organische Chemie* **33**, 708 (1978)

[31] E. Herdtweck, *Acta Crystallographica C* **47**, 1711 (1991)

[32] K. Nag and S. N. Bose, *Structure and Bonding* **63**, 153 (1985)

[33] M. Greenblatt, E. Banks and B. Post, *Acta Crystallographica* **23**, 166 (1967)

[34] A. Tennstedt, R. Kniep, M. Hueber and W. Haase, *Zeitschrift fuer Anorganische und Allgemeine Chemie* **621**, 511 (1995)

[35] O. Hochrein, M. Kohout, W. Schnelle and R. Kniep, *Zeitschrift fuer Anorganische und Allgemeine Chemie* **628**, 2738 (2002)

[36] A. J. Locock, S. Skanthakumar, P. C. Burns and L. Soderholm, *Chemistry of Materials* **16**, 1384 (2004)

[37] G. Buisson, F. Bertaut and J. Mareschal, *C. R. Acad. Sci.* 259, 411 (1964)

[38] G. Buisson, F. Tcheou, F. Sayetal and K. Schenesman, *Solid State Communications* **18**, 871 (1976)

[39] C. E. Rice and W. R. Robinson, *Acta Crystallographica B* **32**, 2232 (1976)

[40] J. M. Montel, S. Foret, M. Veschambre, C. Nicollet and A. Provost, *Chemical Geology* **131**, 37 (1996)

[41] S. G. Manca and E. J. Baran, *Journal of Applied Crystallography* **15**, 102 (1982)

[42] E. Jiménez Melero, J. Isasi and R. Sáez Puche, *Journal of Alloys and Compounds* **323-324**, 115 (2001)

[43] E. Broch, *Zeitschrift fuer Physikalische Chemie* **20B**, 345 (1932)

[44] M. Strada and G. Schwendimann, *Gazzetta Chimica Italiana* **64**, 662 (1934)

[45] J. H. van Vleck, The theory of electric and magnetic susceptibilities, Oxford University Press, London (1965)

[46] K. N. Taylor and M. I. Darby, Physics of Rare Earth Solids, Chapman and Hall Ltd., London (1972)

[47] E. Jiménez, M. J. Torralvo, J. Isasi, and R. Sáez-Puche, *The Chemical Educator* **8**, 1 (2003)

[48] T. Moriya and Y. Takahashi, *Annual Review of Materials Science* **14**, 1 (1984)

[49] E. Jiménez Melero, doctoral thesis, Universidad Complutense de Madrid (2005), http://eprints.ucm.es/tesis/qui/ucm-t28520.pdf (November 2012)

[50] I. V. Mitchell, Nd-Fe Permanent Magnets: their present and future applications, Elsevier Applied Science Publishers Ltd., London (1985)

[51] K. Yoshii, A. Nakamura, M. Mizumaki, N. Ikeda and J. Mizuki, *Journal of Rare Earths* **22**, 6, 733 (2004)

[52] J. Li, H. M. Dahn, R. J. Sanderson, A. D. W. Todd and J. R. Dahn, *Journal of The Electrochemical Society* **155**, 12, A975 (2008)

[53] A. F. Reid and A. E. Ringwood, *Earth Planet Sci. Letter* **6**, 205 (1969)

[54] V. S. Stubican and R. Roy, *Zeitschrift fuer Kristallographie* **119**, 90 (1963)

[55] F. X. Zhang, M. Lang, R. C. Ewing, J. Lian, Z. W. Wang, J. Hu and L. A. Boatner, *Journal of Solid State Chemistry* **181**, 2633 (2008).

[56] S.J. Duclos, A. Jayaraman, G.P. Espinosa, A.S. Cooper, R.G. Maines, *Journal of Physics and Chemistry of Solid* **50** (1), 769 (1989)

[57] V.S. Stubican and R. Roy, *Journal of Applied Physics* **34**, 1888 (1963)

[58] E. Climent Pascual, J. Romero de Paz, J. M. Gallardo Amores and R. Sáez Puche, *Solid State Sciences* **9**, 574 (2007)

[59] E. Climent Pascual, J. M. Gallardo Amores, J. Romero de Paz, N. Taira and R. Sáez Puche, *Journal of Alloys and Compounds* **488**, 524 (2009).

[60] R. Sáez Puche, E. Jiménez, J. Isasi, M. T. Fernández-Díaz and J. L. García-Muñoz, *Journal of Solid State Chemistry* **171**, 161 (2003)

[61] Y. W. Long, L. X. Yang, Y. Yu, F. Y. Li, R. C. Yu and C. Q. Jin, *Physical Review B* **75**, 104402 (2007)

[62] H. Konno, H. Tachikawa, A. Furusaki, and R. Furuichi, *Analytical Sciences* **8**, 641 (1992)

[63] L. Li, W. Yu and C. Jin, *Physical Review B* **73**, 174115 (2006)

[64] D. Errandonea, R. Kumar, J. López-Solano, P. Rodríguez-Hernández, A. Muñoz, M. G. Rabie and R. Sáez Puche, *Physical Review B* **83**, 134109 (2011)

15

2. Sample Preparation and Experimental Methods

2.1 Sample Preparation

The preparation of $R\mathrm{CrO}_4$ different scheelite samples has been done in two main steps: first, the preparation of polycrystalline powders of $R\mathrm{CrO}_4$ zircons at ambient pressure using a precursor method; and second, undergoing high pressure and temperature conditions on these zircons in a controlled press in order to obtain the zircon-to-scheelite phase transition.

2.1.1 The precursor method

In a precursor method, precursor compounds are produced in a way to bring the different reacting cations in close contact by an ideal dispersion. Usually a good mixing of reactants is performed in a melt or solution in order to provide a better homogenization, which in return enhances the diffusion and rate of reactions. For these reasons, unlike some other ceramic methods where the mixed powders are brought in direct contact by pressing and heating at elevated temperature, the precursor method allows for a better control of the stoichiometry of metastable phases at low temperatures due to the shorter diffusion distances. In this method, first, the mixture is heated to the decomposition temperature of the precursor, and then the precursor is heated through certain steps in order to produce the required materials. The decomposition temperatures are generally lower than the temperatures employed in the ceramic methods due to the shorter diffusion distances of the ions. The precursor method can be subdivided in reactions in which the mixed-metal precursor thermally decomposes without change of the oxidation state of the involved elements, and those where the products are formed by redox reactions. The reaction can be supported by a large contact area of the reactants by putting the reactants in a silica boat crucible, which provide a large contact between the precursor and the gas flow. Finally, a stoichiometric oxide is resulted from the preparation. However, the temperature gradient in the furnace with the length of the crucible should be taken into account; otherwise, some secondary phases can be formed at a cold end of the boat crucible.

In this work, a simple precursor method has been adopted to prepare the orthochromate $R\mathrm{CrO}_4$ zircon from the nitrates of its constituents. SIGMA-ALDRICH reactants were used as: 99% Chromium(III)-nitrate nonahydrate and corresponding 99.9% Lanthanide(III)nitrate hexahydrate (or pentahydrate depending on the rare-earth). The ground reactants were packed in a boat silica crucible and placed in a quartz tube of a horizontal tubular furnace with oxygen flow at three temperature steps: 30 min at 433 K, 30 min at 473 K and 12 hours at a temperature between 823 and 853 K. The heating rate is about 20 K/min as in the following reaction:

$$\mathrm{Cr(NO_3)_3{\cdot}9H_2O} + R\mathrm{(NO_3)_3{\cdot}6H_2O} \longrightarrow R\mathrm{CrO_4} + 6\mathrm{NO_2} + 15\mathrm{H_2O} + \mathrm{O_2} \tag{2.1}$$

The first step, at 433 K, is necessary to melt the nitrate salts, which in return shall homogenize the reactants for a better mixing effect. Then, at this stage, the water molecules evaporate followed by the beginning of the exhaust of the nitrogen oxide. In this part, it is worth to say that the colorless NO_2 exhaust exists in the ideal case when there is enough fast flow of oxygen. However, in reality, during this synthesis a big amount of brownish and highly oxidizing NO evolve, which seem to be a big assistance to the oxidation of Cr^{3+} in the reactants until the formation of Cr^{5+} state in the products. If a high flux of oxygen is provided to insure the NO_2 prevalence, then the Cr^{3+} finds a big difficulty to oxidize to Cr^{5+} and a big amount of $R\mathrm{CrO}_3$ impurities result even at lower temperatures than 873 K. By introducing further heating at 473 K, the precursor continues to decompose and evolve more of the nitrogen oxides. At the third step, the main reaction (2.1) takes place in order to produce the $R\mathrm{CrO}_4$ zircon at 853 K.

By further increase of temperature, the $R\mathrm{CrO}_4$ zircons will begin to decompose following the reaction:

$$R\mathrm{CrO}_4 \longrightarrow R\mathrm{CrO}_3 + \tfrac{1}{2}\,\mathrm{O}_2 \qquad (2.2)$$

This decomposition takes place in the temperature range between 873 and 1173 K and results in the orthochromite $R\mathrm{CrO}_3$ oxide with a distorted perovskite structure.

If the samples are left for longer time at the first or second steps, 433 and 473 K, or if a very slow heating rate is used, then some impurities begin to evolve with yellow brownish colors especially at the sides of the boat crucible, which reaches only a lower temperature due to the gradient inside the tube. Such impurities are due to the formation of a compound with a higher oxidation state at temperatures lower than the range necessary to obtain the Cr^{5+} compound. An investigation of this situation shall be further discussed in details within chapter 4. Such a phenomenon can be avoided by high heating rates and subsequent quenching of the final product from 853 K to room temperature. Moreover, a proper storage in a pumped desiccator or a glove box is highly advised to avoid the absorption of moisture at the surface of samples and consequently altering of the valence state.

Finally, for the safety considerations during the synthesis, some nitric acid forms at the internal sides of the quartz tube due to the reaction of the condensed water with NO and oxygen. Therefore, care should be taken when opening the quartz tube and taking out the sample.

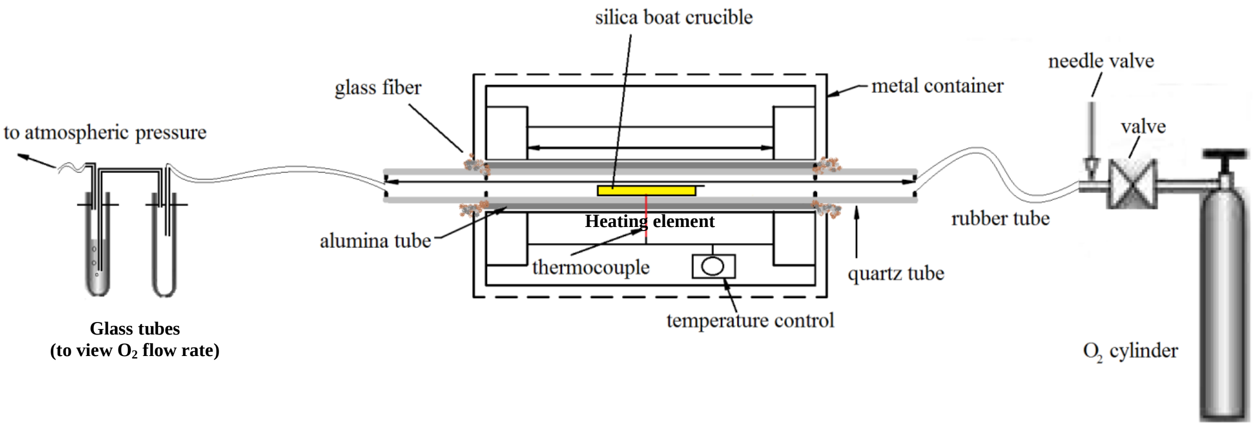

Fig. 2.1 Schematic drawing of the horizontal tubular furnace used for the precursor method.

2.1.2 High-pressure synthesis

The study of materials under of high pressure was pioneered by Percy Williams Bridgman, who received the Nobel Prize in Physics in 1946, for the work he started in 1905 studying the properties of materials under high pressure. Bridgman extended the pressure range from 0.3 GPa to as much as 10 GPa by introducing an unsupported area seal [1]. This revolutionary technique started at the beginning of the 20th century and was further developed until the present days. Owing to this technique, lots of new materials and new phases have been discovered, modified or reproduced in the fields of materials science, mineralogy and earth sciences. Nevertheless, in the field of solid-state chemistry, the high-pressure technique is an important tool for investigating phase transitions under pressure for some polymorphic compounds, as well as inducing new chemical bonds for the synthesis of new materials.

High-pressure experiments can be classified into two types: the *ex-situ* technique and the *in-situ* technique. In an *ex-situ* experiment, the material is studied after it has been already compressed and decompressed; while in an *in-situ* experiment, the studies are carried out while the sample is under compression. The later method is very useful for studying reversible phenomenon and exploring the various phase-induced transitions in the materials. Many methods and various equipments are available nowadays to achieve both kinds of experiments.

The types of high-pressure equipment can be generalized roughly into three categories as shown in Table 2.1. The table explains schematically the main differences between the principals used for the uniaxial presses (belt, opposed anvil and toroidal presses), the multi-anvil press and the diamond anvil cell (DAC). The approximate internal position of the sample is indicated in the table for the three cases by a small yellow mark, while the arrows show the direction of the pressure. For uniaxial presses, the main concept of the Bridgman anvil is shown in the schematic drawing. The usual average range of pressure reached by the equipment is mentioned approximately. However, some labs can provide different values.

Table 2.1 Main categories of the high-pressure equipment.

type	Uniaxial presses	Multi-anvil press	DAC
schematic drawing	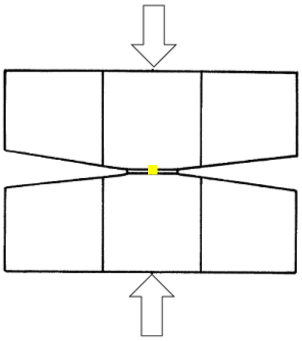	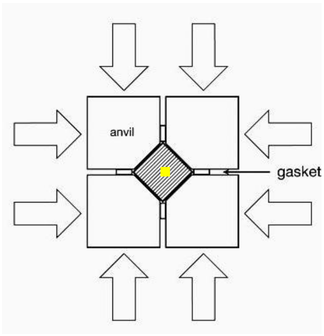	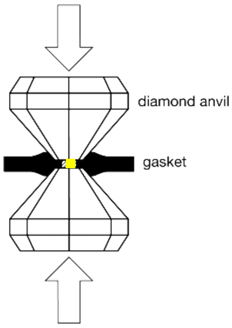
Range of pressure	<10 GPa	<25 GPa	<100 GPa

After Bridgman, continuous development of high-pressure devices were carried out; for detailed reviews about this development see the references by Hazen [1]; Eremets[2]; Holzapfel and Isaacs [3]; Liu and Bassett[4]. The uniaxial devices, with the opposed anvil design helped the appearance of the “belt” press invented by H. Tracy Hall [5] in 1960. Important developments in high-pressure apparatus was introduced by the “toroid” type press [6] and the “Paris–Edinburgh” instrument, which was designed for neutron scattering and *in-situ* experiments by Besson *et al.*[7-8]. Also multi-anvil devices that reach 24 GPa or higher were developed from von Platen’s [1, 9] and T. Hall’s [1] original designs for diamond production. These instruments are used to investigate the synthesis and phase transitions of new solid-state compounds and technological materials, as well as to study geomaterials in the earth’s interior science.

The DAC allow *in-situ* the studies under high-pressure up to a range of 100 GPa (1Mbar). Laser heating and resistive external heating allow the study under both high pressure and temperature parameters, as well as investigating the synthesis of new phases and materials.

The CONAC press at the Complutense University of Madrid is a uniaxial toroid press following the Russian design by Vereshchagin *et al.* [10, 11] in 1972. This press can work at high pressure and temperature up to a range of 10 GPa and 2073 K. In figure 2.2, the fully automatic apparatus of the CONAC is shown. The applied load is controlled hydraulically, while the power supply and temperature controller by a Eurotherm controller.

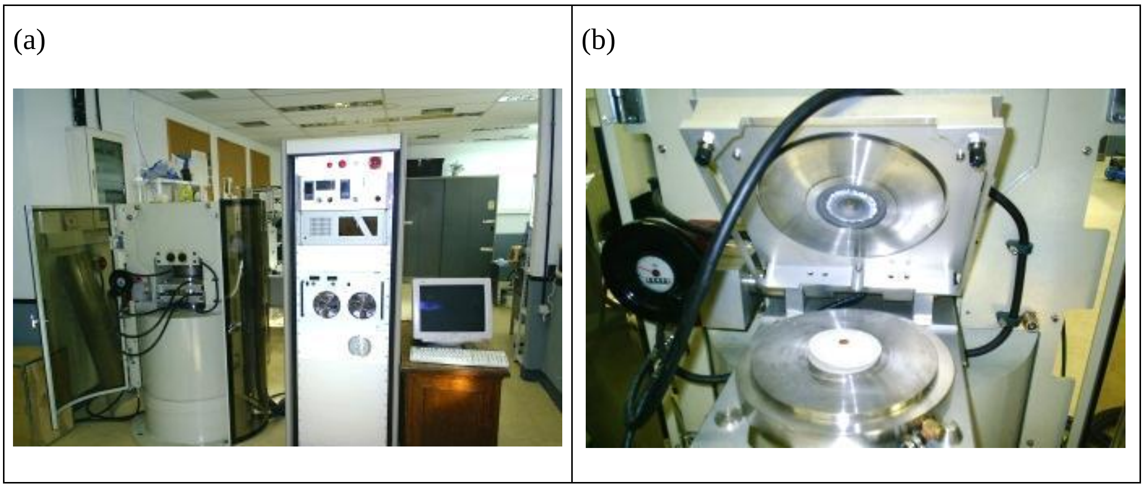

Fig. 2.2 The CONAC press: (a) an overview of the equipment and the control unit; (b) the exchange chamber

Figure 2.2(b) shows the exchange pressure chamber including an internal cooling circuit. Three chambers can be exchanged with each other depending on the required size and pressures to be applied on the samples. The small chamber (CONAC-15) can produce a sample of maximum weight of about 0.2 g, while the intermediate chamber (CONAC-28) can reach about 0.75 g and the big chamber (CONAC-40) can produce about 2.0 g of sample. Table 2.2 compares between the different chambers.

Table 2.2 Performance parameters of the 3 types of CONAC chambers.

	Conac-15	Conac-28	Conac-40
Maximum Pressure (GPa)	10	7.5	6
Applied force (ton)	400	1000	1500
Maximum temperature	1500	1500	1500
Sample volume	50 mm^3	400 mm^3	1 cm^3

In figure 2.3(a), the different components of a pressure cell are shown. The components are: (1) capsule containing the sample, (2) cylinder furnace, (3,4) two concentric calcite cylinder sleeves, (5) two calcite pieces, (6) calcite container, (7) two pyrophyllite caps, (8) two steel pistons, (9) two molybdenum and (10) two tantalum disks, (11) three cartoon rings. The type of the furnace (graphite or Mo) and the type of capsule (Au, Pt, Ta, Cu or steel) to be used depend on the temperature ranges of work and sample composition. A schematic drawing of the sample assembly is shown in figure 2.3(b).

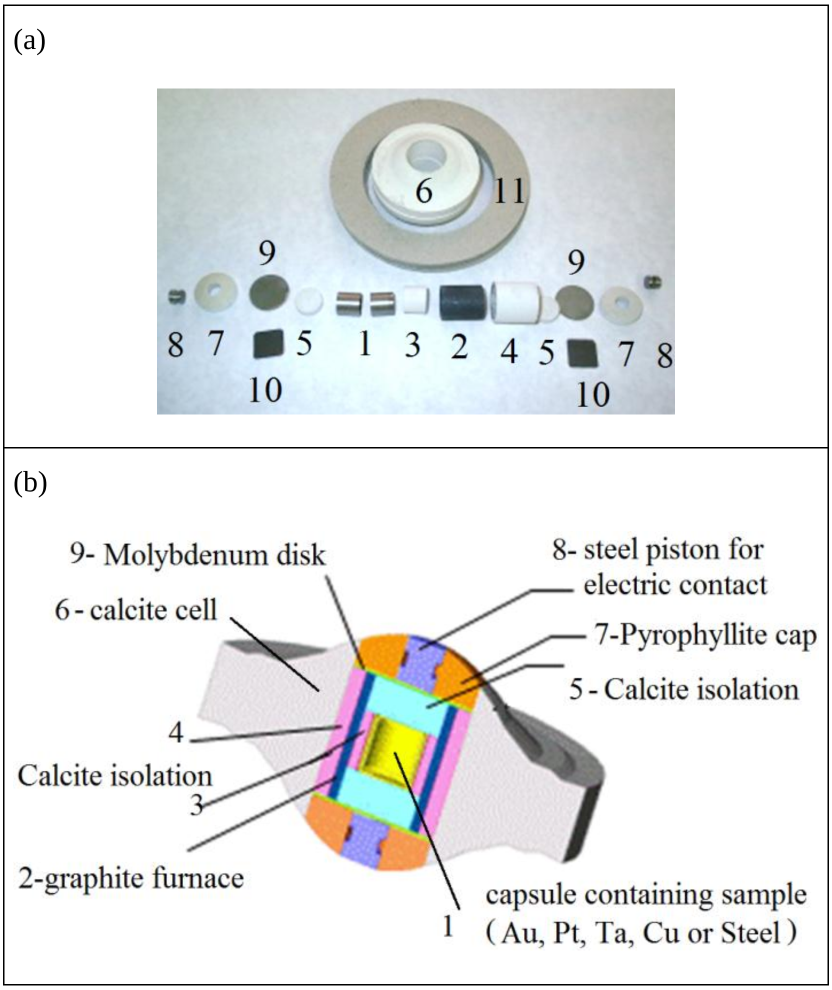

Fig. 2.3 The CONAC pressure cell: (a) different components of the cell; (b) schematic drawing of the cell assembly.

In this work all the zircon-phase samples, which were prepared by the precursor method, have been treated at high pressure and temperature by the CONAC press at the laboratory for high-pressure in the Complutense University of Madrid. A Conac press from Cyberstar (as shown in figures 2.2 and 2.3) was used for the synthesis of all the scheelite phases in this work. Au and Pt capsules were used to contain the samples and were packed in air at atmospheric pressure and then closed manually. The experimental parameters used in the synthesis of each sample are as follows: Pressure, 4 GPa; Temperature, (803 to 833 K); Time, 35-50 minutes.

In the CONAC press, as for many high-pressure apparatus, the temperature is usually controlled by the electrical resistance through the sample and by the electrical power supplied. Therefore, a careful control by the power to produce a gradual heating is highly desirable in order to avoid sudden increase of temperature above the required value. In addition, a good grinding of the sample allows not only a compact packing of the sample but also a homogeneous heating by excluding air voids in the sample. For more details about all control parameters used in the synthesis of each sample, see table 2.3.

As can be seen in figure 2.4, the heating of the sample begins after reaching the required pressure on the sample. Then the material is heated by electric power gradually and is then quenched to room temperature. After quenching, the load is reduced gradually.

Table 2.3 controlled parameters for the high-pressure synthesis

	Pressure (GPa)	Force applied (tons)*	Chamber	T_{max} (K)	Electrical control			Time at T_{max} (min)
					V	A	Wat/min	
$NdCrO_4$	4	515	Conac28	808	1.34	204	8	40
$SmCrO_4$	4	515	Conac28	808	1.36	201	8	40
$EuCrO_4$	4	515	Conac28	808	1.23	206	8	40
$GdCrO_4$	4	515	Conac28	808	1.25	218	8	40
$GdCrO_4$	4	900	Conac40	833	1.23	353	8	40
$DyCrO_4$	4	515	Conac28	808	1.32	207	8	40
$HoCrO_4$	4	900	Conac40	833	1.20	362	8	40
$ErCrO_4$	4	515	Conac28	808	1.33	206	8	40
$TmCrO_4$	4	515	Conac28	808	1.34	205	8	40
$YbCrO_4$	4	515	Conac28	808	1.33	205	5	50
$LuCrO_4$	4	515	Conac28	808	1.29	212	5	35

**The press rate is 7 tons/min in both loading and unloading cycles.*

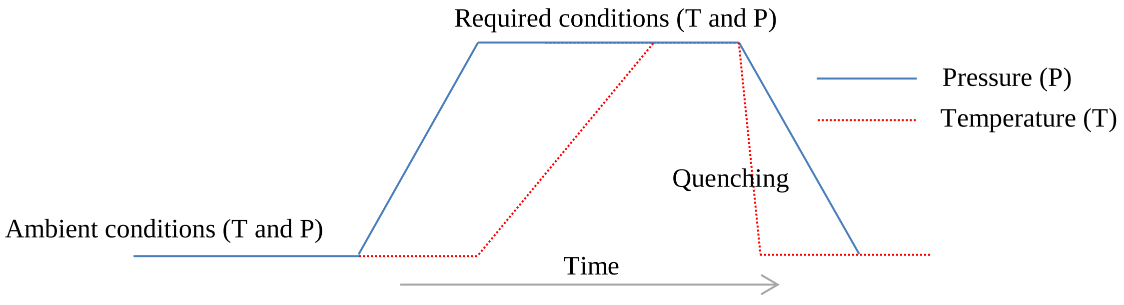

Fig. 2.4 Schematic diagram showing the control of the parameters of high-pressure experiment.

2.2 Powder Diffraction

Diffraction has played a central role in mineralogy, structural physics, chemistry and materials science since von Laue's classical discovery in 1912 that crystals would diffract x-rays. Important advances in the structural studies of materials have relied heavily on the powder diffraction technique. A major advance also is due to the development of the analysis by using the Rietveld method [12], which is a refinement process of structural parameters and factors. The Rietveld method, nevertheless, requires an approximation to the correct structure to be known in advance.

If a structural model is not available, it must first be determined. Structure determination from powder diffraction data is more difficult than that from single crystal data. This is associated with the collapse of the three dimensions of crystallographic information into the single dimension of a powder diffraction pattern. However, there are many materials for which no single crystals are available, which will be the case of the materials studied here.

2.2.1 X-ray powder diffraction

Atomic radii range from a few tenths of an Angstrom to a few Angstroms. A suitable wavelength to observe individual atoms is that of the x-rays, which is electromagnetic radiation having the wavelength appropriate for both the atomic sizes and the shortest interatomic distances.

The relationship between the directions of the incident and diffracted beams in a lattice was first given by Laue in a form of three simultaneous equations, which are commonly known as Laue equations:

$$\begin{aligned} &a\,(\cos\psi_1 - \cos\varphi_1) = h\lambda \\ &b\,(\cos\psi_2 - \cos\varphi_2) = k\lambda \qquad (2.3)^{[13]} \\ &c\,(\cos\psi_3 - \cos\varphi_3) = l\lambda \end{aligned}$$

here a, b and c are the dimensions of the unit cell; $\psi_{1\text{-}3}$ and $\varphi_{1\text{-}3}$ are the angles that the incident and diffracted beams, respectively, form with the parallel rows of atoms in three independent directions; the three integer indices h, k and l are Miller indices. The integers h, k and l are unique for each diffraction peak and define the position of the peak in the reciprocal space. The term λ is the wavelength of the used radiation. More useful in powder diffraction is the law formulated by W. H. and W. L. Bragg, which states that "diffraction from a crystalline sample can be explained and visualized by using a simple notion of mirror reflection of the incident x-ray beam from a series of crystallographic planes" [13]. Diffraction from a set of equally spaced objects is only possible at specific angle(s) and the possible angles, θ, are established from

Braggs' law, which is derived geometrically in figure 2.5. Bragg's law can be described by a short formula:

$$2\, d_{hkl} \sin\theta_{hkl} = \lambda n \tag{2.4}$$

which relates the wavelength λ, diffraction angle θ and interatomic spacing d for a reflection with certain Bragg indexes h, k, l. The integer n is known as the order of reflection.

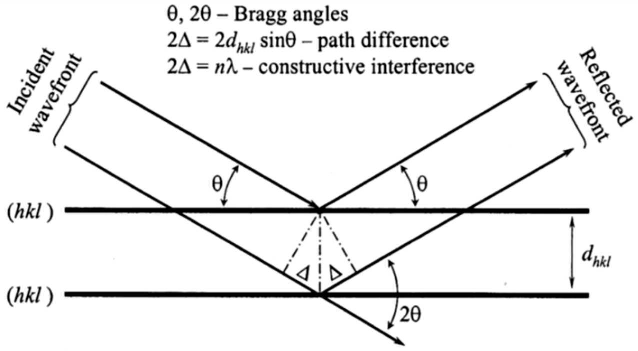

Fig. 2.5 Geometrical illustration of the Braggs' law. [13]

The x-ray beam interacts with the electron clouds distributed around the nucleus of the atom, as shown schematically in figure 2.6. Consequently, not all electrons are expected to scatter in phase. These phase differences lead to partial interference and a net decrease in the scattered amplitude for an atom, so that the scattering efficiency is a function of the Bragg angle θ and falls off with $(\sin\theta)/\lambda$ (figure 2.6).

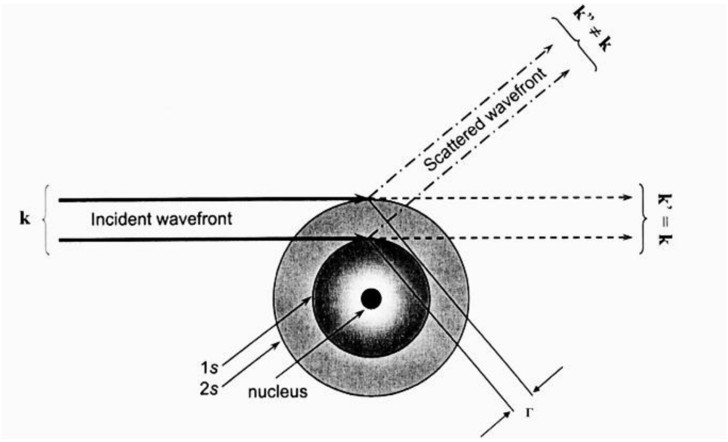

Fig. 2.6 The schematic representation of the elastic scattering of x-rays by s electrons illustrating the introduction of a path difference, Γ, into the wavefront with a propagation vector k'', where k'' ≠ k of the incident beam. The distribution of electrons in two s-orbitals is determined from the corresponding wave functions.[13]

In figure 2.7, the form factors for different elements are shown. One can notice that not only for a certain element the intensities of reflections decreases with increasing the diffraction angle, but also the intensities of the reflection changes from one element to another due to the different number of electrons. Furthermore, the intensity is proportional to the square of the form factor. Therefore, for example, to locate the atomic position of hydrogen, x-ray diffraction would not be the best way.

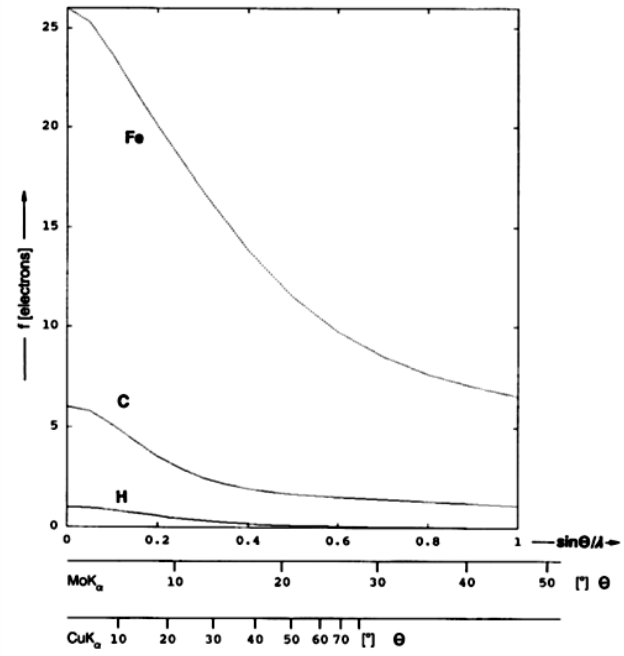

Fig. 2.7 Examples of the dependence of the atomic scattering factor (also called form factor) on the scattering angle. It shows how rapidly the intensity of reflections must decrease with increasing diffraction angle in case of x-ray powder diffraction. [14]

2.2.1.1 XRD at ambient conditions

In this study, *R*CrO_4 scheelite samples were first studied by x-ray powder diffraction using a Philips X'Celerator diffractometer with a primary beam monochromator consisting of a curved Ge (1 1 1) crystal aligned to obtain Cu- $k\alpha_1$ radiation. Furthermore, a Bragg–Brentano geometry in a reflection mode was used. A range of 2θ-angle between 10° and 90° was recorded with a step size of 0.0167°. The diffractograms of rotating samples were finally obtained at ambient temperature and pressure conditions and in air atmosphere. The diffractograms were collected at the CAI center of the Complutense University of Madrid.

2.2.1.2 In-situ XRD at high temperatures

Some selected samples were studied with X’Pert PRO MPD diffractometer in a θ - θ configuration with a high-temperature camera Anton Paar HTK1200 furnace and an X’Celerator RTMS solid-state detector. A nickel filter was used allowing a Cu-$k\alpha_{1,2}$ radiation. The diffractograms were recorded at room temperature, as well as from 373 to 1173 K with a temperature step of 100 K. A heating rate of 10 $Kmin^{-1}$ was applied in addition to a dwelling time of 15 min for each temperature before collecting the diffractogram in order to stabilize the temperature and obtain a uniform homogeneous structure in the sample. For the 2θ-angle range, diffractograms were collected between 10° and 70° with a step size of 0.03°.

For the sample and environment assembly, a higher load circular alumina sample holder was used with a diameter of 18 mm and was coated with a platinum foil in air atmosphere. The diffractograms were collected at the CAI center of the Complutense University of Madrid.

2.2.1.3 In-situ XRD at low temperatures

A diffractometer Panalytical X'Pert PRO MPD in a θ-θ configuration with a low temperature Oxford-PheniX cryostat. A radiation of Cu-k$\alpha_{1,2}$ was used by applying a nickel filter. Selected samples were studied at 100, 50, 28, 20 and 13 K. For the used cryostat, the minimum temperature that can be achieved is between 13 and 12 K. On the other hand, a step size of 0.03° for a range of 2θ-angle between 5° and 90° has been applied. The diffractograms were collected at CAI center in the Complutense University of Madrid.

2.2.2 Synchrotron-radiation powder diffraction

An accelerated charge will radiate some electromagnetic radiation and upon that lose energy. This radiation is called Bremsstrahlung when the accelerating field is electric, which is the base of standard x-ray tubes. However, this radiation is called synchrotron radiation when the charge is accelerated by a magnetic field. Such a radiation is observed for sufficiently high-electron (positron) accelerators. The total synchrotron radiation power which is produced grows rapidly with the electron energy. Therefore, a storage ring is designed to recirculate the beam for as many cycles as possible in a well evacuated chamber. The beam dynamics and component design of particle accelerators can be traced back to Maxwell's equations, and the pioneering work of J. C. Maxwell, H. A. Lorentz and A. Einstein that established the concepts and the physical understanding basics required to build such machines [15].

The unique properties of synchrotron radiation (SR) such as wide-energy tunability, high brilliance, high collimation, polarization and time structure have enabled a number of new and important techniques since the early days of its use in the 1960s. However, the greatest advance occurred in the early 1990s when the first third generation source became available providing extremely brilliant beams in the 100 nm to 1 μm size range. To date there exist more than 100 synchrotron radiation sources in operation in the world serving many areas of science ranging from chemistry, biology, physics, material science, medicine to industrial applications.

DORIS III, at DESY synchrotron facility in Hamburg, is an example for a storage ring for charged particles. The originally double storage ring has been modified to a dedicated synchrotron source. Its circumference of 289 meters allows to store positrons or electrons at an energy of 4.45 GeV and in bunched packages. Typically 2 or 5 bunches of positrons are stored in DORIS III with an initial beam current of up to 120 mA. The corresponding time interval between the bunches is 480 nsec or 192 nsec [16, 17].

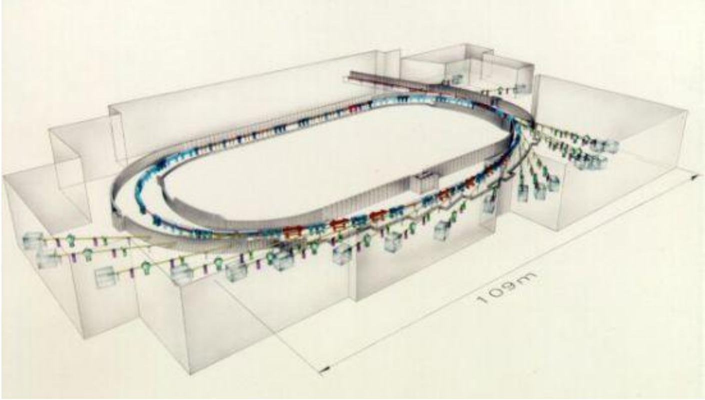

Fig. 2.8 Drawing of the DORIS storage ring and some of its beamlines and experimental stations [6].

Our two samples of $ErCrO_4$ and $SmCrO_4$ scheelites were investigated at room temperature at the Beamline: B2 for high resolution powder diffraction. This beamline is very useful for the structure analyses on polycrystalline samples, which allow the detection and analysis of subtle structural details.

As an attempt to get a high-resolution diffraction pattern for the high-pressure sample containing secondary, the $ErCrO_4$ and $SmCrO_4$ scheelite were investigated by high-resolution powder diffractometry at the B2 beam line of the DESY Synchrotron Facility in Hamburg, Germany. Experiments were carried in transmission geometry at room temperature for a rotating sample. The available wavelength range for the instrument is 0.3 to 2.4 Å, of which a wavelength of $\lambda = 0.769428$ Å was used for our experiment at room temperature.

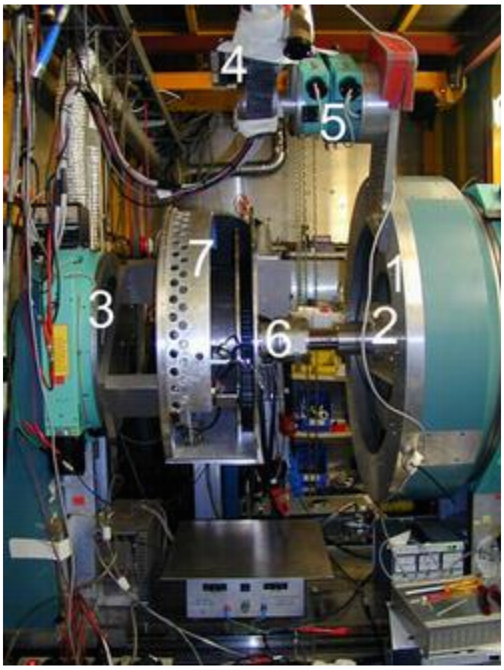

Fig. 2.9 View of the B2 diffractometer. The synchrotron beam enters the hutch from the back. The monochromator vessel is behind the diffractometer inside the hutch. 1: Huber circle 480 carrying the single counter. 2, 3: Huber circles 440 for sample environments or image-plate detector which can be moved laterally. 4: Single counter with analyser crystal and attenuator. 5: Two Huber circles 410 for counter alignment. 6: Stoe furnace. 7: Image-plate detector [17].

2.2.3 Neutron diffraction

When a beam of neutrons hits a material, several things can happen. Some neutrons will be absorbed, others will emerge in a new direction with or without a change in energy, and the rest will pass through the material unaffected. Those that emerge in a new direction are described as "scattered" neutrons, investigated by neutron scattering methods. Neutron diffraction, generally refers to a “no need to determine the change in neutron energy at scattering”. Today’s experiments can use either beams with selected constant-wavelength (CW) generated from steady-state reactors, spallation sources, or pulsed spallation sources. Such a technique is primarily used to determine the nuclear atomic structures of crystalline materials and to determine magnetic structures.

A low energy (non-relativistic) neutron has energy **E**, wave vector **k**, velocity v, and wavelength λ. These quantities are related as follows:

$$|\mathbf{k}| = \frac{2\pi}{\lambda}; \quad \lambda = \frac{h}{mv}; \quad E = \frac{1}{2}mv^2 = \frac{h^2}{2m\lambda^2}, \tag{2.5}$$

where **h** is Planck’s constant and m is the mass of the neutron [18].

Neutrons are scattered by the atomic nucleus but also interact, through magnetic dipolar forces, with unpaired electrons, thus enabling the investigation of magnetic structures. In a scattering event (fig. 2.10a) the energy of the incident neutron is $\mathbf{E_i}$ and that of the scattered neutron is $\mathbf{E_f}$. (The subscripts "i" and "f" mean "initial" and "final" respectively.) Similarly, the incident and scattered neutron wave vectors are $\mathbf{k}_i$ and $\mathbf{k}_f$. The energy transfer $\hbar\omega = \mathbf{E_i} - \mathbf{E_f}$ is the energy transferred to the sample by the neutron when it is scattered. Similarly the wave vector transfer, or scattering vector, is $\mathbf{Q} = \mathbf{k}_i - \mathbf{k}_f$. The cosine rule, applied to the ($\mathbf{Q}$, $\mathbf{k}_i$, $\mathbf{k}_f$) scattering triangle (figure 2.10b), gives $\mathbf{Q^2 = k_i^2 + k_f^2 - 2k_i\, k_f} \cos(2\theta)$, where 2θ is the scattering angle (the angle between the incident and scattered neutron beam directions) [18]. For the special case of elastic scattering, *i.e.*, scattering in which the energy of the neutron does not change, $\mathbf{E_i = E_f}$, $\hbar\omega = 0$, $\mathbf{k_i = k_f}$, and $\mathbf{Q = 2k_i} \sin\theta = 4\pi\sin(\theta) / \lambda_i$ where λ_i is the incident wavelength.

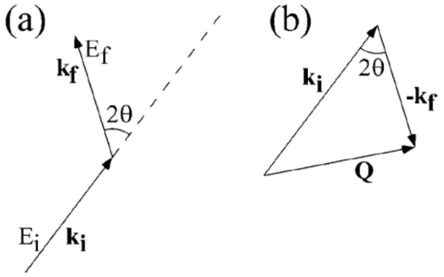

Fig. 2.10 A scattering event is illustrated (a) in real space: (b) shows the corresponding scattering triangle. The symbols are defined in the text. [7]

The scattered intensity in a neutron diffraction experiment is proportional to $\mathbf{I_0NS(Q)}$ where $\mathbf{I_0}$ is the incident beam intensity and **N** is the total number of atoms in the crystal. In other words, the more time to pass, the more intensity we get. The structure factor $\mathbf{S(Q)}$ is given by

$$S(\mathbf{Q}) = \frac{1}{\mathrm{N}} \left|\sum_i^{\mathrm{N}} \mathbf{b_i} \exp(iQ.\mathbf{r_i})\right|^2 \tag{2.6}$$

where the sum is over all atoms, $\mathbf{r}_\mathrm{i}$ is the position of atom **i**, and $\mathbf{b_i}$ is the "scattering length" or scattering amplitude for the nucleus of atom **i**, which is a measure of the strength of the interaction between the incident radiation and the nucleus [18].

Comparing the two techniques of x-rays and neutron diffraction, the scattered intensity per time is generally much greater for x-rays than for neutrons, figure 2.11. On the other hand, neutrons interact with the nucleus while x-rays interact with electron cloud, thus x-rays provide information about the electron density distribution in a material whereas neutrons give nuclear positions. Therefore, qualitatively different information can be extracted from the two probes.

For x-rays, the forward scattering value of f(Q), *i.e.* f (0), is proportional to the number of electrons, *i.e.*, to the atomic number Z, while this does not apply for neutrons and no simple relationship between the corresponding quantity, *b*, and the composition of the scattering nucleus. Thus, new information can be extracted from neutron diffraction like distinguishing between elements close to each other in the periodic table and detecting light atoms including H, C, N and O (see fig. 2.11). The neutron-nucleus scattering length also depends, sometimes dramatically, on the isotope whereas f(Q) does not since x-rays are scattered by electrons. Table 2.4 shows the coherent scattering lengths of the elements contributing to the $R\mathrm{CrO_4}$ oxides under investigation.

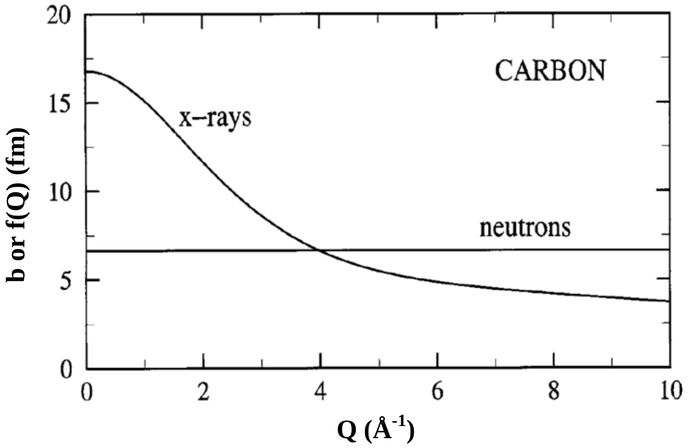

Fig. 2.11 The neutron scattering length of carbon, b, which is independent of Q, and the corresponding x-ray atomic scattering factor, f(Q). [18]

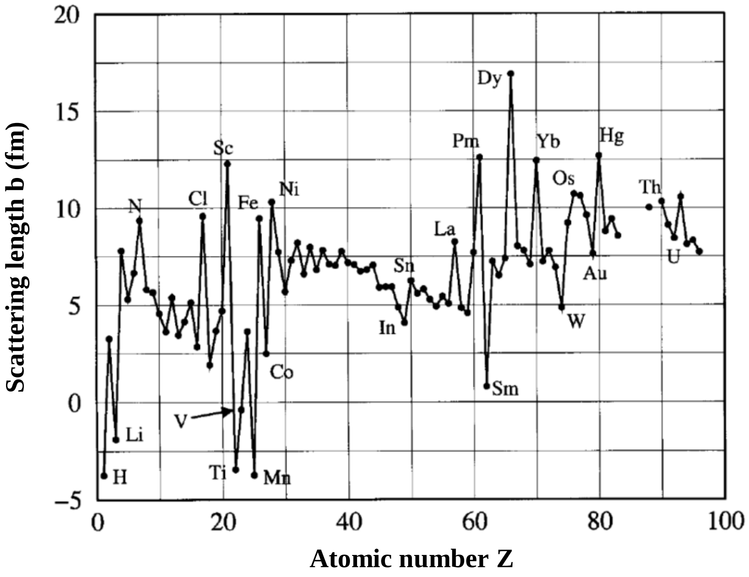

Fig. 2.12 The real part of the neutron scattering length b for the naturally occurring elements. [18]

Table 2.4 The coherent scattering lengths of constituents of the $RCrO_4$ **oxides** [19]

Element	**O**	**Cr**	**Y**	**La**	**Pr**
Coh. b*	5.803	3.635	7.75	8.24	4.58
Element	**Nd**	**Sm**	**Eu**	**Gd**	**Tb**
Coh. b*	7.69	0.80-1.65*i*	7.22-1.26i	6.5-13.82i	7.38
Element	**Dy**	**Ho**	**Er**	**Yb**	**Lu**
Coh. b*	16.9-0.276*i*	8.01	7.79	12.43	7.21

* *Bound coherent scattering lengths (Coh. b) are listed in fm units (1 fm =* 10^{-15} *m)*

On the other hand, as neutrons penetrate materials deeply due to its neutral charge; many advantages appear in investigating bulk materials in addition to a relatively easy-designed sample environment. The neutron beam readily penetrates the various structures that surround the sample, *e.g*. cryostats, furnaces, magnets and high-pressure cells. However, the probability of neutron absorption by nuclei (expressed in barns unit) of the natural elements are shown in fig. 2.13. Once again, there are large fluctuations from one element (or even its isotope) to another.

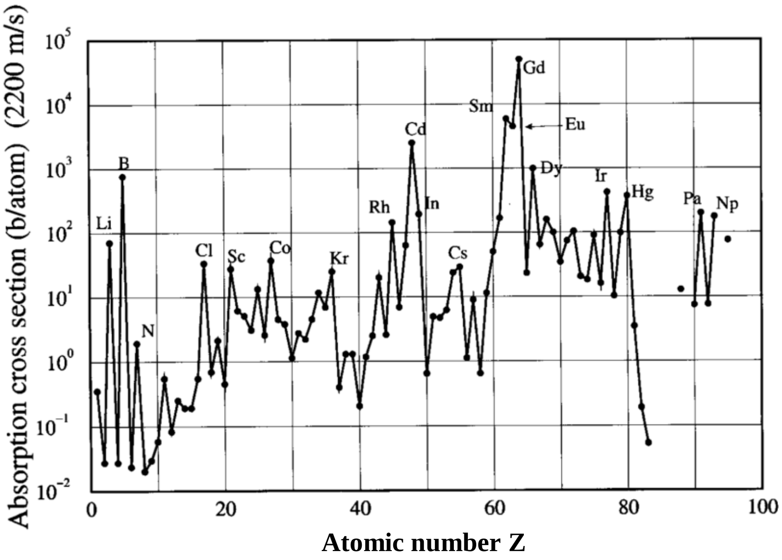

Fig. 2.13 The absorption cross section for 2200 m/s neutrons for the naturally occurring elements. Notice that the ordinate is plotted on a log scale. [18]

Therefore, we can clearly see that some elements, like on the top of them Gd and Sm, absorb the neutron beam and exhibit a very high difficulty in investigating them by neutron diffraction. In these cases, either special equipment would be needed or a use of element isotope shall be considered. In the lanthanide series, the highest absorption results from the elements Gd, Sm, Eu and Dy, in a descending order. In addition, some of these elements like Sm, have already a small scattering length, which makes the investigation by neutron radiation of the naturally occurring Sm-compounds highly complicated.

2.1.3.1 The The Hot Neutron Two-Axis Diffractometer (7C$_2$) at LLB

The Orphée nuclear reactor in the CEA-Saclay Centre, the Léon Brillouin Laboratory (LLB) is located as a joint Laboratory between CNRS (French National Center for Scientific Research) and CEA (French Atomic Energy Commission). Figure 2.14 shows the instruments and beamilines located at this reactor.

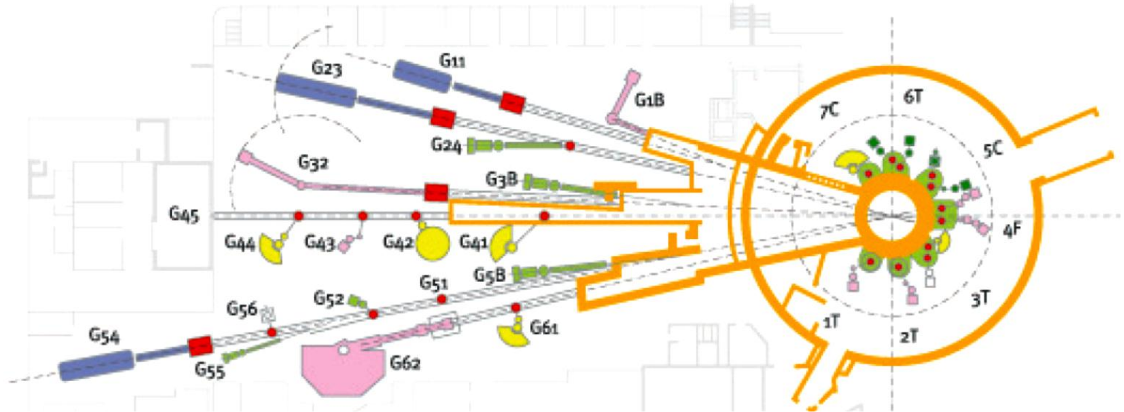

Fig. 2.14 Instruments and beamlines at the Orphée nuclear reactor in the CEA-Saclay [20]**.**

The $7C_2$ instrument is built on one of the two beams of the hot source of the Orphée reactor at Saclay and uses three monochromators in a rotating shield to allow both discrete and continuous variation of the incident wavelength. The standard position for the monochromating angle is 20° and corresponds to wavelengths of 0.58, 0.7 and l.l Å. The instrument is usually used for structural investigations of liquids, glasses and amorphous materials in order to determine the local order on disordered systems. The position sensitive detector is a curved multidetector filled with $^{10}BF_3$. The 640 cells of the detector cover a scattering angle $2\theta = 128°$ (step 0.2°). The sample to detector distance is 1.5 m. Three monochromator crystals of Ge(111), Cu(111) and Ge(311) allow for the three incident wavelengths of 1.1, 0.7 or 0.58 Å [21, 22], respectively.

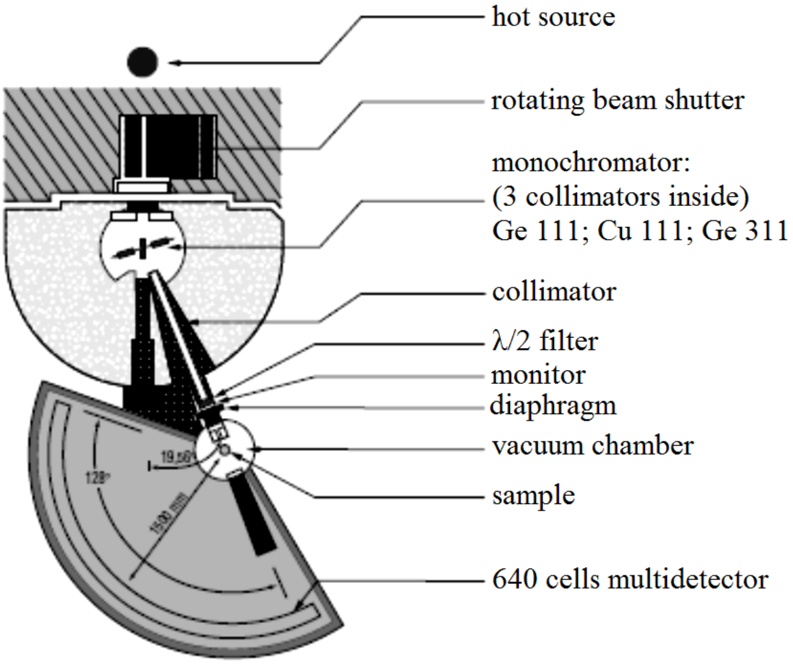

Fig. 2.15 Schematic diagram of the $7C_2$ diffractometer [20]

To investigate $GdCrO_4$-scheelite nuclear and magnetic structures, we carried out the the powder diffraction at $7C_2$ two-axis diffractometer. The instrument was important to be used because of the large absorption cross section of the natural gadolinium nuclei for thermal neutrons, as mentioned in Fig. 2.13. A small incident wavelength of 0.581 Å was selected, corresponding to a Ge(311) monochromator setting, in order to reduce the probability for gadolinium nuclei to absorb neutrons.

The polycrystalline powder was loaded in a vanadium annular can. The sample geometry corresponds to a double-walled cylinder of diameter 10 mm × 12 mm that occupies the whole beam size with a small sample thickness. With this geometry, the intensity signals were improved as absorption was relatively reduced. The sample was placed in a 600 mm diameter vacuum vessel. A cryostat was also installed to investigate the temperatures between

2 and 100 K. The cryostat tail in the beam is made also from vanadium. Subsequently, the residual background of the sample environment was subtracted from the resulted diffraction patterns after measuring the empty vanadium sample holder in the same experimental conditions. The diffractograms were collected in the above mentioned temperature range at 10, 17, 24 and 40 K, while longer times were allowed for the diffractograms taken at 100 and 2 K in order to determine the nuclear and magnetic structures.

2.1.3.1 The WISH powder diffractometer at ISIS

High-resolution cold-neutron powder diffraction excels when multiple nearly overlapping Bragg peaks occur at long *d*-spacing. In this case, sheer flux is not sufficient to extract all the available information, and much better results can be obtained with a high-resolution diffractometer, even at the cost of losing some flux. A The High-resolution cold-neutron powder diffractometer (called WISH) at the ISIS facility in Oxfordshire, UK.

WISH is a long-wavelength diffractometer primarily designed for powder diffraction at long *d*-spacing in magnetic and large unit cell systems, with the option of enabling single-crystal and polarized beam experiments. The diffractometer works as a time-of-flight (TOF) diffractometer, in which no constant wavelength beam is used but rather a wide range of (1.5-15Å).

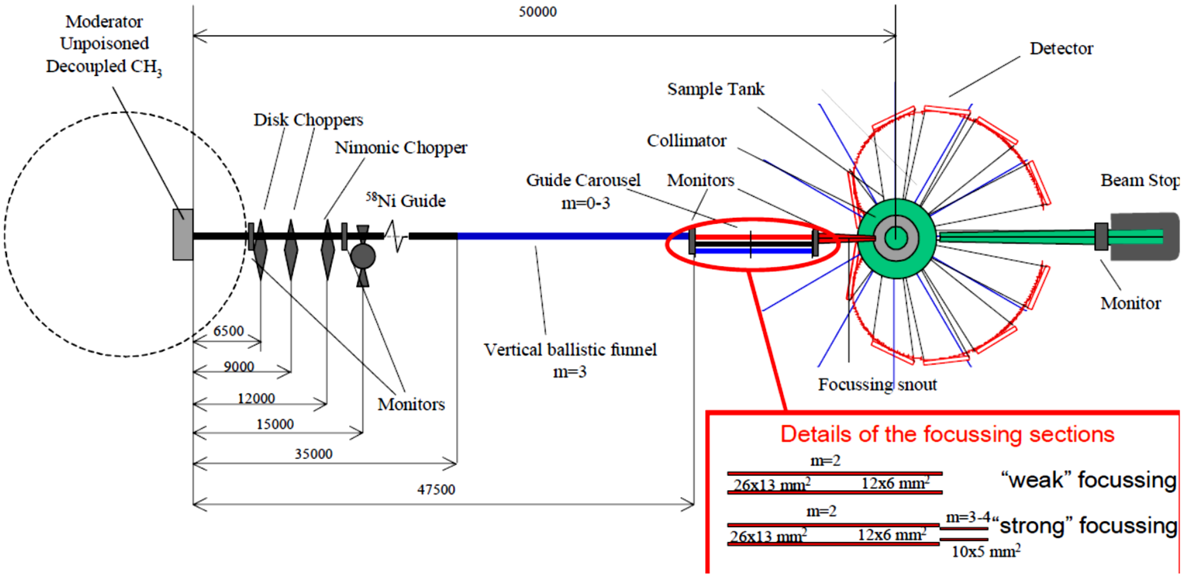

Fig. 2.15 Schematic layout of the WISH diffractometer [23]**.**

The diffractometer is equipped with ZnS scintillator detectors covering all scattering angles between 10º and 175º. A beam size between 20 x 40 mm^2 (unfocussed) and 1 x 1 mm^2 (super-focused) can be used. The WISH instrument, as a TOF powder diffractometer, is very effective in investigating magnetic materials due to its ability to represent clear view of long-range order of the magnetic peaks and consequently the magnetic structure determination.

However, for structural analysis, it is not as competitive as the CW diffractometers. The later have a higher neutron flux on the sample and a more sharply peaked resolution function. Unlike CW difractometers, a high peak overlap at short *d*-spacings can introduce a difficulty in studying some structural features of the material under investigation. Therefore, there are a number of areas where the two types of machines are distinctly complementary to each other.

2.2.4 Refinement of powder diffraction data

Upon the discovery of powder diffraction method in 1916, it was first used almost exclusively for qualitative and semi-quantitative phase analysis. This changed completely after 1969, with the development of the Rietveld method [24, 25], a technique for the refinement of crystal structures using the entire information of a powder diffraction pattern.

As for the position of Bragg-reflections, it is exactly defined by the dimensions of the unit cell. If the unit cell parameters are known, indexing of the diffraction pattern can be done easily [26]. However, indexing of a powder pattern without knowing the lattice parameters is a non-trivial task, as it is the case for powder diffraction of many new materials. There is no guarantee that a powder pattern can be indexed and it is commonly necessary to try out different computer programs employing different algorithms. The method of choice strongly depends on the symmetry of the crystal system. The difficulty lies in the proper selection of reflections for the determination of the reciprocal lattice parameters. A large number of combinations must usually be tested before the correct lattice can be found. After indexing of a sufficient number of reflections the lattice parameters can be refined using the method of least squares. Once a set of lattice parameters has been obtained, it is strongly recommended to check them against all measured reflection positions *e.g.* by applying a Pawley- or LeBail-fit (explained briefly afterwards).

The last step of the structure determination from powder diffraction data is the refinement and powder pattern profile fitting, the main method for which is the Rietveld method. The basic idea behind the Rietveld method is the calculation of the entire powder pattern using a variety of different refinable parameters [25, 26]. The resulting parameters can consequently be roughly divided into structural, profile and background parameters. The weighted sum of the squared differences between the observed and the calculated powder pattern is then minimized by refining a selection of parameters using least squares methods. The quantity minimized in the least-squares refinement is the residual, $\boldsymbol{S_y}$:

$$\boldsymbol{S_y} = \sum_i \boldsymbol{w_i}\,(\boldsymbol{y_i} - \mathbf{y_{ci}})^2 \tag{2.7}$$

where: $\boldsymbol{w_i} = 1/\boldsymbol{y_i}$, $\boldsymbol{y_i}$ is the observed (gross) intensity at the i^{th} step, $\boldsymbol{y_{ci}}$ is the calculated intensity at the i^{th} step, and the sum is overall data points [25]. This will allow comparing the observed and calculated intensities of the whole diffraction pattern. For further details, review the references [25 and 26].

Many different statistical agreement factors have been proposed for judging the quality of a Rietveld refinement. The most common one is the so called weighted profile R-factor which is defines as

$$R_{wp} = \sqrt{\frac{\sum_i w_i \left(y_i(obs) - y_i(calc)\right)^2}{\sum_k w_i y_i(obs)^2}} \qquad (2.8)$$[25]

Finally, the graphical representation of a Rietveld refinement, shows the observed powder pattern, the best Rietveld fit profile, the reflection positions and the difference curve between observed and calculated profiles as a trace underneath.

Nowadays, the LeBail-method is a widely used technique to refine the total envelope of a powder pattern without knowing the crystal structure and to extract intensities, which can later be used for crystal structure determination. In other words, one can check the space group and refine easily the lattic parameters with this method without any knowledge of the atomic positions in lattice. The basic idea used is relatively simple as the LeBail method iterates the Rietveld decomposition formula.

$$\boldsymbol{I_K\,(obs) \underset{i}{=} \sum\{w_{i,K} \cdot S^2{}_K\,(calc) \cdot y_i\,(obs)\,/\,y_i\,(calc)\}} \qquad (2.9)$$

where $w_{i,K}$ is a measure of the contribution of the calculated Bragg peak at position $2\theta_K$ to the diffraction profile y_i at position $2\theta_i$. The sum is over all y_i(obs) that can theoretically contribute to the integrated intensity I_K(obs) [26]. This results in I_K (obs) which are then re-inserted as new $S^2{}_K$(calc) values at the next iteration, while the usual profile and cell parameters (but not the scale) are refined by least-squares.

A feature that increases the stability and effectiveness of the Le Bail fitting process is the ability to recycle the intensities into the next round of fitting. GSAS [27, 28] and Fullprof [29, 30] are two common Rietveld programs with well-developed Le Bail fitting options.

Generally, the sample is a very important leading factor in the structure determination process. Even if the material is not possibly obtainable as a single- or even micro-crystal, the time invested in producing a high-quality polycrystalline sample (*e.g.* high purity and crystallinity), before trying to determine the structure, is a time well spent indeed.

In this work, all obtained diffraction patterns were analyzed using the FullProf Suit Program, version May 2012. The diffraction patterns were refined first by Le Bail fit and then by Rietveld refinements for all samples. Indexing of synchrotron diffraction patterns of $ErCrO_4$ scheelite at room temperature were done using DICVOL04 [31].

Lattice parameters, atomic positions, overall temperature factor and magnetic moments were refined by the Rietveld method using the FullProf Suite program. The symmetry analysis was performed by means of the program BasIreps [32].

2.2.5 Bond-valence method

The bond-valence method is a method recently used in solid-state chemistry, which is very useful in a number of ways. The most obvious application in crystallography is to determine the coordination number [33], predict bond lengths from a given bond valence [34, 35] and *vice versa*. In addition, it is useful for using bond-valence sums at atoms as a check on the reliability of the determined structure. At a lower level, it is useful to decide if there is a significant bonding interaction between pairs of atoms. The method in return can be carried out to estimate the oxidation states of atoms by summing the individual bond valences surrounding an atom in correspondence with the observed bond lengths.

The phenomenological relation between the bond valence and the bond length can be expressed as

$$v_{ij} = \exp \frac{R_0 - R_{ij}}{B} \qquad (2.10)$$ [36]

where R_0 is a constant characteristic of the cation-anion pair, R_{ij} is the bond-valence parameter representing the observed bond length in Å between atom *i* and its *j* coordinated atoms. B is an empirical constant usually used universally as 0.37 Å [36] but was found later to have a range between 0.26 and 0.51 Å [37]. The valence sum rule (VSR) establishes that the sum of valence bonds around a cation (anion) must be equal to the formal valence (charge) of the *i*-cation (anion) (i.e. BVS= $\sum_j v_{ij} = V_{ij} \approx \mathrm{abs(q)}$).

This method has been used by mineralogical crystallography for many years with very useful results because the VSR is verified within a few percent for many inorganic compounds. However, one of the bases of the VSR is that the structure should permit the release of the stress introduced by the coexistence of different structural units, i.e. the structure should have enough degrees of freedom. In case like highly symmetric structures or ions with very strong Jahn-Teller effect, or compounds with disorders or vacancies, such a simple calculation is of limited validity.

Nevertheless, well-determined structures should be used for a detailed interpretation of bond lengths. This is because the small deviations in the bond-length value can result in big deviations in the calculated valence values. For example, a combined error of 0.01 Å in R_{ij} and bond length will result in an error of 2.7% in the derived valence, while an error of 0.05 Å will correspond to 14% error in the valence [38]. Another source for the deviation in bond-length values can result from the relative compression of bonds after a high-pressure synthesis. Therefore, analysis based on laboratory x-ray diffractometers can be difficult to analyze with the bond-valence method.

From the deviation of the valence sum around each ion with respect to the expected value, there is a clear evidence of possible instabilities (or unusual features) in the crystal structure. In chapter 4, the valence bond valence sums (BVS) of the different zircon and scheelite $R\mathrm{CrO}_4$ compounds are calculated. The values for the zircon polymorphs are calculated by Bond_Str program (integrated in the FullProf_Suit[29, 30]) using the cell parameters and atomic positions reported by Jiménez Melero [39].

Bond valence parameters are chosen to normalize the bond valences by ensuring that, on average, they obey the valence sum rule. Ideal bond lengths determined from the theoretical bond valences are required to obey this rule by definition. However, there are occasions when these ideal bond lengths must be strained if the structure is to be mapped into three-dimensional space [37].

The root-mean-square deviation of the experimental bond valence sums (BVS) from the atomic valence is a measure of the extent to which the valence sum rule (VSR) is violated over the whole structure [40]. This is referred to as the global instability index (GII). The deviations are averaged over all the atoms in the formula unit, which provide a measure of the degree of failure of the valence sum rule (VSR) and inform about the distortion of the structure, as presented in four different ways as follows:

$$\text{Old Global Instability Index (GII)}=\sqrt{\frac{\sum|\mathrm{BVS}-\mathrm{abs(q)}|^2}{\text{N of Atoms}}} \qquad (2.11)^{[30]}$$

$$\text{Normalized GII(a)}=\frac{\sum|\mathrm{BVS}-\mathrm{abs(q)}|\times mult}{\text{N of Atoms per U.Cell}} \qquad (2.12)^{[30]}$$

$$\text{Normalized GII(b)}=\frac{\sum\{|\mathrm{BVS}-\mathrm{abs(q)}|\times mult/\mathrm{abs(q)}\}}{\text{N of Atoms per U.Cell}} \qquad (2.13)^{[30]}$$

$$\text{Normalized GII(c)}=\sqrt{\frac{\sum|\mathrm{BVS}-\mathrm{abs(q)}|^2\times mult}{\text{N of Atoms per U.Cell}}} \qquad (2.14)^{[30]}$$

where *mult* is the multiplicity of the atomic position in the crystal structure. The old GII is calculated with the atoms of the symmetric unit (number of atoms). The normalized GII (a,b,c) are calculated by the Bond_Str program [30] using the sum over asymmetric unit but multiplying differences by the multiplicity of the site. In all cases, the resultant of the different indices is multiplied by 100.

2.3 Thermal Gravimetric Analysis

Thermogravimetric Analysis (TGA) measures the change rate and amount in the material weight in a controlled atmosphere as a function of temperature or time. The weight loss curve could require, however, further modification, *e.g.* a derivative weight loss curve, or deconvolution of the overlapping peaks may be necessary before interpreting the results. During the measurement, one of the material components decomposes and produces a gas or vapor that can be carried away usually by a purging gas, e.g. air, oxygen or nitrogen.

Thermal stability of the synthesized scheelite-type compounds has been studied by thermogarvimetric analysis (TGA) and differential scanning calorimetry (DSC) using SDT Q600 TA Instrument. These measurements have been carried out in oxygen flow of 100 ml/min with a heating rate of 5 K min-1 in one ramp from room temperature to 1473 K. A correction of the obtained DSC curve has been done to avoid the difference in heating rate between the studied sample and the reference sample by subtracting the straight line representing this error.

2.4 Spectroscopy

There are many spectroscopic techniques that study the electronic and magnetic structure. Upon absorption of a photon by a solid some kind of excitations would be created, which reveal many properties of the solid by studying them. In this work, x-ray Photoelectron Spectroscopy (XPS) and x-ray Absorption Spectroscopy (XAS) were used to study the chemical and electronic states of $R\mathrm{CrO}_4$ compounds. The XPS spectra probe the occupied electronic states of the material, while the XAS spectra probe the unoccupied ones. In XPS, the electrons of various shells are excited to the vacuum by means of an incident radiation that has a constant photon energy $h\nu$. This photon energy is then transformed into the binding energy E_B taking into account the work function ϕ and the kinetic energy of the excited photoelectron, which is detected by an analyzer. The Binding energy of the electrons is then calculated and plotted for a certain energy range.

In XAS measurements, deeply bound core electrons are excited to an unoccupied state near the Fermi level which is strongly bound to the created core hole. Figure 2.16 illustrates schematically the difference between the XPS and XAS excitation processes.

2.4.1 X-Ray Photoelectron Spectroscopy

Photoelectron spectroscopy refers to the techniques based on the photoelectric effect which was first observed by Hertz in 1887 [41] and explained later in 1905 by Einstein [42] as a demonstration of the quantum nature of light. In 1957, Kai Siegbahn developed with his group a technique which was first called Electron Spectroscopy for Chemical Analysis (ESCA) and allowed the detailed study of core-level binding energies of solids [43]. Afterwards, upon the development of the technique, it has been called x-ray Photoelectron Spectroscopy (XPS) or photoemission spectroscopy. Siegbahn got half of the Nobel Prize in physics in 1981 for his contribution to the development of this high-resolution electron spectroscopy technique [44].

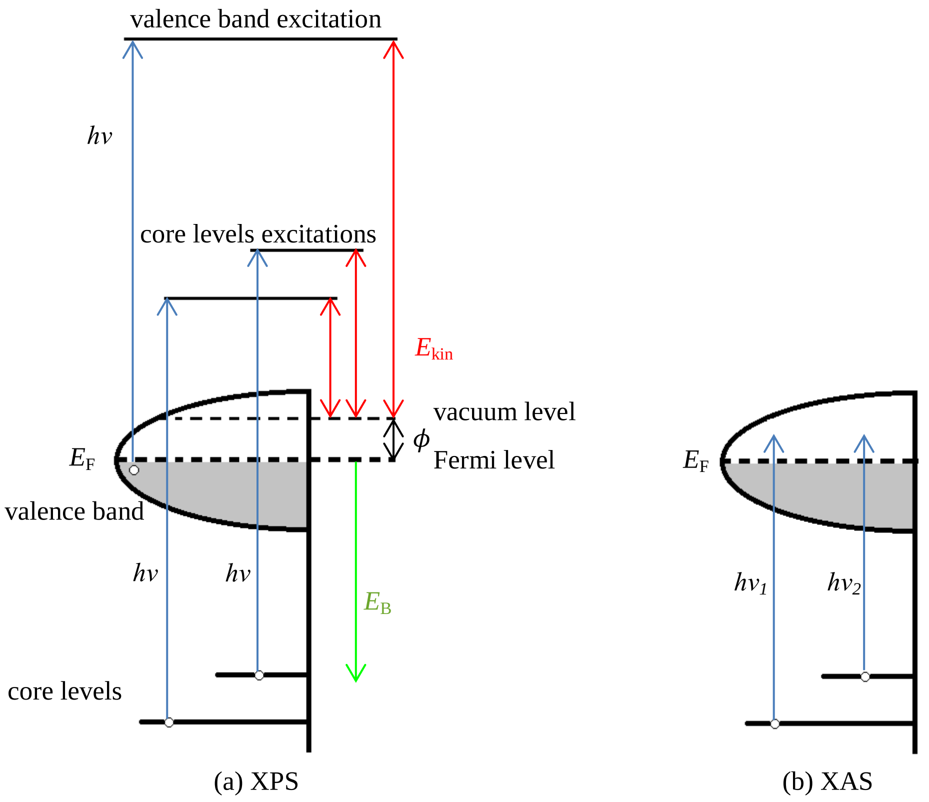

(a) XPS

(b) XAS

Fig. 2.16 Schematic independent particle illustration of excitation processes in case of: (a) XPS and (b) XAS.

In a photoemission experiment, a sample (solid, liquid or gas) is excited with photons of a well-known energy ($h\nu$). The photons absorbed by the sample cause consequently an emission of electrons, whose kinetic energy (E_{kin}) is hence measured by the electron spectrometer. The kinetic energy of the emitted electrons is expressed as:

$$E_{kin} = h\nu - E_B - \phi \tag{2.10}$$

where E_B is the binding energy of the atomic orbital and from which the electron originates. ϕ is the work function, which is the minimum energy needed to move an electron from the Fermi level into vacuum (figure 2.16 (a)). The binding energy we want to know is then calculated from equation (2.10).

2.4.1.1 Surface sensitivity

XPS can be used to identify the elemental concentration at the surface of a material, as each element shows a distinct set of binding energies called as chemical shifts, which are useful to define the chemical bonding of the material, due to differences in the chemical potential and polarizability. This is mainly because a photoemission measurement is highly surface-sensitive. Only the electrons corresponding to a surface layer of tens of angstroms (the first few atomic layers) will be able to leave the surface. Therefore, an XPS measurement must be performed under ultra-high vacuum (UHV) conditions.

This constriction is mainly because of that an excited photoelectron, compared to the incident photon, would have a much higher scattering probability and, in turn, loses a part of its kinetic energy. Thus, electrons of deeper atomic layers will lose most of their energy as and will not be able to escape from the crystal. For the photoelectrons leaving the sample, we can assume an exponential decrease of its relative number N as a function of its distance z from the surface and through an inelastic mean free path Λ:

$$N(z) = N_0\, e^{-z/\Lambda} \tag{2.11}$$

The depth of the sample surface probed by a photoemission experiment, is given by Λ, which is called the escape depth for a certain emission angle. From a large number of measurements, the so-called universal curve has been extracted, given as a solid line in figure 2.17 [45, 46]. The kinetic energy of the photoelectrons escaping from the sample is then detected by an electron spectrometer.

2.4.1.2 Element sensitivity

It is important to notice that the XPS technique is very effective in the analysis of material surfaces due to its element sensitivity. The sensitivity of XPS is therefore element dependent, being more sensitive to larger elements than to smaller ones.[47] From the determined binding energies, a distribution of the atomic species is determined and compared with the tabulated values for each element. The lightest element that XPS can detect is lithium and the lowest detectability limit is about 0.1 atomic percent. On the other hand, in addition to determining the atomic composition of the surface, XPS can also provide semi-quantitative information (expressed in units of atomic percent) by dividing the peak areas of each element by a sensitivity factor [48], which is the probability of a particular element to emit an electron when struck by a photon.

2.4.1.3 Equipment

Figure 2.18 shows a schematic drawing of the assembly of an XPS equipment. The analyzer voltage sets the pass energy and accepts only electrons having an energy within this energy range. As the pass energy is fixed to maintain a constant energy resolution, the incoming electrons are set (accelerated or decelerated) by applying an electrostatic field before entering the analyzer. Finally the number of electrons is detected and stored for a given time and energy. This is what forms the peaks displayed in an XPS spectrum.

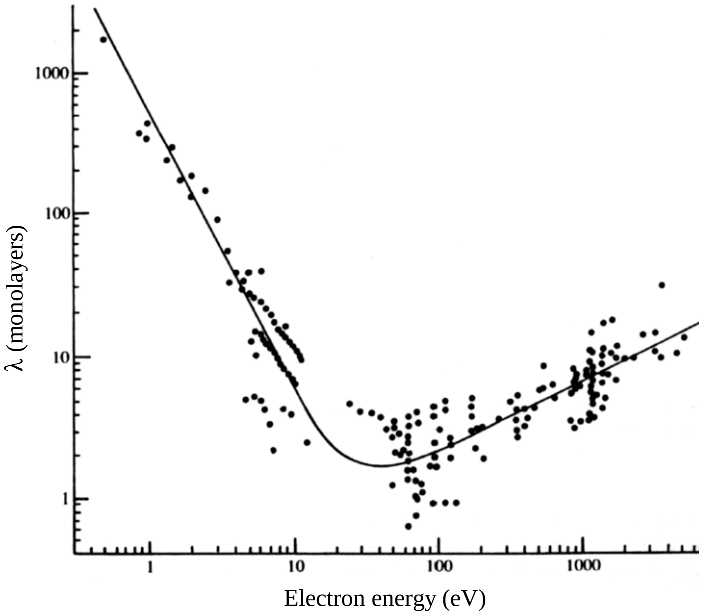

Fig. 2.17 The universal curve of Seah and Dench[45] showing experimental data for the electron escape depth as a function of the kinetic energy for various metals [46]. A minimum of 2 - 5 Å escape depth can be seen for kinetic energies of 10-100 eV.

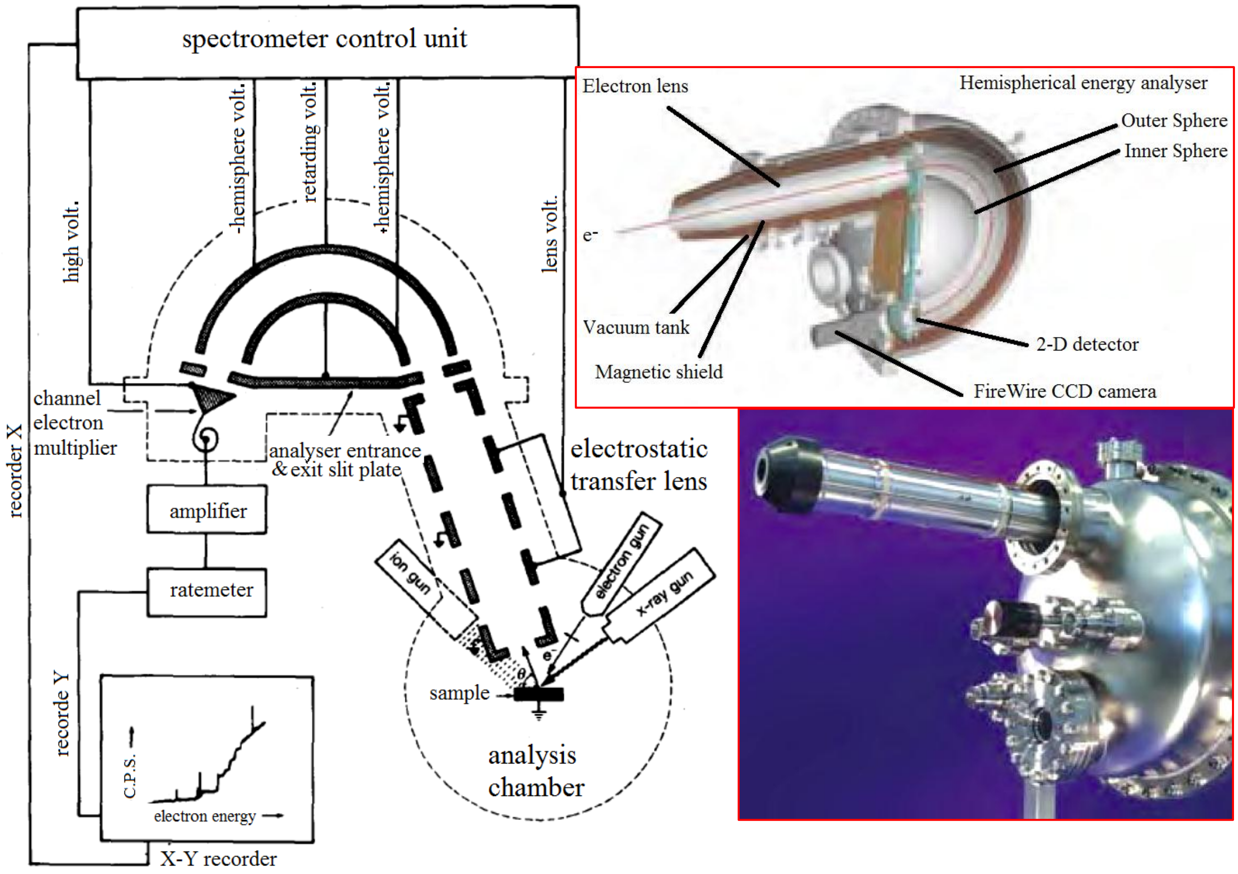

Fig. 2.18 A schematic drawing of an x-ray photoelectron spectrometer. The insets show the main components of the analyzer and a total external view of it [49].

In this work we used an XPS spectrometer equipped with a VG Sienta (formerly called Vacuum Generators) twin crystal monochromatic Al K-α_1 radiation source (*hv* = 1486.6 eV) and VG Scienta electron energy XPS analyzer R3000. This spectrometer is very flexible with capability to cover a wide range of applications, *e.g.* chemical, biological, solid, liquid or gaseous samples. The x-ray photoelectron spectroscopy (XPS) data were collected in a normal emission geometry (sample surface facing analyzer) at room temperature. The overall resolution was set to ≈0.35 eV upon the fitting of the spectrum of a polycrystalline silver foil scratched *in-situ*. The incident photoelectron beam is about 1x3 mm^2.

Two zircon samples were chosen for the XPS measurement. One of the samples was $YCrO_4$, which represents the effect of Cr^{5+} cation on the electronic structure without a contribution of 4*f* electrons. The other sample was $GdCrO_4$ where both 3*d* and 4*f* orbitals contribute. Both samples were in the form of sintered polycrystalline pellets, which were pressed under a load of 5-10 tons and annealed afterwards at 773 K in an oxygen flow for 10 hours. Samples of 10 mm diameter and 1.5 to 3 mm thickness where obtained.

The samples where fixed with silver glue on a flat aluminum sample holder and cleaved *in-situ* under base pressure of about $1\times(10)^{-10}$ mbar in the XPS chamber. The silver glue is important in order to insure the conductivity between the sample and the holder. The $GdCrO_4$ pellet, which was of 1.5 mm thickness, was cut into a half circle and fixed horizontally on the sample holder to ensure enough cross-sectional area for the measurement. The cleaved sample surface was obtained by post-cleaving *in-situ* in the XPS chamber. We measured the samples in the XPS lab at Max-Planck Institute for Chemical Physics of Solids in Dresden.

2.4.2 Soft X-ray Absorption Spectroscopy (XAS)

XAS is a powerful experimental tool to study the valence and spin states of transition metal ions in solids. The XAS experiment is performed at synchrotron radiation sources, which provide the possibility to select radiation energy to be used using a monochromator from a continuous spectrum over a wide energy range. Moreover, some of its advantages are that it provides a high intensity and brightness radiation with a possibility of variable polarizations, small radiation spots and time dependent measurement. On this basis, synchrotron sources provide a radiation with very high brilliance, which is way above the laboratory x-ray sources. Other advantages are the stability and reproducibility of radiation in addition to the fast scanning speed [50].

The concept of XAS is based on core level absorption as illustrated in figure 2.16(b). In this manner, the core level electrons are excited with very high-energy radiation relatively to its chemical binding energy. In the soft x-ray range, important absorption edges are localized which are sharp discontinuities in the absorption spectrum. For example, the *K* edges for C, N and O atoms, the $L_{2,3}$ edges for $3d$ transition metals and the $M_{4,5}$ edges for the $4f$ rare-earth elements. The binding energies for electrons are different from element to another due to the difference in number of protons in the nucleus. As a result, the absorption edges for each element are characteristic. Therefore, XAS is very powerful as we can select the energy of a specific element for the absorption edge and then get information relevant only to the specified element. This feature is highlighted in figure 2.19. Unique of XAS is that the dipole selection rules are very effective in determining which of the $2p^5 3d^{n+1}$ final states can be reached and with what intensity, starting from a $2p^6 3d^n$ initial state. This makes this technique an extremely sensitive local probe that is ideal to study the valence, spin and orbital occupation in the ground state.

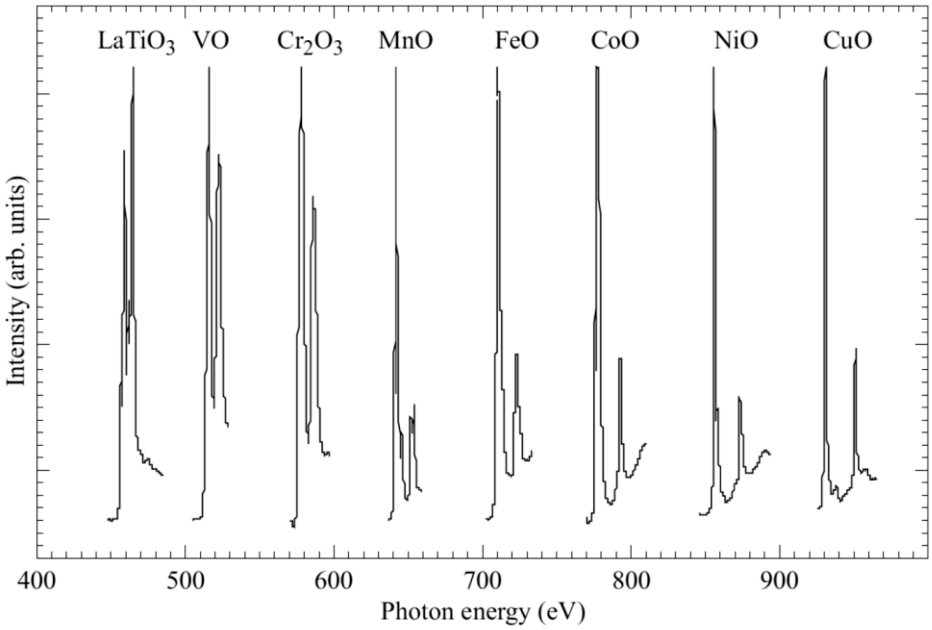

Fig. 2.19 $L_{2,3}$ absorption edges for different 3*d* transition metal compounds [51].

For transmission mode, when light travels through an absorbing medium, the intensity (I) of this light decreases exponentially, by the equation:

$$I = I_0 \times e^{-\mu \times d} \qquad (2.12)^{[52]}$$

where I_0 is the initial intensity of light prior to the absorbing medium and d is the distance cut by light through it, while μ is the absorption coefficient of this medium. In the soft XAS technique, a transmission mode is not possible due to the difficulty of obtaining a very thin sample. Upon absorption, a core hole is created due to the excitation of the electron and then some decay products take place, which lead to different kinds of yield.

2.4.2.1 Electron yield measurement

One of the decay products is the Auger decay followed by the emission of secondary electrons. This is the base of the electron yield measurement in XAS, which is mainly a surface sensitive process. It can be carried out by a total electron yield (TEY), a partial electron yield (PEY) or an Auger electron yield (AEY). In this thesis, only the TEY method was used.

In the TEY, instead of measuring the emitted electron, the sample drain current is measured. The probing depth mainly depends on the escape depth of the secondary electrons as explained in equation 2.11. The probing depth here is in the range of 40-100 Å covering several units. However, a careful preparation and treatment of the surface should be taken care of in addition to charging effects in samples with high electrical resistivity.

2.4.2.2 Fluorescence yield measurement

Another decay product, upon the decay of a created hole, is the emission of a fluorescent photon. It can be measured by a partial fluorescence yield mode or a total fluorescence yield. The later one is one used in this thesis and will be referred to as FY. In this case, a detector measures the radiating photons. This overcomes the discharging of the sample that might occur in TEY mode. Another advantage of FY mode is the high probing depth, which can be up to 1000 Å. This gives an opportunity for bulk investigation especially for the O *K*-edge, which has a much smaller probing depth in the TEY mode. However, the FY signal is much lower than the one obtained from TEY. Therefore, the sample should be scanned repeatedly over a time interval and then we obtain the average of the measurements. Another problem is that the FY mode encounters a self-absorption problem, therefore it cannot be used for investigating the $L_{2,3}$ edge of transition metals. Nevertheless, by comparing both TEY and FY recorded spectra for the same sample, one can obtain a good comparison between the surface and the bulk.

In this work, were measured XAS spectra for $R\mathrm{CrO}_4$ zircon and scheelite samples at NSRRC synchrotron facility in Taiwan, using the beam line BL08B. TEY was applied to ambient pressure polymorphs monazite and zircon samples with *R*= La, Nd, Sm, Gd, Tb, Dy, Ho, Er, and Yb. The high-pressure polymorph of scheelite samples was also investigated with *R* = Nd, Sm, Gd, Ho, Dy, Tm, Er, Yb and Lu. All zircon samples were pressed from poslycrystalline powders into a pellet and sintered at 773 K for 10 hours in a flow of oxygen. The scheelite samples were the direct sample obtained from the CONAC press after quenching and release of the mechanical pressure. A further treatment at 773 K cannot be done with these samples of the high-pressure polymorph, otherwise the material will transform back into the zircon phase. A comment on the sample of ErCrO_4 scheelite is that it contained the highest amount of impurities in all synthesized sample, and it will be reported in chapter 4. The sample preparation for XAS measurement was done as described previously in the XPS section.

2.5 Magnetic Susceptibility and Heat Capacity Measurements

The susceptibility, χ, measurement is a powerful tool to study the magnetic properties of solids and for examining the nature of magnetic phase transitions. Typically, χ diverges at the critical temperature of a ferromagnetic phase transition. Critical exponents characterize the nature of the divergence as a function of temperature and DC applied field. Determination of these critical exponents allows one to distinguish between various models of the magnetic interactions [53].

2.5.1 Magnetic Property Measurement System (MPMS)

The magnetic signature of a material reflects its intrinsic spin and orbital angular momentum. For the study of magnetism in matter, Quantum Design's Magnetic Property Measurement System (MPMS) was designed as an integrated instrument system, whose main components are:

1. Temperature control system for a range between 2 and 400 K, which requires controlling heat flow into the sample space and the active control of cooling gas;
2. Magnet control system for magnetic fields from 0 to ±7 **T**;
3. Superconducting Quantum Interference Device (SQUID) amplifier system, which is the heart of the magnetic moment measurement system;
4. Sample handling system to handle the sample smoothly through the detection coils;
5. Computer operating system.

Moreover, the MPMS system is benefiting from the use of several different superconducting components: the magnet, the detection coil, the SQUID amplifier system and the magnetic shield surrounding the SQUID.

2.5.2 Physical Property Measurement System (PPMS)

The Physical Property Measurement System (PPMS) provides a flexible automated workstation that can perform a variety of experiments requiring precise thermal control. It can be used to execute magnetic, electro-transport, or thermo-electric measurements, or can be modified to suit a desired laboratory experiment. Sample environment in the PPMS include magnetic fields up to ±14**T,** depending on the magnet installed, and a temperature range of 1.9 to 400 K. Temperature is reported with a typical accuracy of ±0.5% [54].

The PPMS has an option for heat capacity measurements at constant pressure:

$$C_p = \left(\frac{dQ}{dT}\right) \tag{2.13}$$

As with other techniques for measuring heat capacity, the Quantum Design Heat Capacity option controls the heat added to or removed from a sample while monitoring the resulting change in temperature. During a measurement, a known amount of heat is applied at constant power for a fixed time, and then this heating period is followed by a cooling period of the same duration. A platform heater and a platform thermometer are attached to the bottom side of the sample platform. Thus, the instrument requires some kind of a surface in the sample to have a thermal connection with the platform.

The Quantum Design's Magnetic Property Measurement System (MPMS) was used in this work to make DC measurement of scheelite samples. The magnetization *vs*. temperature for powder samples were carried out in a temperature range between 300 and 2 K. The magnetization results were divided by the sample weight in order to compare the data of samples on an emu.g^{-1} scale.

On the other hand, for more insight into the transition temperatures and magnetic ordering of the studied samples, specific heat measurements by Quantum Design's Physical Property Measurement System (PPMS) were carried out for scheelite samples. The specific heat was measured against temperature in zero magnetic field, and then the in a field range from 0.1 to 9 **T**. A calibration of the puck sample holder was provided by the PPMS lab at Max-Planck Institute for Chemical Physics of Solids in Dresden. The sample was mounted on Apiezon N grease after an addendum measurement has been measured with only the grease at the relevant temperatures and magnetic fields. The addenda were then subtracted from the total heat capacity measurement by the PPMS software and sample heat capacity was plotted *vs.* the sample temperature.

References

[1] R. Hazen, The Diamond Makers, Cambridge University Press, Cambridge (1999)

[2] M. I. Eremets, High-pressure Experimental Methods, Oxford University Press, Oxford (1996)

[3] W. B. Holzapfel, N. S. Isaacs, High Pressure Techniques in Chemistry and Physics - A Practical Approach, Oxford University Press, Oxford (1997)

[4] L. Liu and W. A. Bassett; Elements, oxides, and silicates: high-pressure phases with implications for the earth’s interior, Oxford University Press, Oxford (1986)

[5] H. T. Hall, *Review of Scientific Instruments* **31**, 125 (1960)

[6] L. G. Khvostantsev, V. N. Slesarev and V. V. Brazhkin, *High Pressure Research: An International Journal* **24**, 3, 371 (2004)

[7] J. M. Besson, G. Hamel, T. Grima, R. J. Nelmes, J. S. Loveday, S. Hull and D. Häusermann, *High Pressure Research: An International Journal* **8**, 5-6 (1992)

[8] J. M. Besson, R. J. Nelmes, G. Hamel, J. S. Loveday, G. Weill and S. Hull, *Physica B: Condensed Matter* **180–181**, 2, 907 (1992)

[9] B. Von Platen, R. H. Wentorf, Modern Very High Pressure Techniques, Butterworths, London (1962)

[10] L. F. Vereshchagin, L. G. Khvostantsev and A. P. Novikov, French Patent 7102157 (1972)

[11] L. G. Khvostantsev, L. F. Vereshchagin and A. P. Novikov, *High Temp.- High Pressures* **9**, 637 (1977)

[12] H. M. Rietveld, *Journal of Applied Crystallography* **2**, 65 (1969)

[13] V. K. Pecharsky and P. Y. Zavalij, Fundamentals of Powder Diffraction and Structural Characterization of Materials, Springer Verlag Gmbh, 2nd Print (2005)

[14] W. Massa, Crystal structure determination, translated by R. O. Gould, Springer Verlag Berlin, Heidelberg, 2nd edition (2004)

[15] D. H. Bilderback, P. Elleaume and E. Weckert, *Journal of Physics B: Atomic, Molecular and Optical Physics* **38**, S773 (2005)

[16] M. Knapp, C. Baehtz, H. Ehrenberg and H. Fuess, *Journal of Synchrotron Radiation* **11**, 328 (2004)

[17] http://hasylab.desy.de (June 2012)

[18] J. R. D. Copley, The fundamentals of Neutron Powder diffraction, National Institute of Standards and Technology, Special Publication 960-2, U.S. Government Printing Office, Washington: November (2001)

[19] Data from *Neutron News* **3**, No. 3, pp. 29-37 (1992)

[20] http://www-llb.cea.fr/en/fr-en/spectros_p.php (June 2012)

[21] J. P. Ambroise and R. Bellissent (editors): P. Convert, B. Forsythe, Position sensitive detection of thermal neutrons, Academic Press, London (1983)

[22] J. P. Ambroise, M. C. Bellissent-Funel and R. Bellissent, *Revue de Physique Appliquée* **19**, 731 (1984)

[23] http://www.isis.stfc.ac.uk/instruments/wish/publications/wish-science-case6636.pdf

[24] H. M. Rietveld, *Journal of Applied Crystallography* **2**, 65-71 (1969)

[25] R. A. Young (editor), The Rietveld Method, Oxford University Press, Oxford, UK, 4-6 (1993)

[26] R. E. Dinnebier and S. J. L. Billinge, (editors), Powder Diffraction Theory and Practice, The Royal Society of Chemistry, v-vi, 155, 206, 211, 219, 230, 243, 268-270, 528 (2008)

[27] A. C. Larson and R. B. Von Dreele "*General Structure Analysis System (GSAS)"*, Los Alamos National Laboratory, report LAUR 86-748 (2000)

[28] B. H. Toby, *Journal of Applied Crystallography* **34**, 210-213 (2001)

[29] J. Rodríguez-Carvajal, *Physica B: Condensed Matter* **192**, 55 (1993)

[30] J. Rodríguez-Carvajal, *Commission on Powder Diffraction (IUCr) Newsletter* **26**, 12 (2001)

[31] A. Boultif and D. Louer, *Journal of Applied Crystallography* **37**, 724 (2004)

[32] J. Rodriguez-Carvajal "BASIREPS-A Program for Calculating Non-Normalized Basis Functions of the Irreductible Representations of the Little Group Gk for Atom Properties in a Crystal" *Laboratoire Leon Brillouin, CEA Saclay*: Gif sur Yvette, France (2004)

[33] D. Altermatt and I. D. Brown, *Acta Crystallographica A* **43**, 125 (1987)

[34] I. D. Brown, *Acta Crystallographica B* **33**, 1305 (1977)

[35] M. O'Keeffe *Acta Crystallographica A* **46**, 138-142 (1990)

[36] I. D. Brown and D. Altermatt, *Acta Crystallographica B* **41**, 244, 41, 240 (1985)

[37] I. D. Brown, *Chemical Reviews* **109**, 6858 (2009)

[38] N. E. Brese and M. O'Keeffe *Acta Crystallographica B* **47**, 192 (1991)

[39] E. Jiménez Melero; doctoral thesis, Universidad Complutense de Madrid (2005) http://eprints.ucm.es/tesis/qui/ucm-t28520.pdf (November 2012)

[40] I. D. Brown, *Zeitschrift fuer Kristallographie* **199**, 255 (1992)

[41] H. Hertz, *Annalen der Physik* **267**, 983 (1887)

[42] A. Einstein, *Annalen der Physik* **17**, 132 (1905)

[43] C. Nordling, E. Sokolowski and K. Siegbahn, *Physical Review* **105** (5), 1676 (1957)

[44] The Nobel Prize in Physics 1981: Nobelprize.org. http://www.nobelprize.org/nobel_prizes/physics/laureates/1981/ (June 2012)

[45] M. P. Seah and W. A. Dench, *Surface and Interface Analysis* **1**, 2 (1979)

[46] M. Prutton, Introduction to Surface Physics, Oxford University Press, Oxford (1994)

[47] C. D. Wagner, *Analytical Chemistry* **44** (6), 1050 (1972)

[48] R. J. Ward and B. J. Wood, *Surface and Interface Analysis* **18** (9), 679 (1992)

[49] Scienta Surface Science Instruments Catalogue;

http://www.vgscienta.com/_resources/File/Catalogue_Sections/VGScienta_Surface_Science_Instruments.pdf

[50] J. Als-Nielsen and D. McMorrow, Elements of Modern X-ray Physics, Wiley, Chichester, England (2001)

[51] M. Haverkort, doctoral thesis, Universität zu Köln (2005) http://arxiv.org/pdf/cond-mat/0505214.pdf (November 2012)

[52] J. W. Robinson, E. M. Skelly Frame and G. M. Frame II, Undergraduate Instrumental Analysis, Marcel Dekker, New York (2004)

[53] Martien D, Introduction to AC Susceptibility, Quantum Design MPMS application notes, (12/02) - 1078-201 (2002).

[54] Quantum Design, Physical Property Measurement System Hardware Manual, Part Number 1070-150B, 3rd Edition (2000)

3. Structural Characterization of *R*CrO$_4$ Zircon-to-Scheelite Transition

3.1 Overview of the Mechanism of Zircon-to-Scheelite Transition

Many ABO_4 compounds are isostructural with the zircon mineral, $ZrSiO_4$, such as phosphates, vanadates, arsenates and chromates. Some ABO_4 are important materials in the engineering of optoelectronic devices, solid-state scintillator detectors and solid-state lasers [1]. $ZrSiO_4$ itself is an important mineral in geophysical and geochronological investigations. It is an important host mineral for radioactive elements like U and Th in the earth crust [2] and a possible material for radioactive waste storage and immobilization due to its interesting properties during radiation damage exposure [3-5].

The transition of $ZrSiO_4$ under pressure was first obtained by Reid and Ringwood in 1969 [6] at 1173 K and 12 GPa (final pressure) and it was confirmed 10 years later by Liu [7] who obtained the high-pressure polymorph at 1273 K in the pressure range 10-20 GPa. The same polymorph was also obtained at room temperature by Kusaba *et al.* [8] in 1984 using shock pressures between 30-53 GPa; by Knittel and Williams in 1993 [9] and by Westrenen *et al.* [10] in 2004 using pressures between 20-23 GPa.

The zircon mineral has a tetragonal structure that crystalizes in the space group $I4_1/amd$ (D_{4h}^{19}, No. 141, Z=4). It transforms under pressure to another structure that is isostructural with the ambient-pressure structure of the $CaWO_4$ scheelite mineral. This high-pressure polymorph is a tetragonal structure with space group $I4_1/a$ (C_{4h}^{6}, No. 88, Z=4). Therefore, this transition results in a decrease in the structural symmetry.

ABO_4 materials, isostructural with the zircon, follow a similar structural behavior when subjected to high pressures. Stubican and Roy [11] discovered earlier in 1963 the structural transition of the majority of arsenates and vanadates from the zircon-type to the scheelite-type structure. They also determined the transition pressure at different temperatures for several compounds and a relationship between the equilibrium transition pressure required and the ionic radii, as shown in figure 3.1 [12]. It will be noticed later that their reference for the reported ionic radii is different from the one we used, which is more updated in our work. However, figure 3.1 is still representative for the rare-earth dependence of the transition pressure. In this chapter, we shall discuss the role of breaking an R-O bond in order to allow a bond switching mechanism, which could be the reason for the different pressures required to break this bond.

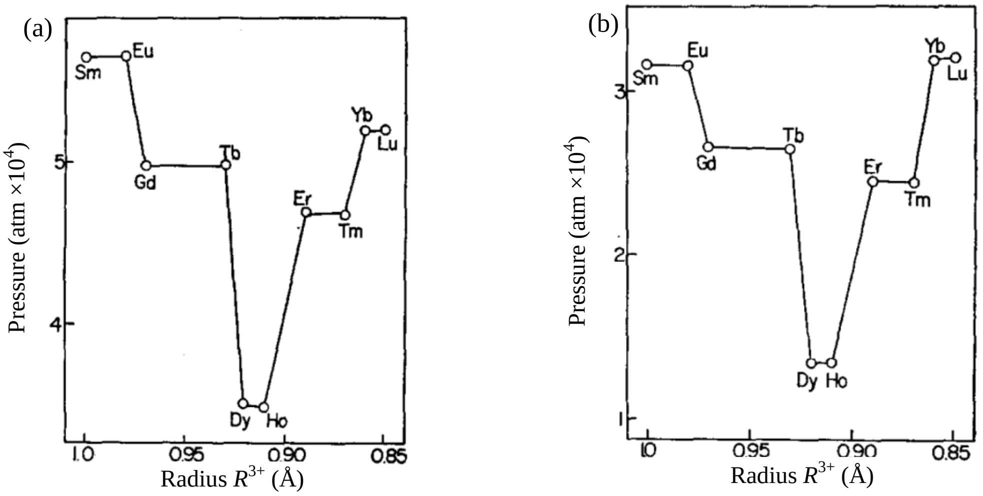

Fig. 3.1 Relationship between applied pressure and ionic radii at 703 K for: (a) RVO$_4$; (b) RAsO$_4$. [12]

The rare-earth orthochromates, RCrO$_4$, crystallize usually in the zircon-like structure and transform under pressure to the scheelite-like structure. However, compared to other ABO$_4$ compounds, RCrO$_4$ oxides have been much less studied in the literature due to their instability. On one hand, it was not easy to prepare a pure polycrystalline sample. In 1960s, Schwarz synthesized the RCrO$_4$ zircon by standard solid-state reaction method but he had some impurities of Cr_2O_3. Purer samples have been synthesized later from corresponding nitrates and acetates [13-16]. On the other hand, a single crystal is not yet possible to make due to the decomposition of these compounds into RCrO$_3$ and oxygen, which begins at about 873 K.

The zircon-type structure of RCrO$_4$ contains isolated CrO$_4$ distorted tetrahedra that surround the R atom to form an RO$_8$ bisdisphenoids (triangular dodecahedra). The main structural units in this structure are chains of CrO$_4$ and RO$_8$ polyhedra which are parallel to the c axis and alternating by an edge sharing as seen in figure 3.2(a). Adjacent rods are connected along a and b-axis by the edge sharing between RO$_8$ polyhedra, which provide additionally extra corner sharing between CrO$_4$ and adjacent RO$_8$ (as seen in figure 3.2(b)). It can be seen in this figure that chains of edge-sharing RO$_8$ isolate the CrO$_4$ tetrahedra from each other. Octahedral and tetrahedral interstitial positions can be seen in figure 3.2(b) and (d), respectively, indicating the rather open nature of the zircon structure. The octahedral positions form voids alternating in the stacking of *ca*-planes, while the tetrahedral positions are above each other and form channels in the *ab*-planes (*c*-direction). This in return affects the high ability of these materials to attract impurities (for further details see chapter 4). A remark about figure 3.2 is that some other publications [17, 18] prefer the centro-symmetrical representation of this space group where a Cr cation is at the center of the unit-cell ($I4_1/amds$) which represents the same model represented here ($I4_1/amdz$) after a translation of the axis and the unit cell.

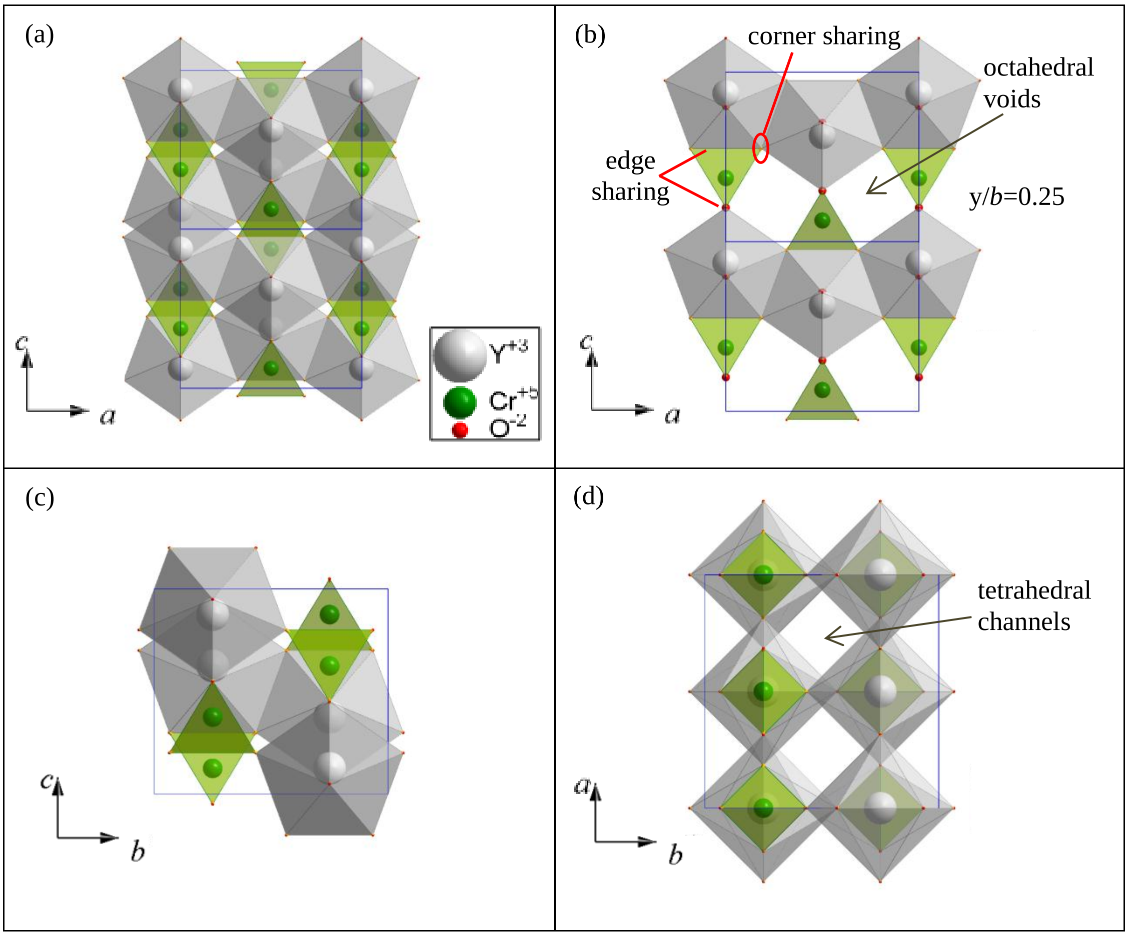

Fig 3.2 Zircon-type crystal structure of YCrO$_4$ taken as an example. *R*O$_8$ dodecahedra are in gray color while CrO$_4$ tetrahedra are in green color: (a) projection on (010) plane "for two unit cells in *c*-direction"; (b) the same projection on (010) but with a single layer for clarification (at y= 0.25) showing octahedral interstitial positions and sharing types between Cr and *R* polyhedra; (c) projection of one unit-cell on (100) plane, (d) projection of one unit cell on (001) plane and the channels of tetrahedral interstitial positions.

In case of the scheelite structure, CrO$_4$ distorted tetrahedra are aligned along the *a* axis, while *R*O$_8$ bisdisphenoids are intercalated between the CrO$_4$ tetrahedra (figure 3.3). The *R*O$_8$ polyhedra shares edges with adjacent *R*O$_8$ polyhedra and form along *a*-direction zigzag chains, which are cross-linked by tetrahedra via corner-sharing (figure 3.3(b)). However, there is no edge-sharing between *R*O$_8$ and CrO$_4$ polyhedra. An illustration of the difference in polyhedra topology between zircon and scheelite structure is shown in figure 3.4. These results, based on the structure refinement of neutron and x-ray powder-diffraction data, are in agreement with the topologies described by Ilyushin *et al.* [19] for the zircon- and scheelite-type structures. The difference in the tilting angle between different polyhedra, as well as in the packing after the transition can be viewed in figure 3.3(d) in comparison with the zircon structure in figure 3.2(d). This tilting difference provides an intense change in the Cr-O-*R* angles as will be seen later in this chapter. Upon the zircon-to-scheelite transition, the CrO$_4$-tetrahedra transform from D_{2d} to D_{4h} point group symmetry, while the *R*O$_8$-dodecahedra preserve its D_{2d} point group symmetry.

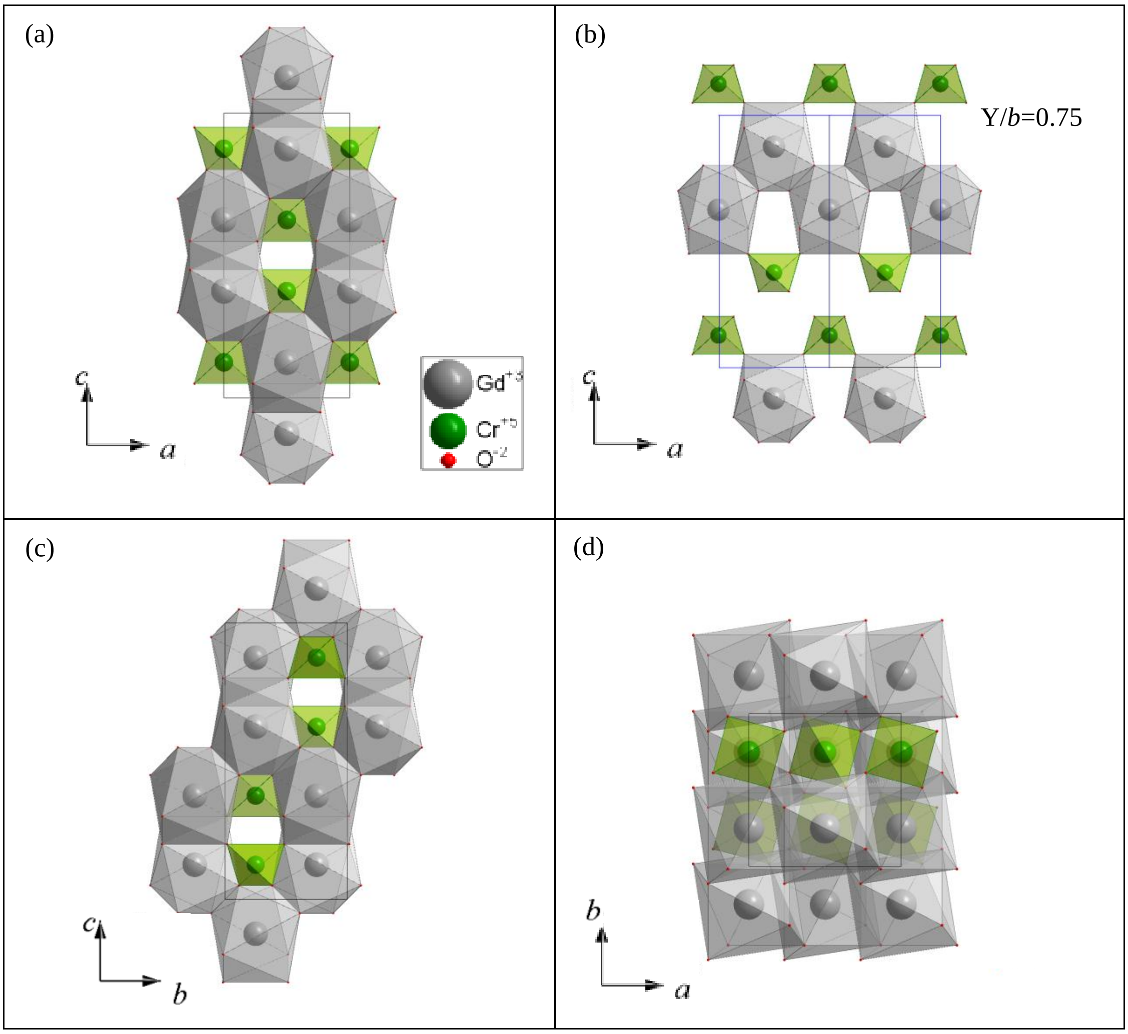

Fig 3.3 Scheelite-type crystal structure of GdCrO$_4$. *R*O$_8$ dodecahedra are in gray color, while CrO$_4$ tetrahedra are in green color: (a) projection on (010) plane "for one unit cell"; (b) the same projection on (010) for two unit cells but with a single layer for clarification (at y= 0.75); (c) projection of one unit-cell on (100) plane, (d) projection on (001) plane for one unit cell.

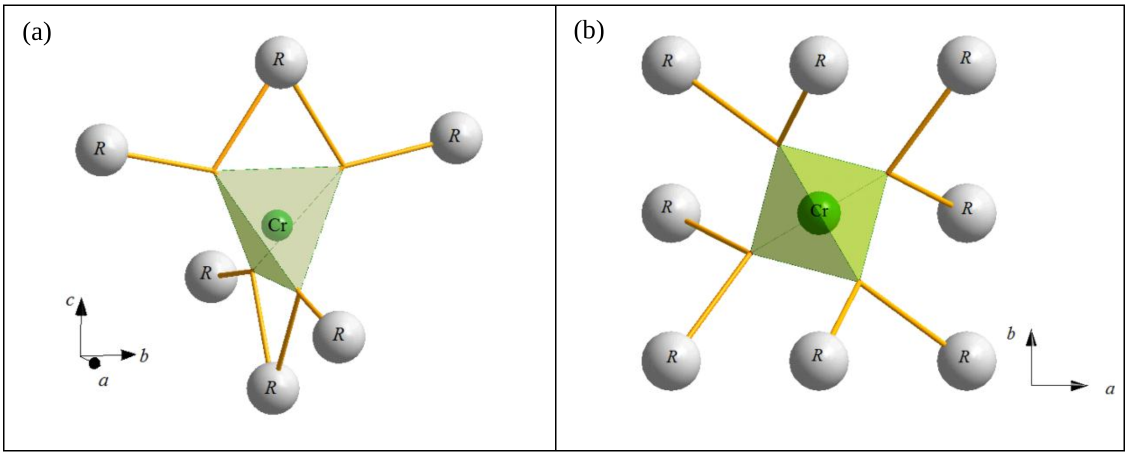

Fig 3.4 Topology of CrO$_4$ with neighboring *R* cations and their corresponding dodecahedra: (a) for the zircon-like structure, showing edge sharing in *c*-direction and corner sharing in *a*- and *b*-directions; (b) for the scheelite-like structure, showing corner sharing only between Cr and *R* polyhedra.

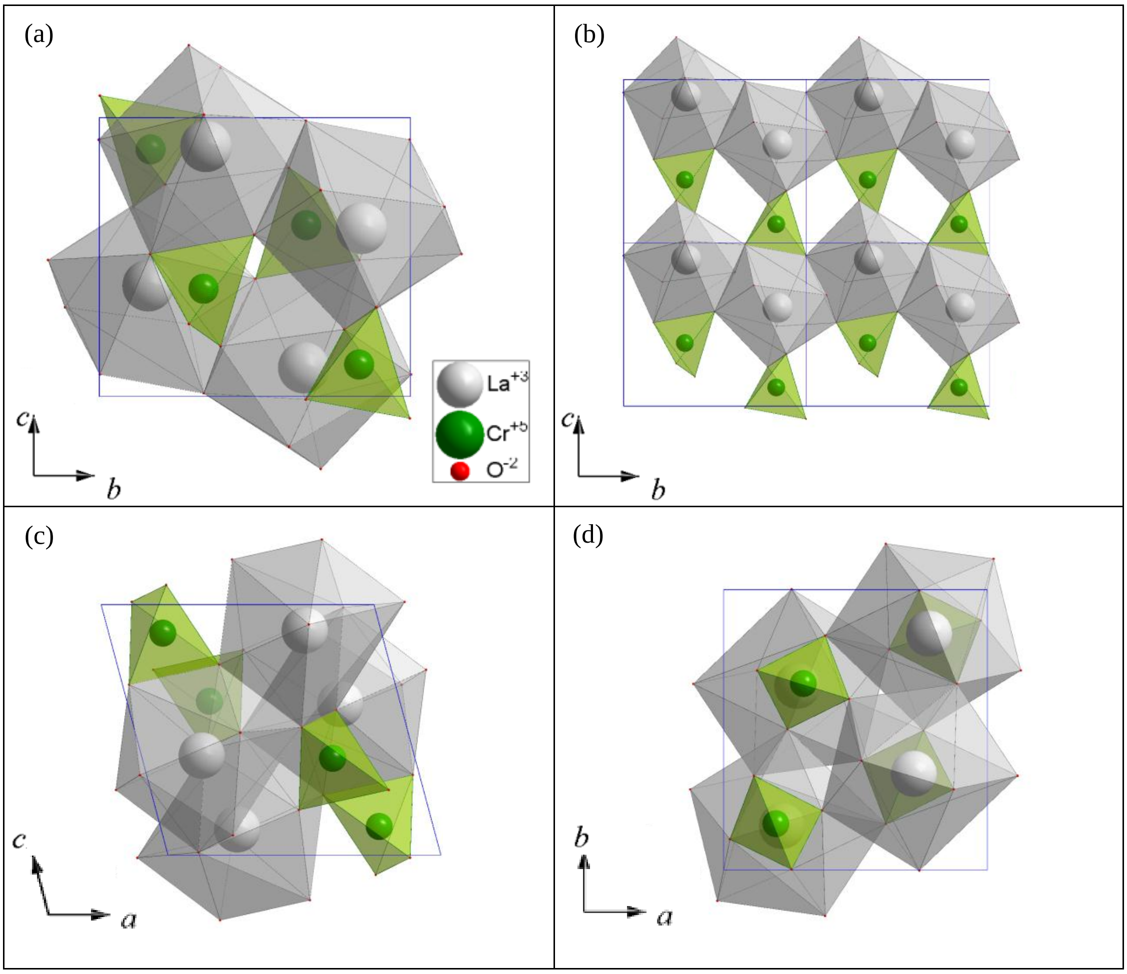

Fig 3.5 Monazite-like crystal structure of LaCrO$_4$ taken as an example. RO$_8$ dodecahedra are in gray color, while CrO$_4$ tetrahedra are in green color: (a) projection on (100) plane "for one unit cell"; (b) the same projection on (100) for four unit cells but with a layer in *c*-direction for clarification; (c) projection on (010) plane for one unit-cell; (d) projection on (001) plane for one unit cell.

The LaCrO$_4$ compound crystallizes at ambient conditions in a monazite-like structure, which is a monoclinic structure with the space group setting $P12_1/n1$ (C_{2h}^5, No.14). The structure of monazite has some similarities with the zircon structure. Although RO$_9$ polyhedra are formed instead of RO$_8$, the CrO$_4$ tetrahedra share corners and edges with RO$_9$ polyhedra, which form edge-shared chains parallel to the *a*-axis. Due to the extra coordinated oxygen atom, the RO$_9$ polyhedron in the monazite structure is coordinated by seven CrO$_4$ (two edge-shared and five-corner-shared); in comparison to only six CrO$_4$ surrounding the RO$_8$ polyhedron in the zircon structure. Therefore, the monazite structure has a greater overall connectivity. Moreover, the edge-sharing chains between RO$_8$ and CrO$_4$ in monazite are rather twisted (see figure 3.5).

Concerning the zircon-to-scheelite transition, an early study in 1984 by Nyman *et al.* described it as the result of consequent twinning operations, which was the first attempt to refer to a possible transformation path [20]. In their model, first the tetragonal zircon structure ($I41/amd$, D_{4h}^{19}, No. 141, Z=4) undergoes twinning on (200) plane to the orthorhombic Anhydrite CaSO$_4$ structure-type ($Bmmb$ ($Cmcm$) , D_{2h}^{17}, No. 63, Z=4), which simultaneously undertakes twinning on (020) plane to produce the tetragonal silver perchlorate AgClO$_4$ structure-type ($I\bar{4}2m$, D_{2d}^{11}, No. 121, Z=2) and finally twinning on (002) (of AgClO$_4$-type) to produce the tetragonal scheelite CaWO$_4$ structure-type ($I4_1/a$, C_{4h}^{6}, No. 88, Z=4). The later twinning causes a doubling in the c axis of the silver perchlorate structure-type. Due to these symmetry relations, it could be concluded that:

$$(c/a)_{zircon} = 2(a/c)_{scheelite} \qquad (3.1)^{[21]}$$

In the same year, Kusaba *et al.* explained the zircon-to-scheelite transition as “of the displacive nature rather than of the reconstructive type” [8]. Their argument was that the scheelite structure achieved easily by shock-loading can then be reverted to the zircon parent phase upon heating to 1473 K at ambient pressure; and that the two structures are closely related to each other. Furthermore, in a later publication, Kusaba *et al.* described the displacive process with a two-step mechanism by which the [110] direction of the zircon-type convert into the [001] direction of the scheelite-type [22]. The two steps consist of pure shear followed by only small displacements of the atoms without a long-range diffusion. In the first step, the zircon unit cell transforms to a “distorted zircon” by pure shear of the intersecting angle between [100] and [010] from 90 to 115°. In figure 3.6(b), the intermediate structure has a diagonal length along *A* direction that is slightly bigger than the *c*-axis in the scheelite ($c_{scheelite}$). Figure 3.6(c) shows the projection of the intermediate structure along the *A* direction marked in figure 3.6(b); along the diagonals *B* (slightly bigger than $a_{scheelite}$) and *C* (slightly smaller than $a_{scheelite}$).

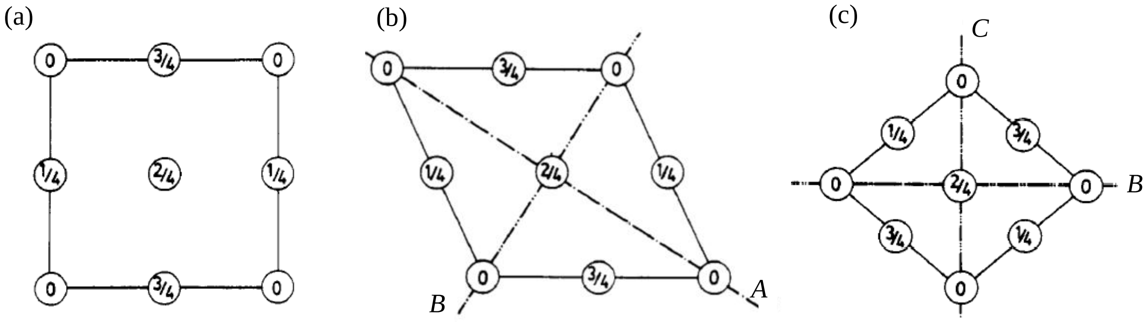

Fig. 3.6 The pure-shear step of the two-step mechanism proposed by Kusaba *et al.* [22] from (a) the zircon-type, projected along the *c*-axis, to (b) what they called as “quasi-scheelite-type” or “distorted-zircon” projected along the same *c*-axis and (c) along the *A* diagonal of the distorted zircon.

Kusaba *et al.* also accounted for the more efficient packing of the scheelite as due to a coherent rotation of the tetrahedra. However, they did not manage to explain why the scheelite-type structure does not return to the zircon-type after only unloading [8]. The model of Kusaba *et al.* provides, nevertheless, limited information to make a general understanding of the transition. In particular, they did not provide any description to the second step, which was described as “small displacements”. In fact, although the $I4_1/a$ space group of the scheelite is a subgroup of the $I4_1/amd$ of the zircon and although both Zr^{4+} and Si^{4+} cations in the zircon mineral maintain eventually their coordination with the oxygen atoms, there are some experimental results that cannot be understood under a displacive phase transition. These results are mainly: the volume compression upon transition of about 10%; the temperature dependence of the required transition pressure; and finally the quick reverse transition from scheelite to zircon at 1473 K in ambient pressure, which does not occur in first place upon pressure release at room temperature.

Many theoretical studies afterwards investigated the mechanism of the zircon-to-scheelite transitions [23-29]. A more detailed analysis of the structural, thermodynamic and experimental data [6, 30-36] supports the first order character of this transformation. Marques *et al.* demonstrated recently that the zircon-to-scheelite transition involves mainly a breaking of *R*-O bonds [27] and a rearrangement of the CrO$_4$ and *R*O$_8$ units. Such a rearrangement is responsible for the efficient packing.

An interesting study is the one done by Smirnov *et al.* [28], who used calculations with density-functional theory and an empirical shell model. They described the transition of ZrSiO$_4$ zircon mneral as a bond-switching mechanism in which a quarter of Zr-O bonds are broken and new Zr-O bonds are formed, which supports the reconstructive character of the transition. Consequently, they proposed two transformation paths: one is for the transition via the lower symmetry structures $D_{4h}^{19} - D_{2h}^{24} - C_{2h}^{6} - C_{4h}^{6}$, which is more likely to happen (see figure 3.7). Another path is via higher symmetry structures, which they described as "energetically expensive" and therefore is unlikely to occur.

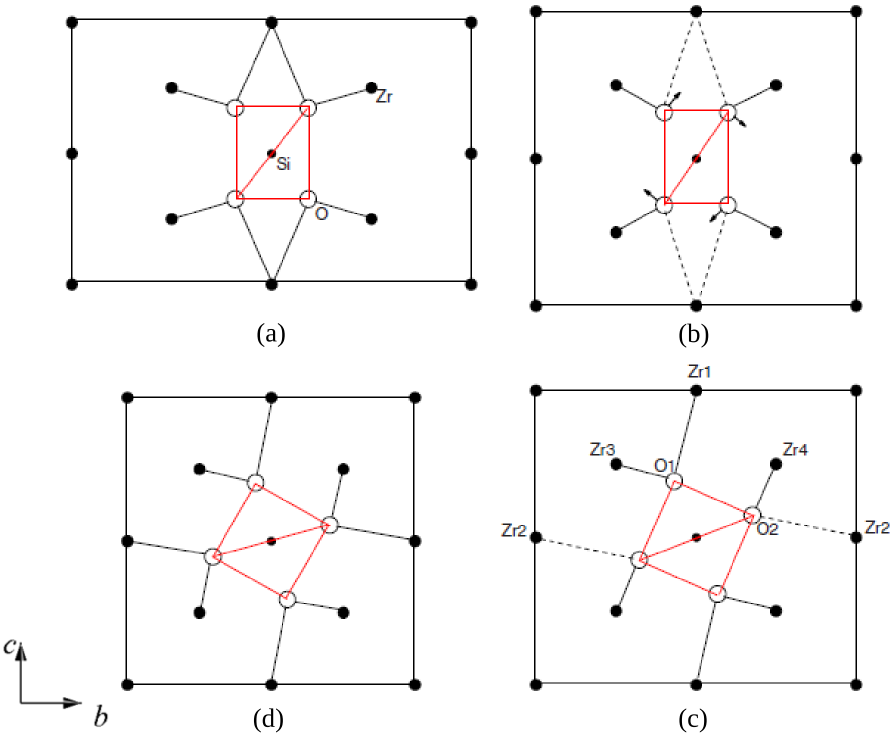

(a) (b)

(d) (c)

Fig. 3.7 Bond-switching model for the zircon-to-scheelite phase transition in ZrSiO$_4$ proposed by Smirnov *et al.* [28]

The results of Smirnov has been confirmed by Flórez *et al.* studying a microscopic description of the energies, bonds and structural changes accompanying the transition by more detailed quantum-mechanical calculations [29]. They used a semiempirical approach to evaluate the thermal barrier at the zircon-to-scheelite transition, which resulted in information in qualitative agreement with Smirnov *et al.* with some small comments on the different calculation approach by the later group, which give a deviation in lattice parameters up to 3% greater in the later Smirnov *et al.* calculations. They also confirmed that the activation barrier for the monoclinic pathway is smaller than that for the tetragonal one. Finally, they provided a detailed geometrical description of the changes in the bond lengths and angles in the dodecahedra and lattice parameters.

The transition from zircon to scheelite is believed therefore to be a first order and involves a volume collapse of about 10%, a compression that is typical for the zircon-to-scheelite transitions in ABO$_4$ compounds. Both structures are containing 24 atoms per unit cell (4 A cations + 4 B cations + 16 O anions). However, for $I4_1/a$ symmetry, the group-subgroup relationships between two phases displaying the same metal coordination is not a sufficient condition to describe a phase transition as displacive.[29]

The Cr-O distances remain almost constant upon the transition from zircon to scheelite, with a very slight change in the O-Cr-O angles. On the other hand, *R*-O distances also barely change, but serious change in one of the O-*R*-O angles take place (as shown later in figure 3.13). This is mainly due to the different compressibilities for CrO$_4$ and *R*O$_8$ polyhedra [21, 37]. Such a difference has to be driven from the nature of the Cr-O bond that seems to have a covalent nature (this will be further discussed in chapter 6). The constant Cr-O distance can also be the reason for the anisotropic thermal expansion of these materials [38, 39].

Upon decreasing the volume, *i.e.* compression, the c/a ratio for the zircon slightly increases due to the relatively higher compressibility of the a_{zircon} axis. In contrast, this ratio decreases in the scheelite phase after the transition point, because the CrO$_4$ tetrahedra sits now on the $a_{\text{scheelite}}$ axis, which accordingly makes this axis in the scheelite less compressible and results in anisotropic compressibility as well [21, 37]. On the other hand, as the *R*O$_8$ bisdisphenoids are forming chains along the *a*-axis in the zircon phase, the previously mentioned twin operations upon the transition to scheelite could be driven through these chains.

The cooperative interaction between the 3*d* electrons of the transition metals could be the reason for the ease of the pressure-induced transition from zircon to scheelite in the *R*CrO$_4$ chromates (4-6 GPa) in comparison with other more stable zircon structures of the silicate (ZrSiO$_4$) and the phosphates (*R*PO$_4$), which require a higher pressure range for the transition (around 20 GPa). [40, 41]

In the case of the orthovanadates, the transition pressure is between 7 and 8 GPa [21], while for the orthochromates *R*CrO$_4$ the transition pressure is about 6 GPa at room temperature[37]. However, these transition pressures can be lowered by the application of temperature. Consequently, the scheelite phase of the chromates can be prepared at lower pressures as 4 GPa by raising the temperature up to 833 K [42-48]. However, the stability of the scheelite polymorph is less than that for the zircon structure of the *R*CrO$_4$. Li *et al.* represented the Gibbs free energies as a function of unit cell volume for both zircon and scheelite phases of YCrO$_4$ [18]. In their calculations, at T= 0 K, the bulk modulus and the phase transition pressure are evaluated from the Murnaghan as the relation of the total energies with unit cell volumes. As shown in figure 3.8, the zircon phase is more stable than the scheelite by having a lower minimum of the total energy curve.

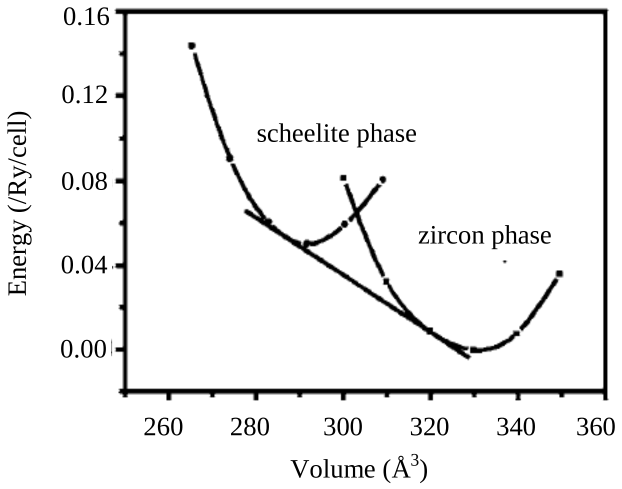

Fig. 3.8 Total energy as a function of unit cell volume for zircon phase and scheelite phase of YCrO$_4$ [18]. The common tangent line to the energy curves of the phases indicates the phase transition pressure at 0 K.

On the other hand, a possible candidate for a further structural transition is the transition of scheelite-type structure to a fergusonite-type one, which is a monoclinic variant of the scheelite with a space group $I2/a$ (C_{2h}^{6}, No. 15) and has been identified as the first high pressure phase of, e.g., YLiF$_4$ [49] and CaWO$_4$ [50]. Recently, the zircon-type of EuVO$_4$ and LuVO$_4$ was found to have a transition to a scheelite-type phase at 8 GPa and then to a fergusonite-type at 21 GPa [51]. In the case of the transition of *R*CrO$_4$ oxides from scheelite to fergusonite, up to our best knowledge, no one has explored this possibility in a wider range above 20 GPa. The results of investigating both NdCrO$_4$ and DyCrO$_4$ by *in-situ* Raman scattering under pressure up to 19.7 GPa indicate a possibility of obtaining a new transition at higher pressures [52]. The fergusonite-type chromates are however out of the focus of this study.

In this work, we prepared zircon-like structures were prepared of *R*CrO$_4$ where *R* is one of the rare earth elements of Nd and Sm-Lu series. These zircon-type structures have been pressurized at 4 GPa and isobarically heated in the temperature range 808 to 833 K to obtain the scheelite-like structure that was quenchable to room temperature. For more details about sample preparation, see chapter 2. The LaCrO$_4$ crystallizes at ambient pressure in the monazite-like structure, high-pressure experiments in the above-mentioned temperature range and between 4 and 6 GPa did not result in any structural transition. The synthesis of CeCrO$_4$ was not possible due to the favorable formation of Ce^{4+} and therefore the quick formation of CeO$_2$ at temperatures as low as 500 K, which is lower than that of the monazite and zircon temperature formation between 773 and 873 K at ambient pressure. The formation of Ce^{3+} needs consequently a reducing atmosphere, while Cr^{5+} requires an oxidizing atmosphere. Until now, there is no successful attempt to synthesize CeCrO$_4$ at ambient pressure. However, it can be worth trying in the future to synthesize this composition under high pressures, e.g. using reactants of CrO$_2$ and CeO$_2$.

PrCrO$_4$ crystallizes, to the best of our knowledge, dimorphically in both zircon and monazite phases. The percentage of the two phases in the compounds varies from one experiment to another. The zircon structure is more stable at the higher temperature range (833 to 853 K), while the other phase, believed to be of the monazite-type, is more stable at a lower temperature range (773 to 833 K). Jiménez Melero *et al.* [53] managed to separate the zircon phase by quenching in air from the high temperature phase. However, their results contained a small amount of a secondary monoclinic phase in 2θ range of 10-30°.

Moreover, a very slow cooling of the synthesized compounds inside the furnace under oxygen flow resulted in over-oxidation of the compounds to a brown-yellow compound, which will be explained in chapter 5 under the stability of *R*CrO$_4$ compounds. On the other hand, the increase in the oxygen flow during the preparation of PrCrO$_4$ obtained at the same preparation conditions for zircons (773 to 833 K) results in a light green powder of the perovskite-like structure of PrCrO$_3$. The structural characterization of *R*CrO$_4$ zircons has been given in details in a previous work [54].

The structural characterization of only the newly prepared scheelite phases of *R*CrO$_4$ (*R*= Nd and Sm-Lu) are presented in this chapter, while in the next chapter more details about their thermal stability are given.

3.2 Structural Characterization of the *R*CrO$_4$-Scheelite Oxides

3.2.1 High-resolution XRD at room temperature

The Rietveld refinements of *R*CrO$_4$ scheelites corresponding to the X-ray diffraction data at room temperature are shown in figure 3.9. The scheelite phase obtained at high-pressure shows purity between 95% and 90% with an inevitable impurity amount of $R\text{CrO}_3$ distorted perovskite with an orthorhombic structure in the space group *Pbnm* (D_{2h}^{16}, No. 62) between 5 and 10%. An exceptionally high amount of impurity (15%) corresponds to the LuCrO_4 then to the YbCrO_4 (10%), which have been taken into account in the study of the magnetic properties of these samples as it will be discussed in chapter 5. However, for the rest of the series, e.g. the GdCrO_4 with 5% impurities, the amounts of impurity have been reduced to less than a half in comparison with most of reported $R\text{CrO}_4$-scheelites [42-45, 46]. Moreover, traces of another impurity are seen, which appears also in these previous publications, but have not been investigated. These impurities have been identified in this work as a monoclinic phase that belongs to the space group $P2_1/n$. The study of this impurity, in addition to other impurities, is extended in chapter 4. In case of HoCrO_4 scheelite, some traces of the corresponding zircon phase (2%) have been found which refers to the need of increasing the pressure of the synthesis to values slightly above 4 GPa.

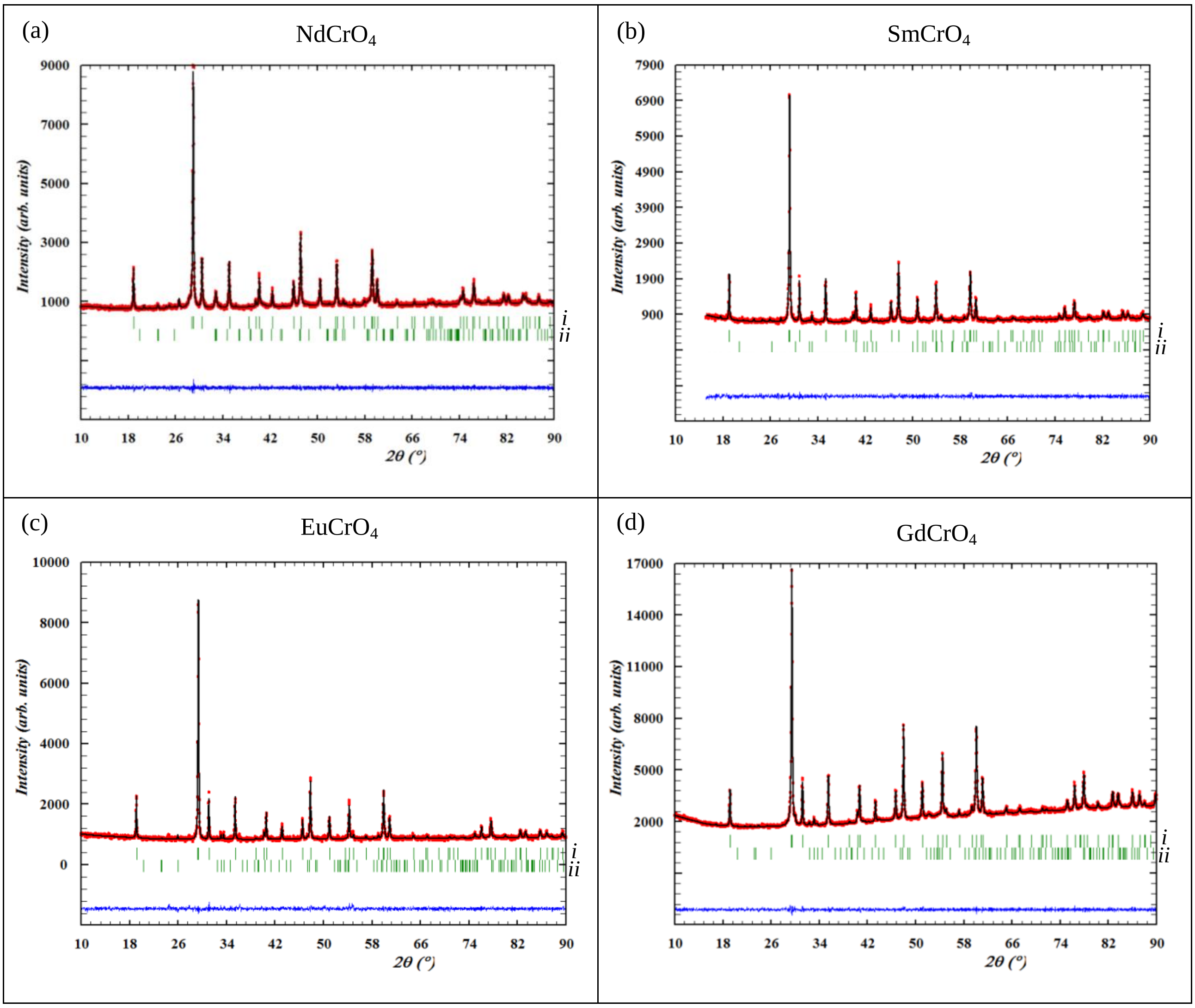

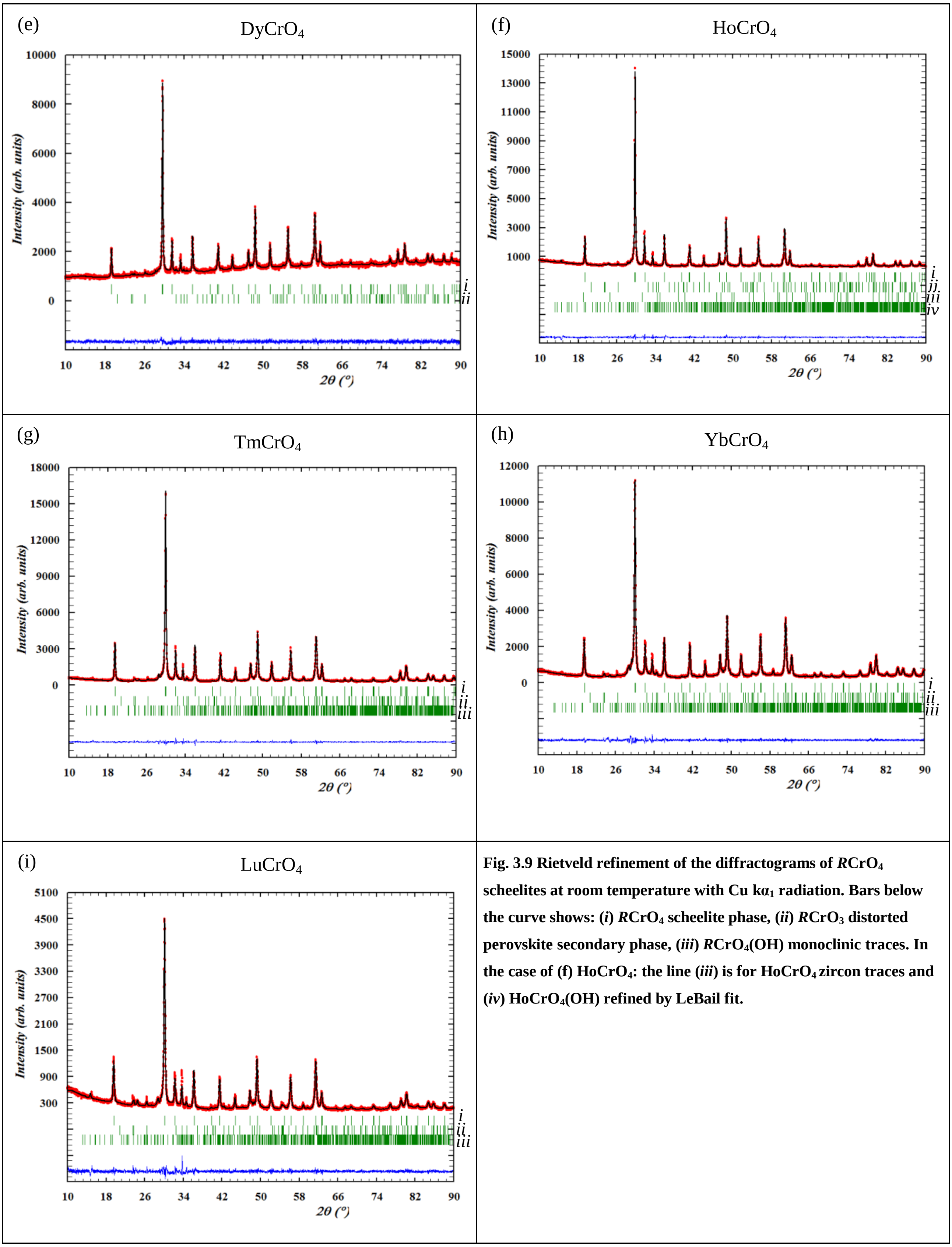

Fig. 3.9 Rietveld refinement of the diffractograms of *R*CrO$_4$ scheelites at room temperature with Cu kα$_1$ radiation. Bars below the curve shows: (*i*) *R*CrO$_4$ scheelite phase, (*ii*) *R*CrO$_3$ distorted perovskite secondary phase, (*iii*) *R*CrO$_4$(OH) monoclinic traces. In the case of (f) HoCrO$_4$: the line (*iii*) is for HoCrO$_4$ zircon traces and (*iv*) HoCrO$_4$(OH) refined by LeBail fit.

In comparison with the corresponding zircon phase, an average reduction of 10.64% in the volume of the *R*CrO$_4$ oxide takes place upon zircon to scheelite transition of these samples. This corresponds to an average increase in density by 11.9%. As previously discussed, at ambient pressure the zircon-like structure belongs to the tetragonal symmetry with a space group *I*4$_1$/*amd*, and atoms take the Wyckoff atomic position as in table 3.1.

Table 3.1 Atomic positions of the zircon *R*CrO$_4$ compounds with a tetragonal symmetry and a space group *I*4$_1$/*amd*

4*a*	*R*	0.0	0.75	0.125
4*b*	Cr	0.0	0.25	0.375
16*h*	O	0.0	*v*	*w*

Upon the pressure-induced transition, the scheelite phase preserves the tetragonal structure but with a lower symmetry (space group *I*4$_1$/*a*) where the atoms of *R*CrO$_4$ are located in the crystallographic positions given in table 3.2.

Table 3.2 Atomic positions of the scheelite *R*CrO$_4$ compounds with a tetragonal symmetry and a space group *I*4$_1$/*a*

4*b*	*R*	0.0	0.25	0.625
4*a*	Cr	0.0	0.25	0.125
16*f*	O	*u*	*v*	*w*

The results of the refinement in addition to the oxygen refined-positions for the scheelite *R*CrO$_4$ polymorphs are shown in tables 3.3 and 3.4. The SmCrO$_4$ and GdCrO$_4$ data has been published as in Appendices (I) and (II), respectively. However, the data for TbCrO$_4$ and ErCrO$_4$ scheelites correspond to publications, as shown in table 3.3, for polycrystalline powders at 40 and 100 K, respectively. The later compound has been partially studied in this work and published, as in Appendix (III). Extra interatomic distances and bond angles, rather than those available in the literature, have been derived in table 3.4 for the two published scheelite compounds and in table 3.5 for the published *R*CrO$_4$-zircon data. These calculations have been carried out from the atomic positions and lattice parameters using the Bond_Str program integrated in the FullProf Suit program [55, 56]. The theoretical density (D_{th}), parameters ratio (c/a), volume-decrease and density-increase for the scheelites have also been calculated in comparison with the corresponding zircon phases. The variation in lattice parameters; atomic positions; interatomic distances and angles will be later represented in figures 3.10-14.

An attempt to calculate the bond-valence sums and global instability indices is explained in the next chapter on the investigation of the scheelite structure stability. For the zircon structures, bond-valence sums have been calculated from the published lattice parameters and from atomic positions of *R*CrO$_4$-zircons explained in table 3.5.

Table 3.3 Lattice parameters, atomic positions and structural relationships calculated from the Rietveld structure refinement of RCrO$_4$ scheelite polycrystalline powders studied by XRD (Cu- kα_1) radiation at room temperature. (The volume-reduction and density-increase values are calculated in comparison with volume and density values of zircon phases in table 3.5)

RCrO$_4$ Scheelites		Nd	Sm	Eu	Gd	Tb[45]	Dy	Ho	Er[47]	Tm	Yb	Lu
a (Å)		5.10903 (8)	5.0771 (10)	5.06263 (9)	5.05051 (5)	5.0367 (10)	5.01866 (6)	5.00369 (8)	4.9989 (10)	4.97907 (9)	4.9667 (12)	4.9551 (14)
c (Å)		11.7127 (4)	11.5622 (4)	11.4998 (4)	11.4519 (3)	11.3734 (4)	11.3168 (4)	11.2682 (3)	11.2332 (23)	11.1679 (3)	11.1203 (4)	11.0889 (5)
c/a		2.2925	2.2774	2.2715	2.2675	2.2581	2.2549	2.2520	2.2471	2.2430	2.2390	2.2379
V (Å^3)		305.727 (14)	298.032 (17)	294.743 (17)	292.111 (11)	288.529	285.034 (16)	282.121 (12)	280.7065	276.866 (12)	274.316 (12)	272.36 (2)
Volume reduction(%) upon transition		10.423	10.776	10.585	9.607	10.547	10.760	10.742	10.420	10.665	10.717	10.731
D_{th} (gm/cm^3)		5.654	5.937	6.039	6.213	6.329	6.490	6.614	6.703	6.836	6.999	7.096
Density increase (%) upon transition		11.629	12.082	11.854	10.630	11.800	12.051	12.025	11.642	11.937	12.002	12.013
Reliability factors	R_p	0.24	0.321	0.378	0.215	0.132	0.315	0.174	0.0115	0.0920	0.115	0.215
	R_{wp}	0.158	0.200	0.207	0.124	0.076	0.175	0.140	0.0147	0.0979	0.119	0.189
	R_B	0.0079	0.0187	0.0477	0.0084	0.010	0.0259	0.0281	0.014	0.0114	0.0832	0.199
	R_F	0.0133	0.0183	0.0435	0.0093	0.014	0.0292	0.0521	0.0201	0.081	0.0678	0.343
	χ^2	1.169	1.00	1.32	1.121	1.67	1.281	1.541	1.9	1.770	2.002	1.748
Atomic positions (16f) O	u	0.2521 (10)	0.2486 (16)	0.2492 (14)	0.2641 (11)	0.2405 (4)	0.2683 (13)	0.2555 (8)	0.2352 (26)	0.2538 (9)	0.2620 (10)	0.2485 (13)
	v	0.6207 (13)	0.608 (2)	0.6129 (19)	0.5866 (16)	0.6115 (25)	0.5982 (17)	0.6077 (11)	0.6044 (20)	0.6147 (12)	0.6258 (12)	0.6160 (16)
	w	0.5593 (5)	0.5517 (8)	0.5511 (7)	0.5543 (5)	0.5475 (13)	0.5511 (6)	0.5476 (4)	0.5478 (6)	0.5499 (5)	0.5473 (5)	0.5425 (7)

$$R_p = \frac{\sum_i (Y_i - Y_{ci})}{\sum_i (Y_i)}$$

$$R_{wp} = \sqrt{\frac{\sum_i (Y_i - Y_{ci})^2}{\sum_i (Y_i)^2}}$$

$$R_B = \frac{\sum_i (I_i - I_{ci})}{\sum_i (I_i)}$$

$$\chi^2 = (R_{wp} / R_{exp})^2$$

Table 3.4 Interatomic distances and angles calculated from the Rietveld structure refinement of *R*CrO$_4$ scheelite polycrystalline powders studied by XRD (Cu-k*α*) radiation at room temperature.

***R*CrO$_4$ Scheelites**	Nd	Sm	Eu	Gd	Tb[45]	Dy	Ho	Er[47]	Tm	Yb	Lu
d(Cr-O) (Å)	1.623 (6)x4	1.693 (9)x4	1.678 (8)x4	1.660 (6)x4	1.7237 (18)	1.622 (7)x4	1.663 (4)x4	1.744 (10)x4	1.631 (5)x4	1.589 (5)x4	1.682 (7)x4
d(*R*-O) (Å)	2.416 (6)x4	2.369 (10)x4	2.385 (9)x4	2.308 (7)x4	2.3582 (18)x4	2.359 (8)x4	2.366 (5)x4	2.295 (11)x4	2.366 (6)x4	2.434 (6)x4	2.375 (8)x4
	2.599 (6)x4	2.507 (9)x4	2.485 (8)x4	2.584 (6)x4	2.4089 (15)x4	2.523 (7)x4	2.434 (4)x4	2.382 (9)x4	2.422 (5)x4	2.397 (6) x4	2.325 (7)x4
Cr-O-*R* (°)	125.7 (2)x1	123.3 (4)x1	122.6 (3)x1	127.6 (3)x1	120.71 (7)x1	125.0 (3)x1	121.88 (20)x1	121.5 (5)x1	122.4 (2)x1	120.2 (2)x1	118.4 (3)x1
	132.6 (2)x1	131.7 (4)x1	132.9 (3)x1	126.8 (3)x1	132.89 x1	130.4 (3)x1	132.87 (19)x1	130.7 (5)x1	133.8 (2)x1	137.6 (2)x1	135.5 (3)x1
O-Cr-O (°)	103.0 (5)x4	104.5 (8)x4	104.9 (7)x4	103.8 (5)x4	105.16 (16)	105.4 (6)x4	106.0 (4)x4	104.4 (10)x4	105.3 (5)x4	107.2 (5)x4	107.2 (7)x4
	123.4 (6)x2	119.9 (8)x2	119.1 (7)x2	121.6 (6)x2	118.5 (15)	117.9 (7)x2	116.7 (4)x2	120.3 (13)x2	118.1(5)x2	114.1(5)x2	114.1 (6)x2
O-*R*-O (°)	95.8 (3)x4	97.2 (5)x4	97.3 (5)x4	97.1 (4)x4	98.03 (11)x4	97.2 (4)x4	97.8 (3)x4	98.2 (8)x4	97.2 (3)x4	97.2 (3)x4	98.5 (4)x4
	141.3 (4)x2	138.1 (7)x2	138.3 (6)x2	138.9 (5)x2	136.11 (13)x2	138.5 (6)x2	136.7 (4)x2	135.5 (9)x2	138.5 (4)x2	138.4 (4)x2	134.7 (5)x2
	70.8 (3)x4	70.2 (5)x4	69.9 (5)x4	70.0 (4)x4	70.17 (8)x4	68.8 (4)x4	69.1 (3)x4	71.0 (5)x2	69.4 (3)x4	67.9 (3)x4	68.6 (4)x4
	133.6 (4)x4	132.0 (6)x4	131.6 (5)x4	129.2 (4)x4	131.56 (11)x4	128.6 (5)x4	129.7 (3)x4	131.5 (6)x4	130.6(4)x4	129.7 (4)x4	129.6 (5)x4
O-O	2.540 (8)x2	2.678 (12)x2	2.660 (11)x2	2.612 (8)x2	2.7378 x2	2.581 (9)x2	2.655 (6)x2	2.7203 9x2	2.594 (7)x2	2.558 (7)x2	2.651 (11)x2
Cr--Cr	3.8858 (9)x4	3.8470 (11)x4	3.8305 (9)x4	3.8175 (7)x4	3.7982 x4	3.7816 (9)x4	3.7676 (7)x4	3.7594 x4	3.7407 (7)x4	3.7276 (7)x4	3.7184 (12)x4
Cr--*R*	3.8858 (9)x4	3.8470 (11)x4	3.8305 (9)x4	3.8175 (7)x4	3.7982 x4	3.7816 (9)x4	3.7676 (7)x4	3.7594 x4	3.7407 (7)x4	3.7276 (7)x4	3.7184 (13)x4
	3.6126 (6)x4	3.5900 (8)x4	3.5798 (8)x4	3.5712 (5)x4	3.5615 x4	3.5487 (7)x4	3.5381 (6)x4	3.5347 x4	3.5207 (6)x4	3.5118 (6)x4	3.5041 (10)x4
R--*R*	3.8858 (9)x4	3.8470 (11)x4	3.8305 (9)x4	3.8175 (7)x4	3.7982 x4	3.7816 (9)x4	3.7676 (7)x4	3.7594 x4	3.7407 (7)x4	3.7276 (7)x4	3.7184 (13)x4

Table 3.5 Lattice parameters, atomic positions, distances, angles and derived relationships from the Rietveld structure refinement of *R*CrO$_4$ zircon polycrystalline powders studied by XRD (Cu- k*α*) radiation at 300 K [46, 57] and neutron diffraction at 50 K [54, 58]. The lattice parameters, atomic positions, and some interatomic distances and angles are taken from the corresponding references, while further distances and angles has been calculated by Bond_Str program based on these published data.

Table 3.5 (Cont.)

RCrO$_4$ zircon		Nd[46,54]	Sm[46]	Eu[57]	Gd[58]	Tb[54]	Dy[54]	Ho[54]	Er[54]	Tm[54]	Yb[54]	Lu[54]
a (Å)		7.306 (2)	7.251 (11)	7.218 (2)	7.170 (2)	7.164 (7)	7.138 (3)	7.1155 (2)	7.0939 (2)	7.0646 (2)	7.0420 (3)	7.023 (1)
c (Å)		6.3934 (2)	6.3530 (10)	6.327 (3)	6.286 (2)	6.2831 (7)	6.2674 (3)	6.2428 (1)	6.2269 (2)	6.2097 (2)	6.1954 (3)	6.185 (1)
*c/a**		0.875	0.876	0.877	0.877	0.877	0.878	0.877	0.878	0.879	0.880	0.881
V (Å^3)*		341.30	334.02	329.63	323.15	322.54	319.40	316.07	313.35	309.91	307.22	305.1
D_{th}* (gm/cm^3)		5.065	5.297	5.399	5.616	5.661	5.792	5.904	6.004	6.107	6.249	6.335
Atomic positions (16*h*) O	*v*	0.4282 (2)	0.4275 (12)	0.428 (2)	0.429 (1)	0.4321 (1)	0.4339 (7)	0.4322 (3)	0.4345 (3)	0.4350 (3)	0.4352 (2)	0.435 (2)
	w	0.2038 (2)	0.2108 (11)	0.210 (5)	0.203 (1)	0.2017 (1)	0.2027 (6)	0.2009 (3)	0.2000 (3)	0.1996 (3)	0.1992 (3)	0.199 (2)
d(Cr-O) (Å)		1.701 (1)x4	1.657 (8)x4	1.597 (5)x4	1.688 (7)x4	1.699 (1)x4	1.700 (4)x4	1.692 (2)x4	1.703 (2)x4	1.701 (2)x4	1.699 (2)x4	1.696 (1)x4
d(*R*-O) (Å)		2.405 (2)x4	2.4011 (16)x4	2.385 (1)x4	2.352 (7)x4	2.328 (1)x4	2.308 (5)x4	2.310 (2)x4	2.286(2)x4	2.273 (2)x4	2.264 (2)x4	2.258 (2)x4
		2.472 (2)x4	2.492 (6)x4	2.486 (5)x4	2.432 (5)x4	2.432 (1)x4	2.438 (4)x4	2.413 (2)x4	2.410 (2)x4	2.402 (1)x4	2.395 (1)x4	2.389 (1)x4
Cr-O-*R* (°) *		152.04 (7)x1	154.1 (4)x1	153.93 (9)x1	151.91 (3)x1	152.10 (4)x1	152.73 (20)x1	151.86 (9)x1	152.00 (9)x1	151.95 (9)x1	151.84 (7)x1	151.7 (6)x1
		98.280 (7)x1	97.900 (3)x1	97.872 (10)x1	98.210 (3)x1	97.406 (3)x1	96.852 (18)x1	97.469 (8)x1	96.888 (8)x1	96.848 (8)x1	96.870 (7)x1	96.97 (5)x1
O-Cr-O (°)		114.5 (2)x4	113.36 (6)x4	113.43 (2)x4*	114.4 (5)x4*	114.23 (6)x4	113.8 (3)x4	114.4 (1)x4	114.2 (2)x4	114.2 (1)x4	114.3 (1)x4	114.3 (1)x4
		99.90 (2)x2	101.95 (2)x2	101.81 (9)x2*	100.0 (4)x2	100.32 (3)x2	101.1 (4)x2	100.1 (2)x2	100.5 (2)x2	100.4 (2)x2	100.3 (2)x2	100.1 (1)x2
O-*R*-O (°)		92.51 (3)x4	92.95 (4)x4*	92.913 (8)x4*	92.5(3) x4	92.46 (3)x4	92.55 (5)x4	92.42 (3)x4	92.39 (3)x4	92.38 (4)x4	92.36 (2)x4	92.38 (3)x4
		155.82 (1)x2	153.76 (6)x2*	153.94 (9)x2*	155.8 (5)x2	156.10 (1)x2	155.65 (3)x2	156.29 (2)x2	156.41 (1)x2	156.49 (2)x2	156.58 (1)x2	156.6 (1)x2
		63.52 (2)x2	62.205 (9)x2*	62.446 (9)x2*	63.80 (2)x2	64.88 (2)x2	65.19 (6)x2	65.00 (2)x2	65.78 (5)x2	65.91 (5)x2	66.00 (4)x2	65.95 (3)x2
		136.30 (1)x4	137.15 (5)x4*	136.99 (2)x4*	136.1 (4)x4	135.42 (4)x4	134.77 (3)x4	135.34 (3)x4	134.84 (1)x4	134.75 (2)x4	134.70 (1)x4	134.7 (2)x4
O-O*		2.6040 (2)	2.5741 (12)	2.5696 (2)	2.5668 (10)	2.6094 (10)	2.6257 (7)	2.5929 (3)	2.6176 (3)	2.6139 (3)	2.6083 (20)	2.60 (20)
Cr--Cr*		3.9875 (9)x4	3.9581 (5)x4	3.9404 (10)x4	3.9143 (9)x4	3.9116 (3)x4	3.8981 (14)x4	3.8850 (9)x4	3.8735 (9)x4	3.8583 (9)x4	3.8466 (14)x4	3.837 (5)x4
Cr--*R**		3.9875 (9)x4	3.9581 (5)x4	3.9404 (10)x4	3.9143 (9)x4	3.9116 (3)x4	3.8981 (14)x4	3.8850 (9)x4	3.8735 (9)x4	3.8583 (9)x4	3.8466 (14)x4	3.837 (5)x4
		3.1967 (10)x2	3.1765 (5)x2	3.1635 (15)x2	3.1430 (10)x2	3.1415 (4)x2	3.1337 (15)x2	3.1214 (5)x2	3.1134 (10)x2	3.1048 (10)x2	3.0977 (15)x2	3.093 (5)x2
R--*R**		3.9875 (9)x4	3.9581 (5)x4	3.9404 (10)x4	3.9143 (9)x4	3.9116 (3)x4	3.8981 (14)x4	3.8850 (9)x4	3.8735 (9)x4	3.8583 (9)x4	3.8466 (14)x4	3.837 (5)x4

* *calculated from corresponding reference by Bond_Str program in the FullProf_Suit* [29, 55, 56]

In figure 3.10, the comparison between lattice parameters and unit-cell volumes for both zircons and scheelites of *R*CrO$_4$ series is illustrated. The relationships compared here and in the following figures plotted against the ionic radii of the radii of R^{3+} cations with dodecahedral coordination [57] where the rare-earth cation is coordinated by 8 oxygen atoms. In figure 3.10(a), one can easily notice the general contraction of the lattice parameters due to the lanthanide ionic radii contraction. This effect for *a* parameter of the scheelite phase is almost the same as that for both *a* and *c* parameters of the zircon phase. However, the contraction of the *c* parameter of the scheelites is four times bigger than that for *a* parameter. This in return affects the development of the *c*/*a* ratio for the scheelite series.

It can be noticed that $(c/a)_{\text{scheelite}}$ is almost as twice the $(a/c)_{\text{zircon}}$, as explained previously in equation (3.1) and illustrated in figure 3.10(a) with a magnified (blue) scale. Due to the bigger contraction in the scheelite *c* parameter, this ratio deviates to lower values at the end of the series (smaller lanthanide ionic radii). Nevertheless, between the two polymorphs another relationship for the lattice parameter (*a*) is found to apply. This is plotted as a dashed (red) line above the $a_{Scheelite}$ curve in figure 3.19(a) and can be expressed as:

$$a_{Scheelite} = a_{Zircon}/\sqrt{2} \tag{3.2}$$

A small deviation appears also in this case between the real and calculated values of equation (3.2), but reversibly, for compounds with bigger lanthanide ionic radii. In figure 3.10 (b), the volume contraction of the zircon and scheelite compounds due to lanthanide contraction is illustrated. The compression upon phase transition can be observed, results an average volume contraction of 10.64% and a density increase of 11.9%.

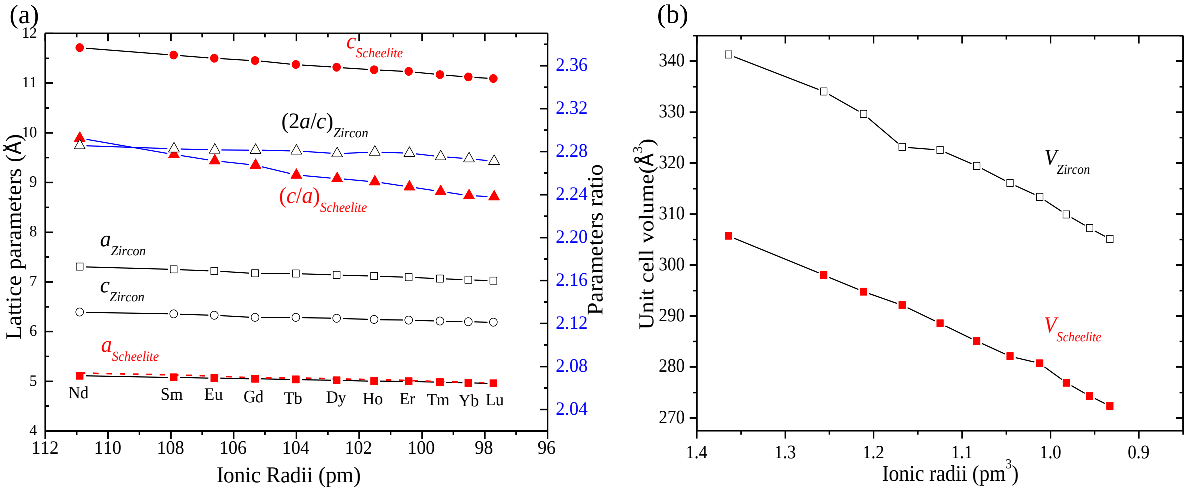

Fig. 3.10 A comparison between the *R*CrO$_4$ zircon and scheelite lattice parameters and their derived relationships. (a) *a* and *c* parameters development *vs.* ionic radii for R^{3+} ions with a dodecahedral coordination [57] (left scale) and derived c/a and a/c ratios for scheelites and zircons respectively (magnified right scale). (b) the calculated unit cell volume for both *R*CrO$_4$ zircons and scheelites. Zircon data are derived from the corresponding references and values in Table 3.5

The main effective change in the structure of RCrO$_4$ compounds upon the pressure-induce transition from zircon-type structure to scheelite-type structure is in the bond angles of Cr-O-*R* interaction. These angles connect the two polyhedra together at an oxygen atom and create a super-exchange mechanism through Cr-O-*R*-O-Cr interaction. Figure 3.11 shows the differences in these angles between zircon and scheelite samples. In the zircon-phase, two Cr-O-*R* angles exist: one with an average value of 152.4° and the other angle is with an average of 97.4° such values are considered to be independent of the effect of lanthanide contraction and seem to be almost constant for the zircon compounds. In the scheelite case, these angles are changed dramatically by both the decrease of the high angle value and the increase of the low angle value. This results in average values of 122.12° and 133.1°. The increase of the 97.4 value alters the magnetic properties as will be seen in chapter 5.

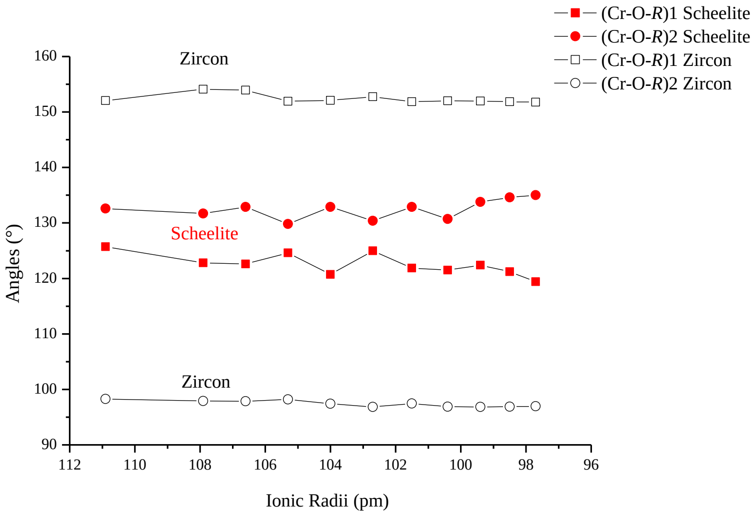

Fig. 3.11 Cr-O-*R* angles of the zircon and scheelite RCrO$_4$ compounds

The interatomic distances, on the other hand, seem to be almost unchanged upon the transition from zircon to scheelite within the experimental resolution available. In figure 3.12(a), the Cr-O distances are averaging around 1.6 Å and are independent of the lanthanide contraction. It is worth to notice that the zircon data are from neutron diffraction data at 50 K [54], therefore their constant value of Cr-O are more representative due to the higher certainty of oxygen atoms position. In each of the zircon and scheelite compounds, the size of the (RO$_8$) polyhedra decreases continuously with the size of the R^{3+} ion, noticing the contraction of *R*–O bond distance due to the higher affinity of electrons for smaller lanthanides. However, the *R*-O distances for a specific compound are almost unchanged upon the pressure-induced transition.

Figure 3.12(b) shows the changes in the shortest O-O distances, which is almost unchanged and corresponds to one of the edges of the *R*-dodecahedron. In the case of zircon, the shortest O-O distances are at the shared edge between *R*- and Cr-polyhedra.

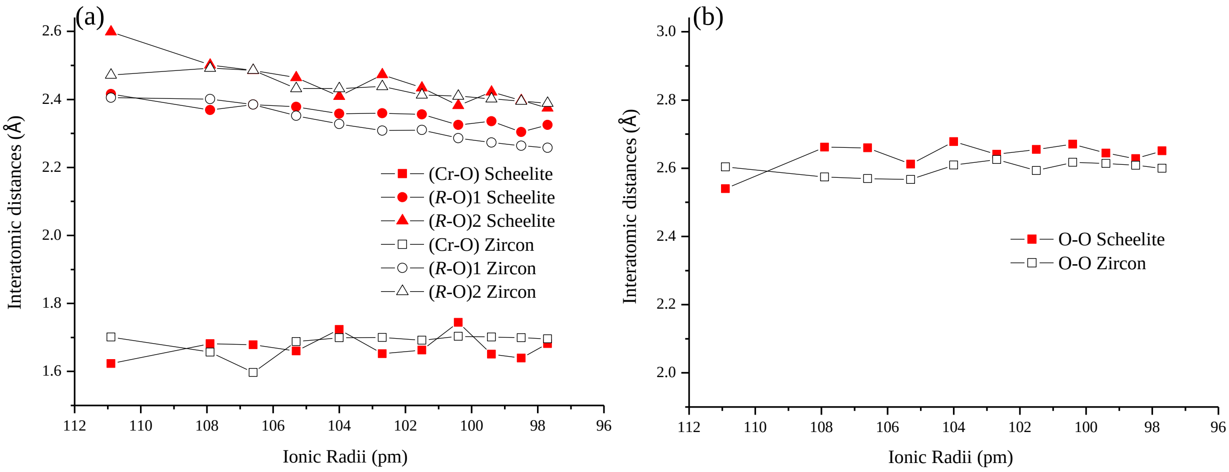

Fig. 3.12 Interatomic distances for (a) Cr-O and *R*-O (b) O-O shortest bonds, in scheelite and zircon phases.

To understand the changes that happen in the independent polyhedra, figure 3.13 explains the changes of the angles inside each polyhedron. In figure 3.13(a), upon the transition a drop in one of the O-*R*-O angles signified by (*i*), can be viewed. Moreover, a slight decrease in the other high angle (*ii*) and an increase in the other two low angles (*iii* and *iv*) takes place. This, in return, contributes to the volume contraction upon the pressure-induced transition by allowing the rotation of Cr-tetrahedra around the *R*-dodecahedron. These results in the increase of the number of the Cr-tetrahedra surrounding *R* and, therefore, a better packing in the scheelite polymorph. Such changes in the O-*R*-O angles, in addition to the previously discussed Cr-O-*R* angles, are supported by the breaking of the edge sharing between Cr- and *R*-polyhedra in the zircons and the ruling of only corner sharing between them in the scheelites through a bond-switching mechanism, as proposed earlier.

Concerning the changes inside the Cr-tetrahedra, one can notice in figure 3.13(b) a general slight increase in both of the O-Cr-O angles upon the high-pressure transition. The Cr-tetrahedra in zircon structure are elongated in the *c*-direction and having D_{2d} point group symmetry, while in the scheelite structure they have D_{4h} point group symmetry.

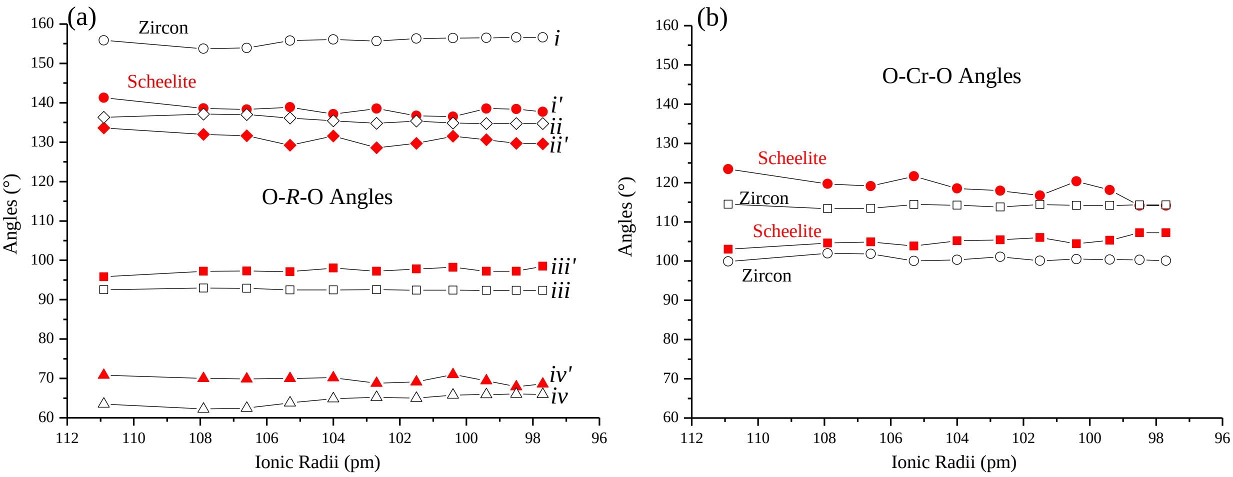

Fig. 3.13 (a) O-*R*-O and (b) O-Cr-O angles for *R*CrO$_4$ zircons and scheelites

Finally yet importantly, the interatomic distances have been calculated for the second-neighboring atoms, the coordination of Cr-tetrahedra around the lanthanide and the shortest distance between Cr atoms. Due to tables 3.3 and 3.4 in addition to figure 3.14, for both zircon and scheelite phases, four Cr--Cr distances are connected through the Cr-O-O-Cr interactions while four *R*--*R* direct distances are represented through *R*-O-*R* interactions. Both Cr--Cr and *R*--*R* distances are equal to each other for a certain zircon or scheelite compound, while these distances decrease with the contraction of the lanthanide radii. Moreover, upon the high-pressure transition, both Cr--Cr and *R*--*R* distances decrease, see figure 3.14.

Upon the zircon-to-scheelite transition, a very important difference is also observed for the Cr--*R* distances, which are linked over the Cr-O-*R* interaction. For the zircon phase, six Cr--*R* distances exist through the Cr-O-*R* interactions; while for the scheelite phase, eight Cr--*R* distances occur. Four Cr--*R* distances are always equal to the Cr--Cr and *R*--*R* distances in both zircons and scheelites “represented as (Cr--*R*)1 in figure 3.14”, while another different distance “referred to as (Cr--*R*)2” occure in the scheelite in double the amount of that in the zircon. In scheelite, (Cr--*R*)1 distances are 0.1 Å smaller than that in zircon, while (Cr--*R*)2 distances are 0.4 Å longer. This can be understood by the breaking of one quarter of the *R*-O bonds in zircon (contributing to the edge sharing between the Cr- and *R*-polyhedra) and forming in the scheelite two extra *R*-O bonds that share corner with two new *R*-dodecahedra.

Concerning these paths it is worth noting that the coordination number between Cr- and *R*-polyhedra increases from six to eight, regarding the second-nearest neighbors in going from zircon to scheelite. This fact also justifies the increasing of the density for the scheelite phases in comparison with the zircon. The topologies of CrO$_4$ tetrahedra in both zircon and scheelite structures are seen in figure 3.4.

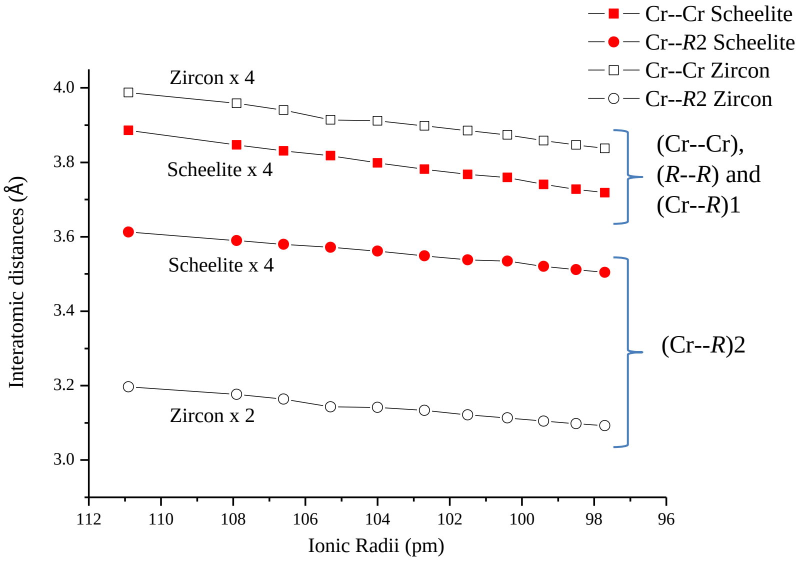

Figure 3.14 Second-neighbor atomic distances for Cr--Cr, *R*--*R* and Cr--*R* distances in *R*CrO$_4$ zircons and scheelites.

3.2.2 *In-situ* XRD at low temperatures

Few scheelite samples have been investigated by x-ray powder diffraction at low temperatures (down to 13 K) in order to investigate any existence of purely structural transitions upon cooling. Unlike zircon structures, which transform upon cooling between 27 and 40 K from tetragonal symmetry ($I4_1/amd$) to an orthorhombic symmetry (*Imma*, *Z*=4, No. 74, D_{2h}^{28}) [14, 15, 59], scheelite structures do not experience a structural transition down to 13 K (with reference to the used instrument resolution). Figure 3.15 shows the diffraction patterns of the TbCrO$_4$ and GdCrO$_4$ scheelites. Due to lattice contractions upon cooling, only a minute 2θ shift could be noticed between the diffraction patterns at room temperature (red thick line in figure 3.15) and low-temperature (black thin line).

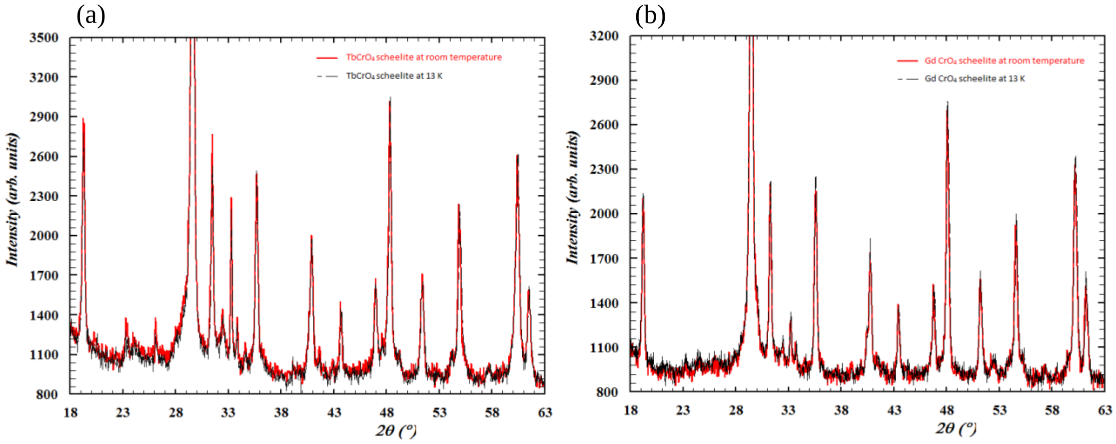

Fig. 3.15 XRD diffraction patterns for (a) TbCrO$_4$ scheelite and (b) GdCrO$_4$ scheelite at room temperature (red color) and at 13 K (black). A magnification is done for lower intensity peaks. TbCrO$_4$ data are measured in this work for a sample published in the work of Climent-Pascual *et al.*[45]

3.2.3 Neutron diffraction

The samples of *R*CrO$_4$ scheelite (*R*= Nd, Gd, Dy, Ho, Er and Tm) have been investigated in this work by neutron diffraction. The work was carried at LLB facility in Saclay, France for the GdCrO$_4$ scheelite using the 7C$_2$ hot-neutron two-axis diffractometer, and at ISIS facility in the UK for the NdCrO$_4$, DyCrO$_4$ and HoCrO$_4$ scheelites using the WISH cold-neutron time of flight (TOF) powder diffractometer. Table 3.6 shows the refinement results of the scheelite phase for NdCrO$_4$ at 30 K, GdCrO$_4$ at 100 K, DyCrO$_4$ at 80 K and HoCrO$_4$ at 26 K. The lower temperature diffraction patterns are explained in chapter 5 with the magnetic structures. We have published the results of GdCrO$_4$ as can be seen in Appendix (II). The results for the high neutron data are in good agreement with those done by XRD. In the calculation in next chapter for the Global instability indices, NPD was taken into account for the studied compounds. The Rietveld refinement of the NPD patterns are shown in figures 3.16-19. The Rietveld refinement data for Tm- and Er- chromates are discussed later in chapter 5.

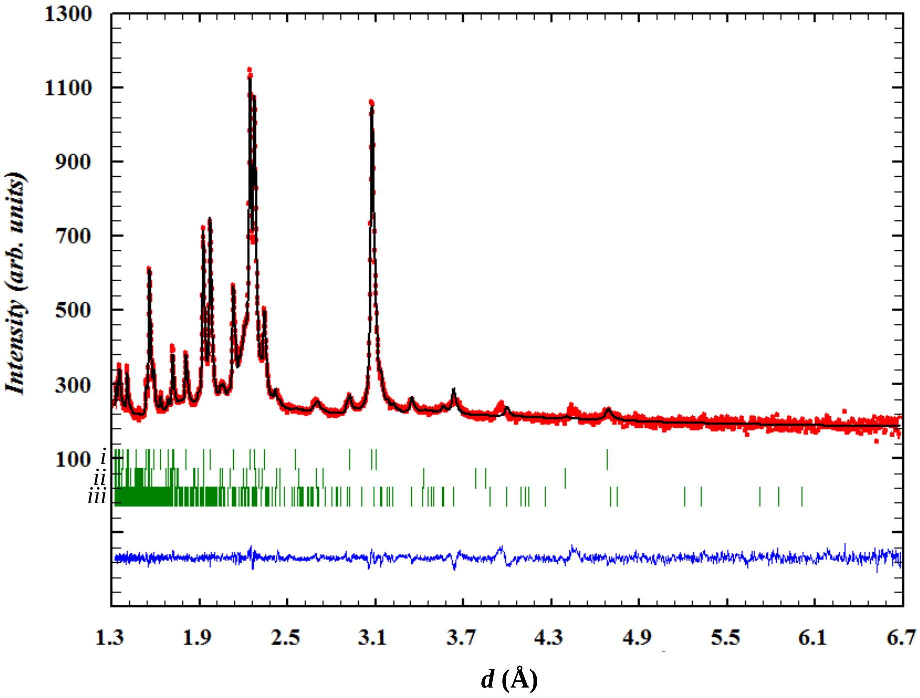

Fig. 3.16 Rietveld refinement of the NdCrO$_4$ scheelite polymorph at 30 K for TOF neutron diffraction data. First line of the vertical bars (*i*) is for the NdCrO$_4$ scheelite. Second line (*ii*) is for NdCrO$_3$ distorted perovskite. Third line (*iii*) is for a monoclinic *P*2$_1$/*n* impurity of Nd(OH)CrO$_4$ traces refined by LeBail fit. An extra peak at 4.4 *d*-spacing is due to the beginning of the appearance of the magnetic peak.

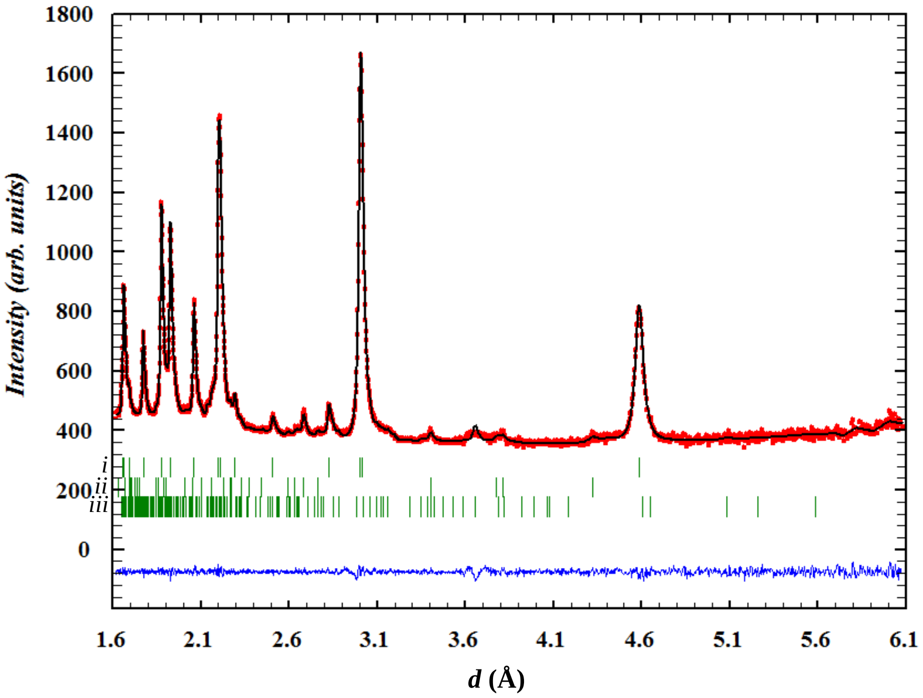

Fig. 3.17 Rietveld refinement of the DyCrO$_4$ scheelite polymorph at 80 K for TOF neutron diffraction data. First raw of the vertical bars (*i*) corresponds to the DyCrO$_4$ scheelite. Second line (*ii*) is for DyCrO$_3$ distorted perovskite. The third line (*iii*) is for a monoclinic *P*2$_1$/*n* impurity of Dy(OH)CrO$_4$ traces refined by LeBail fit.

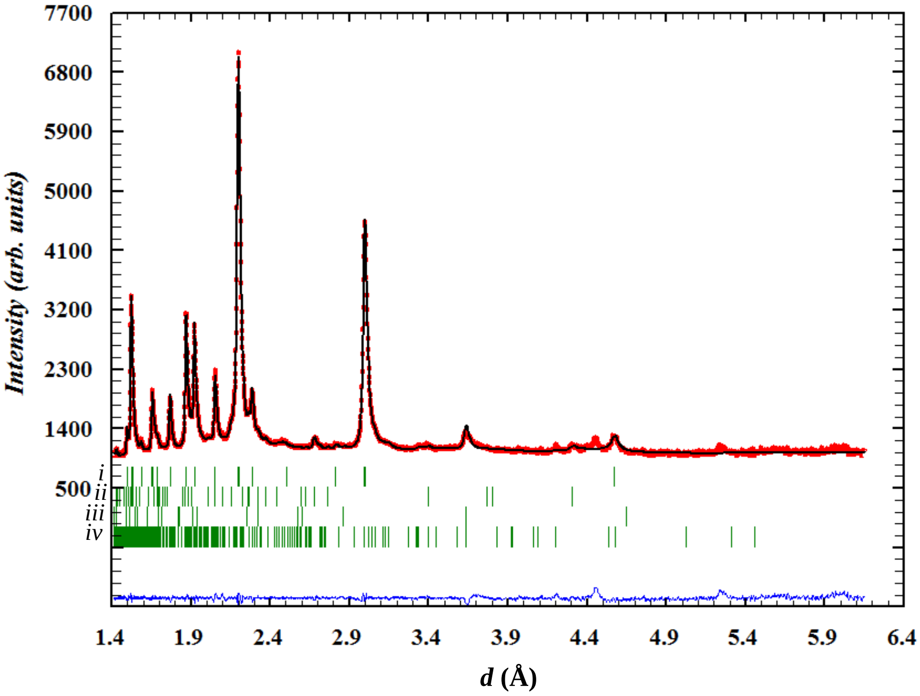

Fig. 3.18 Rietveld refinement of the HoCrO$_4$ scheelite polymorph at 26 K for TOF neutron diffraction data. First line of the vertical bars (*i*) is for the HoCrO$_4$ scheelite. Second line (*ii*) is for HoCrO$_3$ distorted perovskite. Third line (*iii*) is for the zircon phase remaining after high-pressure transition. The fourth line (*iv*) is for a monoclinic *P*2$_1$/*n* of Ho(OH)CrO$_4$ traces refined by LeBail fit. An extra peak at 4.45 and 5.25 *d*-spacing are due to the beginning of the appearance of the magnetic peak.

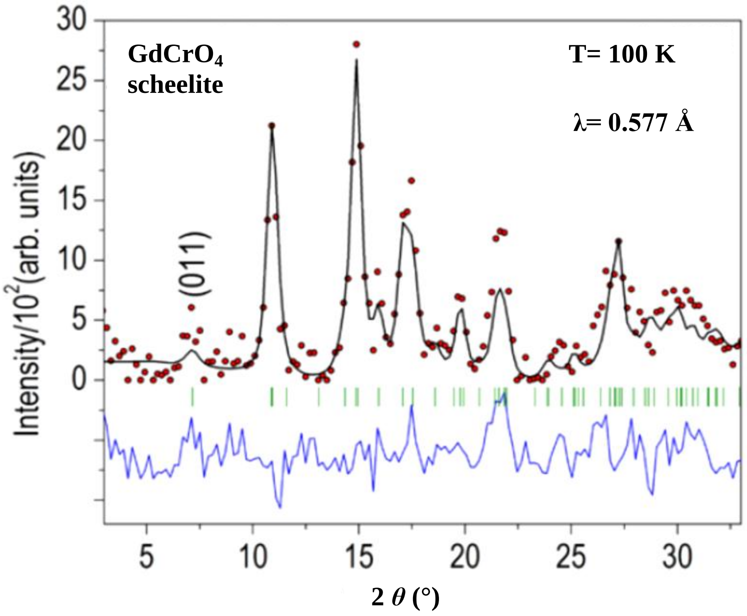

Fig. 3.19 Rietveld refinement of GdCrO$_4$ scheelite polymorph at 100 K for neutron diffraction data with λ= 0.577 Å. [48]

The TbCrO$_4$ and ErCrO$_4$ neutron diffraction data for the scheelite phase has been done in a previous work [45, 47] and explained in table 3.3. The data of the ErCrO$_4$ have been co-published as in Appendix (III) and a further publication is under preparation.

Table 3.6 Lattice parameters and main interatomic and bond angles obtained from the Rietveld refinement of the neutron diffraction data of RCrO$_4$ scheelites.

RCrO$_4$ scheelites		Nd	Gd	Dy	Ho
a (Å)		5.1093(11)	5.050(5)	5.0148(4)	5.0034(2)
c (Å)		11.705(3)	11.401(23)	11.3030(10)	11.2538(5)
c/a		2.291	2.258	2.254	2.249
V (Å^3)		305.549(0.12)	290.111(5)	284.255(1)	281.837(1)
Vol. reduction (%)		10.42331	9.9021	10.76015	10.74241
D_{th} (gm/cm^3)		5.657	6.453	6.508	6.621
Density increase (%)		11.62883	2.26747	12.0511	12.02575
Reliability factors	R_p	0.111	0.36	0.0818	0.0773
	R_{wp}	0.0684	0.44	0.0449	0.0460
	R_B	0.467	0.25	0.2216	0.0990
	R_F	1.22	0.190	0.1607	0.674
	χ^2	1.56	2.85	1.151	2.722
Atomic positions	O$_x$	0.2457(3)	0.2468	0.2421(4)	0.2412(3)
	O$_y$	0.6163(2)	0.6163	0.6092(3)	0.60920(18)
	O$_z$	0.54643(14)	0.5490	0.54867(13)	0.54873(10)
d(Cr-O) (Å)		1.7322(13)	1.6857(13)	1.7075(18)x4	1.7060(11)x4
d(R-O) (Å)		2.4340(13)x4	2.393(17)x4	2.3373(17)x4	2.3291(11)x4
		2.4635(16) x4	2.438(3)x4	2.4137(15)x4	2.4035(11)x42
Cr-O-R (°)		119.31(6)x1	121.24(14)x1	121.71(7)x1	121.78(6)x1
		134.85(7)x1	134.0(3)x1	132.14(7)x1	132.03(6)x1
O-Cr-O (°)		106.37(14)x4	105.32(16)x4	104.79(16)x4	104.67(12)x4
		115.87(14)x2	118.14(15)x4	119.30(18)x4	119.58(13)x4
O-R-O (°)		98.21(9)x4	97.53(13)x4	97.83(12)x4	97.81(9)x4
		135.60(9)x2	137.54(16)2	136.68(12)x2	136.74(9)x2
		69.06(7)x4	69.71(11)x4	70.37(8)x4	70.50(7)x4
		131.56(12)x4	131.5(3)x4	131.41(11)x4	131.44(9)x4
O-O		2.774(2)x2	2.680(3)x2	2.724(2)x2	2.7009(15)x2
Cr--Cr		3.8845(7)x4	3.808(5)x4	3.7777(2)x4	3.7653(4)x4
Cr--R		3.8845(7)x4	3.808(5)x4	3.7777(2)	3.7653(4)x4
		3.6128(6)x4	3.571(2)x4	3.54600(20)	3.5384(4)x4
R--R		3.8845(7)x4	3.808(5)x4	3.7777(2)x4	3.7653(4)x4

References

[1] D. Errandonia and F. Javier Manjón, *Progress in Materials Science* **53**, 711 (2008)

[2] S. Ono, K S. Ono, K. Funakoshi, Y. Nakajima, Y. Tange and T. Katsura, *Contribution to Mineralogy and Petrology* **147**, 505 (2004)

[3] U. A. Glasmacher, M. Lang, H. Keppler, F. Langenhorst, R. Neumann, D. Schardt, C. Trautmann and G. A. Wagner, *Physical Review Letters* **96**, 195701 (2006)

[4] I. Farnan, E. Balan, C. J. Pickard and F. Mauri, *American Mineralogist* **88**, 1663 (2003)

[5] R. C. Ewing, *The Canadian Mineralogist* **39**, 697 (2001)

[6] A. F. Reid and A. E. Ringwood, *Earth and Planetary Science Letters* **6**, 205 (1969)

[7] L. G. Liu, *Earth Planet. Sci. Lett.* **44**, 390 (1979)

[8] K. Kusaba, Y. Syono, M. Kikuchi and K. Fukuoka, *Earth and Planetary Science Letter* **72**, 433 (1985)

[9] Elise Knittle and Quentin Williams, *American Mineralogist* **79**, 245 (1993)

[10] W. V. Westrenen, M. R. Frank, J. M. Hanchar, Y. Fei, R. J. Finch and C.S. Zha, *American mineralogist* **89**, 197 (2004)

[11] V. S. Stubican and R. Roy, *Zeitschrift fuer Kristallographie* **119**, 90 (1963)

[12] V. S. Stubican and R. Roy, *Journal of Applied Physics* **34**, 1888 (1963)

[13] E. Jiménez, J. Isasi and R. Sáez Puche, *Journal of Alloys and Compounds* **312**, 53 (2000)

[14] K. Tezuka and Y. Hinatsu, *Journal of Solid State Chemistry* **160**, 262 (2001)

[15] R. Sáez Puche, E. Jiménez, J. Isasi, M. T. F. Diaz and J. L. G. Munoz, *Journal of Solid State Chemistry* **171**, 161 (2003)

[16] T. Keitaro, D. Yoshihiro and H.Yukio, *Journal of Materials Chemistry* **12**, 1189 (2002)

[17] R. J. Finch and J. M. Hanchar, *Reviews in Mineralogy and Geochemistry* **53** (1), 1 (2003)

[18] L. Li, W. Yu and C. Jin, *Physical Review B* **73**, 174115 (2006)

[19] G. D. Ilyushin, V. A. Blatov and Yu. A. Zakutkin, *Acta Crystallographica B* **58**, 948 (2002)

[20] H. Nyman, B. G. Hyde and S. Anderson, *Acta Crystallographica B* **40**, 441 (1984)

[21] D. Errandonea, R. Lacomba-Perales, J. Ruiz-Fuertes, A. Segura, S. N. Achary and A. K. Tyagi, *Physical Review B* **79**, 184104 (2009)

[22] K. Kusaba, T. Yagi, M. Kikuchi and Y. Syono, *Journal of Physics and Chemistry of Solids* **47** (7), 675 (1986)

[23] J. P. Crocombette and D. Ghaleb, *Journal of Nuclear Materials* **257**, 282 (1998).

[24] R. Mittal, S. L. Chaplot, R. Parthasarathy, M. J. Bull, and M. J. Harris, *Physical Review B* **62**, 12089 (2000)

[25] M. Marqués, M. Flórez, J. M. Recio, L. Gerward, and J. S. Olsen, *Physical Review B* **74**, 014104 (2006)

[26] S. L. Chaplot, L. Pintschovius, N. Choudhury, and R. Mittal, *Physical Review B* **73**, 094308 (2006)

[27] M. Marques, J. Contrera-Garcia, M. Florez and J. M. Recio, *Journal of Physics and Chemistry of Solids* **69**, 2277 (2008)

[28] M. B. Smirnov, A. P. Mirgorodsky, V. Y. Kazimirov, and R. Guinebretiere, *Physical Review B* **78**, 094109 (2008)

[29] M. Flórez, J. Contereras-García, M. Recio and M marqués, *Physical Review B* **79**, 104101 (2009)

[30] E. Knittle and Q. Williams, *American Mineralogist* **78**, 245 (1993)

[31] H. Ozkan and J. C. Jameson, *Physics and Chemistry of Minerals* **2**, 215 (1978)

[32] M. Catti, *Physical Review B* **74**, 174105 (2006).

[33] H. Leroux, W. U. Reimold, C. Koeberl, I. Hornmann, and J.-C. Doukhanl, *Earth and Planetary Science Letters* **169**, 291 (1999)

[34] H. P. Scott, Q. Williams, and E. Knittle, *Physical Review Letters* **88**, 015506 (2001)

[35] S. Ono, K. Funakoshi, Y. Nakajima, Y. Tange, and T. Katsura, *Contributions to mineralogy and petrology* **147**, 505 (2004)

[36] W. van Westrenen, M. R. Frank, J. M. Hanchar, Y. Fei, R. J. Finch, and C.-S. Zha, *American Mineralogist* **89**, 197 (2004)

[37] D. Errandonea, R. Kumar, J. López-Solano, P. Rodríguez-Hernández, A. Muñoz, M. G. Rabie and R. Sáez Puche, *Physical Review B* **83**, 134109 (2011)

[38] C. V. Reddy, K. S. Murthy, and P. Kistaiah, *Journal of Physics C: Solid State Physics* **21**, 863 (1988)

[39] S. J. Patwe, S. N. Achary and A. K. Tyagi, *American Mineralogist* **94**, 98 (2009)

[40] B Manoun, R. T. Downs and S. K. Saxena, *American Mineralogist* **91**, 1888 (2006)

[41] F. X. Zhang, M. Lang, R.C. Ewing, J. Lian, Z.W. Wang, J. Hu and L. A. Boatner, *Journal of Solid State Chemistry* **181**, 2633 (2008)

[42] E. Climent-Pascual, J. Romero de Paz, J. M. Gallardo-Amores, R. Sa´ez-Puche, *Solid State Sciences* **9**, 574-579 (2007)

[43] R. Sáez Puche, J. M. Gallardo, J. Romero de Paz, N.Taira and E. Climent-Pascual, *The Journal of the Argentine Chemical Society* **97** (1), 90 (2009)

[44] E. Climent, J. M. Gallardo, J. Romero de Paz, N. Taira and R. Sáez Puche, *Journal of Alloys and Compounds* **488**, 524–527 (2009)

[45] E. Climent Pascual, J. M. Gallardo Amores, R. Sáez Puche, M. Castro, N. Taira, J. Romero de Paz, L. C. Chapon, *Physical Review B* **81**, 174419 (2010)

[46] R. Sáez-Puche, M. G. Rabie, J. Romero de Paz, J. M. Gallardo-Amores, E. Climent-Pascual, *Journal of Rare Earths* **28** (6), 936 (2010)

[47] R. Sáez Puche, E. Climent, M. G. Rabie, J. Romero, and J. M. Gallardo, *Journal of Physics: Conference Series* **325**, 012012 (2011)

[48] A.J. Dossantos-García, E. Climent-Pascual, J. M. Gallardo-Amores, M. G. Rabie, Y. Doi, J. Romero de Paz, B. Beuneu, R. Sáez-Puche, *Journal of Solid State Chemistry* **194**, 119 (2012)

[49] A. Grzechnik, K. Syassen, I. Loa, M. Hanfland, and J. Y. Gesland, *Physical Review B* **65**, 104102 (2002)

[50] A. Grzechik, W. A. Crichton, M. Hanfland and S. van Smaalen, *Journal of Physics: Condensed Matter* **15**, 7261 (2003)

[51] D. Errandonea, R. Lacomba-Perales, J. Ruiz-Fuertes, A. Segura, S. N. Achary and A. K. Tyagi, *Physical Review B* **79**, 184104 (2009)

[52] Y. W. Long, L. X. Yang, Y. Yu, F. Y. Li, Y. X. Lu, R. C. Yu, Y. L. Liu and C. Q. Jin, *Journal of Applied Physics* **103**, 093542 (2008)

[53] E. Jiménez, J. Isasi, R. Sáez-Puche, *Journal of alloys and compounds* **323-324,** 115 (2001)

[54] E. Jiménez Melero, doctoral thesis, Universidad Complutense de Madrid (2005) http://eprints.ucm.es/tesis/qui/ucm-t28520.pdf (November 2012)

[55] J. Rodríguez-Carvajal, *Physica B: Condensed Matter* **192**, 55 (1993)

[56] T. Roisnel, J. Rodriguez-Carvajal, Ed. R. Delhez and E.J. Mittenmeijer, Materials Science Forum, proceedings of the Seventh European Powder Diffraction Conference (EPDIC 7), 118-123 (2000)

[57] E. Jiménez, J. Isasi, R. Sáez-Puche, *Journal of Alloys and Compounds* **312,** 53 (2000)

[58] E. Jiménez-Melero, P. C. M. Gubbens, M. P. Steenvoorden, S. Sakarya, A. Goosens, P. Dalmas de Réotier, A. Yaouanc, J. Rodríguez-Carvajal, B. Beuneu, J. Isasi, R. Sáez-Puche, U. Zimmerman and J L Martínez, *Journal of Physics: Condensed Matter* **18,** 7893 (2006)

[59] R. D. Shannon, *Acta Crystallographia A* **32**, 751 (1976)

[60] Y. W. Long, Q. Huang, L. X. Yang, Y. Yu, Y. X. Lv, J. W. Lynn, Ying Chen and C. Q. Jin, *Journal of Magnetism and Magnetic Materials* **322,** 1912 (2010)

4. Stability of *R*CrO_4 Scheelites

4.1 Thermal Gravimetric Analysis (TGA)

In order to determine the thermal stability of high-pressure $R\mathrm{CrO}_4$-scheelites, a thermo-gravimetric study was carried out from room temperature up to 1473 K under oxygen flow. TG-DSC diagrams for the scheelite-type of ErCrO_4 and TmCrO_4 are given in figure 4.1. As it can be seen in the figure, the decomposition of these scheelite phases encompasses three steps. The first step occurs between room temperature and 600 K, where the sample loses about 0.15% of its weight, which is due to the removal of moisture absorbed in the sample. Between 600 K and 800 K, a weight loss as small as 0.32% could be due to an incipient decomposition that takes place on the surface of the $R\mathrm{CrO}_4$ samples to produce amorphous $R\mathrm{CrO}_3$ perovskite. However, at 800 K, it can be observed that an endothermic effect in the DSC curve takes place, which refers to the reverse transition from $R\mathrm{CrO}_4$-scheelite to the relatively more stable $R\mathrm{CrO}_4$-zircon at ambient pressures. This phase transition is fully confirmed from the x-ray diffraction data obtained at different temperatures, see figure 4.2. The main step observed in the TG diagram starts at 850 K for both of the compounds, which corresponds to the thermal decomposition of the zircon-polymorph to give $R\mathrm{CrO}_3$ according to the equation:

$$R\mathrm{CrO}_4 \xrightarrow{900-1100\ \mathrm{K}} R\mathrm{CrO}_3 + \frac{1}{2}\mathrm{O}_2 \qquad (4.1)$$

The experimental weight loss in this stage is 4.51 and 4.55% for TmCrO_4 and ErCrO_4 scheelites, respectively. This is in full agreement with the theoretical values expected for the decomposition of these two compounds (4.50%). Simultaneously, a net endothermic effect is observed in the DSC curves (*ii* in figure 4.1) at 980 K, which is associated with the thermal decomposition process where the sample is reduced to the distorted perovskite, as in equation 4.1. The presence of $R\mathrm{CrO}_3$ showing orthorhombic symmetry, space group *Pbnm*, has been also confirmed in figure 4.2 by means of x-ray diffraction data.

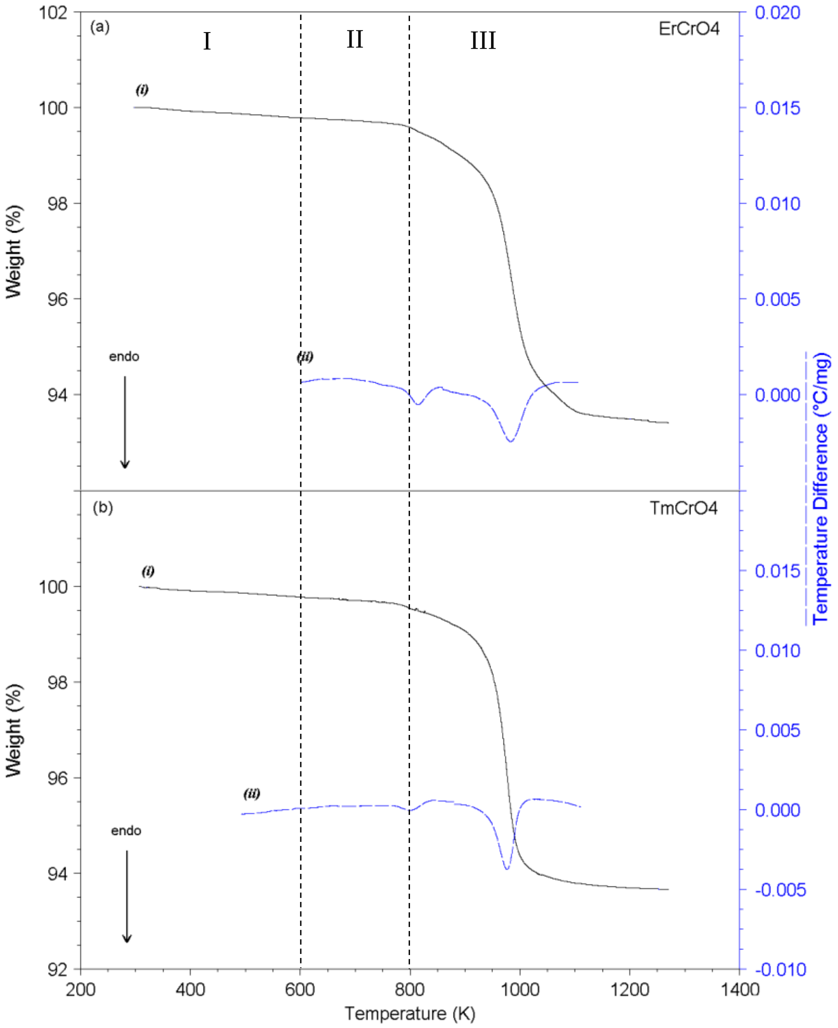

Figure 4.1 Obtained results of (*i*) TGA and (*ii*) DSC for the decomposition in oxygen flow of (a) $ErCrO_4$–scheelite and (b) $TmCrO_4$–scheelite. Regions I shows the evaporation of H_2O absorbed in the sample; region II shows the transition from scheelite to zircon; and region III shows the decomposition of both compounds into oxygen and to the $ErCrO_3$ and $TmCrO_3$.

4.2 *In-Situ* XRD at High Temperatures

In order to confirm the structural changes in the scheelite compounds upon heating, an *in-situ* XRD study has been carried at different temperatures upon heating the samples in air atmosphere. Figure 4.2 shows the x-ray diffraction experiments for $ErCrO_4$ scheelite. The XRD patterns taken at various temperatures for both $ErCrO_4$[1] and $TmCrO_4$ scheelites show the presence of a minor impurity of the *R*CrO_3 distorted perovskite, which appears during the high-pressure synthesis process. By increasing the temperature to 723 K, the onset of the most intense peak reflection from the zircon phase starts to appear, figure 4.2(b). The intensity of zircon reflections increases with the temperature up to 823 K. At higher temperatures, the decomposition of the $ErCrO_4$ zircon starts, see figure 4.2(d), while at the highest temperature of 1173 K, the total decomposition is completed and, in this case, all the reflections represent the

ErCrO$_3$ orthorhombic perovskite, see figure 4.2. The analogous thermal behavior for the decomposition of TmCrO$_4$ scheelite is illustrated in figure 4.3.

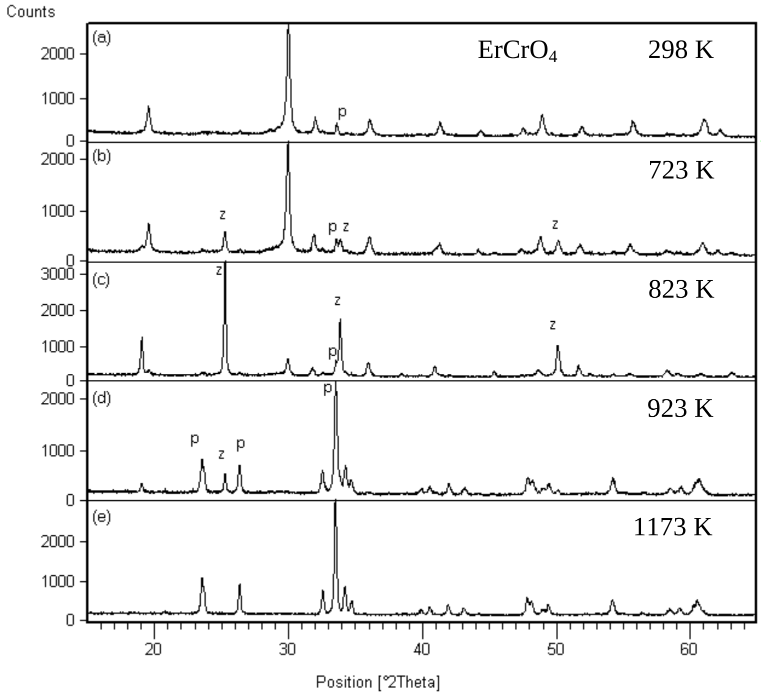

Figure 4.2 XRD patterns taken for ErCrO$_4$ – scheelite [1] taken at: (a) 298 K showing the initial perovskite impurity "p"; (b) 723 K showing the appearance of peaks of the ErCrO$_4$ – zircon "z"; (c) 823 K showing the diminishing of scheelite-type peaks and the dominance of zircon-type peaks; (d) 923 K showing peaks of perovskite and zircon and (e) 1173 K showing a single phase of distorted perovskite.

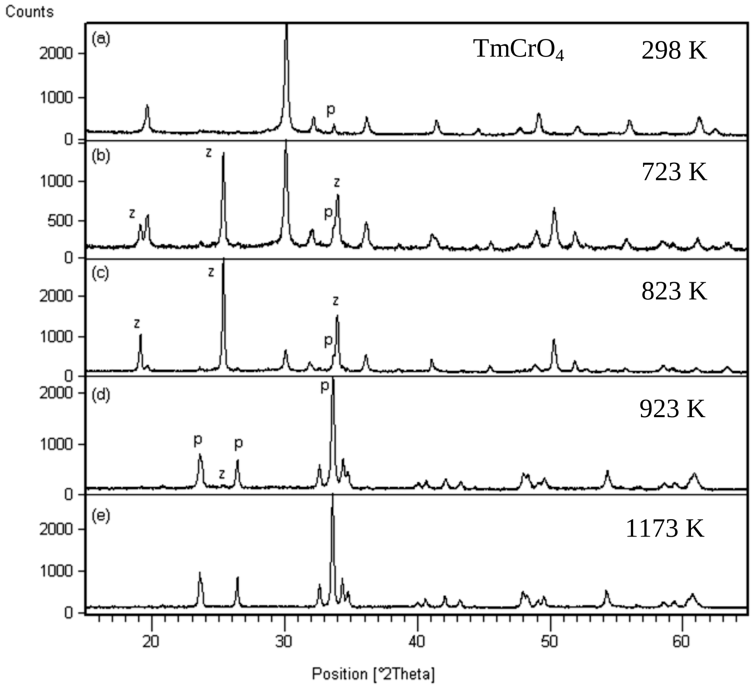

Figure 4.3 XRD patterns taken for TmCrO$_4$ – scheelite taken at (a) 298 K, (b) 723 K, (c) 823 K, (d) 923 K and (e) 1173 K. Behavior is similar to that in Figure 4.2 but with a little shift due to the different lanthanide cation.

We have studied also the same effect in GdCrO_4 scheelite polymorph [2] prepared in this work and has been published, as in Appendix II. This compound showed the lowest amount of perovskite GdCrO_3 impurities in the parent phase. Figure 4.5 shows the low 2θ angle range for the diffractograms taken *in-situ* between room temperature and 1173 K.

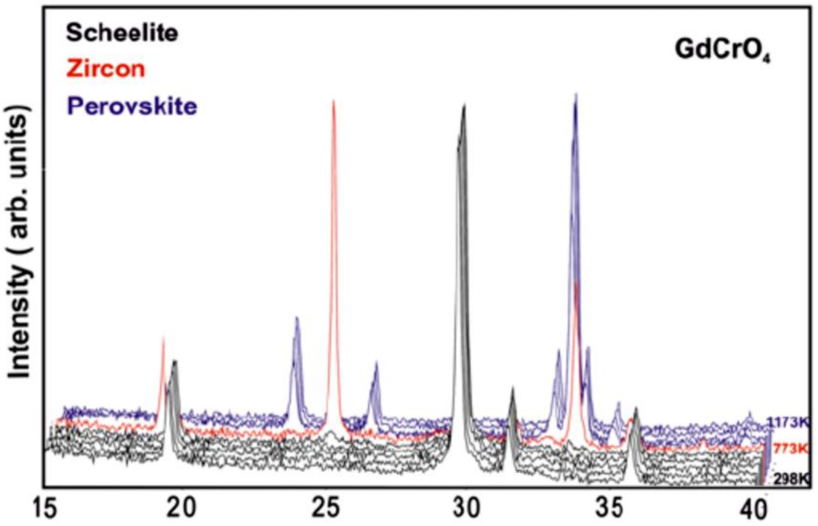

Figure 4.5 Low 2θ angle range (as the horizontal axis) for the GdCrO_4 scheelite sample upon heating from 298 to 1173 K. [2]

The diffractograms of the scheelite phase is represented in the temperature range from 300 to 700 K (black), while at 773 K a quick transition to zircon takes place (red), then it decomposes gradually from 850 to 1000 K (blue), in order to results in the distorted Perovskite structure of GdCrO_3. It is worth noticing that such a transition from the high-pressure polymorph to the ambient-pressure parent phase upon heating, we have also observed and proved for the remaining $R\mathrm{CrO}_4$-scheelite compounds for the first time. On the other hand, in the case of the scheelite polymorph of the zircon mineral (ZrSiO_4), the reverse transition to zircon structure takes place at a much higher temperature, 1473 K [3].

4.3 Secondary-Phases Identification by Powder Diffraction

The existence of secondary phases in the $R\mathrm{CrO}_4$ systems has always hindered the research in these compounds in comparison with other isostructural $RX\mathrm{O}_4$ ones, where X= Si, As, V or P. This is mainly due to the instability of the Cr^{5+} state and its tendency to disproportionate to Cr^{3+} and Cr^{6+} valence states. The most known secondary phase, obtained during $R\mathrm{CrO}_4$ synthesis, is the $R\mathrm{CrO}_3$ distorted perovskite structure that results from the decomposition of the compound at temperatures higher than 873 K. Also during the high-pressure synthesis, the octahedral coordination of the Cr^{3+} in the perovskite-like structure can be stabilized at temperatures lower than that just mentioned above, in comparison with the tetrahedral coordination of Cr^{5+} in the zircon and scheelite phases. This leads to a ferromagnetic component in the magnetic properties due to this secondary phase, as it will be mention in chapter 5.

Moreover, another secondary phase can be noticed in previously obtained zircon and scheelite polymorphs in the literature. Small traces of this phase appear as an amorphous hill in the diffractogram of the zircon phase for a Cu-kα_1 radiation in 2θ range (27-33°) which do not comply with neither the reactants nor the products of the reaction, see [references 4-7]. It can also be observed in these references from the peak shape that these zircon-type structures are experiencing some strain, which can be due to some impurities dissolving in the structure. Such effects can be taken into account for the zircon compounds by activating the strain parameters during the structure refinement.

For the already published *R*CrO$_4$ scheelites, after the high-pressure transition, the secondary phases separate and crystallize as small peaks in the 2θ range between 20-32° and a typical peak at lower angles (10-15°) that cannot be refined by none of *R*CrO$_4$-zircon, *R*CrO$_4$-scheelite, *R*CrO$_3$, *R*$_2$O$_3$ nor Cr$_2$O$_3$, see [references 7-10]. The same peaks can appear also at about 4.5 and 5.5 Å of *d*-spacing [10].

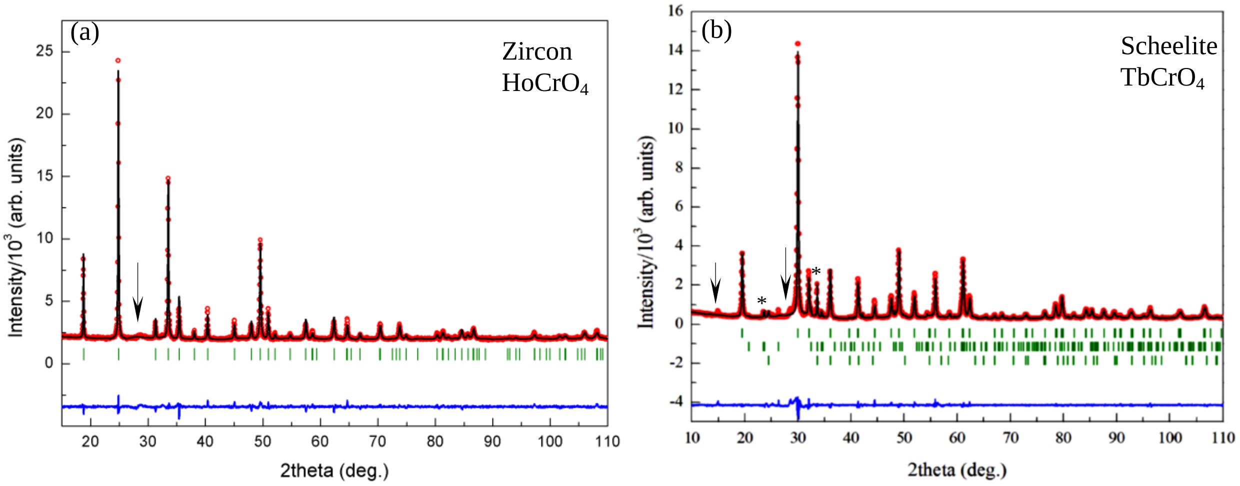

Fig. 4. 6 Example of the impurities that appear in (a) the zircon phase of HoCrO$_4$ [7], and (b) the scheelite phase of TbCrO$_4$ [8]. Both patterns are taken at room temperature for a Cu-kα_1 radiation. The asterisks show the perovskite secondary phase while arrows show the non-identified traces.

The first observation during the synthesis was that by increasing the Cr content in the reactants during the synthesis of zircon phase, the impurities referred to with the arrow in Figure 4.6(a) disappear. An excess amount of Cr up to 5% is possible. The second observation was that the amount of Cr-excess was proportional to the amount of perovskite impurity in the high-pressure polymorph referred to by asterisks in figure 4.6(b). Third observation was that increasing the Cr content shifts the transition pressure to relatively higher values. Samples containing 5% Cr-excess resulted after high-pressure experiments at 4 GPa an amount of 5-10 % of the parent zircon structure, while other samples with less extent of Cr were completely transformed to the scheelite phase at the same pressure value. Finally, the fourth observation was that by reducing the particle size of the zircon, the transition pressure seems to move to lower values. The analyses of the samples with highest amount of impurities are shown in the next section.

4.3.1 Synchrotron radiation powder diffraction at room temperature

One sample with the highest amount of the unknown secondary phase was obtained during an attempts to prepare $ErCrO_4$ scheelite. By carrying out synchrotron powder diffraction for this sample using a wavelength of 0.75 Å, more details of the secondary phase peaks were resolved, due the high intensity of the synchrotron beam in addition to the rotation of the sample on a spinning axis. Soft x-ray absorption of the same sample showed that the impurity phase is a Cr^{6+} compound (see chapter 7), cancelling the suggestion of obtaining monoclinic monazite phase of $ErCrO_4$. With this information, it was possible to narrow the search for possibly altered compositions of the $ErCrO_4$ in the literature that can exhibit the change in the oxidation state. Figure 4.7 shows that the unknown secondary-phase peaks fit well with the structure of the compound $Er(OH)CrO_4$ studied by Bueno *et al.* [11]. The same group has published similar results for the rest of the *R*$(OH)CrO_4$ series [12- 14].

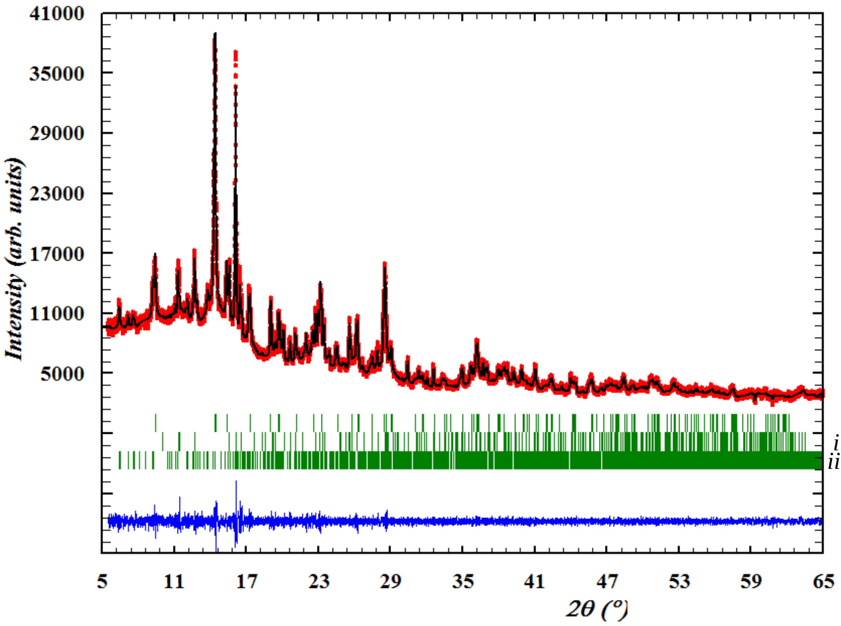

Fig. 4.7 Le Bail fit for $ErCrO_4$ scheelite and coexisting impurities at room temperature and λ= 0.75 Å. Vertical bars shows: (*i*) the $ErCrO_4$ scheelite, (*ii*) the $ErCrO_3$ distorted perovskite and (*iii*) the $Er(OH)CrO_4$.

The phase fitted well with a monoclinic space group of $P2_1/n$ and cell parameters of a= 8.096, b= 11.314, c= 8.255 and β= 93.993°, which are in accordance with the hydroxychromate structure [11]. It is however, worth noting that this structure is very similar to the monazite structure, but the existence of a hydroxyl in the structure causes the change of the Cr valence from Cr^{5+} to Cr^{6+}. However, the monazite structure should show a valence of Cr^{5+} (as observed for the LaCrO$_4$ monazite in chapter 7) and a dark green color. The hydroxychromate shows on the contrary a brown-to-orange color. These brown impurities are sometimes observed during the synthesis of *R*CrO$_4$ zircon when the sample is annealed and cooled slowly to room temperature. These observations should be taken into account during high-pressure experiments that aim to transform the zircon polymorph to the monazite one. An observation of the color and/or measure of the valence state of Cr by spectroscopic techniques can easily distinguish between the monazite and the hydroxychromate.

4.3.2 Separation of the secondary phases

Another interesting sample is the one obtained during several trials to separate the monazite structure from the zircon one in the dimorphic PrCrO$_4$ compound at ambient pressure. A precursor of $Cr^{3+}(NO_3)_3{\cdot}9H_2O$ with excess amount of 2.5% and $Pr^{3+}(NO_3)_3{\cdot}6H_2O$ were heated in a chamber furnace with 1 K/min heating rate to 673 K and then kept at this temperature for 7 hours and then cooled with the same rate. The obtained sample was brown-to-yellow colored and the diffraction pattern of it showed a monoclinic structure similar to that obtained in figure 4.7 but with much bigger lattice parameters. Such a structure is similar to that investigated by Leppä-Aho for the $Pr_3(OH)(CrO_4)_4{\cdot}3.5H_2O$ [15], although he observed a different ratio between Pr and Cr.

Figure 4.8 shows the Le Bail fit of the obtained structure, which fits well with a monoclinic structure of $P2_1/n$ and lattice parameters of a= 32.72, b= 7.14, c= 14.11 and β= 98.25°. The structure is similar to those observed for the hydroxychromates [11] but with a relatively large unit cell like that found for the hydrous compound due to the incorporation of water molecules [15]. Therefore we propose that the compound corresponds to $Pr(OH)CrO_4{\cdot}nH_2O$. More titration, gravimetric and neutron diffraction analyses have to be done in the future for a bigger amount of a sample in order to verify the exact chemical composition and atomic positions. This compound was synthesized as a preliminary work to prove the formation of another Cr^{6+} compound at a temperature range lower than that required for the *R*CrO$_4$ formation. Other publications can be also found in the literature showing the incorporation of water molecules in this system [16-17].

It is worth noting that a particular care has to be taken while preparing these compounds, due to the carcinogenic activity of the hydroxychromates.

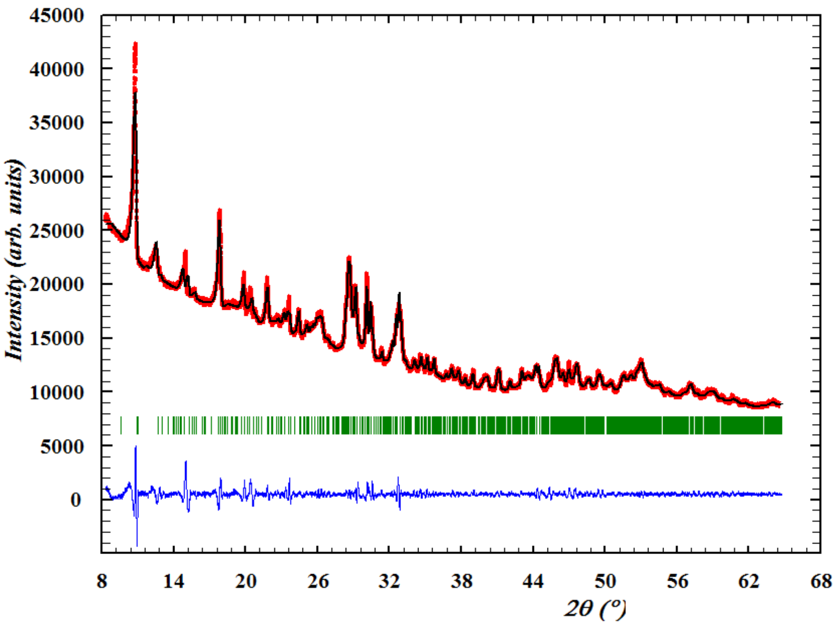

Fig. 4.8 Le Bail fit of Pr(OH)CrO$_4$·nH$_2$O at room temperature for a Cu- kα radiation.

4.4 Role of Interstitial Positions in the Zircon Structure

The zircon-like structure is relatively open as it contains voids and open channels in the structure which represent octahedral and tetrahedral interstitial positions, respectively (as previously discussed in figure 4.2). In the $I4_1/amd$ lattice of the zircon structure, small octahedrally coordinated voids sit on the 8*d* atomic position, while the tetrahedrally coordinated channels sit on the 16*f* positions and form open arrays in the *c* direction. This description is in accordance with that reviewed by Finch and Hanchar [18].

In figure 4.9, using a ball-and-stick model, tetrahedral positions are indicated by the symbol T while octahedral positions are assigned with the symbol C. These interstitial positions are the main reason for the existence of impurities in the zircon-like structures as they accommodate the additional interstitial atoms with small or sometimes negligible structural strain. They account also for the stain effect in the peaks of the diffraction patterns previously published [4-7] and its disappearance by refining strain parameters in the Rietveld method. Even concentrations of these impurities of several tens of ppm, which are hardly detectable by conventional analytical methods, can have a significant impact on charge-balancing heterovalent substitutions on the parent structure atomic positions [18]. Such interstitials are likely positions for both high field-strength cations (at tetrahedral positions) and low field-strength cations (at octahedral positions) [18].

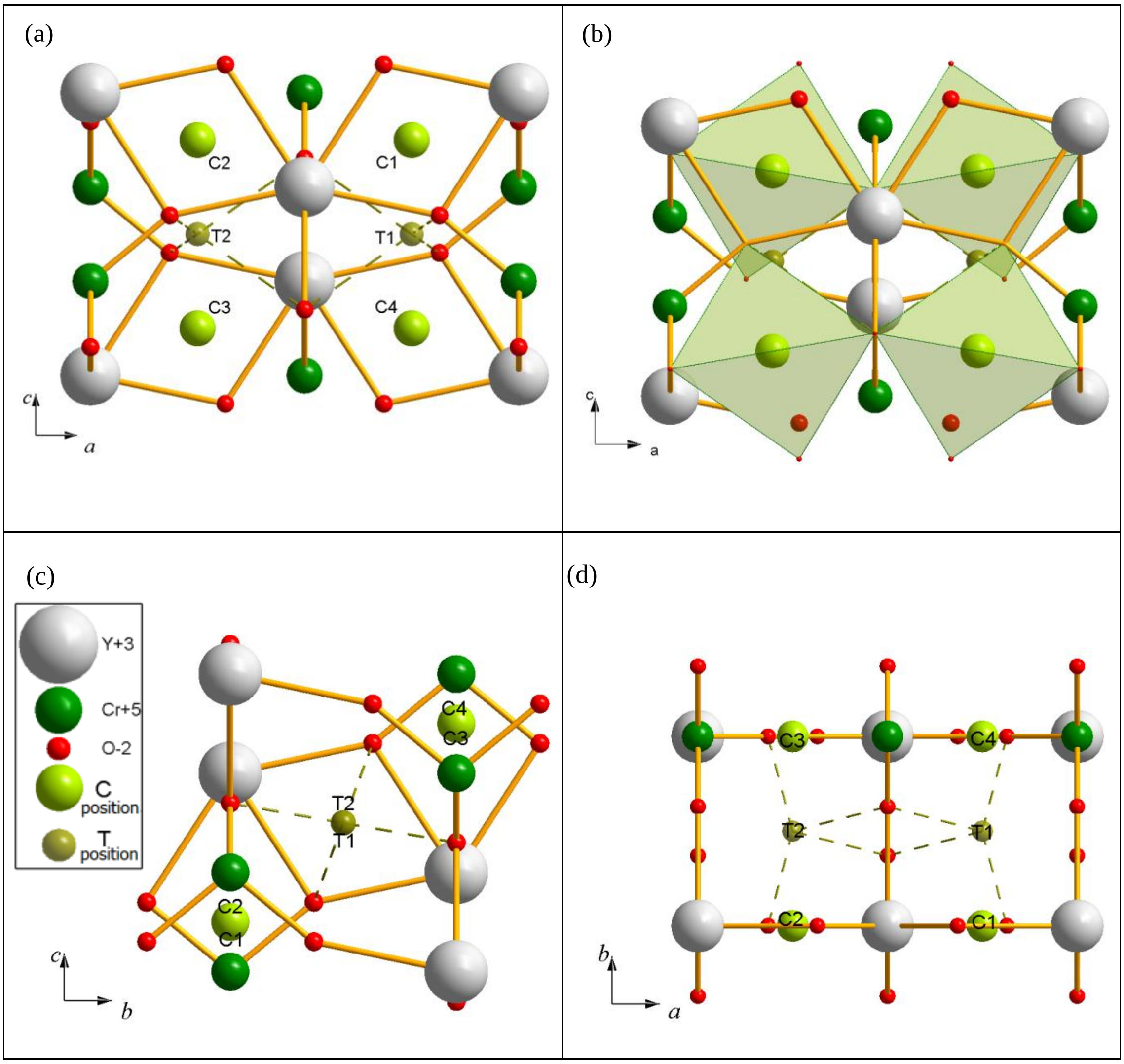

Fig 4.9 Ball-and-stick model showing interstitial positions in the zircon structure with YCrO$_4$ taken as an example. *R* atoms: relatively big gray balls; Cr atoms: smaller dark green balls; octahedral positions "*C*": light green balls at 8*d* atomic positions; tetrahedral sites "*T*": brown-yellow balls at 16*f* atomic positions. (a) Projection on (010) plane "for two unit cells in *a*-direction"; (b) the same projection on (010) showing the octahedral coordination of the interstitial 8*d* atomic positions; (c) projection of same units on (100) plane, (d) projection of same units on (001) plane, T1 and T2 positions are part of the open channels in the *c* direction.

Recently, Trail *et al.* [19] demonstrated the incorporation of hydroxyl into the structure of the zircon mineral but they could not define the OH position in the lattice. Correspondingly, Talla *et al.* [20] provided evidence of the existence of OH defects in the zircon-like structure of (Y,*R*)PO$_4$ xenotime mineral. Based on their infrared measurements at different temperatures, they proposed an orientation of the OH dipoles in directions parallel to and perpendicular *R* the *c*-axis. They also assumed some vacancies on either Y or P positions. Although they did not take into account the role of the interstitial positions, it is interesting to note that their assumed OH positions are in the vicinity of the interstitial positions we indicated in figure 4.9.

Another kind of incorporation into the zircon structure was studied by Belletti *et al.* [21] in order to dope the ZrSiO$_4$ with some Cr atoms. They made their interpretation of the results based on the assumption that the Cr atom upon replacing the Zr^{4+} position will have a Cr^{4+} valence. However, it was proved later by Graft *et al.* [22] that in the later case, Cr^{5+} and Cr^{3+} are unexpectedly the ones occurring in doped zircon crystals.

From these previous works, one can assume that hydroxyl molecules are incorporated easily in the zircon structure of *R*CrO_4 zircon-like structure either during the synthesis from the hydrous nitrates at the temperature step of 433 K (see sample preparation in chapter 2) or after the synthesis by water adsorption from the atmosphere. This could explain the amorphous impurity in the diffraction pattern of the zircon (see figure 4.6(a)). The incorporation of hydroxyl should also play an important role in the charge alteration of $(CrO_4)^{-3}$ at the surface, transforming it into $(CrO_4)^{-2}$ (as will be seen in the x-ray absorption spectra in chapter 7). However, this can be avoided by annealing the sample in an oxygen atmosphere at about 800 K and then quenching to room temperature in an inert atmosphere, since the formed *R*$(OH)CrO_4$ decomposes at this temperature, resulting in *R*CrO_4 [12-16]. This suggests the formation of the hydroxychromate as an intermediate product during the synthesis of *R*CrO_4-zircons, which is in agreement with the recent results of A. Durán *et al.* [24] who synthesized a hydroxide precursor as an intermediate compound to produce $YCrO_4$ and, subsequently, nanometric $YCrO_3$.

On the other hand, it is possible that the excess Cr-content used in the preparation of zircon is stored at one of the interstitial positions forming a solid solution, which introduces strains in the crystal structure as viewed in the neutron diffraction patterns of zircon samples[23]. However, during the high-pressure transition, the interstitial positions dramatically decrease and the excess-Cr is separated as *R*CrO_3. Consequently, the volume reduction upon the pressure-induced transition reduces the solubility of the impurity in the structure and, therefore, it crystallizes as a secondary phase.

Additionally, due to the Gibbs free energies calculated by Li *et al.* [24] for both zircon and scheelite phases of $YCrO_4$, the stability of the scheelite polymorph is less than that for the zircon structure of the *R*CrO_4, as shown previously in figure 3.8. The zircon phase has a lower minimum of the total energy curve than the scheelite and therefore it is more stable.

4.5 Bond-Valence Method

As mentioned in chapter 2, the bond-valence method is very useful to determine the coordination number [25], predict bond lengths from a given bond valence [26, 27] and to get bond-valence sums at atoms as a check on the reliability of the determined structure. Therefore, the bond-valence method has been applied to both zircon and scheelite *R*CrO_4 compounds in an attempt to come to some conclusions about their overall structural behavior.

We have to remind here, like in chapter 2, that this method requires well-determined structures for a detailed interpretation of the bond lengths. Big deviations in the calculated valence values can occur from just small deviations in the bond-length value.[28] Therefore, analysis based on laboratory x-ray powder diffraction can be difficult to analyze with the bond-valence method. For these reasons, only reliable results could be obtained from high-resolution neutron or synchrotron diffraction data.

From the deviation of the valence sum around each ion with respect to the expected valence value, the bond-valence method can help us to see a clear evidence of instabilities (or unusual features) in the crystal structure. Table 4.1 shows the valence bond sums of the different zircon *R*CrO$_4$ compounds. The values are calculated from the cell parameters and atomic positions of corresponding references in table 3.5 (previous chapter) using Bond_Str program integrated in the FullProf_Suit [30, 31]. These BVS values have been also calculated for scheelite polymorphs in this work in table 4.2 according to the data previously shown in table 3.3.

Table 4.1 Bond-valence sums (BVS) for zircon *R*CrO$_4$ and their Global instability indices (GII) calculated from atomic positions cell parameters in table 3.5 (previous chapter).

*R*CrO$_4$ Zircon	Bond-Valence Sums (BVS) valence unit (v.u.)			GII	Norm. GII(a)	Norm. GII(b)	Norm. GII(c)
	R^{+3} Co.= 8	**Cr**$^{+5}$ Co.= 4	**O**$^{-2}$ Co.= 3				
NdCrO$_4$	3.261(0)	4.692(1)	1.988(1)	0.2331	0.1026	2.87 %	0.1650
SmCrO$_4$	3.060(2)	5.288(5)	2.087(3)	0.1771	0.1160	4.19 %	0.1395
EuCrO$_4$	3.063(1)	5.306(2)	2.092(1)	0.1881	0.1231	4.45 %	0.1482
GdCrO$_4$	3.333(0)	4.990(0)	2.081(0)	0.1977	0.1109	4.57 %	0.1510
TbCrO$_4$	3.153(0)	4.712(0)	1.966(0)	0.1892	0.0960	2.94 %	0.1359
DyCrO$_4$	2.971(1)	4.706(2)	1.919(2)	0.1770	0.1077	3.83 %	0.1376
HoCrO$_4$	3.253(1)	4.810(1)	2.016(1)	0.1829	0.0844	2.57 %	0.1298
ErCrO$_4$	3.064(0)	4.665(1)	1.932(1)	0.2007	0.1116	3.73 %	0.1497
TmCrO$_4$	3.261(1)	4.688(1)	1.987(1)	0.2351	0.1041	2.92 %	0.1665
YbCrO$_4$	3.035(0)	4.715(1)	1.937(1)	0.1697	0.0950	3.23 %	0.1279
LuCrO$_4$	3.132(0)	4.760(1)	1.973(0)	0.1589	0.0799	2.43 %	0.1139

Table 4.2 Bond-valence sums (BVS) and global instability indices (GII) for scheelite *R*CrO$_4$ at room temperature calculated from atomic positions cell parameters in table 3.3 (previous chapter).

*R*CrO$_4$ Scheelite	Bond-Valence Sums (BVS) Valence unit (v.u.)			GII	Norm. GII(a)	Norm. GII(b)	Norm. GII(c)
	$\boldsymbol{R}^{+3}$ Co.= 8	$\mathbf{Cr}^{+5}$ Co.= 4	$\mathbf{O}^{-2}$ Co.= 3				
NdCrO$_4$ NPD	3.162(5)	4.312(8)	1.868(5)	0.4151	0.2294	7.58 %	0.3079
SmCrO$_4$ Synchrotron	2.905(6)	5.449(17)	2.089(9)	0.27	0.1497	4.98%	0.2009
EuCrO$_4$ XRD	3.043(24)	4.991(56)	2.008(29)	0.0256	0.0142	0.54 %	0.0190
GdCrO$_4$ XRD	3.061(21)	5.239(47)	2.075(25)	0.1490	0.1001	3.64 %	0.1180
TbCrO$_4$[10] XRD	3.101	4.412	1.878	0.3513	0.1959	6.58 %	0.2629
DyCrO$_4$ NPD	2.924(5)	4.610(11)	1.883(6)	0.2389	0.1553	5.61 %	0.1879
HoCrO$_4$ NPD	3.143(3)	4.730(6)	1.968(4)	0.1776	0.0901	2.76 %	0.1276
TmCrO$_4$ XRD	2.766(14)	5.670(41)	2.109(21)	0.4142	0.2232	7.16 %	0.3029
YbCrO$_4$ XRD	2.371(13)	6.353(47)	2.181(24)	0.8676	0.4510	14.04 %	0.6267

The global instability index[32] (GII) values are plotted in figure 4.10 for both zircon and scheelite polymorphs calculated from various x-rays, neutron and synchrotron powder diffraction data as taken from tables 3.3 and 3.5. As explained in chapter 2, GII represents the deviation of the experimental bond-valence-sums (BVS) from the atomic valence. Therefore, it is a measure of the violation to the valence sum rule (VSR) over the whole structure and it indicates the distortion and instability of the structure. It can be seen in figure 4.10(a) that the zircon compounds represent a minimum of instability indices with GII value around 0.2 in which no big deviations are observed except for a slight increase for NdCrO$_4$ and TmCrO$_4$ zircons. Furthermore, these materials with the zircon structure can incorporate the impurity atoms without a noticeable change in its lattice parameters due to the availability of various interstitial positions.

On the other hand, in the case of the *R*CrO$_4$-scheelite compounds (figure 4.10(b)), GII values show a different behavior than that for the zircon compounds. In general, the scheelites having an intermediate R^{3+} ionic radii (EuCrO$_4$ and GdCrO$_4$) show the lowest instability index and, therefore, are expected to have the highest stability of the scheelite structure in this series. When R^{3+} ionic radii increase or decrease (moving towards the sides of the lanthanide series), the instability index increases as well. Finally, a fitted parabolic curve in figure 4.10(b) can describe the stability of the scheelite *R*CrO$_4$ compounds. It is worth noting that the scheelite samples of $EuCrO_4$ and $GdCrO_4$ where those produced with the highest purity in the series. On the other hand, the high GII at the sides of the series accounts for the difficulty to get pure scheelite compounds for R^{3+} radius smaller than that for the Yb^{3+} or even not yet possible for R^{3+} radius bigger than that for the Nd^{3+}. The instability of the scheelite structure would tend either to alter the valence of its components by the occurrence of secondary phases, *i.e.* disproportionation of Cr^{5+} ion into Cr^{3+} and Cr^{6+}, or by the reverse transition to the zircon parent structure upon heating between 700 and 800 K.

Moreover, the secondary phases in $YbCrO_4$-scheelite compound provide high strains in the scheelite structure as well as the compensation of charge. In case of $LuCrO_4$ scheelite, it contained the highest amount of impurities; therefore, we omitted it from GII calculations.

On the other hand, the scheelite structure is about 10% more compact than the zircon one, as the polyhedra in the high-pressure structure fill most of the free voids that were available before the transition. This compact structure reduces the possibility of the impurities to dissolve in the scheelite structure. The higher the impurities, the higher the strains, and the higher the GII values are. On the other hand, the compression of the structure under pressure can slightly compress some interatomic distances; and, therefore, can alter the GII values.

All these points can be described by the so-called steric distortions if one part of the structure is stretched and another part compressed. The cation with the compressed bonds will have an experimental bond valence sum larger than its atomic valence, while the cation with the stretched bonds will have a smaller sum. Such an effect can happen with the introduction of impurities, pressures, incommensurate effects, or by stretching the lattice due to O-H bonds. [28] Moreover, the zircon and scheelite polymorphs are known for their anisotropic compressibility, refering to the fact that one direction is more compressible than another (see chapter 3).

Finally, it has to be repeated here (as explained in chapter 2) that the calculated Bond-Valence Sums in tables 4.1 and 4.2 are expressing the sums of the valence bonds around a cation (or anion) in comparison with the formal valence (charge). As a result, the method is just a guide to conclude the deviation from the most stable atomic positions. For example, in table 4.2, the highest deviation from the expected BVS values can be found for the scheelite-type compounds $NdCrO_4$ and $YbCrO_4$. This, in turn, results in very high instability of the structure and provides a difficulty to obtain a high purity compound. Furthermore, it explains the difficulty to obtain scheelite compounds in this series for R^{3+} ionic radii smaller than that for Yb^{3+}, *i.e.* Lu^{3+} and Sc^{3+}. Hence, a pure scheelite polymorph of $LuCrO_4$ was not possible. Moreover, it is not yet feasible to obtain a scheelite compound for ionic radii bigger than that for Nd^{3+}. We were not able to obtain $LaCrO_4$ and $PrCrO_4$ scheelites in the range of synthesis conditions and parameters used in this work.

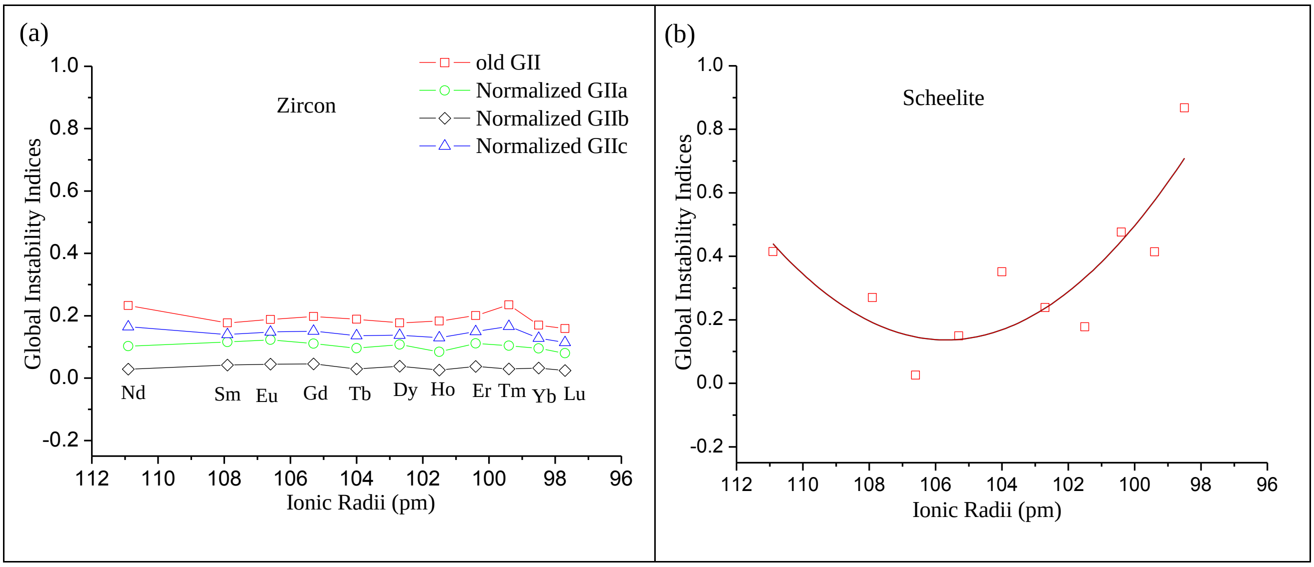

Fig. 4.10 different global instability indices for the (a) zircon polymorph and (b) scheelite polymorph of the *R*CrO$_4$ oxides

References

[1] R. Sáez Puche, E. Climent, M. G. Rabie, J. Romero, and J. M. Gallardo, *Journal of Physics: Conference Series* **325**, 012012 (2011)

[2] A. J. Dossantos-García, E. Climent-Pascual, J. M. Gallardo-Amores, M. G. Rabie, Y. Doi, J. Romero de Paz, B. Beuneu, R. Sáez-Puche, *Journal of Solid State Chemistry* **194**, 119 (2012)

[3] K. Kusaba, Y. Syono, M. Kikuchi and K. Fukuoka, *Earth and Planetary Science Letter* **72**, 433 (1985)

[4] Keitaro Tezuka and Yukio Hinatsu, *Journal of Solid State Chemistry* **160**, 362 (2001)

[5] E. Jiménez, J. Isasi, and R. Sáez-Puche, *Journal of Solid State Chemistry* **164**, 313 (2002)

[6] E. Jiménez, J. Isasi, R. Sáez-Puche, *Journal of alloys and compounds* **323-324**, 115 (2001)

[7] E. Climent-Pascual, J. Romero de Paz, J. M. Gallardo-Amores, R. Sáez-Puche, *Solid State Sciences* **9**, (2007) 574-579

[8] R. Sáez Puche, J. M. Gallardo, J. Romero de Paz, N. Taira and E. Climent-Pascual, *The Journal of the Argentine Chemical Society* **97** (1), 90 (2009)

[9] E. Climent, J. M. Gallardo, J. Romero de Paz, N. Taira and R. Sáez Puche, *Journal of Alloys and Compounds* **488**, 524 (2009)

[10] E. Climent Pascual, J. M. Gallardo Amores, R. Sáez Puche, M. Castro, N. Taira, J. Romero de Paz, L. C. Chapon, *Physical Review B* **81**, 174419 (2010)

[11] I. Bueno, C. Parada, A. Monge and C. Ruiz Valero, *Journal of Solid State Chemistry* **90**, 263 (1991)

[12] I. Bueno, C. Parada, E. Gutiérrey Puebla, A. Monge and C. Ruiz Valero, *Journal of Solid State Chemistry* **78**, 78 (1989)

[13] I. Bueno, C. Parada, *Thermochimica Acta* **235**, 205 (1994)

[14] I. Bueno, C. Parada, R. Sáez Puche, E.J. Baran, *Journal of Alloys and Compounds* **225**, 237 (1995)

[15] J. Leppä-Aho, *Journal of Solid State Chemistry* **106**, 400 (1993)

[16] J. Leppä-Aho and J. Valkonen, *Journal of Solid State Chemistry* **99**, 364-375 (1992)

[17] J. Leppä-Aho and J. Valkonen, *Journal of Solid State Chemistry* **92**, 136-147 (1991)

[18] R. J. Finch and J. M. Hanchar, *Rev. Mineral. Geochem.* **53**, 1 (2003).

[19] D. trail, J. B. Thomas and E. B. Watson, *American Mineralogist* **96**, 60 (2011)

[20] D. Talla, A. Beran, R. Škoda and Z. Z. Losos, *American Mineralogist* **96**, 1799 (2011)

[21] A. Belletti, R. Borromei and L. Oleari, *Inorganica Chimica Acta* **235**, 349 (1995)

[22] M. Graft, G. Boulon, G. Panczer, Y. Guyot, R. Reisfeld, S. Votyakov and G. Bulka, *Journal of Luminescence* **87-89**, 1118 (2000)

[23] E. Jiménez Melero, doctoral thesis, Universidad Complutense de Madrid (2005), http://eprints.ucm.es/tesis/qui/ucm-t28520.pdf (November 2012)

[24] A. Durán, C. Meza F and G. G. Carbajal Arizaga, *Materials Research Bulletin* **47** (6), 1442 (2012)

[25] L. Li, W. Yu and C. Jin, *Physical Review B* **73**, 174115 (2006)

[26] D. Altermatt and I. D. Brown, *Acta Crystallographica A* **43**, 125 (1987)

[27] I. D. Brown, *Acta Crystallographica B* **33**, 1305 (1977)

[28] M. O'Keeffe, *Acta Crystallographica A* **46**, 138 (1990)

[29] I. D. Brown, *Chemical Reviews* **109**, 6858 (2009)

[30] N. E. Brese and M. O'Keeffe, *Acta Crystallographica B* **47**, 192 (1991)

[31] J. Rodríguez-Carvajal, *Physica B: Condensed Matter* **192**, 55 (1993)

[32] J. Rodríguez-Carvajal, *Commission on Powder Diffraction (IUCr) Newsletter* **26**, 12 (2001)

[33] I. D. Brown, *Zeitschrift fuer Kristallographie* **199**, 255 (1992)

5. Magnetic Properties of *R*CrO$_4$ Scheelites

In *R*CrO$_4$ oxides, where *R* refers to rare-earth elements, each of Cr^{5+} and R^{3+} ions contain at least an unpaired electron, except when *R*= Y, La or Lu, in which the R^{3+} ion has no unpaired electron. Consequently, these oxides create a very interesting scenario to study 3*d*–4*f* magnetic interactions and the predominant role that the rare earth anisotropy will play in the resulting magnetic properties. On the other hand, as these oxides undergo a pressure-induced phase transition from a zircon-like structure to a scheelite like structure, it is very interesting to study the changes in the magnetic properties and the exchange pathway occurring upon the structural transition. In this chapter, we explain the magnetic properties and magnetic structure of the scheelite polymorphs of *R*CrO$_4$ oxides and we propose a magnetic structure for some of them. The magnetic properties and structures of *R*CrO$_4$-zircon oxides has been studied previously by Jiménez Melero *et al.*[1].

5.1 Magnetic Susceptibility and Magnetization Measurements

The evolution of the magnetic DC susceptibility has been measured by MPMS Quantum Design's Squid magnetometer in the temperature range of 2-300 K for the different *R*CrO$_4$-scheelite oxides (*R*=Nd-Yb) in magnetic field of 0.1 T. In figures 5.1 to 5.11, the χ *vs.* T plots are given. It can be observed that in these scheelite oxides the magnetic susceptibilities follow a Curie-Weiss behavior of the type

$$\boldsymbol{\chi = C/(T\text{-}\theta)} \qquad (5.1)^{[2]}$$

where *C* is the Curie constant and equals to $(\boldsymbol{N\mu^2_{eff}}/3\,\boldsymbol{k})$, $\boldsymbol{N}$ is the Avogadro's number ($\boldsymbol{N}$=6.022×10^{23}mol^{-1}) and $\boldsymbol{k}$ is the Boltzman constant ($\boldsymbol{k}$=1.38044×10^{-23}JK^{-1}mole^{-1}). If equation (5.1) is obeyed, a plot of (1/$\boldsymbol{\chi}$) *vs.* T will show a straight line, but with an intercept θ on the temperature axis, which is called the Weiss constant. This law applies over a wide temperature range as it can be seen in Table 5.1, where the different magnetic parameters are depicted. The obtained effective magnetic moments, $\boldsymbol{\mu}_{eff}$, fairly agree with the theoretical one, $\boldsymbol{\mu}_{th}$, determined for these trivalent R^{3+} rare-earth cations including the pentavalent Cr^{5+} contribution. As ($C \propto \boldsymbol{\mu^2_{eff}}$) and ($\boldsymbol{\chi = \chi_{Cr} + \chi_{R}}$), then the $\boldsymbol{\mu}_{th}$ moment is given by:

$$(\boldsymbol{\mu}_{th})^2 = (\boldsymbol{\mu}_{R^{3+}})^2 + (\boldsymbol{\mu}_{Cr^{5+}})^2 \qquad (5.2)$$

If spin-orbit coupling is included, the magnetic moment, $\boldsymbol{\mu}_{R^{3+}}$, of different rare earths can be calculated by the Hund´s equation for a state specified by *J*:

$$\boldsymbol{\mu}_{R^{3+}} = g_j[J\,(J+1)]^{1/2}\ (\boldsymbol{\mu}_B) \qquad (5.3)^{[2]}$$

g$_j$ parameter is the Lande factor given by the following expression:

$$g_J = \frac{3}{2} + \frac{S(S+1)-L(L+1)}{2J(J+1)} \quad (5.4)^{[2]}$$

while L, J and S numbers correspond to the ground term of the different R^{3+} lanthanide cations. The quantity $\boldsymbol{\mu_B}$ is the Bohr magneton and is defined as:

$$\boldsymbol{\mu_B} = \frac{|e|h}{4\pi m_e c} = 9.27 \times 10^{-24} \quad JT^{-1} \quad (5.5)^{[2]}$$

where $|e|$ is the electronic charge, h is the Planck constant, m_e is the electron rest mass and c is the speed of light.

Table 5.1 Magnetic parameters for different *R*CrO$_4$ scheelite oxides: μ_{eff} (μ_B) effective magnetic moment; θ(K) Weiss constant; T_{max}(K) temperature corresponding to T_N; μ_{th}(μ_B) expected magnetic moment using equation (5.2) and C-W (K) Curie-Weiss range obtained from the magnetic susceptibility measurements.

Compound	$\mu_{exp}(\mu_B)$	θ(K)	T_{max}(K)	$\mu_{th}(\mu_B)$	C-W (K)
NdCrO$_4$	3.96	-46.4	18	3.95	48-300
*SmCrO$_4$	2.68	--	16	2.3	RT
*EuCrO$_4$	3.78	--	16.8	3.75	RT
GdCrO$_4$	8.01	-12.69	20.0	8.1	25-300
TbCrO$_4$	9.72	-1.94	29	9.83	50-300
DyCrO$_4$	10.76	-0.6	22.3	10.72	45-300
HoCrO$_4$	10.79	-7.1	9.4	10.72	40-300
ErCrO$_4$	9.80	-4.5	11	9.73	60-300
TmCrO$_4$	8.01	-15.2	30.3	7.76	30-300
YbCrO$_4$	4.71	-19.4	34.7	4.77	68-290

* *Magnetic moments obtained at room temperature using equation (5.6)*

It is worth noting that Sm^{3+} and Eu^{3+} constitute odd cases, in which the magnetic moments are temperature dependent and accordingly the simple form of equation (5.3) is not valid. This is a consequence that the ground states $^6H_{5/2}$ and $^7F_0$ corresponding to Sm^{3+} and Eu^{3+}, respectively, are thermally close in energy to the first excited states $^4H_1$ and $^7F_1$ and they should not be excluded when calculating the magnetic moments of these two ions. Under these considerations, the magnetic moment for these two ions has been obtained at room temperature applying the formula:

$$\boldsymbol{\mu} = \left(\frac{3k}{N\mu_B^2}\right)^{1/2} (\chi T)^{1/2} \quad (5.6)^{[2]}$$

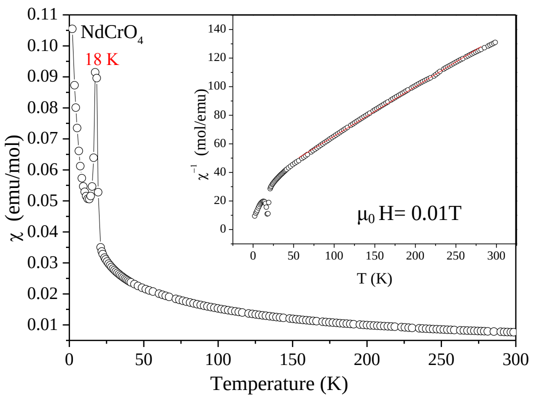

Fig. 5.1 Magnetic susceptibility *vs.* temperature for NdCrO$_4$. Inset shows the temperature dependence of the reciprocal magnetic susceptibility and fit of Curie-Weiss law.

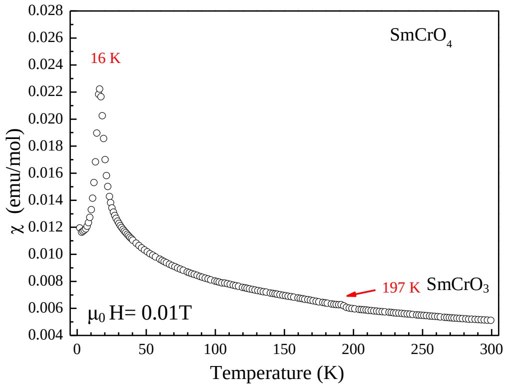

Fig. 5.2 Thermal evolution of the magnetic susceptibility for SmCrO$_4$.

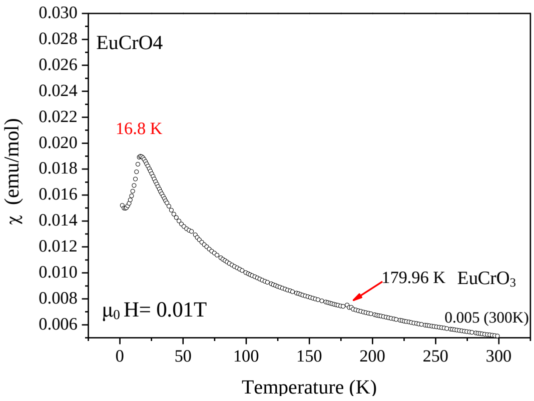

Fig. 5.3 Thermal evolution of the magnetic susceptibility for EuCrO$_4$.

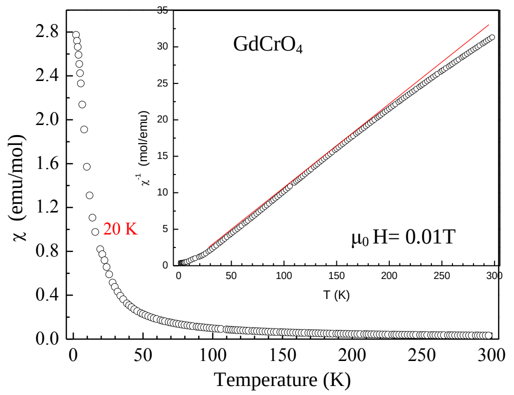

Fig. 5.4 Variation of the molar magnetic susceptibility against the temperature for GdCrO$_4$. Inset shows the temperature dependence of the reciprocal magnetic susceptibility and fit of Curie-Weiss law.

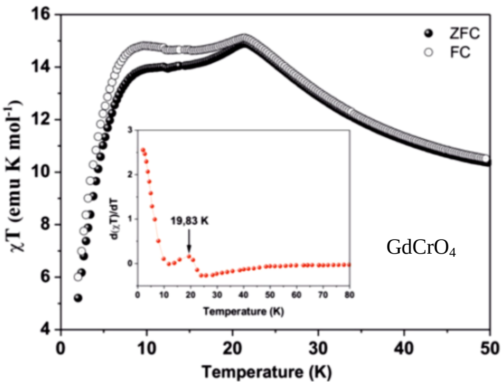

Fig. 5.5 χT *vs.*T plot at ZFC and FC conditions under an external field of μ_0H=0.01T for GdCrO$_4$[3]. Inset shows the temperature where the magnetic entropy starts dropping.[2]

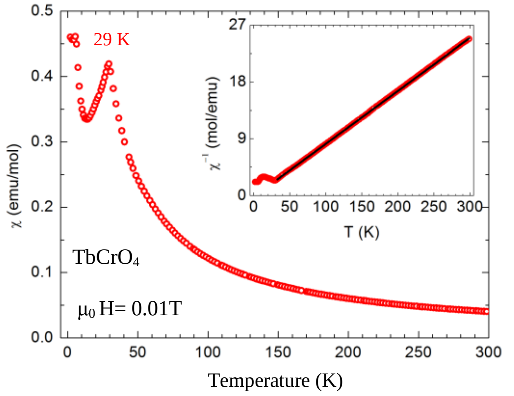

Fig. 5.6 Magnetic susceptibility as a function of temperature for the TbCrO$_4$ by Climent *et al.*[4]. Inset shows the temperature dependence of the reciprocal magnetic susceptibility.[5]

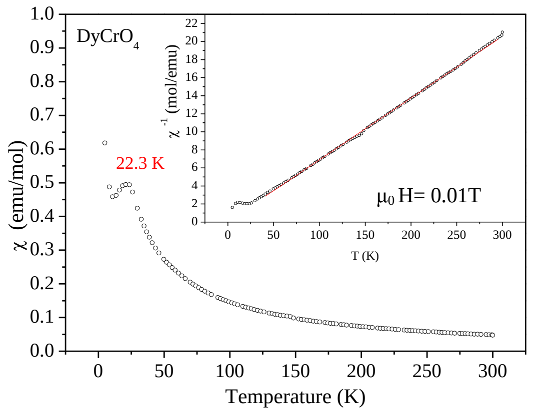

Fig. 5.7 Variation of the molar magnetic susceptibility against the temperature for DyCrO$_4$. Inset shows the temperature dependence of the reciprocal magnetic susceptibility and fit of Curie-Weiss law.

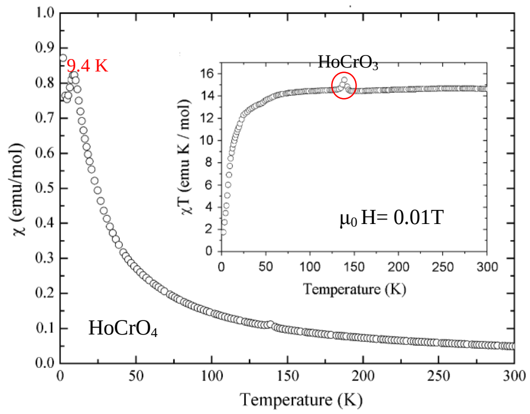

Fig. 5.8 Evolution of the magnetic susceptibility with the temperature for HoCrO$_4$ by Climent *et al.*[6]. Inset shows the variation of χT as a function of the temperature.[6]

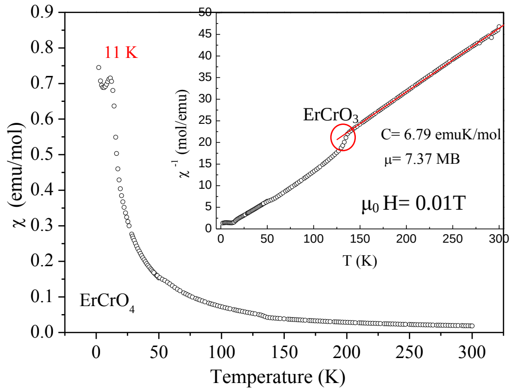

Fig. 5.9 Evolution of the magnetic susceptibility with the temperature for ErCrO$_4$ for the sample used in Ref. [7]. The Inset shows the temperature dependence of the reciprocal magnetic susceptibility and fit of Curie-Weiss law.

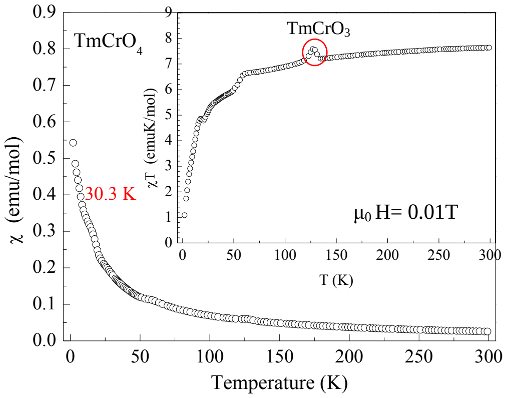

Fig. 5.10 Evolution of the magnetic susceptibility with the temperature for TmCrO$_4$ for the sample used in Ref. [8]. The Inset shows the variation of χT as a function of the temperature.

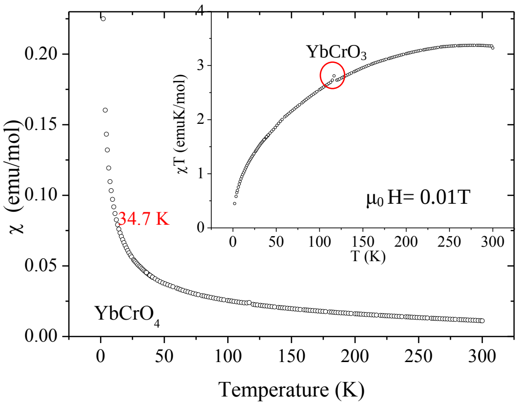

Fig. 5.11 Evolution of the magnetic susceptibility with the temperature for YbCrO$_4$. Inset shows the variation of χT as a function of the temperature.

On the other hand, concerning the Cr^{5+} contribution it is necessary to consider that this ion has an electronic configuration of d^1, leading to a ground term of ^2D that corresponds to the free ion. However the different energy levels of Cr^{5+} as in the case of the other 3*d* metal transition ions are split by both the crystal field effect and the spin-orbit coupling; the former effect being much more intense than the latter, in the case of theses transition metal ions. In these *R*CrO$_4$ scheelite oxides the Cr^{5+} ions are surrounded by four oxygen ions in a tetrahedral coordination and under these conditions the crystal field ground term is ^2E_g. For that reason, the magnetic moment of Cr^{5+} depends on the crystal field splitting parameter 10*Dq* and the spin-orbit constant λ according to the following formula:

$$\boldsymbol{\mu}_{\boldsymbol{Cr}^{5+}} = \boldsymbol{\mu}_{\mathbf{s.o.}}\left(1-\frac{\alpha\lambda}{\mathbf{10}\boldsymbol{Dq}}\right) \qquad (5.7)^{[2]}$$

where λ and Dq are spin-orbit coupling and crystal field parameters, while $\alpha = 2$ for the ^2E_g term. In the case of YCrO$_4$, the value of 10*D*q obtained from the visible spectrum, is 9500 cm^{-1}, while λ = 380 cm^{-1}. The spin-only magnetic moment value for Cr^{5+} is given by the so-called ‘spin-only’ equation:

$$\boldsymbol{\mu}_{\mathbf{s.o.}} = [4S(S+1)]^{1/2}\ (\boldsymbol{\mu}_{\mathbf{B}}) \qquad (5.8)^{[2]}$$

Since this value is equal to 1.73 μ_B, the magnetic moment contribution of this Cr^{5+} sublattice calculated from equation (5.7) is 1.60 μ_B which agrees with the magnetic moment obtained for YCrO$_4$[9]. The Weiss constants, determined by fitting the reciprocal susceptibility to the Curie-Weiss law, shows negative values in all cases as in Table 5.1. This indicates the presence of antiferromagnetic interactions.

At low temperatures, dramatic changes have been observed in the magnetic susceptibility measurements, while deviations from the Curie-Weiss law are present in all *R*CrO$_4$ compounds (see figures 5.1 to 5.11). The onset of a net maximum is clearly noticeable for most of the *R*CrO$_4$ scheelite samples. The negative values of θ and the maximum in χ values confirm the presence of antiferromagnetic interactions, in which both R^{3+} and Cr^{5+} sublattices are involved. In most of the cases, the small increase in the magnetic susceptibility below the $T\chi_{max}$ could be due to the presence of a small amount of the corresponding distorted *R*CrO$_3$ perovskites in these compounds (6-3%), as mentioned in chapter 3 for this issue. In the case of the TmCrO$_4$ and YbCrO$_4$ compounds, although these maxima are not present (figures 5.10 and 5.11), one can indicate the onset of antiferromagnetic interactions from the inflection points at 30.3 K and 34.7 K respectively. These interactions are fully confirmed from the corresponding χT *vs.* T plots where the χT values decrease below these mentioned inflection points, reaching values as small as 0.9 and 0.4 emu.K/mol for the Tm- and Yb-scheelites respectively, as indicated in the insets of figures 5.10 and 5.11.

It has to be noticed that materials showing high percentage of *R*CrO$_3$ distorted perovskites (*R*= Ho, Tm and Er) have been taken from previous references [6-8], while other samples prepared in this work showed a minimal amount of this secondary phase. This results in a small contribution to χ by a ferromagnetic component, which can be seen due to the canted antiferromagnetic order of Cr^{3+} ions (in *R*CrO$_3$) at temperatures ranging between 100 and 200 K, depending on the rare earth ion. Therefore, the susceptibility data of the different *R*CrO$_4$ samples have been corrected accordingly by subtracting this saturated ferromagnetic component The small peaks found (in figures 5.1 to 5.11) at the above-mentioned temperature-range have been assigned to the canted antiferromagnetic ordering in the chromium sublattice of the secondary phase of *R*CrO$_3$. The Néel temperatures for these *R*CrO$_3$ oxides decreases with decreasing the Cr-O-Cr angles from 180^o upon the lanthanide contraction from NdCrO$_3$ to YbCrO$_3$.[10]

Figures 5.12 to 5.20 show the evolution of the magnetization as a function of the magnetic fields at different temperatures for the different scheelite *R*CrO$_4$ samples. In the case of the NdCrO$_4$, figure 5.12, it can be observed that the field dependence of the magnetization, M*vs.*H plot, obtained above the Néel temperature (T_N), namely at 20 and 35 K, fits a straight line according to the paramagnetic character of this sample. However, below T_N=18 K curve-shaped plots are obtained because of the possible metamagnetic transition that takes place below the ordering temperature. Nevertheless, the saturation is not reached even at 5 **T** where the ordered moment at 2 K is as small as 0.7 μ_B. The M*vs.*H curves show a similar evolution in the case of the SmCrO$_4$ and EuCrO$_4$ oxides, see figures 5.13 and 5.15. In both cases, a straight line is observed above the ordering temperature of 16 K, which is in agreement with the paramagnetic character of these oxides above the mentioned temperature. In the case of the Sm-compound, the M*vs.*H plot obtained at 12 K, figure 5.14, shows the S-shape feature characteristic for an antiferromagnetic compound showing a metamagnetic transition. This transition induced by the magnetic field can be better visualized when the derivative *d*(M/H) is plotted against the magnetic field where a maximum can be observed around 3.2 **T** at 12 K, see figure 5.14 inset. By difference, a similar maximum appears to be located above 5 **T** when the temperature is 2 K as it can be observed in figure 5.14 inset. The value of the ordered magnetic moment (σ) at 12 K is 0.21 μ_B at 5 **T,** which indicates that the saturation will be obtained at higher values of the magnetic field.

In the case of the EuCrO$_4$, some deviations of the straight lines are obtained below 50 k, figure 5.15. Though, the deviation from the straight line appear to be more noticeable for the data obtained at 20 K, where the magnetization signify a marked increase when the magnetic field takes the value of 3 **T**, showing a tendency to surpass the M values obtained for the lowest temperatures of 2 and 12 K.

The field-dependent magnetization curves at different temperatures in the case of the GdCrO$_4$ are shown in figure 5.16. As it has been previously described for the isostructural scheelite chromates RCrO$_4$ the M*vs.*H plots fit a straight line at temperatures above the ordering one. However, a slight bending of the plot measured at 30 K is clearly indicative of the incipient magnetic interactions. Indeed, a non-linear M-H variation is observed in the M*vs.*H plots obtained at 1.8, 8 and 2 K. These results are in accordance with those observed in the susceptibility measurements and evince that this GdCrO$_4$ scheelite oxide exhibits a field induced metamagnetic transition as in the case of the other RCrO$_4$ oxides. The critical field is as low as 0.1 **T** according to the isotropic character of the $^8S_{7/2}$ ground term corresponding to the Gd^{3+}. This is also an evidence of the antiferromagnetic ordering in which both Cr^{5+} and Gd^{3+} sublattices are involved. The ordered magnetic moment obtained at 2 K and 5 **T** takes the value of 7.1 μ_B, which is very close to 8 μ_B, the theoretical moment expected for the ordered magnetic moments contributions of σCr^{5+} and σGd^{3+}. The difference between ZFC and FC curves for GdCrO$_4$ is due to the ferromagnetic component.

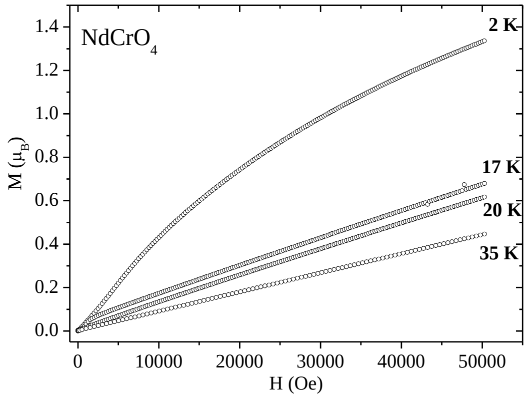

Fig. 5.12 Magnetization versus applied magnetic field at different temperatures for NdCrO$_4$.

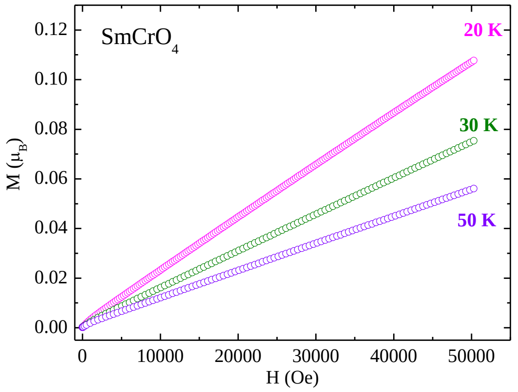

Fig. 5.13 Magnetization versus applied magnetic field plots obtained a different temperatures for SmCrO$_4$ above the Néel Temperatures. [11]

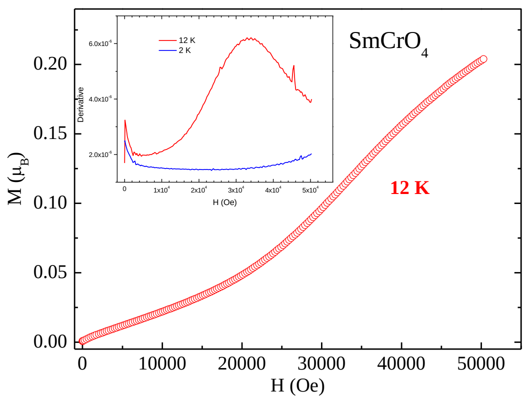

Fig. 5.14 Magnetization versus applied magnetic field at 12 K for SmCrO$_4$. The inset represents the d(M/H)*vs.* H at 12 K (upper curve) and 2K (lower curve).[11]

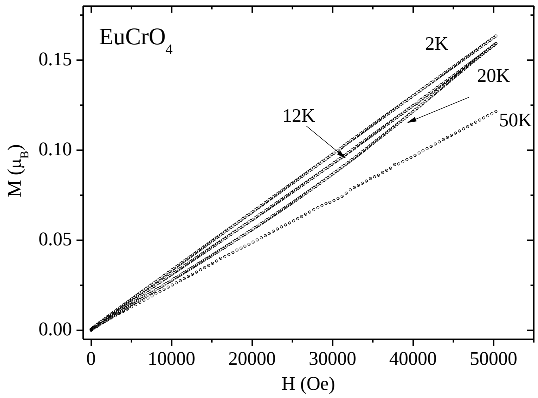

Fig 5.15 Magnetization versus applied magnetic field at different temperatures for EuCrO$_4$.

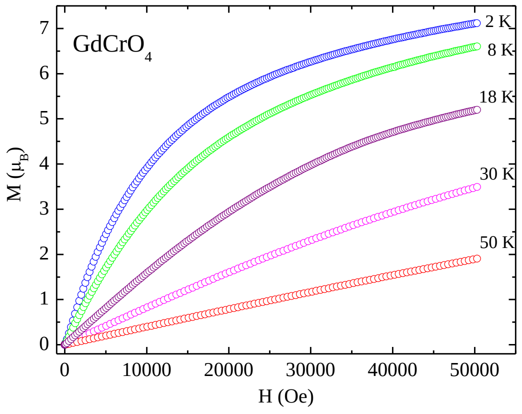

Fig. 5.16 Magnetization versus applied magnetic field at different temperatures for $GdCrO_4$.[3]

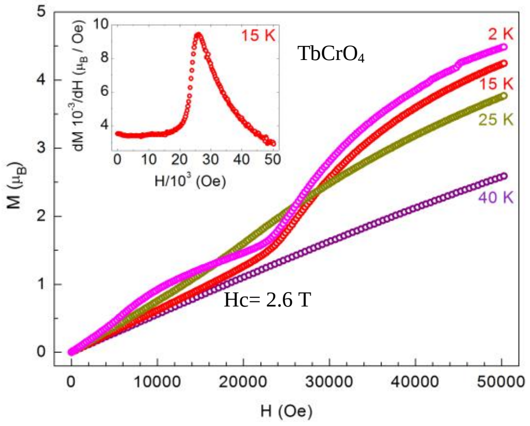

Fig. 5.17 Magnetization versus applied magnetic field at different temperatures for $TbCrO_4$ by Climent *et al.*[4]. The inset represents the d(M/H)*vs.* H at 15 K.

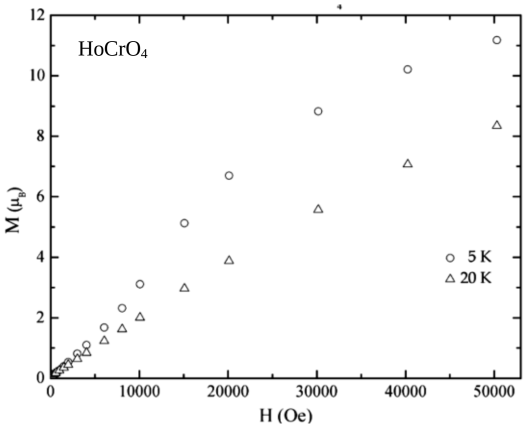

Fig. 5.18 Magnetization versus applied magnetic field at different temperatures for $HoCrO_4$ by Climent *et al.*[6]

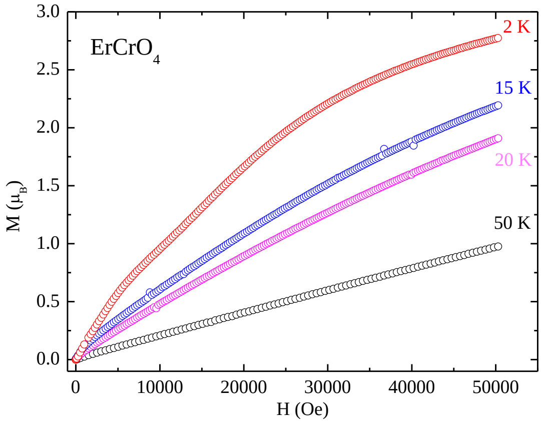

Fig. 5.19 Magnetization versus applied magnetic field at different temperatures for $ErCrO_4$.[7]

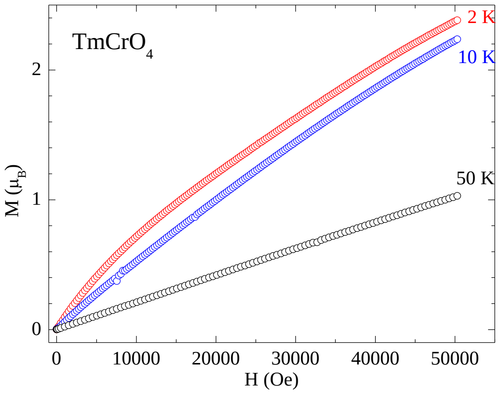

Fig. 5.20 Magnetization versus applied magnetic field at different temperatures for $TmCrO_4$.[8]

Magnetization measurements performed at different temperatures for the scheelite *R*CrO$_4$ oxides where *R*= Tb, Ho, Er and Tm are shown in figures 5.17 to 5.20. They indicate a similar behavior and the isotherms obtained above the Néel temperature exhibits a linear behavior as expected. However, the corresponding M*vs.*H plots obtained below the Néel temperature show an S-shape feature characteristic for a metamagnetic transition in antiferromagnetic materials. On the other hand, since in the case of HoCrO$_4$ the saturation is reached at 5 **T** with a σ =11 μ_B which fairly agrees with the theoretical value expected for Ho^{3+} and Cr^{5+} contributions. At a combination of 2 K and 5 T, the corresponding magnetic moments of the isostructural TbCrO$_4$, ErCrO$_4$ and TmCrO$_4$ scheelites are 2.8, 4.7 and 2.4 μ_B respectively. Concerning the critical fields of these four *R*CrO$_4$ scheelites (*R*= Tb, Ho, Er and Tm), values of 2.6, 1.4, 1 and 1 T are obtained respectively; These similar values are one order of magnitude higher than that obtained for the isostructural GdCrO$_4$. This is due to the different intrinsic anisotropies of these *R*= Tb, Ho, Er and Tm rare earth chromates compared to the Gd one (due to large differences found when we campare the single rare earth ions).

5.2 Specific Heat Measurements

In order to investigate in more details and to get more insight about the antiferromagnetic transitions studied by the magnetic susceptibility and magnetization measurements described above, specific heat measurements have been performed for this *R*CrO$_4$-scheelite family of compounds at different temperatures and magnetic field strengths.

The total measured specific heat (C_p) consists of the magnetic (C_{mag}), electronic (C_e) and lattice (C_{la}) contributions. Then to calculate the magnetic contribution to the specific heat, the electronic and lattice contributions need to be subtracted from the total specific heat. This calculation can be done following different procedures. One way is to use the specific heat data for a diamagnetic compound with the same crystal structure. However, until now, such a compound has not yet been obtained in this family of *R*CrO$_4$ compounds, since the YCrO$_4$, where the Y is the diamagnetic rare earth, behaves as antiferromagnetic due to the interactions in the Cr-sublattice. A second method is based on the fit of the heat capacity data above T_N using a Debye model and Einstein model to reproduce the lattice contribution down to the lowest temperature. However, this data treatment cannot be performed, because of the existence of two unknown heat capacity contributions, which corresponds to: short range magnetic interactions above the magnetic ordering temperature; and the Schottky anomaly resulting from the crystal field splitting consistent with the ground term of the different R^{3+} ions. A third method that can be also used to calculate these two latter contributions is fitting the experimental C_p data to a polynomial function well above the transition temperature.

From the magnetic specific heat (C_{mag}) it is possible to determine the magnetic entropy (S_{mag}) by integrating C_{mag} as a function of the temperature according to:

$$S_{\mathrm{mag}} = \int_0^T \frac{C_{\mathrm{mag}}}{T} dT \tag{5.9}$$

The theoretical magnetic entropy for the different R^{3+} ions is given by:

$$S_{\mathrm{mag}} = 2R\, ln(2J+1) \tag{5.10}$$

,where R is the gas constant and J is the quantum number corresponding to the non-split ground $^{2S+1}X_J$ of the different R^{3+} ions. In the case of the Cr^{5+} with S = ½, this value is given by $2Rln2$= 5.57 Jmol^{-1}K^{-1}.

The C_p *vs*. T plot depicted in figure 5.21(a), which corresponds to the GdCrO$_4$-scheelite, shows a λ-type anomaly at 21 K and a small kink around 5 K, which are almost coincident with those anomalies determined from the magnetic susceptibility measurements. These two magnetic transitions are more visible in the magnetic specific heat plot, after subtracting the lattice contribution (figure 5.21(b)) obtained from a combination of the Debye and Einstein models. Then, the C_{lat} of GdCrO$_4$ scheelite was obtained from the sum of the Debye and Einstein models [12, 13].

$$C_{\mathrm{lat}} = 9R\left(\frac{T}{\theta_D}\right)^3 \int_0^{\theta_D/T} \frac{(\theta_D/T)^4\, \mathrm{e}^{\theta_D/T}}{(\mathrm{e}^{\theta_D/T}-1)^2}\, \mathrm{d}(\theta_D/T) + R\, \sum_{i=1}^{3} \frac{(\theta_{E_i}/T)^2\, \mathrm{e}^{\theta_{E_i}/T}}{(\mathrm{e}^{\theta_{E_i}/T}-1)^2} \tag{5.11}$$

where θ_D (224 K) is the Debye temperature, while θ_{E_1}, θ_{E_2} and θ_{E_3} (372.11, 652.75 and 1082.11 K respectively) are the Einstein temperatures for GdCrO$_4$ scheelite. The calculated C_{lat} values are shown as a solid line in figure 5.21(a). The magnetic specific heat below 4 K was extrapolated by the relation $C_{\mathrm{mag}} \propto T^3$ from spin-wave model proposed for an antiferromagnet[14].

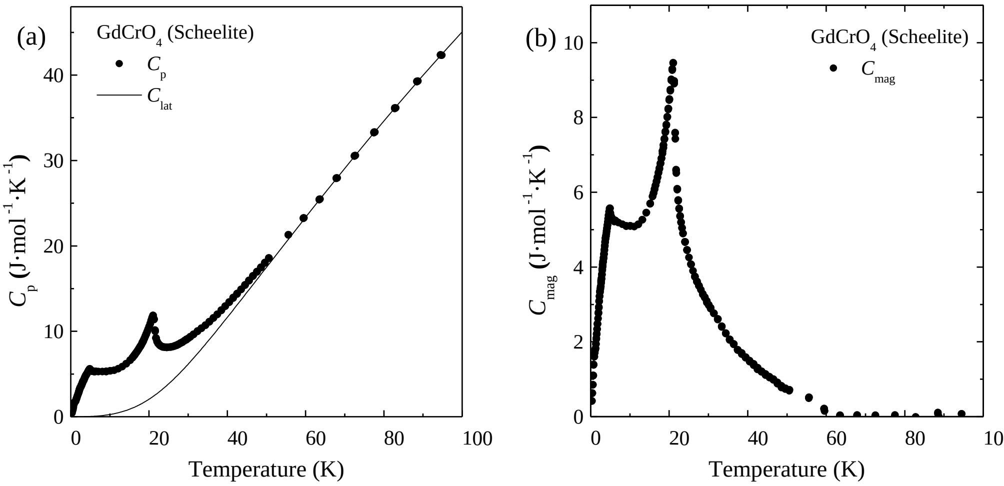

Fig. 5.21 Specific heat of GdCrO$_4$-scheelite: (a) C_p *vs*. T plot of total experimental heat capacity (dots) and calculated C_{lat} values (solid line) by combined Debye and Einstein models; and (b) C_{mag} *vs*. T plot of magnetic specific heat after subtracting the lattice contribution.

The experimental magnetic entropy (figure 5.22) takes the value of 17 Jmol^{-1}K^{-1}, which differs from the theoretical value 23 Jmol^{-1}K^{-1} calculated from the contribution of Cr^{+5} (S = ½) and

Gd^{3+} (S = $^{7}/_{2}$) ions (red dotted line). This is 5.76 and 17.29 Jmol^{-1}K^{-1} respectively, see figure 5.22. The discrepancy between these two values could be due to a covalent bond of the $d_{x^2-y^2}$ empty orbital and Zeeman splitting of the S = $^{7}/_{2}$ ground state[2]. Such an underestimation of spin entropy might be also due to an overestimation of the lattice contribution or the operating of short-range order above the T_N. However, further specific heat measurements need to be performed with much finer temperature steps at the temperature range 21 to 0 K, which might reveal intense anomalies at a narrow temperature range.

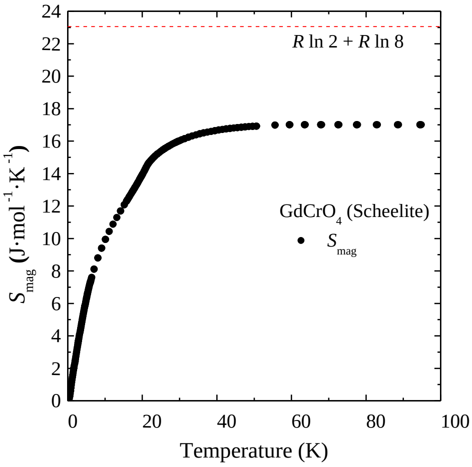

Fig. 5.22 Experimental magnetic entropy of GdCrO$_4$-scheelite calculated by integrating C_{mag} as a function of temperature

As consequence of this splitting, only some of the Zeeman-split lower energy levels will be involved in these magnetic transitions and, consequently, the experimental entropy is reduced. It is interesting to point out here that structural distortions to low-temperature orthorhombic symmetry seem to be common in the RCrO$_4$ family of compounds crystallizing in the zircon-like structure. In the case of the DyCrO$_4$-zircon compound, the λ-type anomaly observed at 23 K is also coincident with that observed in the susceptibility measurements and clearly indicative of a FM ordering. However, the appearance of another anomaly above T_C (32 K) is indicative of a structural phase transition from the tetragonal to orthorhombic symmetry. Recent ^{155}Gd and ^{169}Tm Mössbauer spectroscopy results performed in the zircon-like-structure compounds reveal the existence of two sites for the rare earth element with a proportion 20-80%, which is clearly indicative of a tetragonal to orthorhombic transition [15]. The vast majority of these structural transitions can be understood in terms of a cooperative Jahn-Teller effect or spin-orbit coupling in the rare-earth site arising by a change from the tetragonal D_{2d} to orthorhombic D_2 local symmetries. Nevertheless, the Gd shows neither Jahn-Teller effect nor spin-orbit coupling.

A possible explanation of the origin of the tetragonal to orthorhombic transition in the GdCrO$_4$-zircon and, as extension, for the GdCrO$_4$-scheelite polymorphs is that this change in symmetry has to arise from the Cr-site and not from the Gd-one. In fact, Cr^{+5} ion with d^1 electronic configuration, in a tetrahedral crystal field, is a Jahn-Teller ion. However, a Jahn-Teller transition is a purely structural transition, and the magnetic ordering occurs at lower temperature [16]. This Jahn-Teller transition is clearly operative in the DyCrO$_4$-zircon polymorph [17].

The lattice contribution has been also estimated by fitting the C_p experimental data to a fourth order polynomial function of the type:

$$C_p = a{*}T + b{*}T^2 + c{*}T^3 + d{*}T^4 \qquad (5.12)$$

This different method have been used also along this study as an attempt to obtain better fitting and will be highlighted in a more detail. However, for some compounds it was not possible to obtain a proper fitting with any of the methods used.

Figure 5.23(a) shows the fitting of the C_p by equation (5.12) as the blue dotted line, where the coefficients take the values of a = 0.3127, b = -0.00225, c = 5.5776 $*10^{-5}$ and d = -1.0827$*10^{-7}$. After subtracting this lattice contribution, the magnetic contribution to the specific heat is obtained, C_{mag} , figure 5.23(b). Nevertheless, the determined magnetic entropy S_{mag} shows a value of 21.3 Jmol^{-1}K^{-1}, which is very close to that expected 23.3 Jmol^{-1}K^{-1} for the Gd^{3+} and Cr^{5+} magnetic contribution noted by a solid line, as it can be observed in figure 5.24. However, it should be noticed that this mathematical fitting, in figure 5.23, has some deviations from the physical fitting by Debye and Einstein models represented in figure 5.21.

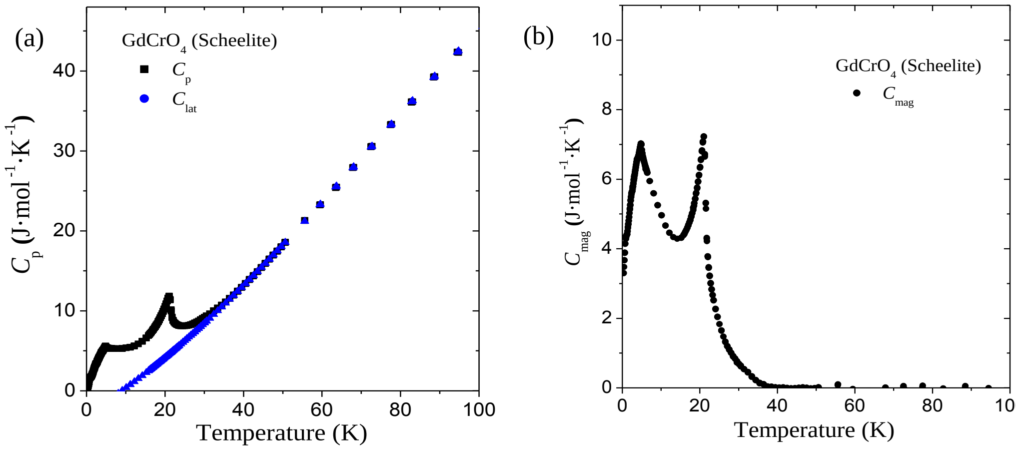

Fig. 5.23 Specific heat of GdCrO$_4$-scheelite: (a) C_p *vs.* T plot of total experimental heat capacity (black) and calculated C_{lat} values (blue) by a fourth order polynomial function; and (b) C_{mag} *vs.* T plot of magnetic specific heat after subtracting C_{lat}.

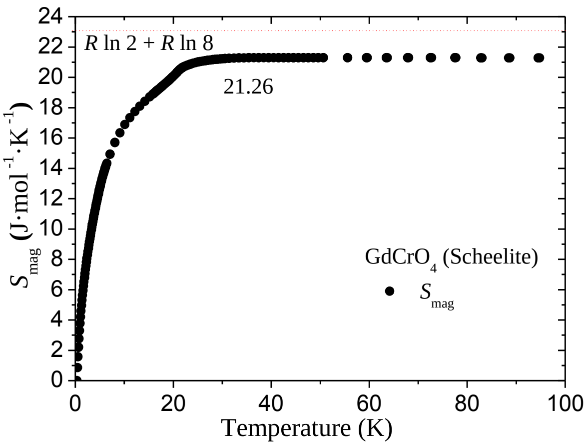

Fig. 5.24 Experimental magnetic entropy of GdCrO$_4$-scheelite calculated by integrating C_{mag} as a function of temperature

In a previous work, Climent *et al.*[4] have studied the magnetic behavior of the scheelite-type TbCrO$_4$ oxide from the magnetic susceptibility temperature dependence and isothermal magnetization curves as a function of the external magnetic field [4]. It was proposed an antiferromagnetic ordering, T_N = 29 K in which both Tb^{3+} and Cr^{5+} sublattices are involved. Furthermore, a metamagnetic transition was observed at 15 K with a critical magnetic field of 2.6**T**. By contrast, the zircon -type TbCrO$_4$ oxide shows the onset of ferromagnetic interactions at 22 K. This behavior is fully confirmed by the determined magnetic structure where the terbium and chromium magnetic sublattices are ferromagnetic coupled in the basal plane of zircon-type structure [1, 18].

The specific heat of the scheelite-type TbCrO$_4$ oxide as a function of the temperature and magnetic field is shown in figure 5.25 [19]. The most striking feature is the sharp λ -peak at T_N= 29 K, which is ascribed, in view of the susceptibility data [4], to the three dimensional antiferromagnetic ordering of the magnetic moments of the Tb^{3+} and Cr^{5+} ions. The application of an external magnetic field influences significantly the mentioned anomaly. The temperature transition decreases gradually with the increasing of the magnetic field and almost disappears at an applied field of 8 **T**. This field-dependent effect also indicates the magnetic origin of this anomaly. At about 15 K a small shoulder in the heat capacity should be noticed. A temperature dependence of the molecular field [20, 21] probably could be the origin of this behaviour. Additionally, a small contribution coming from the Schottky anomaly due to the splitting of the electronic ground state $^7F_6$ of the Tb^{3+} ion from the TbCrO$_3$ oxide present in the sample (7 %wt) will surely exists also in this temperature range.

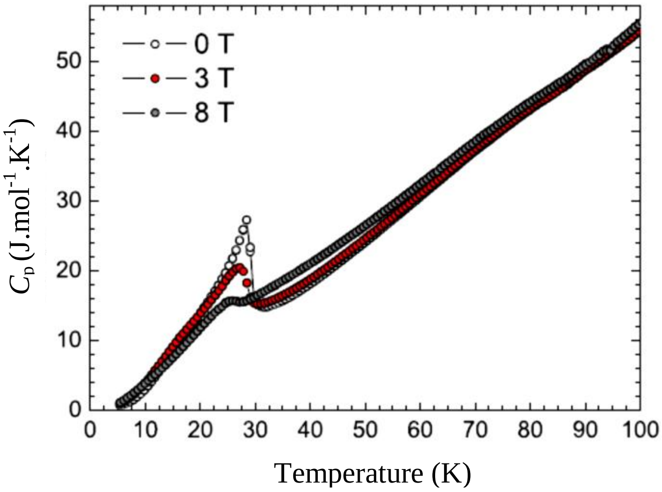

Fig. 5.25 Temperature dependence of the total specific heat measured at different magnetic fields for scheelite-type TbCrO$_4$ [19].

The calculation of the magnetic contribution to the specific heat for the scheelite-type TbCrO$_4$ oxide requires the subtraction of the lattice contribution as it was mentioned earlier. This calculation can be based on the fit of the heat capacity data above T_N using a Debye's model to reproduce the lattice contribution down to the lowest temperature. However, this data treatment cannot be performed since two unknown heat capacity contributions corresponding to short range magnetic interactions above the magnetic ordering temperature and the Schottky anomaly due to the crystal field splitting of the $^7F_6$ ground term of Tb^{3+} are present. Considering these limitations, the lattice contribution was estimated from the specific heat data of the isomorphous YCrO$_4$ oxide recently reported by Long *et al*.[9] This oxide shows an antiferromagnetic transition at T_N= 18.5 K in which only the Cr^{5+} ions are involved. Therefore, as a first approximation, it can be assumed that the data between 40 and 100 K are close to the lattice contribution for the scheelite-type YCrO$_4$ because, in this case and temperature range, there is no Schottky contribution and the magnetic contribution due to short range interactions is small compared with the phonon part. The lattice contribution between 5 and 40 K has been estimated using a Debye function with a characteristic Debye temperature (θ_D) of 407 K. This value corresponds to the effective θ_D for YCrO$_4$ at 40 K. This rough lattice heat capacity for the YCrO$_4$ must be scaled to TbCrO$_4$ using a corresponding state law in order to take into account the mass and volume differences between both compounds.

However, the Schottky anomaly due to the crystal field splitting of the $^7F_6$ ground term of Tb^{3+} cannot be estimated due to the unknown energy level scheme, and unfortunately prevents to determine the appropriate factor. Therefore and in first approximation, a direct subtraction has been done in order to obtain the magnetic contribution to the specific heat, figure 5.26. The magnetic entropy after subtracting of the lattice contribution, is 21.7 J/mol K (calculated between 5 K and 100 K) which deviates from to the theoretical value of 27.08 J/mol K for Cr^{5+} (S=1/2) and Tb^{3+} (J= 6) as can be observed in the inset in figure 5.26 which was proposed by Climent *et al.*[19].

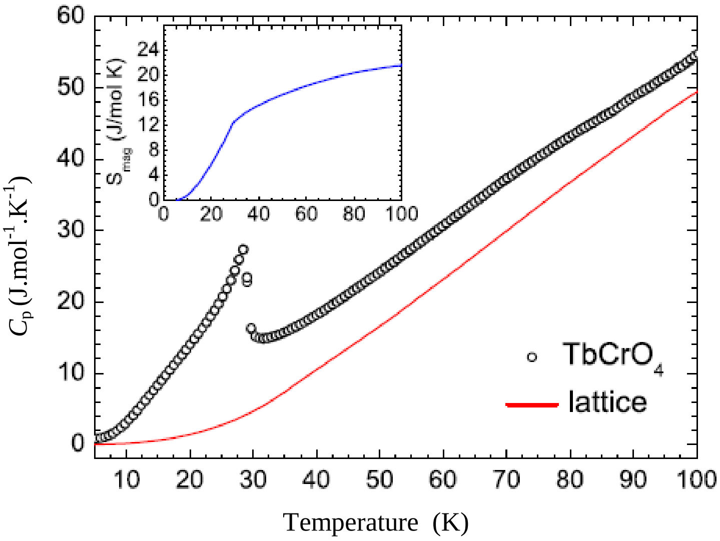

Fig. 5.26 Temperature dependence of the total specific heat measured at 0 T for scheelite-type TbCrO$_4$ (open circles) and lattice contribution (solid line) [19]. The inset shows the variation of the magnetic entropy associated with the magnetic ordering of Cr^{5+} and Tb^{3+} for scheelite-type TbCrO$_4$ at 0 T as proposed by Climent *et al.* [19].

The evolution of the heat capacity with the temperature for SmCrO$_4$ is shown in figure 5.27. The blue line represents the fitting of the experimental data between 30 and 70 K to the equation (5.8) and figure 5.28 shows the magnetic C_{mag} *vs.* T obtained by subtracting values the C_{lat} estimated from the mentioned polynomial fitting from the experimental C_p.

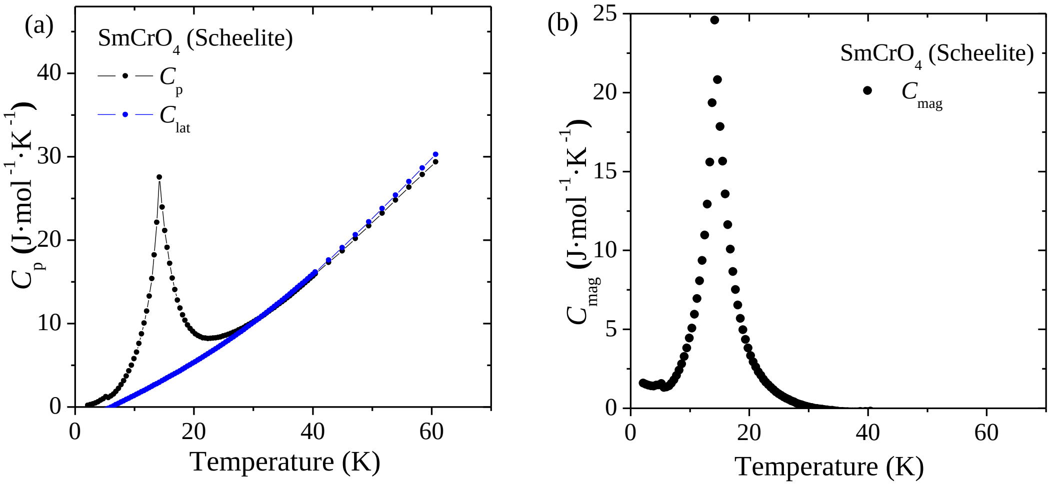

Fig. 5.27 Specific heat of SmCrO$_4$-scheelite: (a) C_p *vs.* T plot of total experimental heat capacity (black) and calculated C_{lat} values (blue) by a fourth order polynomial function; and (b) C_{mag} *vs.* T plot of magnetic specific heat after subtracting the lattice contribution.

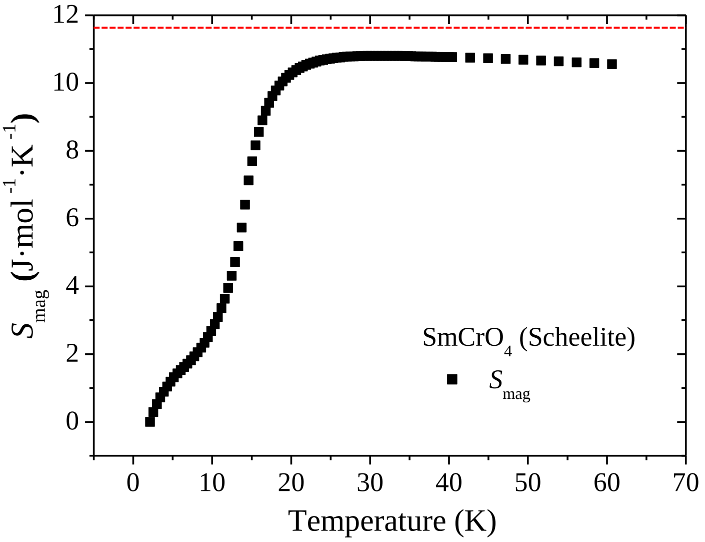

Fig. 5.28 Experimental magnetic entropy of SmCrO$_4$-scheelite calculated by integrating C_{mag} as a function of temperature

From the evolution of this C_{mag} value against the temperature, we can notice that C_{mag} remains almost constant in the temperature range 30-60 K. Nevertheless, at 20 K the onset of a sharp increase can be visualized, reaching a net maximum at 14.5 K, which corresponds to the Néel temperature that agrees well with the one determined from magnetic susceptibility measurements. The estimated magnetic entropy (S_{mag}) takes the values of 10.7 Jmol^{-1}K^{-1}, in the paramagnetic state, and shows a decrease around 18 K associated to the onset of the antiferromagnetic state. This value of the magnetic entropy fairly agrees with that expected for the Cr^{5+}, Rln2=5.76 Jmol^{-1}K^{-1}, and Sm^{3+} which show a characteristic behavior mentioned earlier. It appear to behave as a doublet with an expected entropy value of 5.76 Jmol^{-1}K^{-1} too that yields a total value of the entropy of 11.52 Jmol^{-1}K^{-1} indicated by the red line given in figure 5.28.

Polynomial fitting procedure has been used for the remaining *R*CrO$_4$ samples to obtain the lattice contribution to the total specific heat (C_p). However, the results concerning the final determination of the magnetic entropy were unsatisfactory. This is probably due to the weaker effects associated with the λ-anomalies (figure 5.29), where the C_p *vs.* T data are given for other members of the *R*CrO$_4$-scheelite series. On the other hand, as it can be observed in figure 5.29, the temperature of the λ-transition increases with the increasing of the atomic number of the corresponding trivalent rare earth cation R^{3+}. This effect can be explained taking into account the decrease of the bond length distances *R*-O-Cr, through which the pathway of magnetic interactions occur, with the decreasing of the ionic radius of the R^{3+} cations going from Nd^{+3} to Yb^{3+} according to the well-known lanthanide contraction.

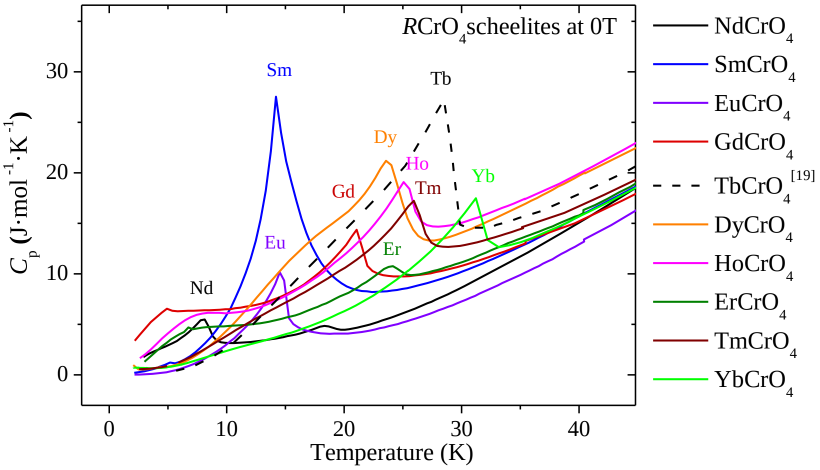

Fig. 5.29 Temperature dependence of the total specific heat for *R*CrO$_4$-scheelite oxides at zero field. The TbCrO$_4$ data are taken from reference [19].

On the other hand, the effect of the magnetic field on the λ-transition depends on the nature of the R^{3+} ion. In this sense in the case of the SmCrO$_4$, EuCrO$_4$, TmCrO$_4$ and YbCrO$_4$ compounds, figure 5.30, the magnetic field does not affect very much the transition. It is worth noting that for TmCrO$_4$ and YbCrO$_4$, the C_p plots at zero fields are almost identical with those obtained up to 9T.

In the case of the remaining members of these scheelite family, a clear influence of the magnetic field is observed in the case of the GdCrO$_4$ compound, , as it was expected. The first transition disappears for a magnetic field of 5 **T**, figure 5.31(a). This is due to the metamagnetic transition that takes place at this magnetic field, which is also detected from the magnetization *vs.*field measurements. Similar effects have been observed in the case of NdCrO$_4$, DyCrO$_4$ and HoCrO$_4$, figure 5.31 (b, c and d). In the case of the latter compound, this effect is less marked. In some cases as for example in the Erbium, Neodymium, Holmium, Dysprosium and Gadolinium compounds weak shoulders have been also observed in the *C*p *vs.* T plots, as in figures 5.29 and

5.31, that could be due to some structural transitions from the tetragonal symmetry to lower ones. In this sense, it is worth noting that in the case of DyCrO$_4$ and TbCrO$_4$ compounds crystallizing with the zircon-type structure, a structural transition has been described from tetragonal to orthorhombic symmetry at low temperatures [22]. Therefore, high-resolution neutron and synchrotron powder-diffraction experiments are needed to be done for these high-pressure samples.

The specific heat for YCrO$_4$ scheelite has been measured by Long *et al.*[9] and is shown in figure 5.32 to illustrate the difference between the different *R*CrO$_4$ compounds. However, this difference is not the same for all compounds of the series, for example the GdCrO$_4$ compound show different changes in the specific heat curve between zircon and scheelite polymorph, see figure 5.33. The GdCrO$_3$ specific heat curve (red in figure 5.33) shows that such impurities of this compound can possibly affect the scheelite polymorph at very low temperature.

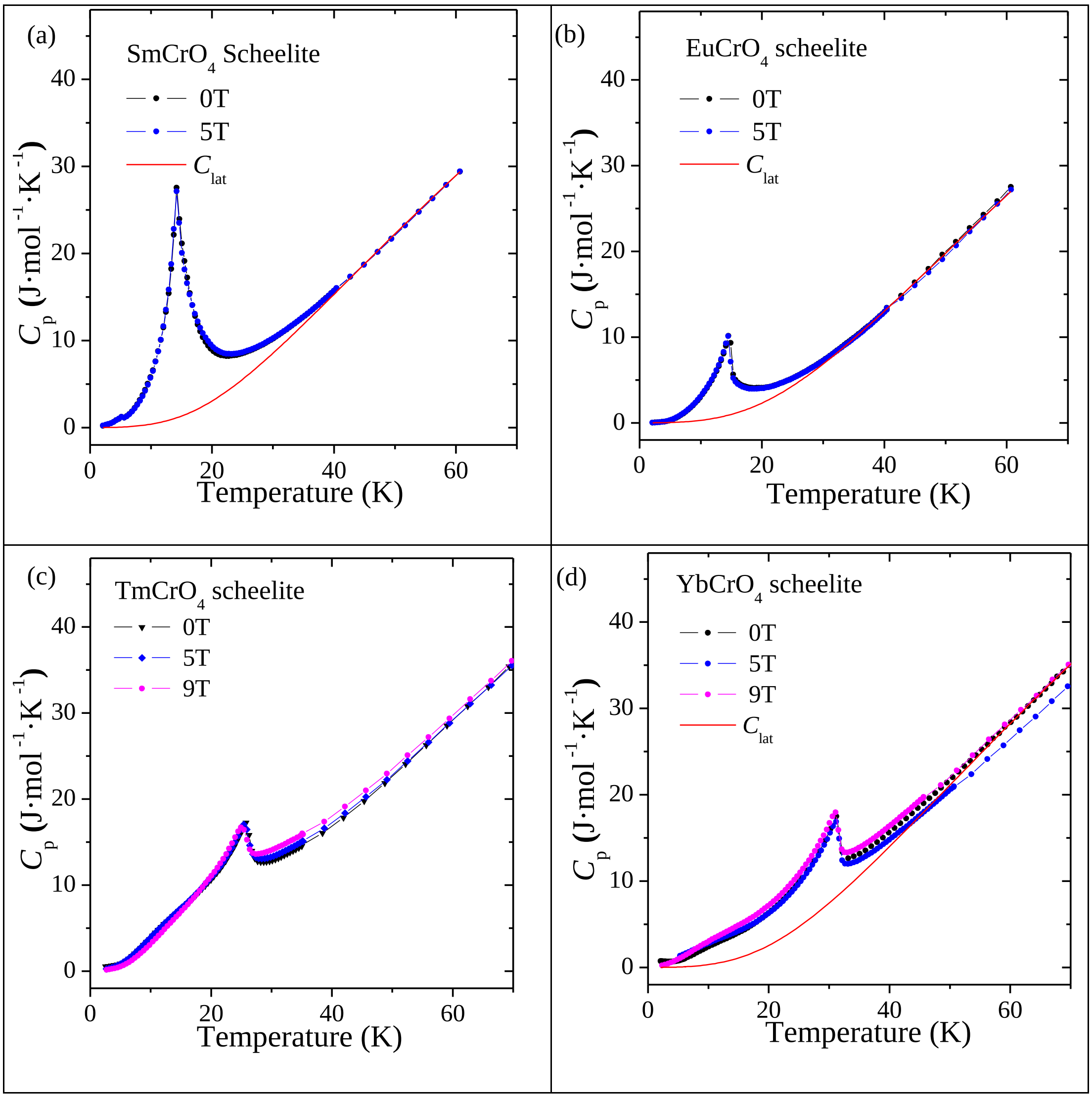

Fig. 5.30 Temperature dependence of the total specific heat measured at different magnetic fields for scheelite-types: (a) SmCrO$_4$, (b) EuCrO$_4$, (c) TmCrO$_4$ and (d) YbCrO$_4$. The continuous (red) lines are C_{lat} calculated by equation (5.11).

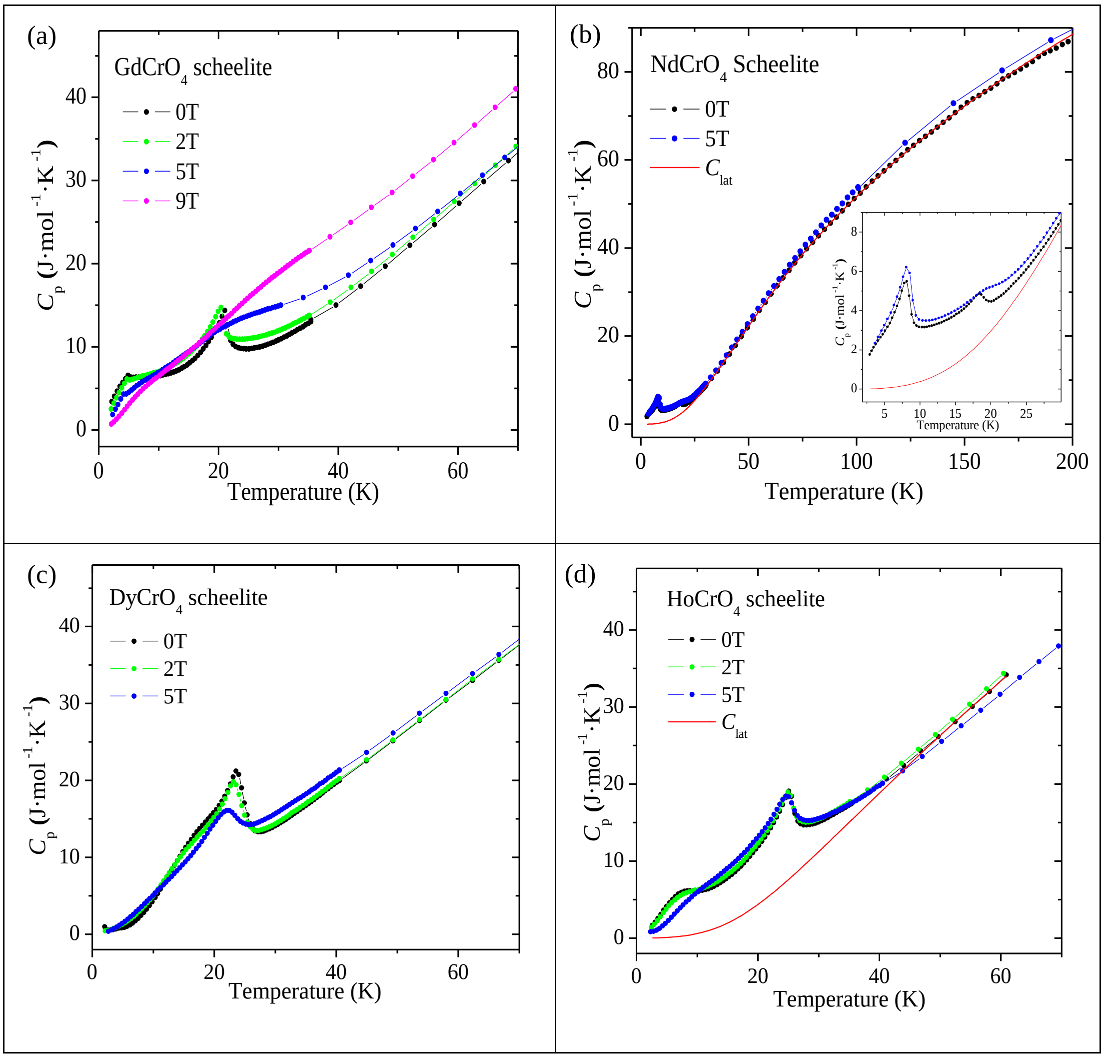

Fig. 5.31 Temperature dependence of the total specific heat measured at different magnetic fields for scheelite-types: (a) GdCrO$_4$, (b) NdCrO$_4$, (c) DyCrO$_4$ and (d) HoCrO$_4$. The continuous (red) line represents the C_{lat} calculated by equation (5.11)

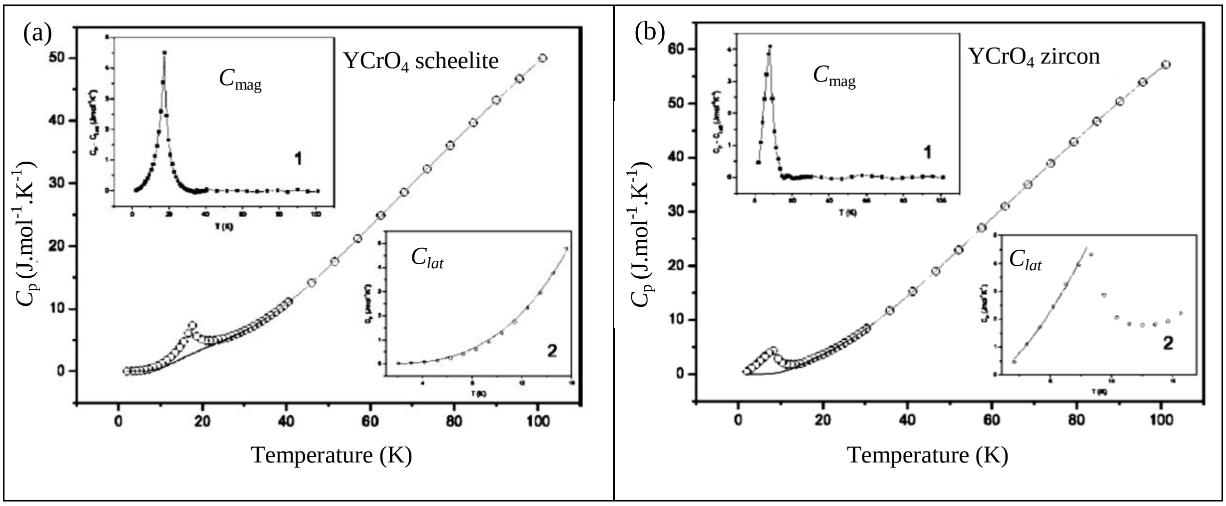

Fig. 5.32 Temperature dependence of specific heat for YCrO$_4$ done by Long *et al.* [9]: (a) scheelite polymorph; (b) zircon polymorph. In both graphs, insets 1 represent the magnetic contribution to the specific heat, while insets 2 show the lattice contribution to the specific heat.

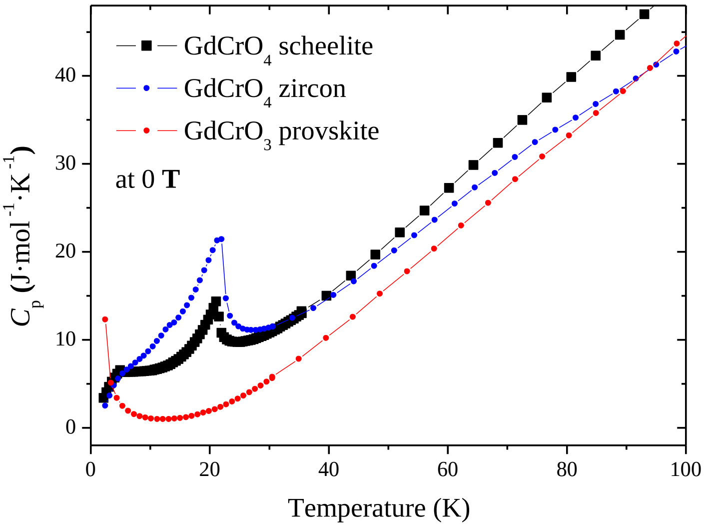

Fig. 5.33 Temperature dependence of specific heat for GdCrO$_4$ scheelite, GdCrO$_4$ zircon and GdCrO$_3$ perovskite.

The red continuous lines in figures 5.30 and 5.31 represent the lattice contribution to the heat capacity calculated from the combined Debye and Einstein models as in equation (5.11). The corresponding Debye temperature (θ_D) and three Einstein temperatures (θ_{E_1}, θ_{E_2} and θ_{E_3}) are listed in table 5.2. Although there is a good fitting between the calculated C_{lat} and observed C_p above the Néel Temperature, the Debye and Einstein temperatures seems to be incompatible. This is probably due to the small RCrO$_3$ contribution at the temperature-range between 100 and 200 K as discussed before. In general, it is difficult to determine the exact magnetic specific heat of lanthanide orthochromate compounds due to the complicated crystal field splitting occurring in these compounds.

Table 5.2 Debye (θ_D) and Einstein temperatures (θ_{E_1}, θ_{E_2} and θ_{E_3}) as a result of the fitting using equation (5.11) for the C_p plots of some RCrO$_4$ scheelites.

	θ_D (K)	θ_{E_1}(K)	θ_{E_2}(K)	θ_{E_3}(K)
NdCrO$_4$	197	304.4	651.9	1054.2
SmCrO$_4$	195	311.9	672.4	992.1
EuCrO$_4$	215	319.1	669.5	981.0
GdCrO$_4$	224	372.11	652.75	1082.11
HoCrO$_4$	171	286.2	561.7	727.0
YbCrO$_4$	208	305.3	579.2	703.0

5.3 Superexchange Pathways in *R*CrO$_4$

It is important to study the magnetic interactions taking into account the possible pathways of the magnetic exchange mechanisms occurring in the RCrO$_4$ compounds and the changes accompanying these pathways upon the structural transition from the zircon to the scheelite phase. Based on the discussion of the structural characterization in chapter 3, it can be concluded that the superexchange mechanisms can be quite complex. This is because CrO$_4$ tetrahedra are isolated from each other by the RO$_8$ polyhedra and since several kinds of interactions should be considered. In this section, we will explain these various interactions in the zircon-like structure and hence describe the changes to these interactions upon the transition to the scheelite-like structure and highlight the accompanying change in the magnetic properties.

In the RCrO$_4$-zircon structure, two kinds of zigzag chains, Cr-O-*R*-O-Cr (*J*1) and *R*-O-*R*-O-*R* (*J*2) have effect along the *x*-axis of the zircon structure. Identical exchange pathways of *J*1 and *J*2 occur along the y-axis as well, demonstrating the 3-dimensional character of these exchange pathways (denoted as *J*1* and *J*2* in figure 5.34(a)). Along the *z*-axis, there are two identical Cr-O-*R*-O-Cr (*J*3) chains. These interactions in the RCrO$_4$ zircons are illustrated in figure 5.34(a), while a view of the 3-dimensionality of these interactions can be viewed in figure 5.34(b). On the other hand, Cr-O-O-Cr (*J*4) interaction pathway is represented, which was suggested by Jiménez *et al.*[23] and Tezuka *et al.*[24]. It was proposed by Long *et al.*[25] to ignore this later pathway due to the large O-O distance, which results in a small interaction intensity compared to that of Cr-O-*R*-O-Cr. However, we can still consider it as a competing mechanism in the system as the average O-O distance of 2.6 Å is quite comparable to that of the *R*-O distance for the large lanthanides.

In fact, each of these exchange pathways has a special character that can affect its expected role in the exchange (following Goodenough-Kanamori rule [26-30]). The pathway *J*1 occurs due to the corner sharing between Cr- and *R*-polyhedra resulting in two zigzag chains of Cr-O-*R*-O-Cr: one in *x*-direction and the other in *y*-direction. The *R*-O-Cr angle in this pathway is about 152° (angle 1 in figure 5.34(b)), which can introduce an antiferromagnetic interaction. However, a ferromagnetic interaction is expected from *J*3 due to the edge sharing between Cr- and *R*-polyhedra resulting a bond angle of *R*-O-Cr of about 98°. This significant difference will lead to different orbital overlapping between the 3*d*-Cr^{5+} ions and 4*f*-R^{3+} ions, and consequently different magnetic interactions. Moreover, all *J*3 pathways are in the z-direction and of double the amount of *J*1 pathways, which refers to the strong ferromagnetic resultant of the interaction. Such an effect is expected to increase by decreasing the *R*-O distance for smaller lanthanides and therefore reinforcing the ferromagnetic feature of the interaction.

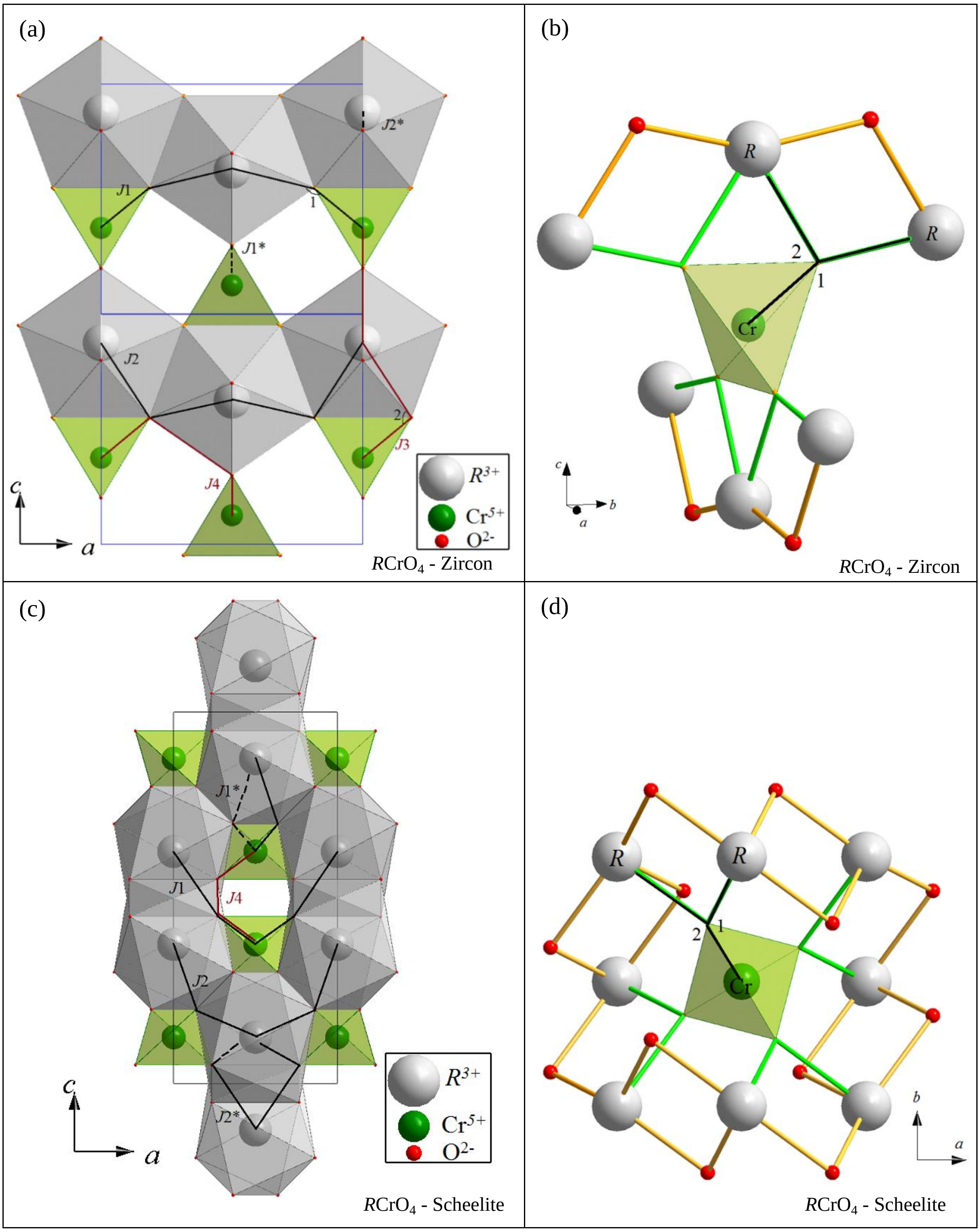

Fig. 5.34 Different superexchange pathways in *R*CrO$_4$ compounds for the zircon-type (a and b) and the scheelite-type polymorphs (c and d). (a) Zircon structure projected on (010) showing *J*1 and *J*2 AFM pathways in *x*-direction, AFM *J*1* and *J*2* in *y*-direction, *J*3 FM pathway in *z*-direction and *J*4 FM pathway in *ab* plane. (b) The topology of Cr-tetrahedra in the zircon structure showing different *R*-O-Cr angles and the zigzag chains of *R*-O-*R* in x- and y-directions. (c) Scheelite structure projected on (010) plane showing *J*1 and *J*2 AFM pathways in *x*-direction, AFM *J*1* and *J*2* in *y*-direction and *J*4 FM pathway in *ab* plane. (d) The topology of Cr-tetrahedra in the zircon structure showing different *R*-O-Cr angles and the connectivity of *R*-O-*R* zigzag chains of in a 3-dimensional manner. The dotted lines show the pathways perpendicular the plane of the paper

A small interaction can be referred to by *J*2 pathway for *R*-O-*R*-O-*R* zigzags in *x*- and *y*-directions due to the edge sharing between *R*-polyhedra. In the isostructural compounds DyVO$_4$ and DyAsO$_4$ where no magnetic ions are in the 4*b* site, antiferromagnetic orderings appears due to *J*2 interactions at low temperatures (<3.5 K).[31,32] However, this effect appears to be very small in *R*CrO$_4$ compounds. The sequence Cr–O–O–Cr results in the *J*4 interaction pathway, which should generate ferromagnetic interactions. Although a short Cr-O distance (about 1.6 Å) takes place, the O-O distance is relatively large (about 2.6 Å), but is though comparable to *R*-O distances for big lanthanides in this system.

It can be concluded that the strongest effect in the zircon structure on the magnetic properties comes from *J*3, where *R*- and Cr-polyhedra share edges in the *z*-direction. It seems that the *z*-direction in the zircon compounds is not only important for the magnetic properties but also for the mechanical and thermal properties as referred to in chapter 3. However, there is an antiferromagnetic minor effect arising from *J*1 and *J*2 zigzag chains, which are perturbed when an applied magnetic field exceeds a critical value (H_c), giving rise to a the ferromagnetic component, as can be observed from the obtained susceptibility and magnetization data for zircon compounds [23-25]. Therefore most of the *R*CrO$_4$ zircon compounds are ferromagnetic (with *R*= Gd-Yb). However, for the zircon chromates with *R*= Nd, Sm, Eu and Lu, antiferromagnetic interactions prevail [33]. There were some trials to explain the difference between the two zircon types by taking into consideration the *R*-*R* distance and the superexchange pathway [33], but however it is still not confirmed about the main reasons behind the dominance of AFM or FM behavior between various zircons.

Let us now consider the transition from zircon- to scheelite-like structures. In *R*CrO$_4$ scheelites, an intense change in the exchange pathways takes place, as illustrated in figure 5.34(c and d). The *J*3 FM pathway corresponding to Cr-O-*R*-O-Cr in the z-direction disappears due to the break of the edge sharing between Cr- and *R*-polyhedra. Consequently, one of the *R*-O-Cr angles increases from about 98° to about 124° and therefore changing from ferromagnetic to an antiferromagnetic pathway similar to *J*1. Moreover, now the scheelite structure is compact and the Cr-tetrahedron is coordinated with 8 *R*-dodecahedra instead of the 6 in the zircon case. This result in the increase of the number of the AFM interactions through the Cr-O-*R*-O-Cr pathway, as shown in figure 5.34(d).

On the other hand, the number of *J*2 through *R*-O-*R*-O-*R* pathways increases by increasing the number of the edge sharing between *R*O$_8$ polyhedra themselves. Moreover, all *R*-dodecahedra surrounding the Cr-tetrahedra are connected together with a *J*2 AFM pathway through edge sharing. Therefore, the role of the rare-earth element increases in the scheelite phase. This is also assisted by the slight decrease in *R*-*R* distance in the scheelite structure compared to the zircon one and the decrease of *R*-O distance by lanthanide contraction. Finally, the *J*4 FM pathway through Cr-O-O-Cr interaction exists and experiences a slightly shorter Cr-Cr distance but the O-O distances remain almost the same. Therefore, the antiferromagnetic interactions are the dominant ones in the *R*CrO$_4$ scheelite, but a component of a ferromagnetic interaction can appear at low temperatures due to Cr-O-O-Cr pathway, which can produce a canting effect between the atomic magnetic moments, as it is the case for GdCrO$_4$.

5.4 Magnetic Structure

After the structural characterization and our systematic study of the magnetic properties of *R*CrO$_4$, by magnetic susceptibility, magnetization and specific heat measurement, we used the results as basis for planning the low-temperature neutron diffraction experiments in order to determine the relevant magnetic structures. We started with the GdCrO$_4$ scheelite which we obtained first in high purity and we carried out temperature-dependent neutron diffraction experiments using constant wavelength of $\lambda = 0.577$ Å at the 7C2 diffractometer of the Laboratoire Léon-Brillouin in Saclay, France. Then we carried out the time of flight neutron diffraction experiment using the Wish diffractometer for the scheelite compounds DyCrO$_4$ NdCrO$_4$ und HoCrO$_4$ at the ISIS pulsed neutron and muon source at the Rutherford Appleton Laboratory in Oxfordshire, England. A contribution has been carried out to the study of ErCrO$_4$ and TmCrO$_4$ scheelites previously prepared before this PhD project. The TbCrO$_4$ scheelite has been prepared, studied and published by Climent Pascual *et al.* [12] and is summarized here. On the oter hand, the magnetic properties and magnetic structure determination of the zircon polymorphs of *R*CrO$_4$ oxides were studied previously by Jiménez [1] and are out of the scope of this study.

5.4.1 GdCrO$_4$

By analyzing the neutron powder diffraction patterns at 100 and 2 K as in figure 5.35(a) and (b) respectively, an agreement with the lattice parameters obtained by XRD previously has been obtained see table 5.3. Because of the large absorption cross section of natural gadolinium nuclei for thermal neutrons [34], difficulties for gadolinium-containing samples occur. Therefore, a small wavelength of 0.577 Å was chosen to reduce the probability for gadolinium nuclei to absorb neutrons and in return provide a compromise between the absorption and the beam flux, which increases with the wavelength.

Figure 5.35 shows the Rietveld refinement for neutron diffraction patterns of GdCrO$_4$ scheelite at 100 and 2K. The atomic and lattice parameters at 100K have been explained in chapter 4 (table 4.3). In figure 5.35, one can see the difference between the patterns, which correspond to the peaks of the magnetic structure of the scheelite polymorph. The pure magnetic peak at (002) can be observed in figure 5.35(b) as well as the magnetic weak (110) peak. The evolution of this peak and other magnetic peaks can be viewed in figure 5.36, from which the Néel temperature can be estimated at about 20 K. These magnetic reflections can be indexed in a commensurate lattice related to the crystallographic one by a propagation vector k=(0,0,0). This refers to the fact that no loss in translational symmetry arises from the spin arrangement.

The peaks of (002) and (110), appearing upon cooling under 20 K, can be explained by an arrangement of the magnetic moments in the *ab*-plane. However, additional peaks intensity below 7 K appear for (011) and $(1\bar{1}0)(110)$ reflections which are in accordance with the heat capacity previously discussed. In fact, this could be attributed to a lattice distortion from the tetragonal $I4_1/a$ to a pseudo-tetragonal symmetry. However, it is difficult to analyze this effect due to the high background resulting from the Gd absorption for the neutron radiation. On the other hand, The Néel temperature estimated from the temperature dependence of the strongest magnetic reflection (002) was found to be 20 K, which agrees with the magnetic susceptibility and specific heat measurements discussed previously.

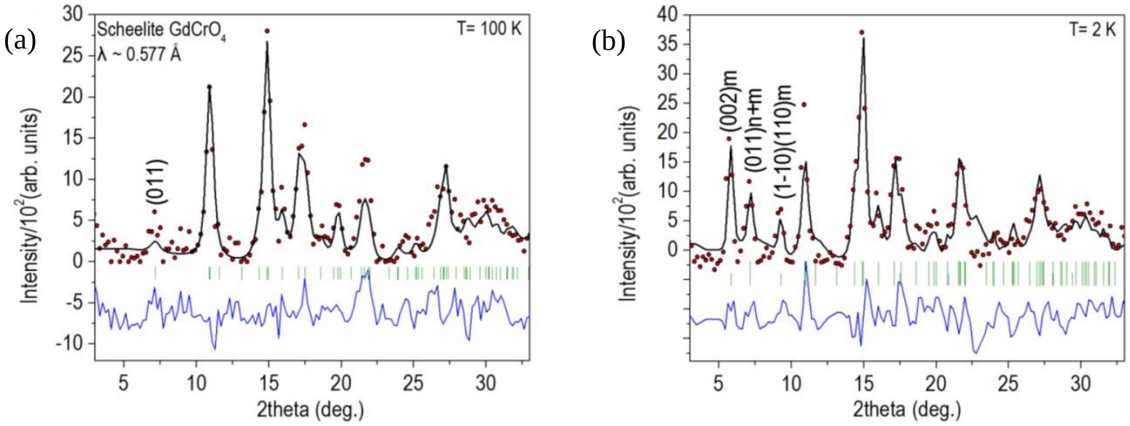

Fig. 5.35 Rietveld refinement of the neutron diffraction pattern of the GdCrO$_4$ scheelite polymorph at (a) 100 K and (b) 2K. First and second rows of vertical ticks correspond to the nuclear and magnetic reflections respectively.[3]

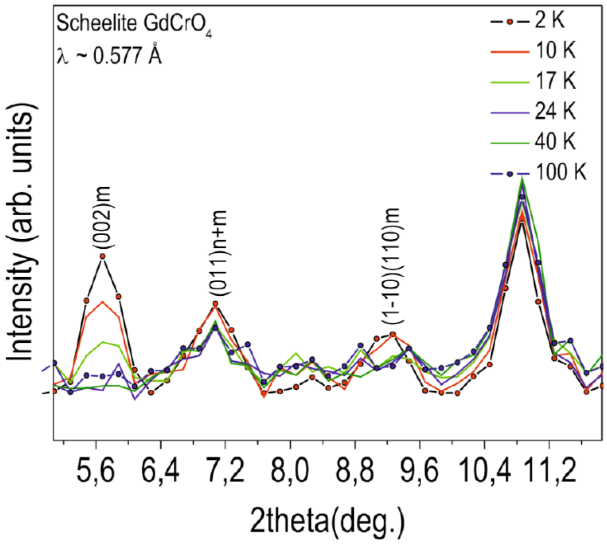

Figure 5.36 The low-angles range of the neutron diffraction patterns of the GdCrO$_4$ scheelite between 100 and 2K. [3]

The possible arrangements of the ordering magnetic moments were determined following the method of the representations proposed by Bertaut [35], which gives the possible magnetic structures compatible with the crystal symmetry.

Table 5.3 shows the basis vectors of the irreducible representations of the wave vector, G_K, generated by the program BasIreps (integrated in the FullProf program [36, 37]). G_K contains only those symmetry operations of the high temperature space group, $I4_1/a$, which keep the propagation vector invariant or transform it into an equivalent vector. Upon generating all the spin configurations compatible with the crystal symmetry and the antiferromagnetic behavior of this oxide, eight irreducible representations Γ_i (i=1 to 8) were found for the little group G$_\mathrm{K}$ (4/*m*) with k=(000). Among these, only the mixed representation $\Gamma_6 \otimes \Gamma_8$ allows for a simultaneous antiferromagnetic coupling of the gadolinium and chromium sublattices.

Table 5.3 Basis vectors of the irreducible representations for the little group G_k "k=(000)"and magnetic representations associated with Cr^{5+} and Gd^{3+} Wyckoff sites in the space group $I4_1/a$.[3]

IR	Basis vectors											
	4*a*						4*b*					
	Cr^{5+} (1)			Cr^{5+} (2)			Gd^{3+} (1)			Gd^{3+} (2)		
	x	y	z	x	y	z	x	y	z	x	y	z
Γ_1	0	0	1	0	0	1	0	0	1	0	0	1
Γ_4	0	0	1	0	0	-1	0	0	1	0	0	-1
Γ_5	1	$-i$	0	1	$-i$	0	1	$-i$	0	1	$-i$	0
Γ_6	1	i	0	-1	$-i$	0	1	i	0	-1	$-i$	0
Γ_7	1	i	0	1	i	0	1	i	0	1	i	0
Γ_8	1	$-i$	0	-1	i	0	1	$-i$	0	-1	i	0

Therefore, we propose for the GdCrO$_4$ scheelite a magnetic structure at 20 K in which the Gd^{3+} and Cr^{5+} moments are lying in the *ab*-plane and the collinear AFM structure is observed between the magnetic moments lying in the (00l) planes as shown in figure 5.37. At 2 K, the Rietveld refinement in figure 5.35(b) for the neutron diffraction pattern corresponds to the magnetic moment values: $\boldsymbol{\mu}_{\mathrm{Gd}^{3+}}$ = 6.6(4); $\boldsymbol{\mu}_\mathrm{B}$ and $\boldsymbol{\mu}_{\mathrm{Cr}^{5+}}$ = 0.7(3) $\boldsymbol{\mu}_\mathrm{B}$ (with a magnetic *R*-factor "R_M= 0.19").

The investigations by Mössbauer spectroscopy in a previous study for GdCrO$_4$ zircon [38] indicate that only 20% of Gd order magnetically at 22 K, while the remaining 80% do not show any magnetic order down to around 10 K. This 80% Gd site may be attributed to a low-temperature orthorhombic phase. Therefore, an investigation of the structure at low temperatures by high-resolution synchrotron powder diffraction can be of a high benefit, in order to verify if any structural changes can take place at low temperatures. Such a synchrotron beamtime was not approved during the limited time of this thesis.

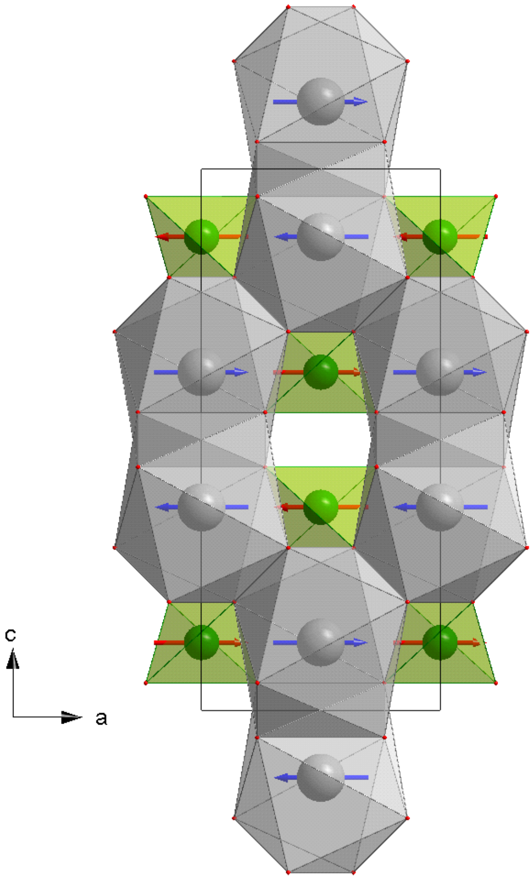

Fig. 5.37 Schematic representation of the magnetic structure of the GdCrO$_4$ scheelite at 2 K. Large gray and smaller green balls correspond to Gd and Cr atoms respectively.

5.4.2 ErCrO$_4$, TmCrO$_4$ and DyCrO$_4$

Figures 5.38(a) and (b) show the Rietveld refinement of the neutron diffraction data for the obtained scheelite-type ErCrO$_4$ oxide at 100 and 2 K, respectively. The data have been refined according to the scheelite-type structure, space group $I4_1/a$. The oxygen atoms are located in the general positions 16*f* (*x*,*y*,*z*), while the Er^{3+} and Cr^{5+} ions are placed in the special 4*b* (0,1/4,5/8) and 4*a* (0,1/4,1/8) sites, respectively. Note that the impurities Cr$_2$O$_3$ (4 wt %) and ErCrO$_3$ (10 wt%) have been also included in the refinement. Neutron powder diffraction data were collected in the temperature range of 2-100 K using the medium resolution powder diffractometer D1B (λ= 2.5251Å, $20° \leq 2\theta \leq 90°$) at the Institut Laue Langevin (Grenoble, France). The structural parameters obtained from the Rietveld refinement, main bond distances, angles and agreement factors are included in table 5.4.

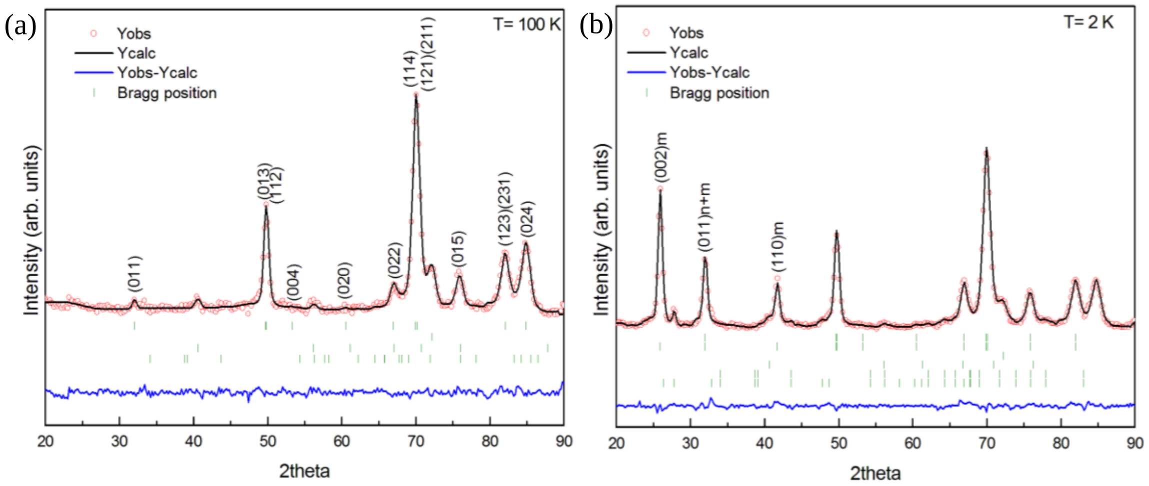

Fig. 5.38 Rietveld refinement of neutron diffraction patterns obtained with λ= 2.5251 Å at (a) 100 K and (b) 2 K for scheelite-type ErCrO$_4$. Vertical marks denote the position of (a) nuclear allowed reflections for the scheelite polymorph (first line), Cr$_2$O$_3$ (third line, 4 wt %) and ErCrO$_3$ (fourth line, 10 wt %); and (b) nuclear and magnetic reflections for the scheelite-type polymorph (first and second lines), Cr$_2$O$_3$ (fourth line), ErCrO$_3$ (fifth line) and magnetic reflections for ErCrO$_3$ (sixth line). Nevertheless, the second row of vertical marks in (a) and the third in (b) refer to the shoulder in the main reflection resulting from the sample environment equipment during the experiment [7].

The neutron powder diffraction patterns show the onset of new reflections forbidden for the space group $I4_1/a$ along with a progressive increase of certain reflections below T_N = 20 K. These magnetic reflections, see Fig. 5.38(b), have been indexed on the basis of the coincidence between the crystal and magnetic cells, with the propagation vector k= (0,0,0). The thermal evolution of the integrated intensity of the (002) and (011) magnetic reflections reveals that these magnetic reflections disappear at 22 K, a higher ordering temperature than the observed one from the magnetic susceptibility measurements. The magnetic structure is defined in the primitive *P*1 space group. The best agreement between the experimental and calculated neutron diffraction profiles (R_M= 0.032) was obtained when Cr^{5+} and Er^{3+} magnetic moments are aligned parallel to the *ab*-plane in the same manner observed for GdCrO$_4$ scheelite (see figure 5.37). The saturation moments obtained from the Rietveld refinement are 0.62(4) μ_B and 5.11(7) μ_B for the Cr^{5+} and Er^{3+}, respectively.

The scheelite polymorphs of TmCrO$_4$ [8] and DyCrO$_4$ follow also the same magnetic structure for ErCrO$_4$ and GdCrO$_4$ scheelite as illustrated in figure 5.37. On the other hand, for both NdCrO$_4$ and HoCrO$_4$ scheelites, further high-resolution neutron diffraction and synchrotron diffraction experiments are required in order to determine the magnetic structure of them and to exclude any contribution of a possible structural distortion at low temperatures. In the case of NdCrO$_4$, the magnetic reflections were too week to enable the determination of the magnetic structure.

Table 5.4 Atomic parameters, main interatomic distances and bond angles for the scheelite-type ErCrO$_4$ polymorph, calculated from the Rietveld refinement of neutron diffraction data obtained at 100 K. The corresponding reliability factors are also included [7].

Space group				$I\,4_1/a$
Cell parameters (Å)	a			4.9989(10)
	c			11.2332(23)
Rietveld R-factors	$R_{p.}$			0.0115
	R_{wp}			0.0146
	χ^2			1.90
Bragg R-factors	R_B			0.0140
	R_F			0.0202
Atoms, wyckoff	Er	4*b*	1	0,1/4,5/8
Positions	Cr	4*a*	1	0,1/4,1/8
x/a, y/b, z/c	O	16*f*	1	0.2352(26), 0.6044(20), 0.5478(6)
B_{iso} (Å^2)				0.065(3)

Main interatomic distances (Å) and bond angles (deg.)

d (Cr-O)	1.744(10)×4	*d* (Er-O)	2.295(11)×4
			2.382(9)×4
∠ (O-Cr-O)	120.3(13)×2	∠ (O-Er-O)	135.5(9)×2
	104.4(10)×4		98.2(8)×4
			131.5(6)×4
			71.0(5)×2
∠ (Cr-O-Er)	121.5(5)×1		
	130.7(5)×1		

Neutron diffraction patterns obtained at 80K and 1.2 K for DyCrO$_4$ are given in figure 5.39. The onset of new reflections can be observed that are forbidden in the $I4_1/a$ space group of the scheelite-type structure. In order to better visualize these mentioned reflections, the difference diffractogram is shown at the bottom of figure 5.39(a) between the experimental neutron diffraction data taken at 80 K and 1.2 K. These magnetic reflections can be indexed with the propagation vector k= (0,0,0), as it can be observed in figure 5.39(b) in the first row of the vertical marks. The same analysis used for the previous neutron diffraction data have been followed in the present case and it permits to describe the magnetic structure as a collinear one, where both Cr^{5+} and Dy^{3+} sublattices are antiferromagnetically ordered in the basal plane of the scheelite structure. This fact can be ascribed by the occurrence of an antiferromagnetic ordering in the same manner as that ascribed for the Gd, Er and Tm scheelites, studied previously in this chapter. In the same figure, some additional reflections have been indexed taken into account the magnetic structure of the distorted perovskite DyCrO$_3$, which is the main impurity present in this scheelite, as it was mentioned previously in chapter 4.

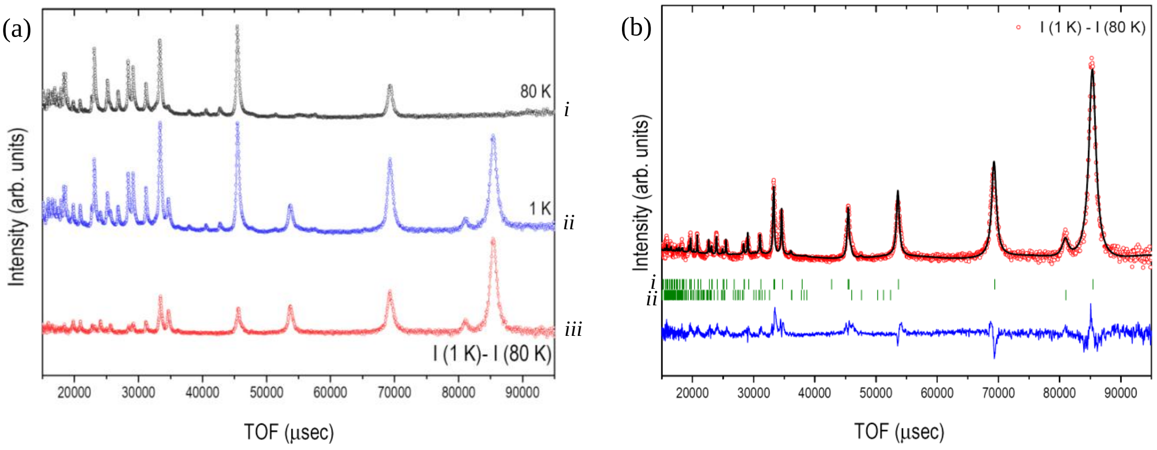

Fig. 5.39 (a) Neutron diffraction patterns for scheelite-type DyCrO$_4$ obtained at: (*i*) 80 K; (*ii*) 1 K and (*iii*) the difference curve between *i* and *ii*. (b) Rietveld refinement of the magnetic reflections; vertical marks denote the position of: (*i*) magnetic allowed reflections of scheelite polymorph and (*ii*) the allowed magnetic reflections for the secondary phase of DyCrO$_3$ distorted perovskite.[39]

Table 5.5 Structural and magnetic parameters obtained from powder neutron diffraction data of DyCrO$_4$ scheelite.[39]

T (K)	80	1.2
a (Å)	5.0170(2)	5.0148(2)
c (Å)	11.3079(6)	11.3037(5)
V (Å^3)	284.62(2)	284.27(2)
U_{Dy} (Å^2)	0.0003(8)	0.0002
U_{Cr} (Å^2)	0.019(3)	0.0002
x_O	0.2437(5)	0.2437
y_O	0.6091(4)	0.6091
z_O	0.54862(20)	0.54862
U_O (Å^2)	0.0105(14)	0.0002(8)
$d_{Cr\text{-}O}$ (Å)	1.7020(22) ×4	1.7020×4
$d_{Dy\text{-}O}$ (Å)	2.3413(22)×4	2.3413×4
	2.4177(23) ×4	2.4177×4
Cr-O-Dy (deg.)	121.759(114)	121.759
	132.242(82)	132.242
$\mu_{xy,Dy}$ (μ_B)	—	9.67(10)
$\mu_{xy,Cr}$ (μ_B)	—	0.99(12)
R$_{Bragg}$ (%)	2.44	5.49
R$_p$ (%)	3.81	4.02
R$_{wp}$ (%)	2.10	5.18
χ^2	2.62	1.32
Magnetic R-factor (%)	—	6.82

The magnetic structure is identical to that corresponding to GdCrO$_4$ given in figure 5.37, where obviously the Gd cations are replaced by the Dy ones. Table 5.5 shows the structural and magnetic parameters obtained after the Rietveld neutron diffraction refinement. A small decreasing in the lattice parameters can be observed in going from 80 K to 1.2 K due to the thermal contraction. The calculated ordered magnetic moments for Cr^{5+} and Dy^{3+} take the values of 0.99(12) μ_B and 9.67(10) μ_B respectively that agree with those expected.

5.4.4 TbCrO$_4$

Figures 5.40(a) and (b) show the Rietveld refinement of the neutron diffraction data for the scheelite-type TbCrO$_4$ oxide at 40 and 2 K, respectively, obtained by Climent *et al.* [12]. The magnetic structure of the scheelite polymorph was determined from the analysis of the neutron powder diffraction pattern collected at 2 K, figure 5.40(b). Long-range magnetic ordering and the magnetic reflections can only be indexed successfully with a propagation vector k= (0,0,0). The onset of the magnetic ordering was estimated from the thermal variation of the integrated intensity of the magnetic reflections with *d*-spacing of 3.6 and 4.6 Å, figure 5.40(b) and 5.41. The estimated ordering temperature, T_N = 29 K, agrees with that one determined from magnetic susceptibility measurements [12]. Moreover, the plot indicates that Cr^{5+} and Tb^{3+} magnetic sublattices become ordered at the same temperature.

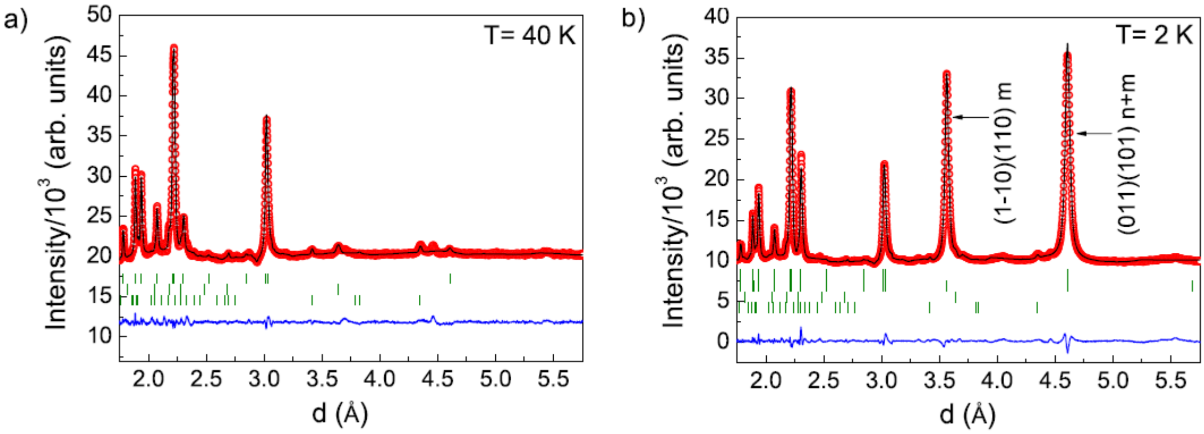

Fig. 5.40 Rietveld refinement of neutron diffraction patterns obtained at (a) 40 K and (b) 2 K for scheelite-type TbCrO$_4$. Vertical marks denote the position in (a) for nuclear allowed reflections of scheelite polymorph (first line), Cr$_2$O$_3$ (second line, 2 wt%) and TbCrO$_3$ (third line, 7 wt%); and in (b) for allowed nuclear reflections of scheelite polymorph (first line), Cr$_2$O$_3$ (third line), TbCrO$_3$ (fourth line) and allowed magnetic reflections for scheelite polymorph (second line) [12].

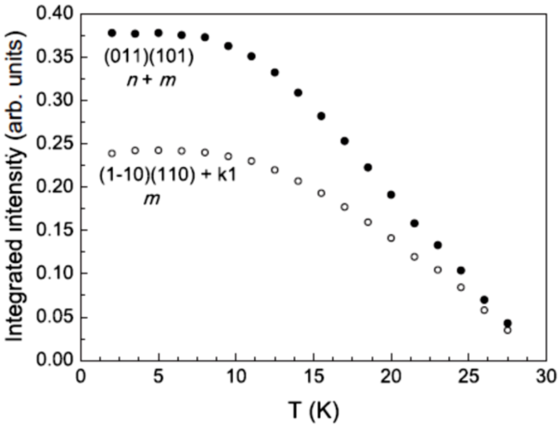

Fig. 5.41 Integrated intensity of two selected magnetic reflections as a function of temperature [12].

Unlike other Scheelites, it was found for the TbCrO$_4$ polymorph that the same irreducible representations as in table 5.3 are involved, but only Γ_4 (G_z) allows for the antiferromagnetic coupling of the magnetic moments of Cr^{5+} and Tb^{3+}. This shows a collinear magnetic structure, in which both magnetic moments are parallel to the *c*-axis, see figure 5.42. The magnetic structure is defined in the primitive *P*1 space group and the best agreement between the experimental and calculated neutron diffraction profiles was obtained when Cr^{5+} and Tb^{3+} magnetic moments take values of 1.089(9) $\boldsymbol{\mu}_B$ and 8.97(3) $\boldsymbol{\mu}_B$, respectively. Therefore, in this magnetic structure, the Tb^{3+} cations are antiferromagnetically coupled with each other between *ab*-planes along the *c*-axis. The Cr^{5+} cations also show antiferromagnetic couplings along the *c*-axis.

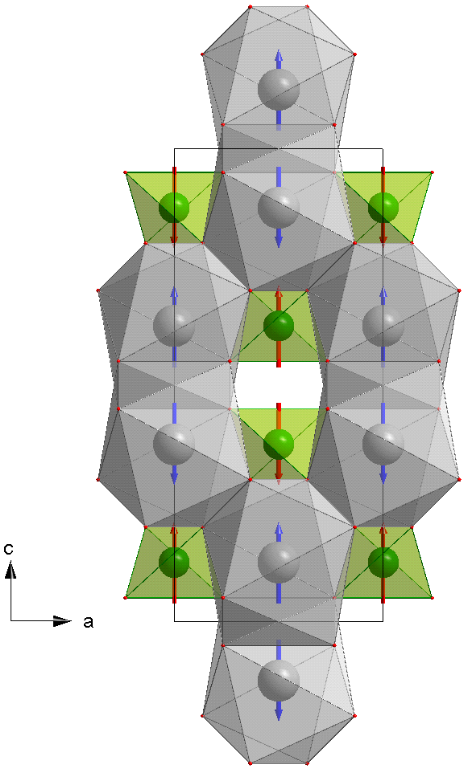

Fig. 5.42 Proposed magnetic structure for scheelite-type TbCrO$_4$ at 2 K. Large gray and smaller green balls correspond to Tb and Cr atoms respectively [after Ref. 12].

References

[1] E. Jiménez Melero, doctoral thesis, Universidad Complutense de Madrid (2005), http://eprints.ucm.es/tesis/qui/ucm-t28520.pdf (November 2012)

[2] F. E. Mabbs, D. J. Machin, Magnetism and Transition Metal Complexes, Dover Publications, New York, (2008)

[3] A. J. Dossantos-García, E. Climent-Pascual, J. M. Gallardo-Amores, M. G. Rabie, Y. Doi, J. Romero de Paz, B. Beuneu, R. Sáez-Puche, *Journal of Solid State Chemistry* **194**, 119 (2012)

[4] E. Climent Pascual, J. M. Gallardo Amores, J. Romero de Paz, N. Taira and R. Sáez Puche, *Journal of Alloys and Compounds* **488**, 524 (2009)

[5] R. Sáez Puche, J. M. Gallardo, J. Romero de Paz, N.Taira and E. Climent-Pascual, *The Journal of the Argentine Chemical Society* **97** (1), 90 (2009)

[6] E. Climent Pascual, J. Romero de Paz, J. M. Gallardo Amores and R. Sáez Puche, *Solid State Sciences* **9**, 574 (2007)

[7] R. Sáez Puche, E. Climent, M. G. Rabie, J. Romero, and J. M. Gallardo, *Journal of Physics: Conference Series* **325**, 012012 (2011)

[8] E. Climent *et al.*, (under preparation)

[9] Y. W. Long, L. X. Yang, Y. Yu, F. Y. Li, R. C. Yu and C. Q. Jin, *Physical Review B* **75**, 104402 (2007)

[10] J.B. Goodenough and J.M. Longo, Landolt-Bornstein, Chapter 3: "Crystallographic and magnetic properties of perovskite and perovskite- related compounds" Springer-Verlag, Berlin (1970)

[11] R. Sáez-Puche, M. G. Rabie, J. Romero de Paz, J. M. Gallardo-Amores, E. Climent-Pascual, *Journal of Rare Earths* **28** (6), 936 (2010)

[12] G. Grimvall, Thermophysical Properties of Materials in Selected topics in Solid State Physics, Elsevier/North-Holland, New York (1986)

[13] T. Endo, Y. Doi, M. Wakeshima, Y. Hinatsu, *Inorganic Chemistry* **49,** 10809 (2010)

[14] S. J. Joshua, A. P. Cracknell, *Physical Review Letters A* **28**, 562 (1969)

[15] E. Jiménez-Melero, P. C. M. Gubbens, M. P. Steenvoorden, S. Sakarya, A. Goosens, P. Dalmas de Réotier, A. Yaouanc, J. Rodríguez-Carvajal, B. Beuneu, J. Isasi, R. Sáez-Puche, U. Zimmerman and J. L. Martínez , *Journal of Physics: Condensed Matter* **18**, 7893 (2006)

[16] K. I. Kugel, D. I. Khomskii, *Soviet Physics Uspekhi* **25**, 231 (1982)

[17] K. Tezuka, Y. Hinatsu, *Journal of Solid State Chemistry* **160**, 362367 (2001)

[18] E. Jiménez, J. Isasi and R. Sáez-Puche, *Journal of Solid State Chemistry* **164**, 313 (2002)

[19] E. Climent Pascual, J. M. Gallardo Amores, R. Sáez Puche, M. Castro, N. Taira, J. Romero de Paz, L.C. Chapon, *Physical Review B* **81**, 174419 (2010)

[20] M. Griffel, R. E. Skochdopole and F. H. Spedding, *Physical Review* **93**, 657 (1954)

[21] L. D. Jennings, R. M. Stanton and F. H. Spedding, *Journal of Chemical Physics* **27**, 909 (1957)

[22] Y. W. Long, Q. Huang, L. X. Yang, Y. Yu, Y. X. Lv, J. W. Lynn, Ying Chen, C. Q. Jin, *Journal of Magnetism and Magnetic Materials* **322**, 1912 (2010)

[23] E. Jiménez, J. Isasi, R. Sáez-Puche *Journal of Alloys and Compounds* **323 –324**, 115 (2001)

[24] K. Tezuka, Y. Doi, and Y. Hinatsu, *Journal of Materials Chemistry* **12**, 1189 (2002)

[25] Y. Long, Q. Liu, Y. Lv, R. Yu and C. Jin, *Physical Review B* **83**, 024416 (2011)

[26] J. Kanamori, *Progress of Theoretical Physics* **17**, 177 (1957)

[27] J. B. Goodenough, *Journal of Physics and Chemistry of Solids* **6**, 287 (1958)

[28] J. Kanamori, *Journal of Physics and Chemistry of Solids* **10**, 87 (1959)

[29] J. Kanamori, *Journal of Applied Physics* **31**, S14 (1960)

[30] H. C. Nguyen, J. B. Goodenough, *Physical Review B* **52**, 324 (1995)

[31] J. C. Wright and H. W. Moos, *Journal of Applied Physics* **41**, 1244 (1970)

[32] A. Kasten, *Zeitschrift fuer Physik B* **38**, 65 (1980)

[33] E. Jiménez, J. Isasi, R. Sáez-Puche *Journal of Alloys and Compounds* **312**, 53 (2000)

[34] A. J. C. Wilson, (editor), International Tables for Crystallography, Volume C, Kluwer Academic Publishers, Dordrecht, The Netherlands, (1995)

[35] E. F. Bertaut, *Acta Crystallographica A* **24**, 217 (1968)

[36] J. Rodríguez-Carvajal, *Physica B: Condensed Matter* **192**, 55 (1993)

[37] J. Rodríguez-Carvajal, *Commission on Powder Diffraction (IUCr) Newsletter* **26**, 12 (2001)

[38] E. Jiménez-Melero, P. C. M. Gubbens, M. P. Steenvoorden, S. Sakarya, A. Goosens, P. Dalmas de Réotier, A. Yaouanc, J. Rodríguez-Carvajal, B. Beuneu, J. Isasi, R. Sáez-Puche, U. Zimmerman and J. L. Martínez, *Journal of Physics: Condensed Matter* **18**, 7893 (2006)

[39] A. J. Dos Santos Garcia, E. Climent Pascual, M. G. Rabie, J. Romero de Paz, J. M. Gallardo Amores, and R. Sáez Puche , *Journal of Physics, Conference Series,* Submitted (2012)

6. X-Ray Photoelectron Spectroscopy of $YCrO_4$ and $GdCrO_4$ Zircons

*R*CrO$_4$ compounds attract special attention due to the pentavalent state of the chromium cation in which an electronic configuration of [Ar] $4s^2 3d^1$ is realized. The Cr^{5+} demonstrates an unpaired electron with its electronic spin $S = ½$ in the $3d^1$ orbital. There has been big interest in $3d^1$ systems within the study of electron correlations, which are for transition metal oxides particularly at the center of present solid-state research. Among inorganic materials, vanadium-, and titanium-based oxides, for example, with one electron (V^{4+};$3d^1$) and (Ti^{3+};$3d^1$) in the *d* shell often realize structurally well-defined spin-½ systems[1, 2]. We aim therefore to validate and characterize the $3d^1$ configuration of *R*CrO$_4$ oxides.

6.1 Electronic Properties of *R*CrO$_4$

An illustrative schematic drawing of energy levels is established in figure 6.1 for Cr^{5+} ion in zircon type structure. In the zircon-like structure, four oxygen atoms surround the Cr^{5+} ion, forming a tetrahedral environment. In general, considering tetrahedral point symmetry (T_d), the 3*d* orbitals would give rise to a doublet and a triplet, *E* and T_2 excited states respectively. The energy separation between the two energy terms is of the order of $\approx 10^4$ cm^{-1}. However, the tetrahedra in zircon-like structure are elongated along the *c*-axis, which reduces the point symmetry to D_{2d}. This elongation is manifested with a decrease in the O-Cr-O-angles, which bisect the *c*-axis in respect to a tetrahedral angle of 109.5°. The remaining four corners O-Cr-O have values greater than the tetrahedral angle [3]. The tetragonal D_{2d} point symmetry implies extra split energy levels *E* and T_2, stabilizing the energy $d_{x^2-y^2}$ orbital in respect to d_{z^2}. However, the results of spin paramagnetic resonance (ESR), polarized absorption and luminescence indicates that the d_{z^2} orbital is occupied in the ground state instead of the orbital $d_{x^2-y^2}$ as derived from the crystal field effect considering the four oxygen atoms in the first coordination sphere of the Cr^{5+} ion [4] and in comparison with *ab-initio* calculations done by Greenblatt *et al.*[5] and Hazenkamp *et al.*[6]. They used density functional theory to demonstrate that both orbital energies come from the interaction of d_{z^2} orbital along the *c*-axis with two rare earth ions, which are situated at a distance of 3.13 Å from the chromium atom.

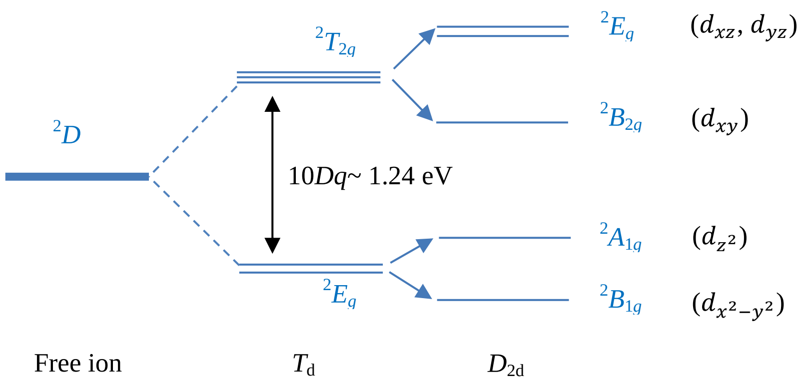

Fig. 6.1 Schematic drawing of Cr^{5+} energy levels in 4-fold coordination of T_d and D_{2d} point symmetry.[4]

However, *R*CrO$_4$ compounds are usually insulators, which is in contradiction with an expected half-metallic property calculated from the spin-dependent density of states [7]. This insulator behavior has been confirmed by Li *et al.*[7] for YCrO$_4$ and by our resistivity measurement for GdCrO$_4$, see figure 6.2. This insulating behavior indicates that the *R*CrO$_4$ compounds have a strongly correlated electronic character.

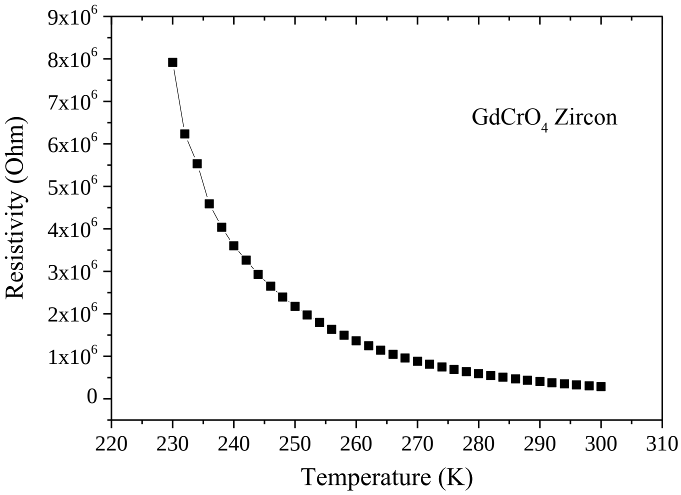

Fig. 6.2 Resistivity of GdCrO$_4$ zircon measured by PPMS Quantum design.

6.2 Previous Work on electronic structure calculations of *R*CrO$_4$

Li *et al.* [7] calculated the electronic structure for the zircon-type YCrO$_4$ with the WIEN2K package [8] using full potential linearized augmented plane waves (LAPW) within the density functional theory [9,10]. In their work they calculated the spin-dependent density of states with the generalized gradient approximation (GGA) [11] combined with a U value of 7.08 eV within the SIC method [12-13]. Figure 6.3 shows the total and partial spin dependent density of states for YCrO$_4$ zircon.

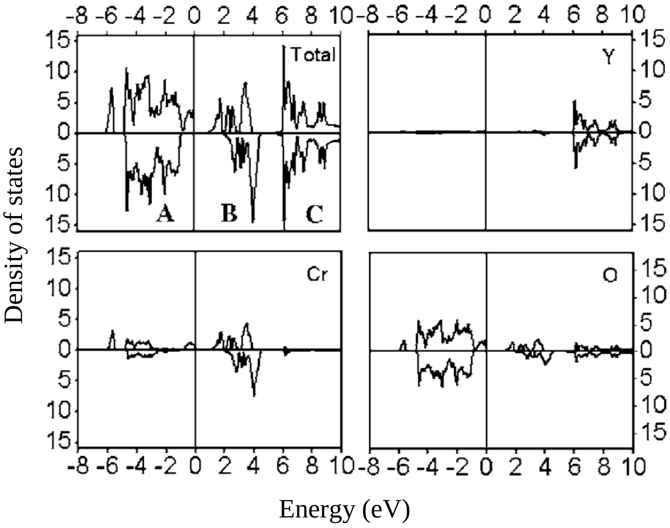

Fig. 6.3 Total and partial spin-dependent density of states of YCrO4 zircon [7].

Partial density of states helps to understand the bonding of the components in the material. It can be seen in figure 6.3 that the yttrium states are far from the Fermi level (E=0) and its effect on the electronic properties is very small. Most of the chromium states are located near to the Fermi level, and dominate the bottom of the conduction band (B part), while some states contribute to the valence band (part A). The oxygen states, however, dominate the character of the valence band. In addition, there is some hybridization of oxygen ions with chromium and yttrium ions in the total energy range. The calculated spin-dependent energy bands of $YCrO_4$ zircon are illustrated in figure 6.4, which shows a bandwidth W of about 6 eV for the majority spins. As a result, they defined an energy gap of 0.93834 eV for majority spins and 2.93783 (eV) for minority spins. They concluded, though, that their calculated value of U (7.08 eV) can be more accurately determined later by carrying out optical or photoemission measurements.

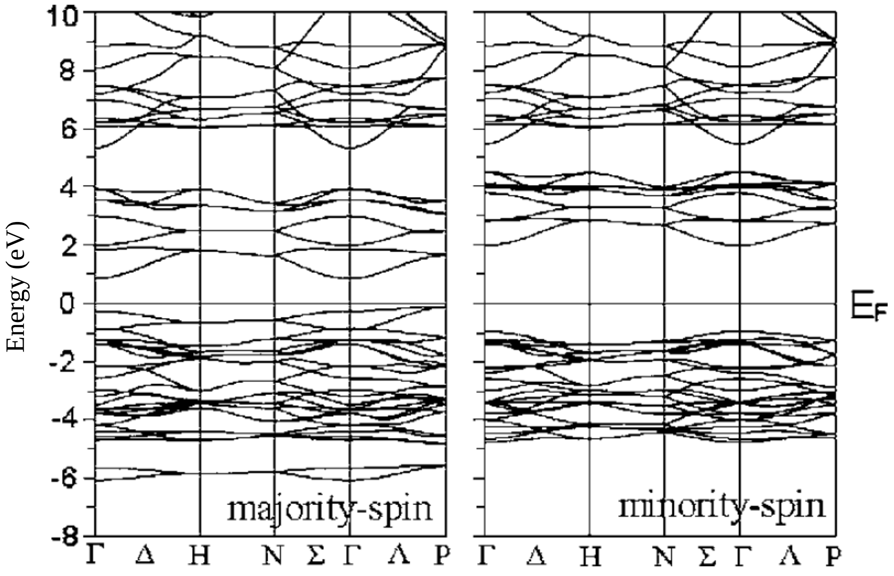

Fig. 6.4 Spin-dependent energy bands of $YCrO_4$ zircon. The left-hand panel is for majority spins and the right-hand panel are for minority spin [7].

In the work of Errandonea *et al.* [14] a band-gap energy of $E_g = 3.2$ eV was determined with reflectivity measurements on powder samples. They expected that chromium 3*d* states and O 2*p* states would dominate the band structure near the band edges in $YCrO_4$ compound. They also suggested that cation substitution can be used for band-gap manipulation in YXO_4 compounds, where X= As, Cr, P, and V.

6.3 Previous Work on Photoelectron Spectroscopy of *R*CrO$_4$

The first reported XPS study for Cr^{5+} compound is that for Cr 2*p* spectra of Na_3CrO_4 which was done in 1976 by Lavielle and Kessler [15]. However, their results had a very low resolution. Konno *et al.* [16] have provided similar results in 1992 with a relatively higher resolution for the $LaCrO_4$ monazite-like structure in which the chromium is pentavalent. They reported binding energies, E_B, for $LaCrO_4$ as: E_B[Cr $2p_{3/2}$]= 578.8 eV and E_B[Cr $2p_{1/2}$]= 588.0 eV with an uncertainty of (0.21 eV) and (0.22 eV) respectively [16] (see figure 6.5 (b)). The binding energies were calibrated by Konno *et al.*[16] with E_B[Au $4f_{7/2}$]= 84.0 eV for gold particles sputter-deposited on the samples. Similar results were obtained by Aoki *et al.* [17-19] for the Cr 2*p* XPS spectra for $NdCrO_4$ zircon (see figure 6.5(a)). They reported that the binding energies, E_B, for $NdCrO_4$ are: E_B[Cr $2p_{3/2}$]= 579.0 eV and E_B[Cr $2p_{1/2}$]= 588.3 eV [17]. However, they did not provide a valence band spectrum for this compound. Finally, they concluded from molecular orbital calculations [17, 18] that the charge density on Cr ions in the tetrahedra is much less than the nominal 5+, due to the migratory electrons from oxygen atoms, and nearly the same irrespective of the tetrahedral symmetry, suggesting a strongly covalent nature of the Cr-O bonds.

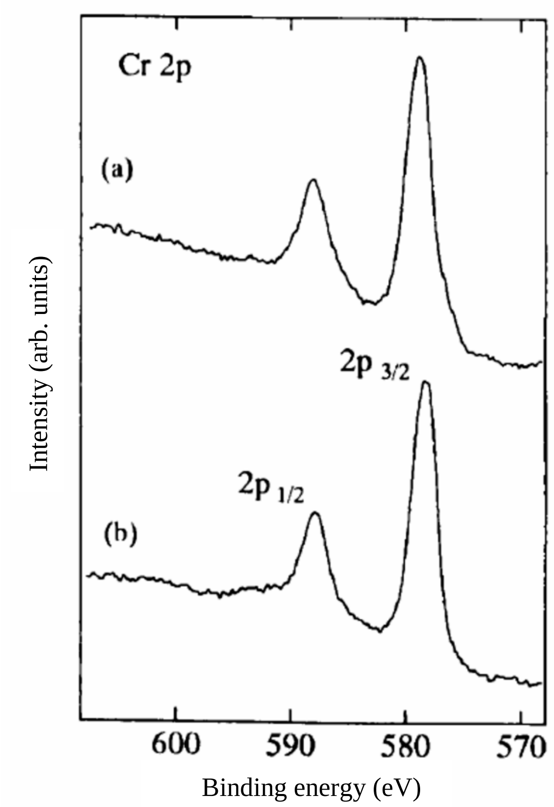

Fig. 6.5 XPS spectra of Cr 2*p* $_{1/2}$ and $_{3/2}$ for: (a) $NdCrO_4$ zircon; (b) $LaCrO_4$ zircon measured by Konno *et al.* [18] using Al-kα_1 radiation.

However, to my best knowledge, the only experimental valence band measurement of $RCrO_4$ compounds found in the literature is an XPS measurement done by Konno *et al.* [16] for $LaCrO_4$. In this study, it was reported that the valence band for $LaCrO_4$ starts at E_B = 7.5 eV, as shown in figure 6.6. The peak positions of La 5*p* and O 2*s* are separated from the valence band, indicating no interaction between them. Konno *et al.* [16] have done *ab-initio* restricted open shell Hartree-Fock calculations (ROHF-MO) [20, 21] and they concluded that the covalence plays a significant role in the Cr-O bonds of the CrO_4^{3-} tetrahedral structure and consequently stabilizing it. However, they were not sure if O 2*p* non-bonding levels should be assigned to the weak peak just below the Fermi edge or included in the large peak. They suggested that if O 2*p* non-bonding levels are included in the strong peak from about 2 to 7.5 eV, then the weak peak from 0 to 2 eV might be assigned to a 3*d* unpaired electron level. They also did not estimate the band gap and they determined the Fermi energy E_F directly at the beginning of what they called a “weak peak”.

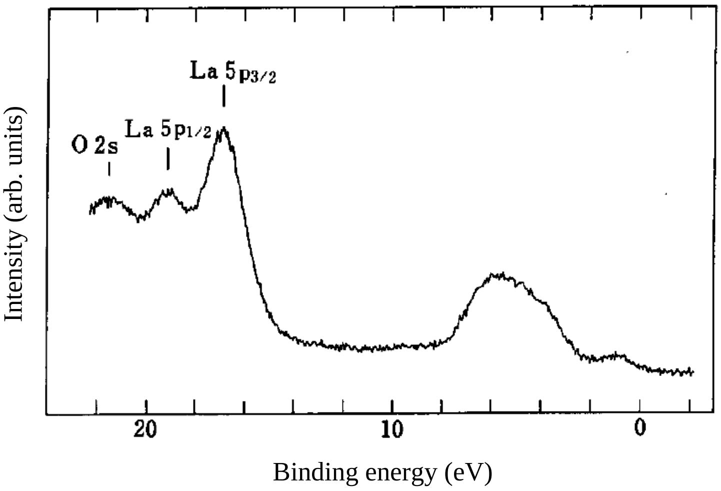

Fig. 6.6 XPS spectrum of the valence band and some core levels for $LaCrO_4$ monazite-like compound measured by Konno *et al.* [16] using Al-kα_1 radiation.

From this state of the previous work, the clear understanding of the $RCrO_4$ compounds require a further study for these materials by XPS spectroscopy. A high resolution of a measured valence band for a well-prepared compound in comparison with the calculated data can provide well understanding of the electronic properties and the contribution of different elements of the material to the valence band.

6.4 XPS Measurements and Electronic Structure Calculations for $YCrO_4$ and $GdCrO_4$ Zircon Compounds

The Zircon-like structure of $RCrO_4$ oxides was chosen for the samples to be investigated with XPS rather than the scheelite ones for two reasons. First, the high purity of the samples as verified by XRD and XAS techniques provide a good basis for a reproducible high quality XPS data. Second, the small size of the sintered fragments of scheelite phase obtained by high-pressure techniques provide an experimental difficulty for the XPS measurements. These fragments had average cross-sectional dimensions of about 2x2 mm^2, while that of the incident photoelectron beam is 1x3 mm^2.

The XPS spectra were recorded in a photoelectron spectrometer equipped with a Vacuum Generators twin crystal monochromatic Al-kα_1 source ($h\nu$ = 1486.6 eV) and a Scienta electron energy analyzer R3000. The overall resolution was set to ≈0.35 eV obtained from the fitting of the spectrum of silver polycrystalline foil scratched *in-situ*. The geometry of the measurement was taken care to be with a normal emission, *i.e.* sample surface facing analyzer, and all spectra were measured at room temperature. The sample preparation is described in chapter 2 (section 2.4.1).

The wide energy-range spectrum for both $YCrO_4$ and $GdCrO_4$ zircons taken with 1486.6 eV photon energy (Al-kα$_1$ radiation) at 300 K are shown in figure 6.7. For both materials, the purity of the samples can be shown in the figure from the corresponding peaks for the elements constituting the compositional elements. This is mainly due to the element sensitivity of the photoemission spectroscopy in which each element is denoted by sharp distinctive peaks representing different energy levels of that element. No peaks where observed for carbon, referring to no absorption of CO_2 in the samples. Some extra peaks can be viewed in the Auger radiation lines of the Cr, O, Y and Gd, which are intrinsic features for each element.

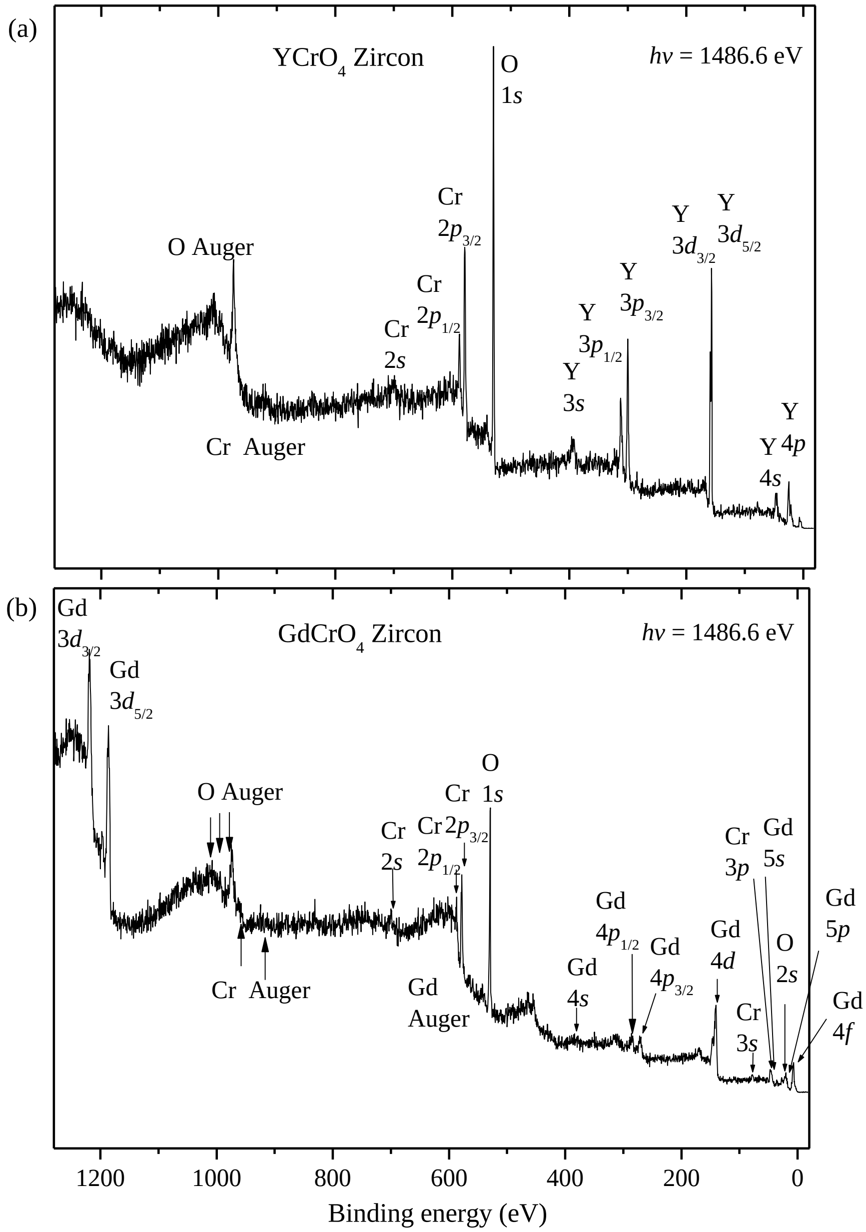

Fig. 6.7 photoemission wide scans spectra at 300 K for: (a) $YCrO_4$ zircon and (b) $GdCrO_4$ zircon.

The spectra of the O 1*s* core level for both samples is shown in figures 6.8(a) and (b), comparing different spots during the measurements time. In this manner, it can be seen that the samples showed a similar quality of the oxygen content with a very weak satellite above the main peak appearing after long measurement time when degradation to other oxidation states might take place, see figure 6.8(a) and (b). This indicates high reliability of our XPS data. It is worth noticing, in the case of $GdCrO_4$, that a shoulder of the O 1*s* occurs at E_B= 531 to 533 eV due to the the incorporation of Cr^{3+} and hydration of the surface after extended days of measurements. This can be viewed in comparison with the spectra of the hydrous compound.

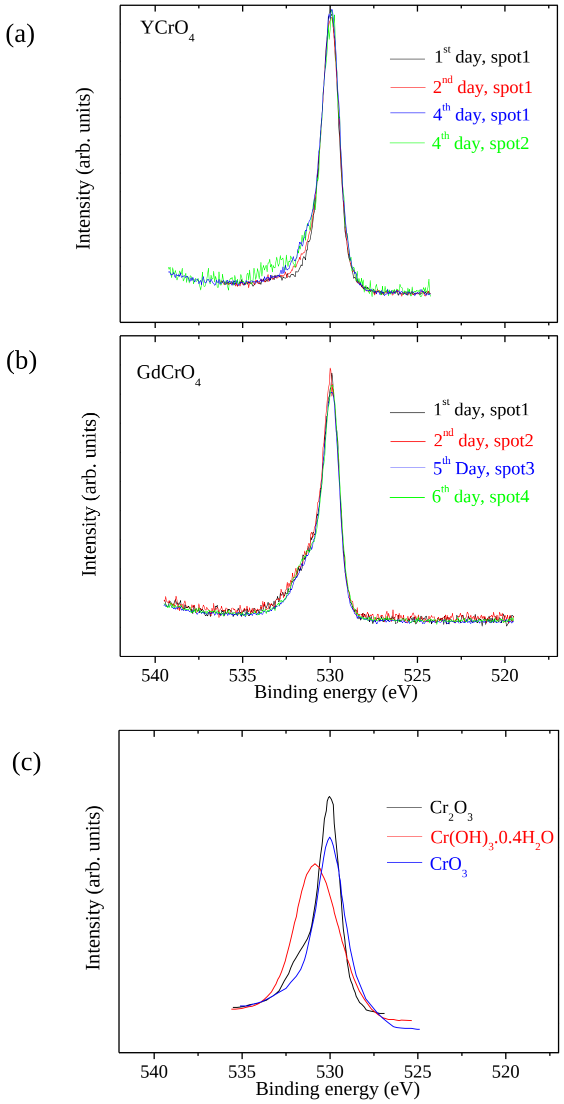

Fig. 6.8 XPS spectra of O 1*s* core level taken at different spots during the history of the measurements of (a) $YCrO_4$ and (b) $GdCrO_4$. Some O 1*s* core level spectra are shown in (c) for Cr^{3+} compound (Cr_2O_3), hydrous compound ($Cr(OH)_3.0.4H_2O$) and a Cr^{6+} compound (CrO_3).[Modified from Ref. 22]

The splitting of the Cr 2*p* energy level can be seen in figure 6.9 for both $YCrO_4$ and $GdCrO_4$ zircon compounds. A binding energy of 588 eV corresponds to the $2p_{1/2}$, while that of 578.45 eV matches $2p_{3/2}$.

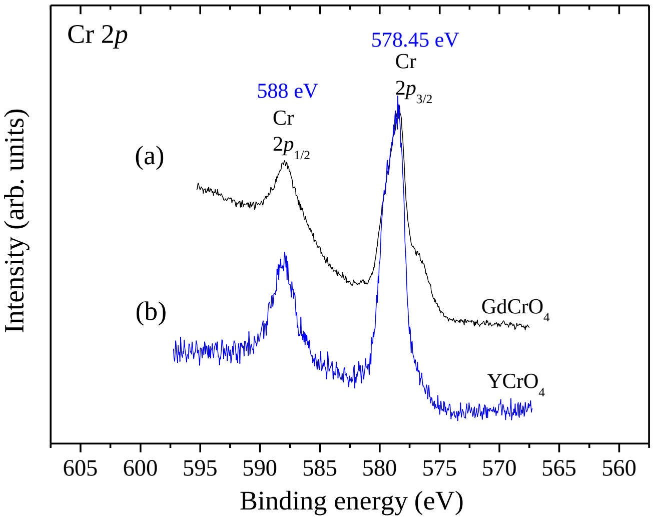

Fig 6.9 photoemission spectra of Cr 2*p* for zircon-like compounds of: (a) $GdCrO_4$ and (b) $YCrO_4$.

The valence band measured and calculated spectra of $YCrO_4$ zircon at 300 K for 36.5 hours (1050 sweeps) is shown in figure 6.10. Our spectra are in comparison with others from the literature for $LaCrO_4$ [16], which is the only previously available valence band spectrum of an *R*CrO_4 compound in the literature. Moreover, in the same figure, the valence band spectrum of $YTiO_3$ measured by Roth *et al.* [23] is shown as a comparison with another $3d^1$ system.

First observation to the valence band spectrum is its agreement in shape with that published for $LaCrO_4$ by Konno *et al.*[16] (figure 6.6). The main features of the valence band of $YCrO_4$ can be seen in figure 6.10 in a weak broad peak between about 0.625 and 2.275 eV followed by a strong broad peak between 2.85 and 8.7 eV. This effect is seen in the valance band spectrum for $LaCrO_4$ in figure 6.6. A gap of about 0.625 eV can be observed between the valence band and our measured Fermi energy (E_f), which refers to the insulating nature of these compounds. The overall spectral feature is similar to various $3d^1$ systems in the literature for (V^{4+};$3d^1$) and (Ti^{3+};$3d^1$) [1,2] where usually the weak peak is due to the 3*d* unpaired electron which is usually overlapping with the larger peak that signifies the O 2*p* band in these Ti and V oxides. Moreover, the photoionization cross section of O 2*p* is about 2 times larger than that for Cr 3*d* at photon energy of 1486.6 eV [22], so that the total contribution of the Cr 3*d* has a smaller weight in the spectra. On the other hand, both values of Δ1 and Δ2 in figure 6.10 where resolved and pronounced for the first time in comparison with the previous studies (figure 6.6).

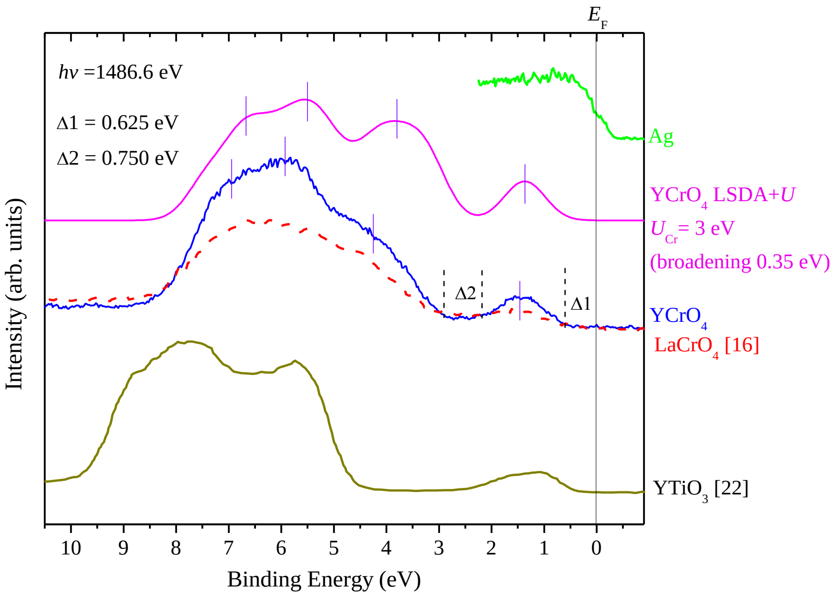

Fig. 6.10 Valence band photoelectron measured (blue) and calculated (pink) spectra at 300 K of an *in-situ* fractured $YCrO_4$ polycrystalline sintered sample taken at normal emission (blue continuous line). The light green line refers to the as measured Fermi edge of a silver foil. A comparison with $LaCrO_4$[16] (dotted red curve) and $YTiO_3$[22] $3d^1$ systems is illustrated. The spectrum of $LaCrO_4$ has been shifted 0.625 eV for comparison.

The main observation in the valence-band spectra of $YCrO_4$ is the band Δ1 that separates the valence band from the Fermi energy (E_f) and in turn, we proved experimentally that this material is an isolator.

To understand the obtained valence-band spectrum, we performed spin-polarized DFT+U calculations using the full-potential local-orbital FPLO code [23]. Here, DFT+U imply the mean-field procedure for treating strong electronic correlations in the Cr 3*d* shell, similar to the computational method of Refs. [12, 13] (Sec. 6.2). Different DFT functionals, local density approximation (LDA) [24] and generalized gradient approximation (GGA) [11] arrive at very similar results. Therefore, we will focus on the LSDA+U results only. In DFT+U calculations, we used the constant Hund's coupling J= 1 eV and varied the Coulomb-repulsion parameter U in the 2-6 eV range.

Regarding magnetic configurations, there is a tiny energy difference of about 1 meV/f.u. between the ferromagnetic and antiferromagnetic spin arrangements, in agreement with the very weak low-temperature magnetism observed experimentally for $YCrO_4$ [25]. We consider the results for the ferromagnetic spin configuration.

The energy spectra and the order of orbital states are consistent with earlier results. LDA yields the energy difference of about 80 meV between the $3z^2$-r^2 and x^2-y^2 levels. In contrast to the crystal-field picture, the $3z^2$-r^2 level is lower in energy, which should be attributed to the strong Cr-O covalency. The energy difference between the orbital states is drastically increased in LSDA+U, where the electronic configuration with the half-filled $3z^2$-r^2 orbital and empty x^2-y^2

orbital is about 350 meV/f.u lower in energy than the alternative configuration with $3z^2$-r^2 empty and x^2-y^2 half-filled. This way, electronic correlations stabilize the $3z^2$-r^2 orbital state in $YCrO_4$. Since the 'U' parameter of DFT+U is essentially an adjustable parameter, we performed calculations for different 'U' values and found the optimal value of U= 4 eV that reproduces the experimental band gap of about 1 eV.

The respective energy spectrum calculated [27] for $YCrO_4$ zircon is shown in figure 6.10. While the broad oxygen band spans the energy range between -5 eV and -1 eV, two isolated and somewhat symmetric side bands are observed. The band around -6.5 eV is dominated by Cr 3*d* states. The highest-occupied band above -1 eV is, on the contrary, of the O 2*p* origin with a sizable admixture of Cr 3*d* states. This picture is rather unusual. The single-band Hubbard model predicts the formation of the lower Hubbard band, which is separated from the upper Hubbard band by energy that is on the order of 'U'. In our case, this lower Hubbard band should be around -2 eV (note the upper band at +2 eV in figure 6.11). However, the lower Hubbard band is strongly hybridizing with O 2*p* states and eventually forms mixed Cr-O states lying below (bonding, -6.5 eV) and above (antibonding, -1 eV to 0 eV) the expected position.

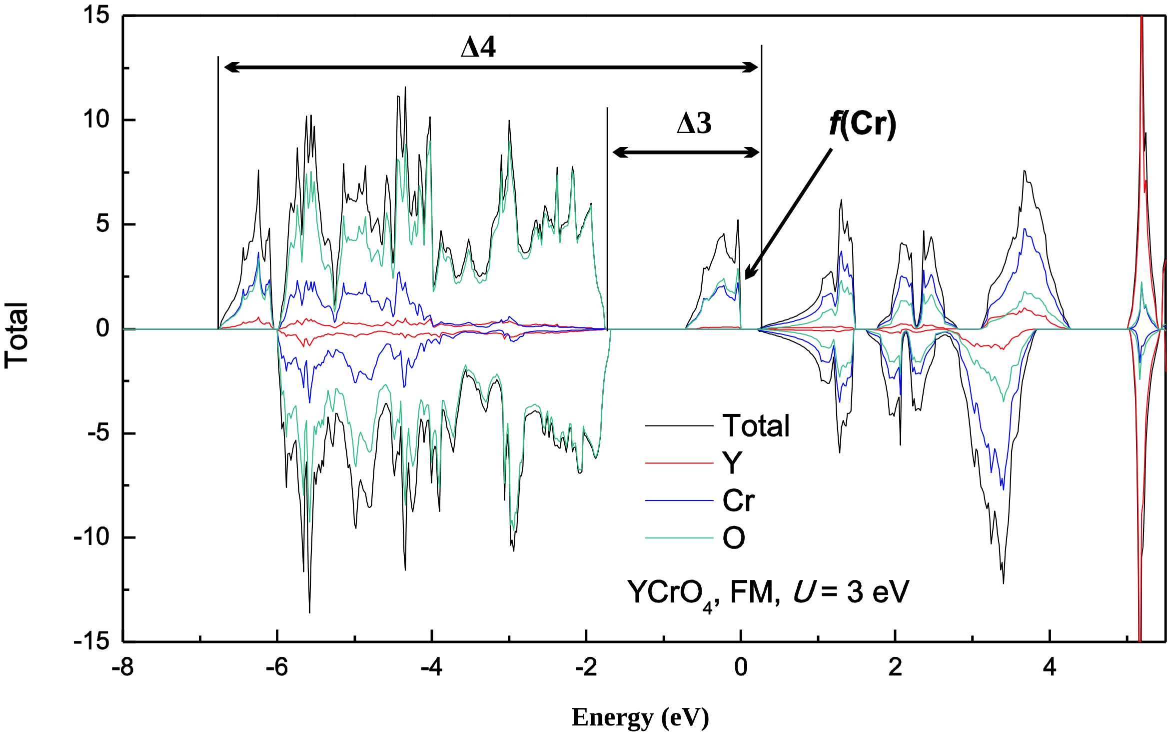

Fig. 6.11 Density of states for $YCrO_4$ Zircon [26]

The DFT+U picture is in good agreement with the experimental XPS spectra that show the isolated band of about 1 eV width right below the Fermi level. The broad band at lower energies spans the energy range of about 6 eV and likely combines the oxygen states (between -5 eV and -1 eV, i.e., 4 eV width) with the lowest-lying Cr states at about -6.5 eV. However, the direct comparison between the XPS data and DFT+U results reveals several discrepancies in the positions of the energy bands. Most importantly, in DFT+U with U=4 eV the isolated oxygen band nearly touches the bulk of the oxygen states, whereas a finite separation of Δ2=0.75 eV is seen in the experimental data (figure 6.10). This discrepancy originates from the slightly wrong position of oxygen states, which is a general and well-known shortcoming of DFT functionals. This problem can be mitigated by choosing a different U value, because the effect of Hubbard 'U' is to shift the Cr 3*d* states with respect to the oxygen 2*p* states. Indeed, we find a decent agreement between the experimental data and the energy spectrum computed at U=3 eV.

Altogether, our results put forward the formation of a localized oxygen state right below the Fermi level in $YCrO_4$. This bound state is a result of the strong Cr-O covalency and may be a fingerprint of strongly correlated Cr^{5+} oxides. Indeed, we observed a similar feature in the XPS experiment (Fig. 6.12) for $GdCrO_4$, where the valence band is dominated by the Gd 4*f* states, but the states near the Fermi level are basically the same as in $YCrO_4$.

It is noticed in figures 6.10 and 6.11 that the experimental $3d^1$peak has a higher binding energy than that reproduced by band structure calculations in the case of $YCrO_4$. Furthermore, the gap between O 2*p* and Cr 3*d* bands in the experimental results are bigger than the calculated one for $YCrO_4$. This results from the dependence of the position of this small peak on the value of U in the calculated DFT+U method. In addition, this peak highly depends on the Cr valence and disappears in the experimental data by the oxidation of Cr^{5+} to Cr^{6+}. However, the separations referred to as Δ3 and Δ4 in DFT+U curves, are always in a good agreement with the relevant experimental values. This refers to the high covalency in the Cr-O bond, which continues to exist after the transformation of the Cr-tetrahedra from $[CrO_4]^{-3}$ to $[CrO_4]^{-2}$.

Here we shall remind with some characteristics of the zircon-type structure, in which the $[CrO_4]^{3-}$ tetrahedra are well separated from each other by $[YO_8]^{13-}$ dodecahedra, so that the Cr ions are isolated from each other in the structure. The $[YO_8]^{13-}$ dodecahedra, on the contrary, are sharing edges between each other, forming well-connected chains in which Y-O-Y exchange mechanism takes place. Such chains, which separate $[CrO_4]^{3-}$ tetrahedra from each other, provide a big barrier to the transport of electrons between the Cr ions.

The valence band of $GdCrO_4$ zircon is illustrated in figure 6.12 in comparison with that of $YCrO_4$ zircon measured at the same conditions. The Cr 3*d* and O 2*p* bands look almost identical for both compounds. However, for the $GdCrO_4$ compound, the peak of Gd 4*f* core level overlaps with the valence band. It is worth noticing that $RCrO_4$ compounds tend to lose oxygen at the surface layer after extended experimental days of XPS measurement, thus creating Cr^{3+} sites. Moreover, the surface condition is very important for these compounds as well. A surface contamination with water can alter the valence band and result in the disappearance of the $3d^1$ peak (between 0.625 and

2.1 eV) due to the formation of Cr^{6+} compounds (as referred to in chapter 4) and going from a d^1 to a d^0 system.

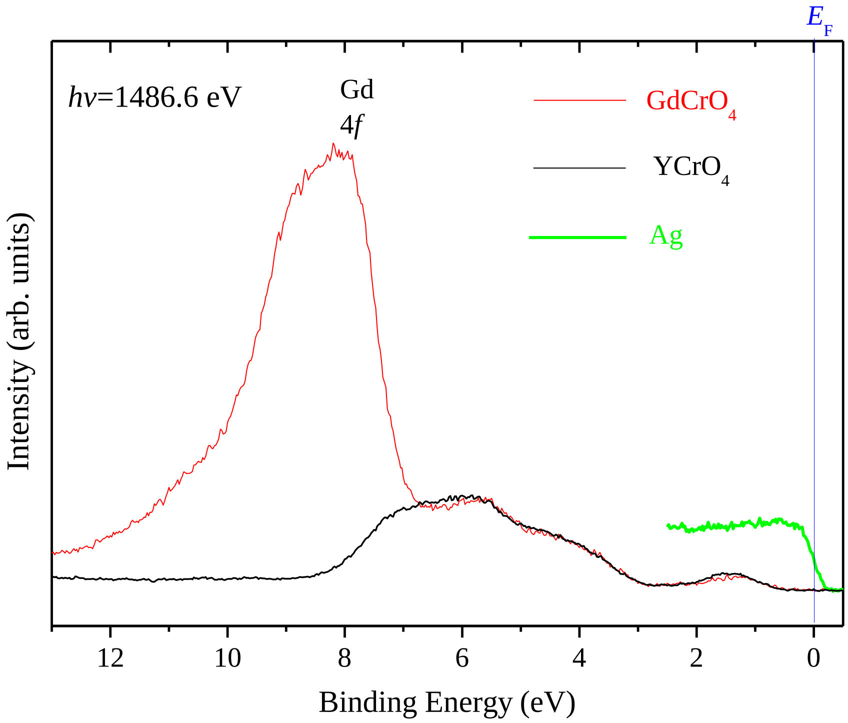

Fig. 6.12 Valence band photoemission spectra at 300 K of: $GdCrO_4$ zircon (red) $YCrO_4$ zircon (black). The green line refers to the as measured Fermi edge of a silver foil.

In general, if you calculate the band structure of $RCrO_4$ in a paramagnetic phase, then you will find that the *d*-band will struggle across the Fermi level. This has to do with the fact that the *d*-band is only partially filled and one has an odd number of electrons per unit cell (d^1). The fact that $RCrO_4$ oxides show an isolating behavior and have a reasonably large band gap, as suggested from XPS (namely at least 1 eV) indicates that electron correlation effects must play an important role.

Band structure calculation LSDA+U approach with U=3 eV can indeed produce the band gap and show an agreement with the experimental results. At first sight, we may classify $RCrO_4$ as Mott-Hubbard insulators but a closer look at the LSDA+U reveals that the states close to the Fermi level have a strongly mixed Cr 3*d* - O 2*p* character. This is related to the fact that $RCrO_4$ oxides are highly covalent.

References

[1] A. Fujimori, *Journal of Physics and Chemistry of Solids* **53**, 12, 1595 (1992)

[2] K. Maiti, D. D. Sarma, M. J. Rozenberg, I. H. Inoue, H. Makino, O. Goto, M. Pedio and R. Cimino, *Europhysics Letters* **55** (2), 246 (2001)

[3] J. A. Baglio, G. Gashurov, *Acta Crystallographica B* **24**, 292 (1968)

[4] F. E. Mabbs, D. J. Machin, Magnetism and Transition Metal Complexes, Dover Publications, New York, (2008)

[5] M. Greenblatt, J. H. Pifer, B. R. McGarvey, B. M. Wanklyn, *Journal of Chemical Physics* **74**(11), 6014 (1981)

[6] M. F. Hazenkamp, A. C. Stückl, E. Cavali, H. U. Güdel, *Inorganic Chemistry* **39**(2), 251 (2000)

[7] L. Li, W. Yu and C. Jin, *Physical Review B* **73**, 174115 (2006)

[8] P. Blaha, K. Schwarz, P. Sorantin, and S. B. Trickey, *Computer Physics Communications* **59**, 399 (1990)

[9] P. Hohenberg and W. Kohn, *Physical Review* **136**, B864 (1964)

[10] W. Kohn and L. J. Sham, *Physical Review* **140**, A1133 (1965)

[11] J. P. Perdew, K. Burke, and M. Ernzerhof, *Physical Review Letters* **77**, 3865 (1996)

[12] V. I. Anisimov, I. W. Solovyev, M. A. Korotin, M. T. Czyżyk, and G. A. Sawatzky, *Physical Review B* **48**, 16929 (1993)

[13] A. I. Liechtenstein, V. I. Anisimov, and J. Zaanen, *Physical Review B* **52**, R5467 (1995)

[14] D. Errandonea, R. Kumar, J. López-Solano, P. Rodríguez-Hernández, A. Muñoz, M. G. Rabie and R. Sáez Puche, *Physical Review B* **83**, 134109 (2011)

[15] L. Lavielle and H. Kessler, *Journal of Electron Spectroscopy and Related Phenomena* **8**, 95 (1976)

[16] H. Konno, H. Tachikawa, A. Furusaki, and R. Furuichi, *Analytical Sciences* **8**, 641 (1992)

[17] Y. Aoki, H, Konno, H. Tachikawa, and M. Inagaki, *Bulletin of the Chemical Society of Japan* **73**, 1197 (2000)

[18] Y. Aoki, H. Konno, H. Tachikawa and M. Inagaki, *Bulletin of the Chemical Society of Japan* **73**, 1197 (2000)

[19] Y. Aoki and H. Konno, *Journal of Solid State Chemistry* **156**, 370 (2001)

[20] H. Kashiwagi, T. Takada, E. Miyoshi, S. Obara and F. Sasaki, *ab-initio RHF calculation program*, JAMOL4 (1988)

[21] C. C. J. Roothan, *Reviews of Modern Physics* **32**, 179 (1960)

[22] H. Roth, doctoral thesis, Universität zu Köln (2008),
http://kups.ub.uni-koeln.de/2335/ (November 2012)

[23] J. J. Yeh and I. Lindau, *Atomic Data and Nuclear Data Tables* **32**, 1 (1985)

[24] K. Koepernik and H. Eschrig, *Physical Review B* **59**, 1743 (1999)

[25] J. P. Perdew and Y. Wang, *Physical Review B* **45**, 13244 (1992)

[26] Y. W. Long, L. X. Yang, Y. Yu, F. Y. Li, R. C. Yu and C. Q. Jin, *Physical Review B* **75**, 104402 (2007)

[27] Alexander Tsirlin (personal communication)

7. Soft X-ray Absorption of *R*CrO$_4$ oxides

The Cr^{5+} ion represents an example for a unique electron spin of (S = ½) that occupies the [Ar] $4s^2 3d^1$ orbital. It exists in the tetragonal zircon-type structure of $RCrO_4$ oxides in a distorted tetrahedra environment with a D_{2d} local point group symmetry while upon pressure-induced transition, it becomes a D_{4h} point group symmetry. However, the Cr-O distances do not change and only a small change in the O-Cr-O angles occurs (see chapter 3). The energy level diagram of the Cr^{5+} ion in the zircon structure was previously discussed in figure 6.1. To study the electronic structure of the $RCrO_4$ and to confirm Cr^{5+} state, we have performed a soft x-ray absorption spectroscopy (XAS) study at the Cr-$L_{2,3}$ edge and the O-K edge.

7.1 XAS of Zircon-type *R*CrO$_4$ and the proof of Cr^{5+}

The Excitations of the 2*p* subshell in $RCrO_4$ zircons have been studied using soft XAS at the NSRRC synchrotron facility in Taiwan. Figure 7.1(a) depicts the isotropic Cr-$L_{2,3}$ XAS spectrum of zircon-type $ErCrO_4$ at 300 K, which arise from dipole transitions to unoccupied *d* states. The Cr-2*p* core-hole spin-orbit coupling splits the spectrum roughly in two parts, namely the L_3 (at 580 eV) and L_2 (at 589 eV). To analyse the Cr-$L_{2,3}$ spectrum, we have performed theoretical simulations based on the full-multiplet cluster method using the XTLS 8.3 code [1, 2] and taking into account the local environment of the Cr^{5+} ions. Electron-Electron Coulomb repulsion parameters has been used as U_{3d3d}=4.5 eV[3], U_{3d2p}=6.1 eV[3], while the charge transfer energy parameter (from oxygen ligand to Cr 3*d*) was used as Δ=2.5 eV[3].

Figure 7.1(a) compares between the measured Cr-$L_{2,3}$ XAS spectra and the calculated $L_{2,3}$ edge for a Cr^{5+} ion in a tetrahedral symmetry. This comparison shows that the simulation fairly agrees with the experimental spectrum. We also represent in figure 7.1(b) the measured and calculated Cr $L_{2,3}$ electron-loss spectrum studied recently by Radtke *et al.*[4] for the $Sr_3Cr_2O_8$ compound, *i.e.* $Sr_3(CrO_4)_2$, which also contains Cr^{5+} state. It can be seen in figure 7.1 that our results are in accordance with those of the $Sr_3Cr_2O_8$ compound. The $RCrO_4$ zircon crystallizes at room temperature in a tetragonal structure and with D_{2d} point group symmetry for the Cr site; while the $Sr_3Cr_2O_8$ compound has rhombohedral structure at room temperature with C_{3v} point group symmetry for the Cr site. Nevertheless, in both compounds, the Cr^{5+} conserves its tetrahedral coordination and shows similar spectra for the Cr-$L_{2,3}$ edge which is in agreement with the multiplet cluster calculation. However, a shift of about 8 eV occur between the spectra in figures 7.1(a) and (b) for the $L_{2,3}$ edge energies due to the difference in the experimental technique (different references for energy calibration). Nevertheless, Radtke *et al.* [4] did not mention the calibration reference for neither Cr-$L_{2,3}$ edge nor O-K edge.

The energy of each *R*CrO$_4$ spectrum was calibrated using a (simultaneously recorded) reference Cr$_2$O$_3$ spectrum identifying the Cr-$L_{2,3}$ peak of Cr$_2$O$_3$ to be at 577.1±1.1 eV [5]. The Total Electron Yield (TEY) was divided by 10 (the intensity of the incoming beam). Then a (constant) pre-edge background was subtracted.

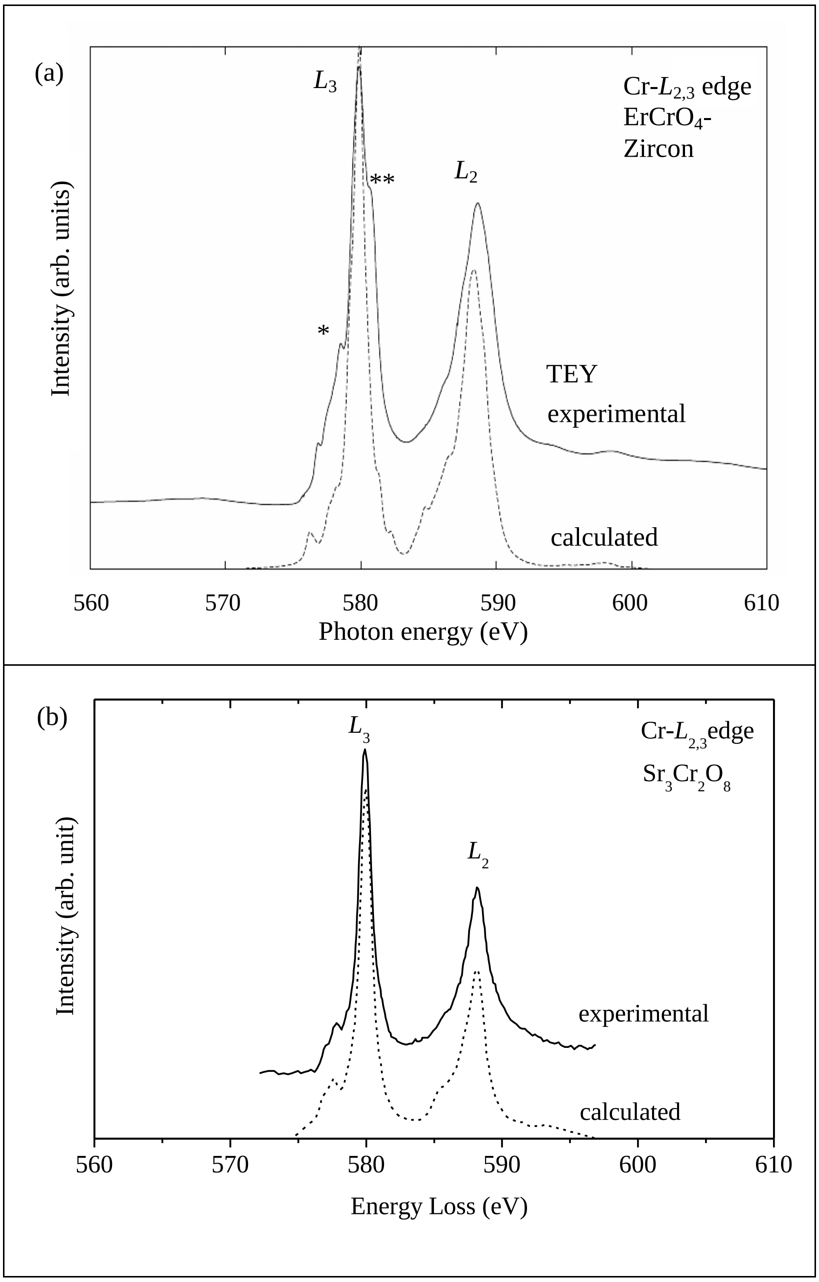

Fig. 7.1 (a) Experimental (solid line) and calculated (dashed line) Cr-$L_{2,3}$ XAS spectrum for ErCr^{5+}O$_4$ zircon. The features * and ** refer to Cr^{3+} and Cr^{6+} shoulders respectively resulting from secondary phases at the sample surface. (b) Cr-$L_{2,3}$ energy-loss spectrum of Sr$_3$Cr$_2$O$_8$ as measured (solid line) and calculated (dashed line) by Radtke *et al.* [4] after shifting the energies -8 eV in the *x*-direction.

Due to the element and charge sensitivities of the XAS method, it is very effective in probing various valence states of the Cr ion. In comparison between the calculated and experimentally measured spectra of ErCrO$_4$ zircon compound, figure 7.1(a), the main peak at about

580 eV corresponds to the Cr^{5+} cation. However, due to the charge sensitivity of the XAS measurement, a small contamination of Cr^{3+} and Cr^{6+} sites at the surface can be seen by the shoulders at slightly lower and slightly higher energies as indicated in figure 7.1(a). Such small amounts can be very difficult to identify by x-ray and neutron powder diffraction techniques, but can be noticed in the XAS spectra.

We have also carried out the soft x-ray absorption in total electron yield (TEY) mode for a wide range of $R\mathrm{CrO}_4$ polycrystalline sintered compounds together with Cr_2O_3 single crystal as a Cr^{3+} reference. These results can be seen in figure 7.2, where a demonstration of the consistent behavior of all samples independent of the rare-earth can be seen. The very similar spectral features for all rare-earth ions can be also found in the O-*K* edge XAS spectra of $R\mathrm{CrO}_4$ in figure 7.2. For all $R\mathrm{CrO}_4$ samples, the energy of each spectrum was calibrated using a NiO spectrum (simultaneously recorded), which was in turn compared with a Cr_2O_3 spectrum taken under the same conditions. The NiO spectrum was calibrated by comparing it to the relevant electron energy loss spectrum done by Mitterbauer *et al.* [6].

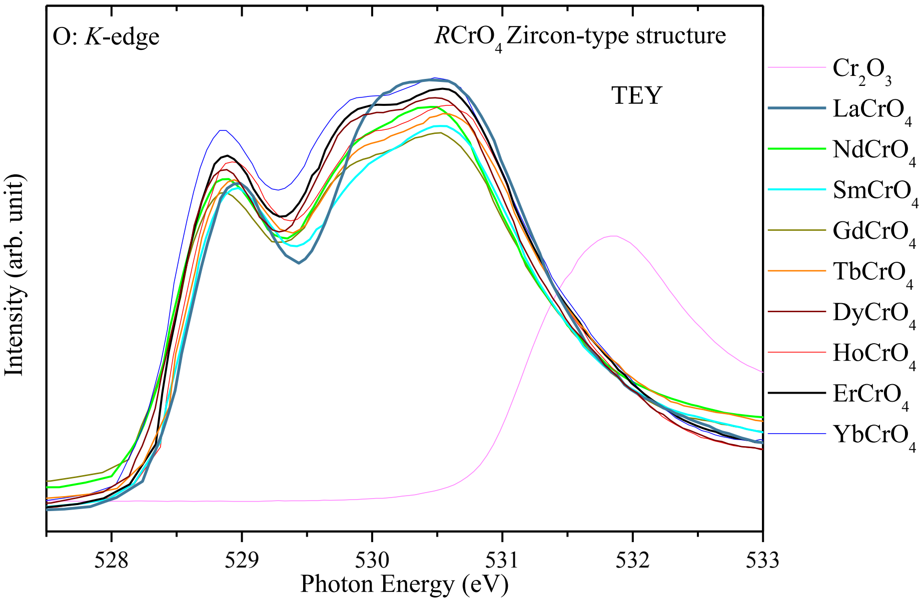

Fig. 7.2 The O-*K* XAS spectra of $R\mathrm{CrO}_4$ (*R* = rare earth) and of Cr_2O_3 single crystal.

The peak at 528.7 eV is assigned to a transition from an O 1*s* core electron to an O 2*p* state hybridized with Cr 3*d*–*e* orbitals, while the broad peak above 529.5 eV is related to a mixture between O 2*p* and Cr 3*d*-t_2 orbitals, as well as *R* 5*d* states. An exception is the $LaCrO_4$, whose O-*K* edge shows a slightly different behavior. $LaCrO_4$ O-*K* spectrum shows a spectral weight transfer from below to above 530 eV. This is because the $LaCrO_4$ has a monoclinic monazite-structure, which is different from the tetragonal zircon-structure of the rest of the $R\mathrm{CrO}_4$ compounds. In the monazite-like structure, the rare earth element is coordinated with nine oxygen atoms in an $R\mathrm{O}_9$ polyhedron, while in the zircon-like structure a dodecahedron of $R\mathrm{O}_8$ is the case.

Such a structure difference alters the *R*-O hybridization as seen on the O-*K* edge of $LaCrO_4$ in figure 7.2. Though, this monazite structure still shows a clear Cr^{5+} main peak of the $L_{2,3}$ edge which is similar to that of other $RCrO_4$ zircon compounds (figure 7.3).

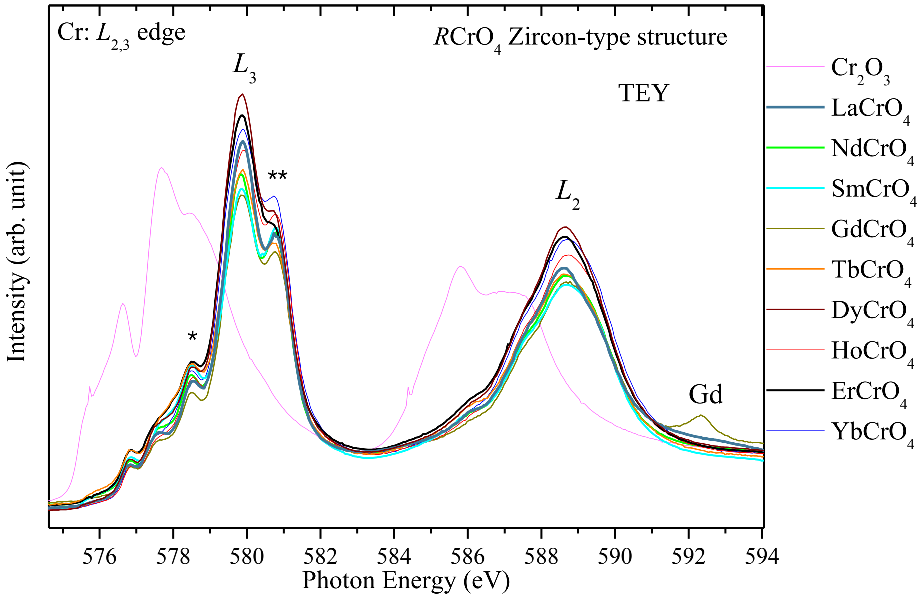

Fig. 7.3 The Cr-$L_{2,3}$ XAS spectra of $RCrO_4$ (R = rare earth) compared with the spectrum of Cr_2O_3 single crystal. The features * and ** refer to the Cr^{3+} and Cr^{6+} shoulders respectively.

It is worth noting that, in the zircon compounds, the amount of interstitial positions in the crystal structure makes it very easy for the material to absorb water molecules, either during the preparation from hydrous nitrates or after preparation by absorbing humidity at the surface from the atmosphere. This can allow the formation of an amorphous secondary phase at the surface that corresponds to the hydroxy chromate, $R(OH)CrO_4$, as discussed in chapter 4. Therefore, it is important for these compounds to be treated and stored after preparation either in vacuum or inert atmospheres.

In order to investigate if the TEY spectra, which are bulk representative, the XAS spectra of the oxygen *K*-edge for four zircon samples were investigated by summing several spectra of the bulk sensitive fluorescence yield mode (FY) measured at the same conditions. All samples were measured after fracturing them *in situ* in the XAS chamber. A probing depth of 2-6 nm coexists with the TEY mode, and therefore, only few atomic layers near the surface are probed. In FY, more than 100 nm in depth is investigated and, therefore, the bulk properties of the samples are probed. The FY can thus be used to validate the bulk sensitivity of the TEY mode. From comparing O-*K* edge obtained in both FY and TEY modes in figure 7.4, we can conclude that the spectra collected in TEY mode are reproduced by the FY mode. The figure also shows that the TEY collected spectra for Cr-$L_{2,3}$ represents enough bulk signal as compared to the FY spectra.

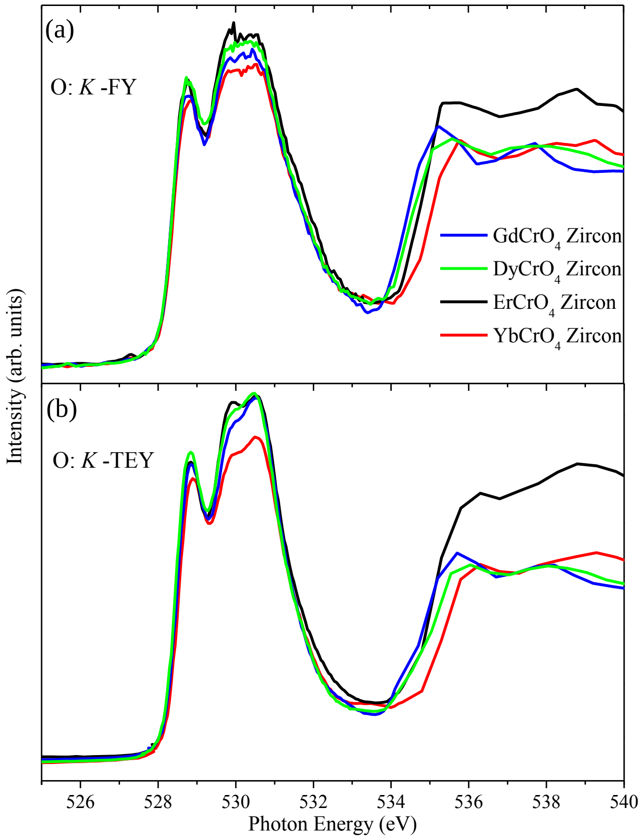

Fig. 7.4 Soft x-ray absorption spectra for *R*CrO$_4$-zircon compounds (*R*= Gd, Dy, Er and Yb). (a) Florescence yield (FY) for the O *K*-edge. (b) Total electron yield (TEY) for the O *K*-edge. Both (a) and (b) has the same x-axis scale.

It is worth noticing that all samples showed higher amount of Cr^{6+} impurities at the surface before fracturing it in vacuum inside the XAS chamber. This refers to the effects of adsorbing the humidity of the atmosphere at the surface, whereas the deep inside of the sintered pellet remains unaffected.

7.2 XAS of Scheelite-Type *R*CrO$_4$

Similar measurements of O *K*-edge in TEY and FY modes in addition to Cr $L_{2,3}$ edge in TEY mode have been carried out for the scheelite high-pressure polymorph of the same compositions discussed in the previous section, *R*CrO$_4$ (*R*= Gd, Dy, Er, Yb). The results of this study can be seen in figure 7.5. All the samples have shown a slightly large Cr^{6+} secondary phase in the scheelite phase as compared to the zircon phase, figure 7.5(c). EELS spectra at the Cr-$L_{2,3}$ edge of Cr^{5+} and Cr^{6+} compounds measured by Daulton and Little [7] are shown in figure 7.6, where one can see that the main peak in Cr^{6+} spectrum is shifted by more than one eV to a higher photon energy with respect to the Cr^{5+} spectrum.

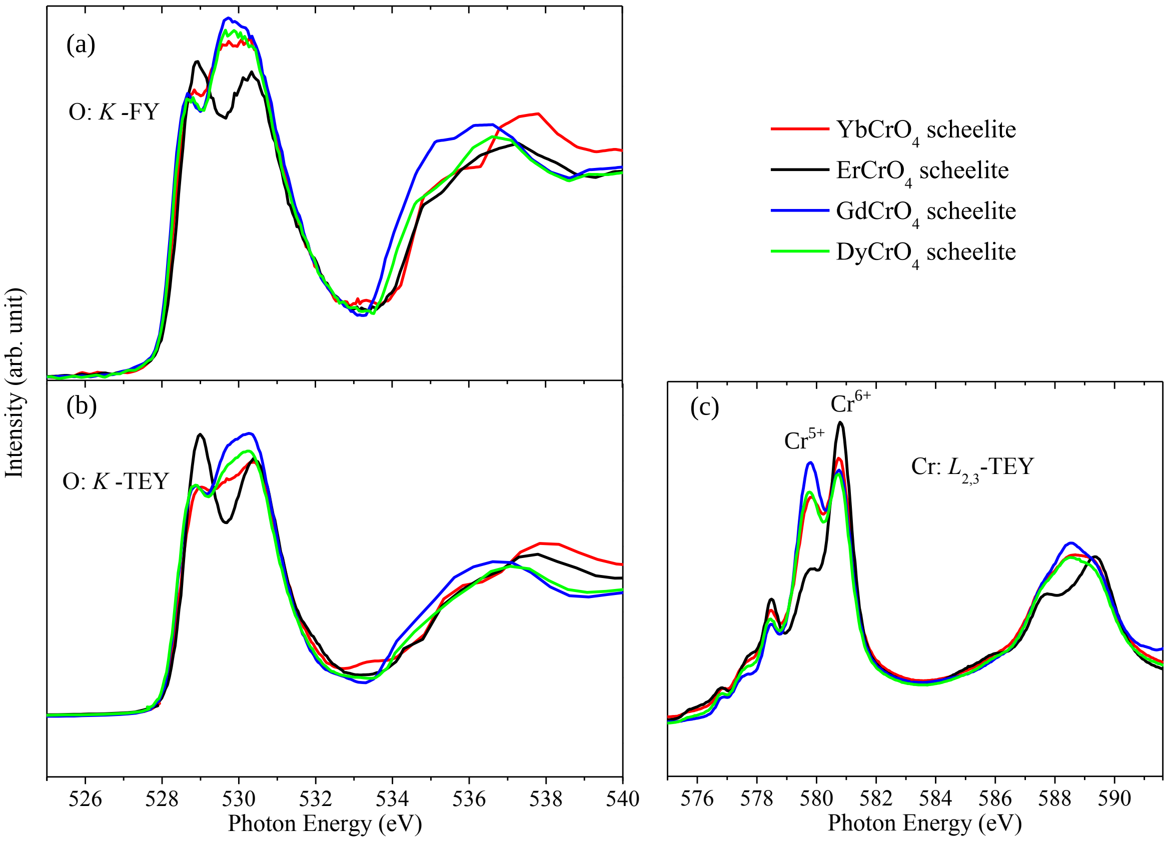

Fig. 7.5 Soft x-ray absorption spectra for *R*CrO_4 -scheelite compounds (*R*= Gd, Dy, Er and Yb). (a) Florescence yield (FY) spectra for the O *K*-edge. (b) Total electron yield (TEY) spectra for the O *K*-edge. (c) TEY spectra for Cr $L_{2,3}$ edge. Both (a) and (b) has the same x-axis scale.

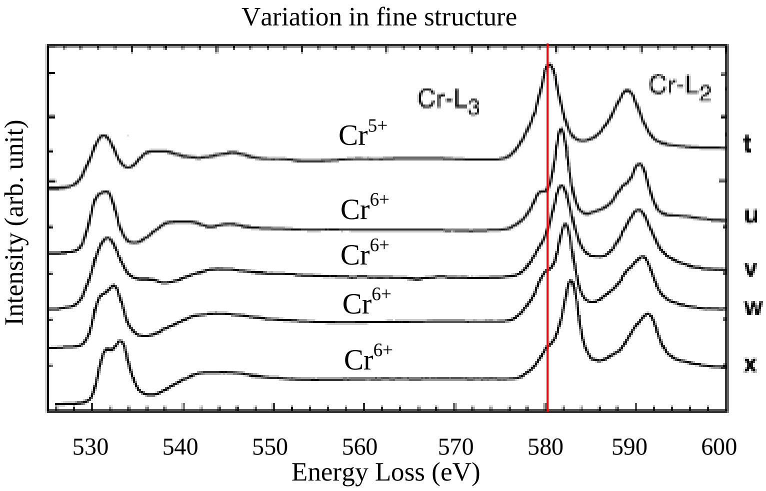

Fig. 7.6 Electron energy loss spectra taken from Daulton and Little [7] for: (t) $NdCr^{5+}O_4$, (u) $K_2Cr^{6+}O_4$, (v) $PbCr^{6+}O_4$, (w) $Na_2Cr^{6+}O_4$, and (x) $K_2Cr^{6+}{}_2O_7$. The vertical line shows the L_3 peak of Cr^{5+} in comparison with other compounds.

As discussed in chapter 4, the interstitial positions play an important role in the interpretation of the differences between the zircon and scheelite samples. The zircon has a quite open structure, in which open channels of interstitial tetrahedral positions are in the c-direction of the lattice, while other octahedral voids take place between the polyhedra. These empty interstitials are very attractive to impurities, especially at the sample surface. Upon adsorption of water molecules at the surface, OH molecules can alter the charge balance in some parts of the crystal and represent a few amount of Cr^{6+} in the sample, producing the $R(OH)CrO_4$ hydroxy chromate, which leads to the large spectral weight at 581 eV at the Cr-L_3 edge and 589 eV at the L_2 edge. The oxygen-depleted part of the crystal separates therefore as $RCrO_3$ (Cr^{3+}) presenting the high spectral weight at 578 eV at the Cr-L_3 edge. Both secondary phases were confirmed by powder diffraction (see chapter 4). Figure 7.7 shows the proof of the Cr^{6+} in the over-oxidized sample of $ErCrO_4$ scheelite. It can be seen that an increase of the Cr^{6+} amount is accompanied with an increase in the Cr^{3+} as well.

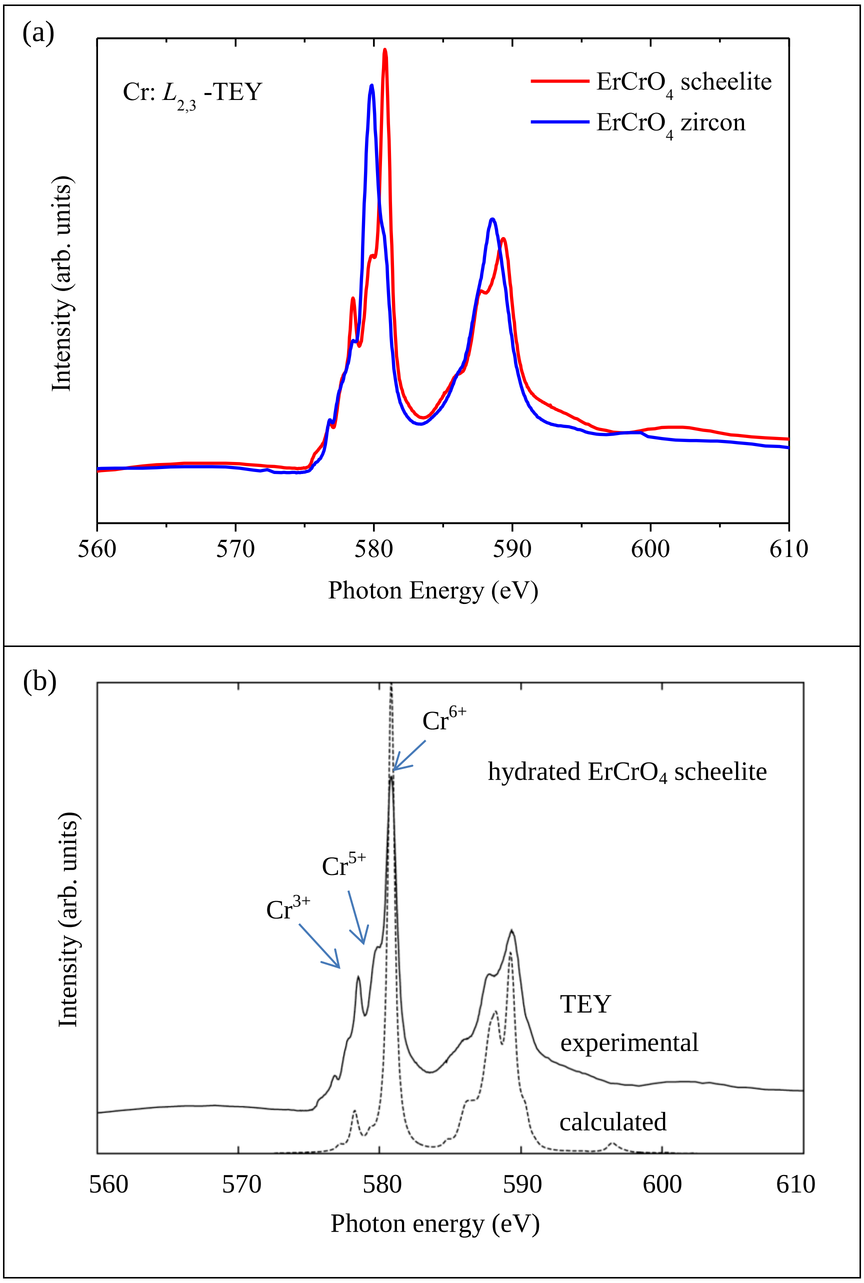

Fig. 7.7 (a) Cr-$L_{2,3}$ edge for two different $ErCrO_4$ zircon and scheelite samples as viewed experimentally by x-ray absorption. (b) experimental (solid line) Cr-$L_{2,3}$ XAS for overoxidized $ErCrO_4$ scheelite sample compared with theoretical spectrum (dashed line) of Cr^{6+} ion in a tetrahedral environment calculated by full-multiplet cluster calculations[1, 2].

The amount of Cr^{6+} secondary phase was reduced in the case of the zircon compounds by sintering them at about 800 K, which cannot be done to the scheelite samples which transform back to the zircon phase at about 700 K. This is assisted by the fact that $R(OH)CrO_4$ compounds decompose to $RCrO_4$, H_2O and O_2 in the range between 750 and 850 K [8-11]. A further heating to around 873 K will result in the decomposition into $RCrO_3$ and O_2. However, the formation of Cr^{3+} in the sample is not possible to reverse to Cr^{5+} due to the stable perovskite structure of $RCrO_3$ oxides. Therefore, the existence of Cr^{6+} and Cr^{3+} entities at the surface of the scheelite phase is inevitable in most of the cases, but can be avoided in the zircon phase by careful temperature control during the synthesis.

The fact that $RCr^{5+}O_4$ compounds transform into $R(OH)Cr^{6+}O_4$ in hydrous atmosphere between 300-673 K and then decompose to $RCr^{5+}O_4$ between 750-850 K refers to the potential application of these materials in the field of catalysis. This has been suggested in 2006 by Orlovskaya *et al.*[12] and very recently Xing *et al.*[13] found that the Cr^{6+} (CrO3) and Cr^{5+} ($YCrO_4$) species were easy to fluorinate, and generated CrO_2F_2 or/and $CrOF_3$, while the Cr^{3+} (Cr_2O_3) species were difficult to fluorinate. Some earlier research groups, as Hoang *et al.* [14], investigated the catalysis and Redox reactions in La-Cr system, in which $LaCrO_4$ is one of the formed compounds. $RCrO_4$ compounds were also suggested to be used for separation membranes and solid oxide fuel cell (SOFC) components.[12]

References

[1] A. Tanaka and T. Jo, *Journal of the Physical Society of Japan* **63**, 2788 (1994)

[2] N. Hollmann (personal communication)

[3] M. W. Haverkort, Z. Hu, A. Tanaka, W. Reichelt, S. V. Streltsov, M. A. Korotin, V. I. Anisimov, H. H. Hsieh, H.-J. Lin, C. T. Chen, D. I. Khomskii and L. H. Tjeng, *Physical Review Letters* **95**, 196404 (2005)

[4] G. Radtke, A. Saúl, H. A. Dabkowska, G. M. Luke and G. A. Botton, *Physical Review Letters* **105**, 036401 (2010)

[5] R. D. Leapman, L. A. Grunes, P. L. Fejes, *Physical Review B* **26**, 614 (1982)

[6] C. Mitterbauer, G. Kothleitner, W. Grogger, H. Zandbergen, B. Freitag, P. Tiemeijer and F. Hofer, *Ultramicroscopy* **96**, 469 (2003)

[7] T. L. Daulton and B. J. Little, *Ultramicroscopy* **106**, 561 (2006)

[8] I. Bueno, C. Parada, A. Monge and C. Ruiz Valero, *Journal of Solid State Chemistry* **90**, 263 (1991)

[9] I. Bueno, C. Parada, E. Gutiérrey Puebla, A. Monge and C. Ruiz Valero, *Journal of Solid State Chemistry* **78**, 78 (1989)

[10] I. Bueno, C. Parada, *Thermochimica Acta* **235**, 205 (1994)

[11] I. Bueno, C. Parada, R. Sáez Puche, E. J. Baran, *Journal of Alloys and Compounds* **225**, 237 (1995)

[12] N. Orlovskaya, A. Coratolo, M. Lugovy, C. Johnson and R. Gemmen, *Thin Solid Films* **515** (4), 1741 (2006)

[13] L. Xing, Q. Bi, Y. Wang, M. Guo, J. Lu and M. Luo, *Journal of Raman Spectroscopy* **42** (5), 1095 (2011)

[14] D. L. Hoang, A. Dittmar, J. Radnik, K.-W. Brzezinka and K. Witke, *Applied Catalysis A: General* **239**, 95 (2003)

8. Summary and Conclusions

The RCrO$_4$ oxides, where R is a rare earth, form a large family of compounds, which crystallize at ambient conditions in two different structural types. LaCrO$_4$ oxide crystallizes as a monoclinic monazite-type structure (space group $P2_1/n$); while the remaining RCrO$_4$ oxides (R= Nd-Lu and Y) crystallizes in the tetragonal zircon-type structure (space group $I4_1/amd$). PrCrO$_4$ crystallizes as a dimorphic compound of a mixture of both monazite-type and zircon-type structures, while CeCrO$_4$ is yet not possible to be synthesized. RCrO$_4$ zircon structures can be obtained at ambient pressure at 873 K under oxygen flow and they have been used in this work as precursors to prepare the high-pressure polymorph of the tetragonal scheelite-type RCrO$_4$ (space group $I4_1/a$). When these precursors were pressed under 4 GPa and heated isobarically up to 808-833 K, the new series of scheelite phases were obtained.

The zircon-type structure of RCrO$_4$ contains isolated (CrO$_4$) distorted tetrahedra that surround the R atom to form an (RO$_8$) bisdisphenoids (triangular dodecahedra). The main structural units in this structure are chains of (CrO$_4$) and (RO$_8$) polyhedra, which are parallel to the *c*-axis and alternating by an edge sharing. A first order reconstructive model has been proposed to explain the pressure-induced zircon-to-scheelite transition by taking into consideration a bond switching mechanism.

The scheelite samples behave as antiferromagnets, showing Néel temperatures relatively high in comparison with the isostructural RXO$_4$ (X= P, As, and V), in which the X element is diamagnetic and consequently only the R^{3+} sublattice is involved in the magnetic order. The T_N for these latter RXO$_4$ scheelites takes a value lower than 2 K, due to the inner character of the *f*-orbitals involved in the magnetic interactions. However, in the case of the RCrO$_4$, the paramagnetic character of the Cr^{5+} ($3d^1$) explains the higher values of T_N found for these chromium scheelites, where the Cr^{5+} ion appears to play an important role as a promoter of the superexchange interactions of the type Cr-O-R in these compounds.

On the other hand, the ferromagnetic character that is observed in most of the zircon phases contrast with the antiferromagnetism we found in the high-pressure polymorphs RCrO$_4$-scheelites. We explained these opposing behaviors by considering the change in the R-O-Cr angle in both structures. Taking into account these results, these two families of RCrO$_4$ oxides constitute an ideal scenario for studying the structure-magnetic properties relationships, which are of a great importance in the solid-state chemistry.

The crystal structure of different samples has been fully characterized by x-ray and high-resolution neutron powder diffraction studies. The neutron diffraction studies were done at different European neutron facilities: ISIS (UK), LLB (France) and ILL (France). The magnetic properties of the samples have been studied by magnetization, magnetic susceptibility and specific heat measurements.

In addition, we have also studied in this work the electronic structure of *R*CrO$_4$ compounds by comparing our x-ray photoelectron spectroscopy (XPS) data to the results of band-structure calculations. Such a comparison of both experimental and calculated data has been carried in this work for the first time. In addition, we performed *K*-edge and *L*-edge soft x-ray absorption spectroscopy (XAS) for the first time for both zircon and scheelite polymorphs. XPS has been done only for YCrO$_4$ and GdCrO$_4$ zircons. Nevertheless, XAS has been measured for eight *R*CrO$_4$ scheelites, ten *R*CrO$_4$ zircons, one LaCrO$_4$ monazite and one GdCrO$_3$ perovskite.

The main conclusions from this research work are:

- The *R*CrO$_4$-scheelite polymorphs, where *R*= Nd-Lu, have been synthesized under high pressure and high temperature conditions using the *R*CrO$_4$–zircon phases as precursors which have the tetragonal structure with the space group $I4_1/amd$ (D_{4h}^{19}, No. 141, Z=4). Nine compounds of the twelve *R*CrO$_4$ scheelites have been prepared for the first time in this work.
- The crystal structure of the *R*CrO$_4$ scheelites has been fully characterized by x-ray and neutron powder-diffraction data using the Rietveld structural refining method. All the compounds crystallize in the tetragonal scheelite-type structure with space group of $I4_1/a$ (C_{4h}^{6}, No. 88, Z=4). The dependence of the lattice parameters on the R^{3+} ionic radii has been studied for the *R*CrO$_4$ family.
- Two structural relationships between the zircon and scheelite structures have been verified:
  - $(c/a)_{zircon} \approx 2(a/c)_{scheelite}$
  - $a_{scheelite} \approx a_{zircon}/\sqrt{2}$

  A small deviation in these relationships is due to small atomic displacements that occur after the displacive step and are responsible for the rearrangement of Cr- and *R*-polyhedra and the efficient packing in the scheelite structure.
- Upon the transition, one quarter of the *R*-O bonds are broken in the zircon structure (contributing to the edge sharing between the Cr- and *R*-polyhedra) and two extra *R*-O bonds are formed in the scheelite structure (sharing corner with two new *R*-dodecahedra). Although the coordination numbers of 8 and 4 remain the same along the transition for R^{3+} and Cr^{5+} cations respectively, an increase of about 10% in density is observed in going from the zircon-type to the more compact scheelite-type structure. Therefore, the transition from zircon to scheelite is believed to be of a first order.

- The first-neighbor interatomic-distances remain almost unchanged in the zircon-to-scheelite transition; *i.e.* *R*-O, Cr-O and O-O distances. The main change between the two structures can be observed in the interatomic angles; *i.e.* *R*-O-Cr, O-*R*-O and O-Cr-O. Of these angles, the change in the *R*-O-Cr angle upon the transition is the most profound and the most important. One of the *R*-O-Cr angles changes from an average value of 97.4° (in zircon) to about 122° (in scheelite). The other *R*-O-Cr angle decreases from about 152° (in zircon) to about 133 ° (in scheelite).
- We have also calculated the interatomic distances for the second-neighboring atoms; *i.e.* the distance between Cr--Cr, *R*--*R* and Cr--*R*. The zircon-to-scheelite transition leads to a change in the coordination of Cr-tetrahedra around the *R*-dodecahedra and vice versa. In the zircon-structure, the Cr-tetrahedron is surrounded by 6 *R*-dodecahedra; while in the scheelite-structure it is surrounded by 8 *R*-dodecahedra. In addition, the Cr--Cr, *R*--*R*, and two thirds of Cr--*R* distances are smaller in the scheelite (by 0.1 Å), while one third of the Cr--*R* distances becomes longer (by 0.4 Å) after the transition and is doubled in number.
- Four Cr--Cr distances are connected through the Cr-O-O-Cr interactions, while four *R*--*R* distances are represented through *R*-O-*R* interactions. Both Cr--Cr and *R*--*R* distances are equal to each other for a specific zircon or scheelite compound.

- We have also studied the thermal stability of $R\mathrm{CrO}_4$-scheelites by *in-situ* XRD and we have proven for the first time for these compounds that the high-pressure scheelite polymorph reversely transforms to the zircon parent phase upon heating between 723 and 823 K (the final required temperature depends on the rare-earth cation).

- A comparison between the scheelite and zircon polymorphs has been also reviewed by applying the Bond Valence Method to the refined lattice parameters and atomic positions in order to investigate the phase stability of these two polymorphs. $R\mathrm{CrO}_4$-zircons represent a minimum stable value of the global instability index (GII ≅ 0.2) which refers to the stability of the zircon structure for all $R\mathrm{CrO}_4$ compounds. Furthermore, the zircon structure can incorporate the impurity and/or doping atoms without a noticeable change in its interatomic distances due to the availability of various interstitial positions. On the other hand the GII for $R\mathrm{CrO}_4$-scheelites show a parabolic curve with a minimum of GII≅0.1 in the middle of the series (intermediate R^{3+} radii) and a maxima of GII≅0.4 and 0.7 at the sides of the series (small and big R^{3+} radii). This refers to the instability of the scheelite compounds in comparison with the zircon ones.

- Magnetic susceptibility, specific heat and neutron diffraction measurements in a wide temperature range reveal that all the $R\mathrm{CrO}_4$-scheelite phases behave as antiferromagnets. This behavior has been fully explained by considering the *R*-O-Cr superexchange pathways through the interactions taking place between both R^{3+} and Cr^{5+} sublattices. The role of the paramagnetic Cr^{5+} as a promoter of the interactions on the R^{3+} sublattice has been considered in order to explain the higher Néel temperatures found for $RCrO_4$-scheelites in comparison with the isostructural RXO_4 (X = As, P and V). The diamagnetic character of these X elements strongly diminishes the exchange integral, since the only involved magnetic interactions are those between the R^{3+} sublattices through *R*-O-*R* pathways.

- The comparison between the magnetic properties of the zircon and scheelite polymorphs reveals that the zircon phases behave as ferromagnetic, while all of the scheelite phases are antiferromagnetic. This different magnetic behavior has been explained by considering the differences found in the bond angles and distances within the superechange pathways promoting the magnetic interactions.
- Most of these scheelite compounds show field induced magnetic transitions, “metamagnetic transitions”, with critical magnetic fields depending on the anisotropy of the rare earth element.
- The magnetic structure for the different members of this family of $RCrO_4$-scheelite compounds has been described at 2 K with a propagation vector of k=(000). For instance, in the case of the $TbCrO_4$ compound the Cr and Tb moments are aligned along the *c*-axis in the tetragonal scheelite structure, while in the case of the isostructural $RCrO_4$ (R=Gd, Dy, Tm and Er) the corresponding moments lie in the *ab*-plane of the structure. These different magnetic structures appear to be related with the Stevens coefficient α_J, which takes positive or negative values depending on the anisotropy of the rare earth element. Thus, we conclude that the crystal electric field (CEF) anisotropy of the rare earth ion determines the moment orientation in the magnetically ordered state of $RCrO_4$ compounds.
- X-ray Photoelectron spectra of the zircon structure of $YCrO_4$ and $GdCrO_4$ demonstrated the purity of the samples, no characteristic peak was observed for carbon, referring to no absorption of CO_2 in any of the samples. Furthermore, the measured valence band spectra of the compounds have been compared with results of DFT+U calculations.
- If the band structure of $RCrO_4$ is calculated in a paramagnetic phase, then it will be found that the *d*-band will struggle across the Fermi level. This has to do with the fact that the *d*-band is only partially filled with an odd number of electrons per unit cell (d^1). The fact that $RCrO_4$ oxides show an isolating behavior and have a reasonably large band gap, as suggested from XPS (namely at least 1 eV) indicates that electron correlation effects must play an important role.
- Band structure calculation LSDA+U approach (with U=3 eV) can reproduce the experimental band gap. At the first sight, we may classify $RCrO_4$ as Mott-Hubbard insulators but a closer look at the LSDA+U reveals that the states close to the Fermi level

have a strongly mixed Cr 3*d* - O 2*p* character. This is related to the fact that *R*CrO_4 oxides are highly covalent.

- Soft XAS spectra have been measured for *R*CrO_4 zircon, monazite and scheelite structures. After comparison with the theoretical simulations based on the full-multiplet cluster method, we confirmed that these compounds contain Cr^{5+} ions. Furthermore, we demonstrated that upon hydration of the surface by moisture, the surface of the samples transforms to Cr^{6+} due to the formation of the hydroxyl chromates *R*(OH)CrO_4. This has been confirmed by synchrotron radiation powder diffraction and by high resolution XRD for a sample prepared in the favorable conditions for hydroxyl chromates. Therefore, *R*CrO_4 compounds should be always stored either in vacuum or in inert atmospheres.

9. Resumen

Los óxidos de fórmula general RXO_4, donde R es una tierra rara y X=P, As, V y Cr , forman una gran familia de compuestos que cristalizan con el tipo estructural zircón presentando simetría tetragonal, G.E. $I4_1/amd$ o el polimorfo tipo monacita con simetría monoclínica, G.E. $P2_1/n$. La estabilidad de estos dos polimorfos depende de la relación de radios R^{3+}/O^{--} y X/O^{--}, de tal manera que la fase monacita se encuentra favorecida en los casos de la tierras raras de mayor tamaño; mientra que para las tierras raras de mayor número atómico la fase estable en condiciones normales es la tipo zircón. Los compuestos RXO_4 localizados en la frontera entre estos dos polimorfos, presentan el fenómeno de polimorfismo y la estabilización de uno de ellos depende del método de síntesis seguido en su preparación. Así por ejemplo en el caso de la fase zircón correspondiente al $TbPO_4$ se obtiene cuando se prepara a 1673K; mientras que, la fase monazita se aísla a temperaturas menores del orden de 1273 K.

En el caso de los óxidos $RCrO_4$ solo fase $LaCrO_4$ cristaliza con el tipo estructural monacita debido al tamaño relativamente grande del ión La^{3+} en relación a las otras tierras raras. En el caso del siguiente miembro de la serie $PrCrO_4$ en condiciones normales se obtienen mezclas de los dos polimorfos zircón y monacita. En el caso de la hipotética fase “ $CeCrO_4$” su síntesis no ha sido posible hasta el momento debido a la alta inestabilidad del Ce^{3+} en las condiciones requeridas para realizar la síntesis de estos compuestos.

En lo que respecta a las transiciones de fase inducidas a alta presión han sido numerosos los trabajos llevados a cabo en el caso del mineral zircón $ZrSiO_4$ así como en algunos casos para los óxidos análogos RXO_4 (X=As y V) que se transforman en la estructura tipo scheelita presentando también simetría tipo tetragonal pero el grupo espacial $I4_1/a$. Recientemente, a partir de las medidas in situ de difracción de rayos X a alta presión en el sincrotrón se han descrito para el caso de los fosfatos $YbPO_4$ y $LuPO_4$ transiciones de fase del tipo zircón–scheelita inducidas por presión que son reversibles, pero la fase scheelita no puede congelarse en condiciones normales de presión y temperatura. En el caso de los vanadatos y arseniatos se han descrito asimismo transiciones de fase inducidas a alta presión del tipo monacita-scheelita y zircón–scheelita que tiene lugar a 8 GPa y 773K en las que se produce un incremento en la densidad del 6% y 11% respectivamente. En lo referente a las transiciones de fase inducidas por presión en los óxidos $RCrO_4$ los estudios realizados son escasos. Ello probablemente sea debido al alto grado de inestabilidad que presenta el ión Cr^{5+} y su tendencia a ser reducido para dar lugar a las fases $RCrO_3$ que presentan estructura tipo perovskita distorsionada. Es de destacar, que recientemente que en el grupo de trabajo en el que se ha realizado la presente memoria ha sido pionero en este aspecto llevando a cabo la preparación de la fase scheelita correspondiente a los óxidos $HoCrO_4$ y $TbCrO_4$

a 4 GPa y 813 K. Es de destacar que dicho polimorfo scheelita obtenido a alta presión y temperatura es estable en condiciones normales de presión y temperatura.

Estos óxidos $R\mathrm{CrO}_4$ presentan un interés especial en comparación con los homólogos arseniatos .fosfatos y vanadatos, debido a la coexistencia de dos iones paramagnéticos Cr^{5+} ($3d^1$) y R^{3+} ($4f^n$) que hacen que estos óxidos constituyan el escenario idóneo para el estudio de las interacciones magnéticas entre los orbitales $3d$-$4f$. Además, el estudio de las propiedades magnéticas en estos óxidos va a permitir poner de manifiesto el importante papel que el catión Cr^{5+} juega como promotor de las interacciones en la subred de las tierras raras, así como el estudio sistemático que la anisotropía de las tierras raras ejerce en las estructuras magnéticas que presentan los compuestos preparados a lo largo de este trabajo. En este sentido cabe destacar que la transición estructural zircón-scheelita va acompañada por profundos cambios en las propiedades magnéticas que presentan ambos polimorfos. La mayoría de los óxidos tipo zircón son ferromagnéticos; mientras que, los correspondientes polimorfos tipo scheelita son antiferromagnéticos. El análisis detallado de las estructuras scheelita y zircón a partir de los datos obtenidos mediante difracción de rayos X y neutrones ha permitido establecer relaciones estructura-propiedades magnéticas que es uno de los objetivos mas importantes de la Física y Química del Estado Sólido.

En este trabajo, el objetivo fundamental es el estudio de la estructura, asi como de las propiedades magnéticas y electrónicas que presentan la familia de óxidos $R\mathrm{CrO}_4$ que cristalizan con el tipo estructural scheelita. En primer lugar nuestro trabajo ha estado dirigido al estudio de la transición estructural zircón-scheelita en los óxidos $R\mathrm{CrO}_4$ que tiene lugar a altas presiones y temperaturas. Para ello se han buscado las condiciones de síntesis necesarias para preparar muestras tipo scheelita de alta pureza que una vez caracterizadas se ha procedido al estudio de la estabilidad de las mismas y al origen del mecanismo de la transición zircón-scheelita. En segundo lugar se ha procedido al estudio de las propiedades magnéticas y electrónicas que presentan estas nuevas fases. Para llevar a cabo estos objetivos se han preparado muestras de scheelita y zircón y se han estudiado sus propiedades estructurales, magnéticas y electrónicas utilizando las técnicas experimentales descritas en el capitulo 2 de esta memoria. En el capítulo 3 se hace una revisión pormenorizada de la transición zircón-scheelita. El estudio de la estabilidad de la fase scheelita ha sido muy importante a la hora de optimizar las condiciones de síntesis y comprender los factores que dan lugar a fases secundarias. Para ello, se han analizado en detalle los datos obtenidos a partir de las medidas de difracción de rayos X y neutrones cuyo estudio se recoge en el capítulo 4. El estudio de las propiedades magnéticas de estas fases $R\mathrm{CrO}_4$ tipo scheelita a partir de los datos de susceptibilidades magnéticas, magnetización y calores específicos se lleva cabo en el capítulo 5. Dicho estudio se completa con la determinación de la estructura magnética de los materiales preparados a partir de los diagramas de difracción de neutrones realizados en diferentes laboratorios europeos como el ILL-Grenoble (Francia), ISIS- Inglaterra y LLB- Saclay (Francia).

En lo referente a la estructura electrónica no existen apenas trabajos publicados referentes a estos materiales. En este sentido, solo el estudio de fotoelectrones de rayos X de la banda de valencia de la fase monacita correspondiente al $LaCrO_4$ ha sido realizado por Konno y col. 1992 sin ofrecer una interpretación de los datos. Posteriormente en 2006 Li y col. han llevado a cabo un cálculo de la estructura de bandas pero no la comparan con datos experimentales. Muy recientemente, Errandonea y col. han determinado experimentalmente el “band gap” de la fase zircón correspondiente al $YCrO_4$ a partir de medidas de espectroscopia óptica. Con estos antecedentes en el presente trabajo se ha llevado a cabo el estudio de la estructura electrónica de los compuestos $R\mathrm{CrO}_4$ mediante la espectroscopia de absorción de rayos X, espectroscopía de fotoelectrones y cálculo de bandas. El objeto principal era verificar mediante la espectroscopia los estados de valencia del Cr así como el origen y naturaleza de los estados más próximos al potencial químico. Específicamente justificar si el sistema es aislante, porqué lo es. En el capítulo 6 se discuten las propiedades electrónicas de los compuestos $R\mathrm{CrO}_4$ a partir de las medidas XPS para las muestras $YCrO_4$ y $GdCrO_4$ que cristalizan con la estructura tipo zircón. Asimismo se han realizado el estudio de las propiedades electrónicas a partir de las medidas XAS para varios polimorfos zircón y scheelita de los óxidos $R\mathrm{CrO}_4$.

En este trabajo la preparación de los diferentes cromatos $R\mathrm{CrO}_4$ se ha llevado a cabo utilizando un método simple a partir de los nitratos correspondientes de cromo y tierras raras. Las cantidades estequiométricas de estos reactivos se homogeneizaban en un mortero de ágata y se colocan en una navecilla de porcelana en el interior de un horno tubular en corriente de oxígeno siguiendo el programa de tratamiento a las temperaturas que se indican: 30 min a 433 K, 30 min a 473K y 12 horas a temperaturas comprendidas entre 823 y 853 K. La velocidad de calentamiento fue en todos los casos de 20 K/min y la reacción que tiene lugar puede escribirse como:

$$\mathrm{Cr(NO_3)_3.9H_2O} + R\mathrm{(NO_3)_3.\,6H_2O} \longrightarrow R\mathrm{CrO_4} + 6\mathrm{NO_2} + 15\mathrm{H_2O} + \mathrm{O_2}$$

Las muestras $R\mathrm{CrO}_4$ preparadas por el método descrito anteriormente han sido tratadas a altas presiones y temperaturas en una prensa tipo CONAC instalada en el Laboratorio de Altas Presiones de la Universidad Complutense de Madrid y han permitido obtener los óxidos $R\mathrm{CrO}_4$ que cristalizan con el tipo estructural scheelita y que constituyen el objeto de la presente memoria. El procedimiento experimental consiste en encapsular el polimorfo zircón, obtenido previamente, en crisoles de Au o Pt que son sometidos a presiones de 4 GPa, a temperaturas comprendidas entre 803 y 833 K durante periodos de tiempo comprendidos entre 35 a 50 minutos.

Los datos de difracción de rayos X han sido analizados mediante el método de Rietveld utilizando el programa FullProf Suite, versión Mayo 2012. En el caso de los datos de difracción de rayos X obtenidos en el sincrotrón correspondientes a la muestra $ErCO_4$-scheelita se utilizo el programa DICVOL04 en el refinamiento. El análisis de la simetría se llevó a cabo mediante el programa BasIreps implementado en el FullProf.

La estabilidad relativa de las fases zircón y scheelita se estudio a partir del método de las valencia del enlace conocido en la bibliografía ingleas como “Bond Valence Method(BVS)” que permite determinar el índice de inestabilidad global de los diferentes polimorfos. A partir de la desviación de la suma de las valencias del enlace con respecto al valor teórico es posible determinar las posibles inestabilidades existen en la estructura. Las Tabla 4.1 y 4.2 mostradas en el capítulo 4 muestra los valores de BVS determinados para ambos polimorfos zircón y scheelita.

Los diferentes mecanismos propuestos para explicar la transición zircón –scheelita han sido discutidos en el presente trabajo. La mayoría de los trabajos consideran que dicha transición es de primer orden y se ha observado una disminución de volumen del 10% en una amplia variedad de compuestos con estequiometría ABO_4. Ambas estructuras poseen 24 átomos por celda unidad (4 cationes A, 4 cationes B y 16 aniones O^{--}). Sin embargo, la relación grupo-subgrupo ($I4_1/amd$-zircón, $I4_1/a$-scheelita) con respecto a la simetría que presentan ambos polimorfos, en los que la coordinación 4 y 8 es la misma para los cationes A y B respectivamente no es condición suficiente para describir esta transición de fase como desplazativa.

Por otra parte se ha observado que las distancias Cr-O permanecen constantes en ambos polimorfos; mientras que los ángulos de enlace O-Cr-O y las distancias *R*-O varian ligeramente. Sin embargo, se han observado importantes cambios en los ángulos de enlace O-*R*-O y *R*-O-Cr. Ello es debido a las diferentes compresibilidades de los poliedros CrO_4 y RO_8. Como consecuencia de ello, la compresibilidad a lo largo del eje c es mayor en el zircón que en la scheelita como se demuestra en el capítulo 4 al hacer un análisis detallado de ambas estructuras. Uno de los cambios mas significativos que tiene lugar durante la transición de fase es la variación en los ángulos Cr-O-R, que tiene una gran importancia a la hora de justificar las diferentes propiedades magnéticas que presentan estos polimorfos. En el caso del zircón existen dos ángulos de enlace Cr-O-*R* con valores medios de 154º y 97º que apenas varían a lo largo de la serie lantánida. En el caso de la scheelita estos ángulos son muy diferentes tomando los valores medios de 122º y 133º. Estos valores sensiblemente distintos como se discute en el capítulo 5 son los responsables del diferente comportamiento magnético que presentan ambas fases. Además en el caso del zircón, cada tetraedro CrO_4 posee seis poliedros RO_8 como vecinos más próximos, mientras que en el caso de la fase scheelita dicho número es de ocho. Ello justificaría plenamente el aumento de la densidad en torno al 10% que tiene lugar al pasar de la fase zircón a la scheelita.

Cálculos recientes han puesto de manifiesto que la transición de fase zircón –scheelita tiene lugar a 7-8 GPa para el caso de los óxidos RVO_4, mientras que para las fases análogas $RCrO_4$ dichas transiciones ocurren a 6 GPa a T=0 K. Sin embargo, a partir de nuestro estudio ha quedado demostrado que la mencionada transición inducida por presión tiene lugar a presiones sensiblemente mas bajas del orden de 4 GPa a temperaturas de 833 K. Cálculos recientes han confirmado que la fase zircón es más estable que la correspondiente scheelita.

La estabilidad térmica de la fase scheelita ha sido estudiada mediante análisis termogravimétrico (TGA) y calorimetría diferencial de barrido (DSC) mediante un equipo SDT Q6000 TA Instrument. La descomposición ocurre en varias etapas. En una primera etapa comprendida entre la temperatura ambiente y 600 K la muestra pierde 0.15% de su peso como consecuencia de la eliminación de agua y humedad que la scheelita posee adsorbida en su superficie. Entre 600 K y 800 K , asimismo se observa una ligera pérdida de peso del orden de 0.32% debido a la incipiente descomposición superficial que experimenta la muestra. La pérdida de peso observada a 850 K que está en torno al 5.5% corresponde a la pérdida de un átomo de oxigeno lo que indica que la descomposición de la fase scheelita $R\mathrm{CrO}_4$ ha tenido lugar de acuerdo con el siguiente esquema reacciónal:

$$R\mathrm{CrO}_4 \xrightarrow{850-1000\,K} R\mathrm{CrO}_3 + \tfrac{1}{2}\,\mathrm{O}_2$$

Los datos de difracción de rayos X confirman que el producto final de reacción corresponden a la fases $R\mathrm{CrO}_3$ que cristalizan con el tipo estructural perovskita distorsionada presentando simetría ortorrómbica y grupo espacial *Pnma*. El diagrama correspondiente de DSC muestra la existencia de un marcado efecto endotérmico a la temperatura de 900 K.

La estabilidad del polimorfo scheelita ha sido estudiada a partir de la la evolución de los diagramas de difracción in situ a diferentes temperaturas en el margen comprendido entre 373 K y 1173 K. Los resultados obtenidos confirman los comentados a partir de ATG y DSC, de tal manera que el diagrama de difracción de rayos X obtenido a 1173 K muestra las reflexiones correspondientes al estructura perovskita con simetría ortorrómbica.

El análisis detallado de la estructura que se lleva cabo en el capítulo 4, indica que el tipo estructural zircón presenta una estructura relativamente abierta en la que existen posiciones intersticiales vacantes. A estas posiciones vacantes se les ha considerado como las responsables de la existencia de impurezas el los zircones que no darían lugar a deformaciones de la red del zircón. En este sentido destacar, que recientemente Trail y col., han propuesto la existencia de grupos OH^- en la estructura del mineral xenotimo $(\mathrm{Y},R)\mathrm{PO}_4$. Efectos similares pueden tener lugar en los óxidos $R\mathrm{CrO}_4$ en los que pueden adsorber moléculas de agua en la superficie dando lugar a procesos de dismutación en los que se pueden generar iones Cr^{6+} y Cr^{3+}. Sin embargo, el análisis de las diferentes scheelitas obtenidas en el presente trabajo muestra solo en algunos casos trazas de Cr^{6+} y cantidades apreciables de fases $R\mathrm{CrO}_3$ mediante difracción de rayos X. Ello indica que las posibles fases en las que el cromo presenta el estado de oxidación 6+ se forman solo en la superficie de estos materiales como consecuencia de la humedad. Este efecto se ha confirmado mediante espectroscopia XAS mediante la cual se han detectado importantes concentraciones de Cr^{6+} en la superficie de estos óxidos $RCrO_4$. En este sentido y con objeto de determinar la posible existencia de fases secundarias en estos óxidos en la presente memoria se han investigado las scheelitas de Sm y Er a la temperatura ambiente utilizando alta resolución en la línea B2 del sincrotrón DESY situado en Hamburgo. Los resultados obtenidos han permitido detectar la existencia de la fase $Er(OH)CrO_4$ en la que el estado de oxidación del cromo es 6+.

El capítulo 5 de la memoria está dedicado al estudio de las propiedades magnéticas que presentan los óxidos $RCrO_4$ que cristalizan con el tipo estructural scheelita. Dicho estudio se ha llevado a cabo a partir de las medidas de susceptibilidades magnéticas, magnetización y calores específicos a temperaturas comprendidas entre 2 y 300 K y a campos de hasta 9T. Los datos de susceptibilidades magnéticas siguen en todos los casos estudiados con la excepción de los óxidos de Sm y Eu una ley de Curie- Weiss en amplios márgenes de temperatura. Debido a la impureza presente en todas las muestras de la fase perovskita $RCrO_3$, se observan pequeñas anomalías entre 280 K y 150 K debido al ordenamiento antiferromagnético con espines desalineados que presentan dichas perovskitas a esa temperaturas. Estas pequeñas contribuciones se han tenido en cuenta en la determinación del momento magnético de las diferentes fases, obteniéndose valores experimentales para los momentos magnéticos que concuerdan muy bien con los teóricos calculados para las diferentes fases $RCrO_4$. A bajas temperaturas en todos los casos se observan máximos en la susceptibilidad magnéticas que son indicativos de la existencia de interacciones antiferromagnéticas en las que las subredes del cromo y la tierra rara están implicadas. La determinación de la temperatura a la cual la susceptibilidad es máxima ha permitido estimar las temperaturas de Néel que presentan estos compuestos que están comprendidas entre 34.7 K para el $YbCrO_4$ y 9.4 K para el $HoCrO_4$ (ver Tabla 5.1, capítulo 5). Los valores relativamente altos de $T_{\chi max}$ para estos compuestos $RCrO_4$ en comparación con los obtenidos para los óxidos isoestructurales RXO_4 (X= P, As y V) indican el papel predominante que ejerce el Cr^{5+} con S=½ como promotor de las interacciones magnéticas en las sured de la correspondiente tierra rara.

La medida de la magnetización en función del campo magnético a diferentes temperaturas ha permitido poner de manifiesto la existencia de transiciones metamagnéticas para la mayoría de los óxidos $RCrO_4$-scheelita en los que el valor del campo crítico depende de la anisotropía de la tierra rara R. En este sentido cabe destacar que el valor de dicho campo es de solo 0.1 T para el compuesto $GdCrO_4$ en perfecto acuerdo con el carácter isotrópico del ión Gd^{3+} cuyo estado fundamental es $^8S_{7/2}$.

La medida de calores específicos es otra de las tareas abordadas en la presente memoria, su interpretación ha sido muy útil para completar el estudio de las propiedades magnéticas que presentan estos óxidos $RCrO_4$. La determinación de las denominadas transiciones λ en los diferentes materiales así como su evolución con el campo ha sido uno de los objetivos del trabajo.

Además, en todos los casos se ha procedido a la determinación de la contribución magnética al calor específico (C_{mag}) al calor específico total. Para ello, es preciso determinar las contribuciones electrónica (C_e) y de la red (C_{la}) que descontadas del valor experimental van a permitir conocer la mencionada contribución magnética. Estos cálculos se pueden hacer utilizando diferentes métodos. Uno de ellos muy frecuentemente utilizado consiste en restar el valor del calor específico medido a temperaturas superiores a la T_N de un compuesto isosestructural que no posea iones paramagnéticos; ello evidentemente conduce al valor de C_{mag}. Otro procedimiento se basa en el ajuste de los datos de C_{exp} a los modelos de Einstein y Debye por encima de la temperatura de Néel para reproducir el C_{la} en todo el margen de temperaturas de medida. Sin embargo, este método presentan inconvenientes en el sistema estudiado debido a la existencia de interacciones a corto alcance que son operativas a temperaturas superiores a la de Néel y además tampoco tienen en cuenta las anomalías de Schottky que están presentes a bajas temperaturas y son el resultado del desdoblamiento del estado fundamental de las diferentes tierras raras bajo el efecto del campo del cristal. Otro método utilizado frecuentemente para el cálculo de las contribuciones C_{lat} y C_e consiste en ajustar los datos experimentales del calor específico (C_{ex}) a una función polinómica. Los datos obtenidos de C_{ex} en función de la temperatura y campo han permitido determinar las temperaturas a las que aparecen las anomalías tipo λ que coinciden en la mayoría de los caso con la T_N determinada a partir de los datos de susceptibilidades magnéticas. Se ha estudiado asimismo la evolución dicha transición con la temperatura y se ha comprobado que disminuye en intensidad al incrementar los valores del campo. Dicha señal se hace cero cuando el campo magnético adquiere el valor correspondiente al denominado campo crítico, Hc. A partir de los valores calculados de C_{mag} utilizando los métodos mencionados anteriormente se ha calculado la entropía magnética asociada a las transiciones antiferromagnéticas presentes en los diferentes óxidos $RCrO_4$. Los valores obtenidos en todos los casos son ligeramente inferiores calculados teniendo en cuenta las contribuciones de los iones Cr^{5+} y R^{3+} presentes en estos compuestos que viene dada por: S_t= 2Rln(2J+1)+2Rln(2S+1): donde J y S son los números cuánticos correspondientes a los estados fundamentales de la tierra rara R^{3+} y del Cr^{5+} respectivamente. La diferencia observada entre valores experimentales y calculados es debida fundamentalmente al desdoblamiento del estado fundamental del ión R^{3+} bajo la influencia del campo del cristal.

La memoria incluye un estudio detallado de los diferentes caminos a través de los cuales tienen lugar las interacciones de superintercambio *R*-O-Cr tratando de justificar el cambio de signo de la interacción de ferromagnetismo a antiferromagnetismo al pasar del polimorfo zircón a las fase tipo scheelita objeto del presente trabajo.

La parte final del capítulo 5 está dedicada al estudio de las estructuras magnéticas que presentan estos óxidos $RCrO_4$. En primer lugar se ha abordado el estudio de la estructura del $GdCrO_4$ que debido a la elevada absorción del Gd ha requerido la utilización del difractómetro 7C2 una longitud de onda corta λ=0.577Å instalado en el Laboratorio Leon Brillouin en Saclay (Francia). Los datos de difracción de neutrones para los óxidos $DyCrO_4$, $NdCrO_4$ y $HoCrO_4$ se obtuvieron en el difractómetro WISH utilizando la fuente pulsada de ISIS existente en Laboratorio Rutherford Appleton en Oxfordshire en Reino Unido. Los experimentos de difracción de neutrones para las muestras de $ErCrO_4$ y $TmCrO_4$ se llevaron a cabo en los difractómetros D1B y D2B instalados en el ILL de Grenoble en Francia.

El refinamiento de los datos de difracción de neutrones obtenidos a temperaturas superiores a la de Néel han sido utilizados para la determinación de la estructura cristalina que presentan estos compuestos y su estudio se incluye en el capítulo 3.

En todos los casos se ha llevado a cabo el estudio de la evolución de los diagramas de difracción en función de la temperatura lo que ha permitido determinar la temperatura de Néel para todas las muestras y se observa un buen acuerdo con las determinadas a partir de los datos de susceptibilidades magnéticas. La determinación de las estructuras magnéticas se ha llevado a cabo a partir del método de las representaciones propuesto por Bertaud e implementado en el programa FulProf. La aparición de máximos de difracción a bajas temperaturas alguno de ellos prohibidos por la simetría del grupo espacial es indicativo de la naturaleza magnética de los mismos. La asignación de índices a dichos máximos permite determinar el denominado vector de propagación que en el caso de los óxidos estudiados resulta ser conmensurable k=(0 0 0). Ello indica que la estructura magnética posee una celda unidad coincidente con la celda cristalina. El análisis de representaciones ha permitido determinar la estructura que presentan los diferentes óxidos. Los resultados obtenidos indican que en el caso de los compuestos $R\mathrm{CrO}_4$ (R= Gd, Dy, Er, Tm) los momentos se acoplan antiferromagneticamente en el plano ab de la estructura; mientras que para el óxido $TbCrO_4$ dichos momentos están acoplados a lo largo del eje c de la estructura. Las diferentes estructuras magnéticas que presentan estos óxidos $R\mathrm{CrO}_4$ se deben fundamentalmente a la diferente anisotropía que presentan los cationes R^{3+} que son los responsables de las estructuras magnéticas de estos compuestos. En este sentido, cabe destacar que el factor de Stevens $\alpha_J>0$ para el Tb^{3+}; mientras que en el caso de los iones Tm^{3+} y Er^{3+} el correspondiente $\alpha_J<0$; aunque en el caso del Gd^{3+} $\alpha_J=0$, la orientación de los momentos en el plano ab parece estar controlada por la anisotropía de la estructura cristalina.

El ión Cr^{5+} representa el caso típico de un orbital d con un solo electrón (S=1/2) con configuración electrónica [Ar $4s^2 3d^1$]. En el caso de la estructura tipo zircón se ha propuesto que este ión Cr^{5+} se encuentra en una simetría puntual D_{2d}, mientras que el caso del polimorfo scheelita la simetría puntual es D_{4h}. Sin embargo, a lo largo de la transición las distancias de enlace Cr-O no cambian y solo se han observado pequeños cambios en los ángulos de enlace O-Cr-O correspondiente al tetraedro [CrO_4] como se recoge en el capítulo 3 de la presente memoria. El diagrama de niveles de energía en el caso de la estructura tipo zircón del Cr^{5+} se recoge en el capítulo 6 el que además se discute y estudia en detalle la estructura electrónica del Cr5+ mediante espectroscopia de absorción de rayos X (XAS) en el borde del Cr-$L_{2,3}$ y en el borde O-K.

Muestras diferentes de zircón y scheelita han sido investigadas mediante XAS en sincrotrón NSRRC en Taiwán utilizando la línea BL08B. TEY se aplicó a la presión ambiente a los polimorfos scheelita y zircón de los óxidos RCrO$_4$ con R=La, Nd, Sm, Gd, Tb, Dy, Tm ,Er, Yb y Lu. En el caso de las muestras tipo zircón se prensaron y sinterizaron en forma de pastillas a 773 K durante 10 horas en un horno tubular en corriente de oxígeno. Las muestras correspondientes a la fase scheelita que presentaban un alto grado de sinterización se midieron después de ser obtenidas a alta presión sin ser sometidas a ningún tipo de tratamiento térmico. Una descripción detallada de la preparación de las muestras para su medida XAS se recoge en el capítulo 2 de la presente memoria.

Los resultados obtenidos están de acuerdo con los obtenidos para el óxido $Sr_3Cr_2O_8$ en el que aún a pesar de la diferente simetría puntual para el Cr^{5+}, sin embargo la coordinación tetraédrica para el Cr^{5+} permanece en ambos compuestos por lo que los espectros del Cr en el borde de absorción Cr-$L_{2,3}$ son similares lo que está de acuerdo con el cálculo del cluster del multiplete.

Por otra parte, también se ha llevado a cabo el estudio de absorción de rayos X en el modo de campo de electrón total (TEY) para una gran variedad de muestras RCrO$_4$ policristalinas sinterizadas junto con un monocristal Cr_2O_3 con objeto de tener el Cr^{3+} como referencia. En el capítulo 7 se ha demostrado que el comportamiento es análogo para todas las muestras estudiadas RCrO$_4$ y no depende de la tierra rara. Características espectrales similares han sido también encontradas para todos los iones de tierras raras en lo referente al borde del O-K en los espectros XAS de las muestras RCrO$_4$. El pico observado a 528.7eV se ha asignado a la transición del electrón del oxígeno desde el orbital interno 1*s* al orbital 2*p* del oxígeno hibridado con los orbitales del cromo 3*d*-e, mientras que el pico a 529.5 eV está relacionado con una mezcla entre los orbitales del oxígeno 2*p* y los del cromo 3*d*-t_2, así como también los estados 5*d* de las tierras raras.

El espectro correspondiente al borde O-*K* del oxígeno muestra un comportamiento ligeramente distinto con una transferencia por encima y debajo de 530 eV y ello se debe fundamentalmente a que su estructura tipo monacita es ligeramente diferente de la correspondiente al zircón y a la scheelita. En el caso de la monacita la tierra rara está coordinada a 9 átomos de oxígeno, mientras que en el caso del zircón y la scheelita la coordinación es 8. Esta diferencia en la estructura altera la hibridación *R*-O como puede verse en el borde O-*K* en el caso del LaCrO$_4$. Es de destacar que en el LaCrO$_4$ que el pico principal del borde $L_{2,3}$ es similar al observado en el resto de los óxidos RCrO$_4$ que cristalizan con el tipo estructural zircón.

Con objeto de investigar si los espectros TEY son representativos del interior de la muestra, se estudiaron los espectros XAS en el borde K del oxígeno en modo florescencia de campo sensible al interior (FY). En el modo TEY la medida de las muestras se llevada a cabo después de raspar la muestra en vacío con una profundidad de 2-6 nm. Sin embargo, los resultados obtenidos solo eran representativos de unos cuantas capas superficiales. En la modalidad FY, se pueden estudiar mas de 100 nm en profundidad de la muestra lo que hace que los resultados obtenidos sean representativos del conjunto de la muestra. Así pues estos resultaos obtenidos a partir de FY pueden ser utilizados para validar la sensibilidad del modo TEY en el estudio de las diferentes muestras. A partir de la comparación del borde O-*K* obtenido en los modos FY y TEY se ha podido concluir que el espectro obtenido en modo TEY se reproduce en el modo FY.

Medidas similares se ha realizado del borde O-*K* en modos TEY y FY además del borde Cr-$L_{2,3}$ en modo TEY en las fases scheelita $R\mathrm{CrO}_4$ (R=Gd, Dy, Er e Yb) y los resultados de este estudio se muestran en le capítulo 7. En todas las muestras estudiadas se observa una mayor concentración de Cr^{6+} en comparación con las muestras tipo zircón. Los espectros de EELS en el borde del Cr-$L_{2,3}$ de Cr^{5+} y Cr^{6+} medidos por Daulton y Little muestran que el pico principal en el espectro del Cr^{6+} se desplaza mas de 1eV a energías mas altas con respecto al espectro correspondiente al Cr^{5+}.

Como se ha discutido en detalle a lo largo de la memoria, las posiciones intersticiales vacantes en la estructuras zircón y scheelita juegan un papel muy importante en las diferencias mostradas por las diferentes muestras de estos dos polimorfos. El zircón posee una estructura bastante abierta en la que existen canales y posiciones intersticiales tetraédricas a lo largo del eje c de la estructura, mientras que huecos octaédricos están localizados entre los poliedros. Estos huecos intersticiales son candidatos para ser ocupados por impurezas especialmente en la superficie. La adsorción de agua en la superficie puede dar lugar a grupos OH^- que producen la oxidación parcial de Cr^{5+} a Cr^{6+} dando lugar a la formación del hidroxicromato de cromo de fórmula $R(\mathrm{OH})\mathrm{CrO}_4$ dando lugar al espectro en el que se observan el borde Cr-L_3 a 581eV y el borde L_2 a 589eV. En el caso de que la impureza sea $R\mathrm{CrO}_3$ (Cr^{3+}) el borde Cr-L_3 aparece a 578 eV. La presencia de ambas fases que aparecen como impurezas se han confirmado mediante difracción de rayos X.

La cantidad de Cr^{6+} se reduce cuando las muestras $R\mathrm{CrO}_4$ tipo zircón se tratan durante el proceso de sinterización a 800 K; dicho tratamiento no puede llevarse a cabo en el caso de las muestras tipo scheelita ya que como se ha apuntado anteriormente se produce la descomposición térmica de las mismas. Por tanto la existencia de Cr^{6+} y Cr^{3+} en la superficie de la scheelita parece inevitable en la mayoría de los casos, pero puede reducirse considerablemente en el caso de las muestras que cristalizan con el tipo estructural zircón controlando la temperatura en el proceso de su síntesis.

El estudio de la estructura del zircón mediante XPS se ha realizado en lugar de la scheelita por dos razones. En primer lugar la alta pureza de las muestras tipo zircón verificas mediante XRD y XAS proporciona una buena base para la obtención de data de XPS de alta calidad y que sean reproducibles. El segundo motivo es de tipo experimental y radica en que los fragmentos sinterizados de scheelita poseen dimensiones pequeñas lo que dificulta la medida de XPS. Estos fragmentos poseen unas dimensiones de alrededor de 2x2 mm^2, mientras que la sección del haz de fotones incidente es de 1x3mm^2.

En el presente trabajo se midieron dos muestras correspondientes a las composiciones $YCrO_4$ y $GdCrO_4$ en las que en la primera solo el Cr^{5+} contribuye a la estructura electrónica; mientras que en la segunda los orbitales 3*d* y 4*f* contribuirán al diagrama de bandas correspondiente. Ambas muestras se sinterizaron a 773 K durante 10 horas y se prepararon pastillas de 10 mm de diámetro con un espesor comprendido entre 1.5-3 mm. Los espectros de XPS se registraron con un espectrómetro de fotoelectrones equipado con una fuente Al-kα_1 ($h\nu$=1486.6eV) y un analizador Scientia R3000 con una resolución de 0.35 eV. Mas detalles experimentales se recogen en el capítulo 2.

El desdoblamiento del nivel del cromo 2*p* para ambos zircones se recoge en el capítulo 6. La energía de enlace de 588eV corresponde a $2p_{1/2}$, mientras que la correspondiente a 578.45 eV se asigna al $2p_{3/2}$. El espectro de la banda de valencia del $YCrO_4$ medido a 300 K durante 36.5 horas (1050 barridos) también está incluido en el capítulo 6.

La forma de la banda de valencia del espectro está de acuerdo con la publicada por Konno y col. para el $LaCrO_4$. Las principales características de la banda de valencia del $YCrO_4$ incluyen la existencia de un pico ancho y débil localizado entre 0.625 eV y 2.275 eV seguido por un pico ancho y muy intenso entre 2.85 y 8.7 eV. El "gap" de 0.625eV observado (Δ1) justifica el carácter aislante de estos compuestos. La caracteristica general del espectro es análoga a la mostrada para otros sistemas $3d^1$ en la bibliografía como por ejemplo el ión V^{4+} o Ti^{3+} donde el pico débil observado es debido al electrón desapareado que normalmente solapa con un pico más intenso que corresponde a la banda 2*p* del oxígeno en estos óxidos. Además, la sección transversal de fotoionización del orbital 2*p* del oxígeno es alrededor de dos veces mayor que la del orbital 3*d* para una energía del fotón de 1486.6 eV, por tano la contribución total del orbital 3*d* posee un peso pequeño en el espectro. Es preciso indicar que es la primera vez en la que se ha resuelto el "band gap" en esta familia de óxidos.

Estos óxidos $RCrO_4$ tienen tendencia a perder oxígeno en la superficie cuando el experimento XPS se lleva a cabo en varios días y ello conlleva a la creación de iones Cr^{3+}. El estado de la superficie es muy importante en estos compuestos y una pequeña contaminación con agua puede alterar la banda de valencia dando como resultado la desaparición del pico correspondiente a 3*d*, que tiene lugar en la formación de compuestos de Cr^{6+} en los que configuración cambia de $3d^1$ (Cr^{5+}) a $3d^0$ (Cr^{6+}).

Para interpretar el espectro obtenido de la banda de valencia se llevaron a cabo cálculos de spín polarizado DFT+U utilizando el código FPLO (full-potential local-orbital). DFT+U implica el procedimiento de campo medio para tratar las fuertes correlaciones que tienen lugar en la capa 3*d*. Funcionales diferentes DFT, como por ejemplo la aproximación de densidad local (LDA) y la aproximación de gradiente generalizado (GGA) conducen a resultados similares. Por tanto, en el presente trabajo se ha centrado solo en los resultados LSDA+U. En los cálculos DFT+U se utilizó el acoplamiento constante de Hund J=1 eV y se varió el parámetro de repulsión de Coulomb U en el margen comprendido entre 2-6 eV.

Los cálculos DFT+U están en buen acuerdo con los espectros experimentales de XPS que muestran la existencia de una banda aislada con una anchura de 1 eV por debajo del nivel de Fermi. La banda ancha localizada a energías más bajas expande el margen de energías aledeedor de 6 eV y combina los estados del oxígeno (entre -5 eV y -1 eV, es decir una anchura de 4 eV) con los estados más bajos del cromo localizados alrededor de -6.5 eV. Sin embargo, la comparación directa entre los datos de XPS y los resultados DFT+U revelan serias discrepancias en lo referente a la posición de las bandas de energía. Mas importante aún cabe destacar que los datos DFT+U con U=4 eV la banda aislada del oxígeno solapa con los estados del oxígeno, mientras que los datos experimentales muestran una separación finita para estas dos bandas de 0.5 eV. Esta discrepancia se ha atribuido a la posición errónea de los estados del oxígeno que es una delas limitaciones bien conocidas de los funcionales DFT. Este problema puede minimizarse eligiendo un valor diferente de U, ya que el efecto de este parámetro U es cambiar los estados 3*d* del cromo con respecto a los 2*p* del oxígeno. Finalmente el mejor valor de U resultó ser de 3 eV.

Así pues los resultados obtenidos indican la formación de un estado localizado para el oxígeno por debajo del nivel de Fermi en el $YCrO_4$.

El cálculo de la estructura de bandas de los óxidos RCrO$_4$ en las fases paramagnéticas muestra que la banda *d* cruza el nivel de Fermi. Ello es debido a que la banda d está parcialmente llena con un número impar (d^1) de electrones por celda unidad. El hecho de que los óxidos muestren un carácter aislante con un " band gap" elevado como sugieren los datos de XPS indican que los efectos de correlación deben jugar un papel muy importante. El cálculo de la estructura de bandas LSDA+U con U=3 eV da lugar a un "band gap". En primera instancia pues podemos clasificar los óxidos RCrO$_4$ como aislantes del tipo Mott-Hubbard pero una revisión con el modelo LSDA+U revela que los estados próximos al nivel de Fermi tienen un carácter de mezcla Cr 3*d* - O 2*p*, todo ello está relacionado con el hecho de que estos óxidos RCrO$_4$ presentan un grado de covalencia elevado.

Acknowledgement

I would like to thank Prof Regino Sáez Puche at the Complutense University of Madrid (UCM) for transmitting to me scientific experience, interest and enthusiasm in the fields of rare-earth orthochromates, high-pressure synthesis, inorganic synthesis and high-oxidation states of transition elements during his supervision in the past three years. His enthusiasm and encouragement to me were the main pillars of realizing this doctoral thesis and overcoming many obstacles not only on the scientific level but also on the administrational level. For his positive patient attitude and for the extended supervision time he dedicated for me, I am very grateful. I also would like to thank him for giving me the opportunity to participate in various international conferences and European training courses, which helped me in a great extent to improve my knowledge and skills in the scientific research.

I also thank Prof Liu Hao Tjeng, at Max-Planck Institute for Chemical Physics of Solids (MPI-CPfS) in Dresden, for accepting me in his group, supervising and directing me towards my study of the electronic properties of Cr^{5+} compounds during the last year of the thesis. Thanks to his directions, recommendations and ideas, I gained an experience in the spectroscopy field that has enriched my experimental approach for solid-state materials, and will definitely affect my future career. I am also grateful for his support with not only facilitating the experimental opportunities for me in the labs at MPI-CPfS and awarded beam-times at NSRRC facility in Taiwan for his group, but also for facilitating my stay in Germany and energizing the personnel department to take care of the procedures concerning my residence permit issues. I thank him also for granting me a scholarship for three months after the end of my contract.

During three years, this project have been supported and funded under the Marie-Curie EU Seventh Framework Programme (FP7) by the initial training network SOPRANO. The network was coordinated by Dr. Sylvie Hébert at CRISMAT lab in Caen (France), and had the scientists in charge: Prof. Miguel Alario Franco and Susana Garcia Martin at the Complutense University of Madrid (Spain); Dr. Andrea Severing and Dr. Thomas Koethe at the University of Cologne (Germany). For all of them, I am thankful for their coordination and organization of the program. No doubt, my experience during this training network has enriched my horizon not only because of the scientific content but also due to the movement between laboratories in Europe. This allowed me during the training activities and the network meetings to be in contact with various scientists at several institutions in Europe.

I would like to give special thanks to Dr. Z Hu for his training for me during the sample preparation and the measurements of x-ray absorption spectroscopy in Taiwan. During almost one month in Taiwan, he continuously supported me during my measurements and analysis of various zircon and scheelite polymorphs of the $R\mathrm{CrO}_4$ oxides. Afterwards, due to his directions, discussions and recommendations I have managed to substantially improve the work discussed in chapters six and seven.

I also thank both Alexander Tsirlin and Nils Hollman for their theoretical calculations for XPS spectrum of YCrO_4 and for XAS spectrum of ErCrO_4, respectively. These calculations were necessary to compare my experimental work with the theory, and improved my understanding of the studied system and gave me helpful ideas for further experimental procedures to prove some of my conclusions.

A very special gratitude goes to Dr. habil. Martin Rotter at MPI-CPfS for his enormous effort for correcting the grammar and style in this thesis; and for his continuous advices to improve the quality of this thesis. I am very thankful to his spontaneous support and constant encouragement.

I would like to acknowledge my coworkers: Dr. Yoshihiro Doi (at Hokkaido University in Japan), Dr. Julio Romero de Paz (at UCM), Dr. Esteban Climent Pascual (at Carlos III University of Madrid) and Dr. Antonio J. Dos santos-García (at Universidad Politécnica de Madrid). I would like to thank also the later for attending my beam time, which I was granted at the beamline of WISH instrument at ISIS facility (UK), after I could not travel to the UK because of the delay in the visa procedures. Equally acknowledged are my colleagues at MPI-CPfS: Dr. Alexander Komarek, Dr. Diana Rata, Dr. Sahana Rößler, MSc. Anna Efimenko and Dipl. Phys. Yvo Drees. These colleagues have facilitated for me the use of various labs and have offered help whenever it was needed.

Furthermore, I would like to acknowledge the technical support of: Dr. José Manuel Gallardo Amores at the high-pressure lab in UCM; Dr. Emilio Matesanz Saéz, Dr. Julian Velázquez Cano and Dr. Fernando Conde López at the Center of Assistance for X-Ray Diffraction Research (CAI) in UCM; Chang-Yang Kuo at NSRRC in Taiwan; and finally Mr. Thomas Mende for his support with cryonic liquids in the MPMS lab at MPI-CPfS.

The experiments at the LLB neutron facility in France were supported by the European Commission through the Access Activities of the Integrated Infrastructure Initiative for Neutron Scattering and Muon Spectroscopy (NMI3), supported by the European Commission under the 7th Framework Program through the Key Action: Strengthening the European Research Area, Research Infrastructures, with the contract NMI3/FP7 No: 226507. In addition, I appreciate the assistance of Dr. Brigitte Beuneu at the 7C2 instrument.

I would like to extend my thanks to the whole group of research assistants at NSRRC synchrotron facility in Taiwan, and in particular to: Ying Jiun Chen, Chang-Yang Kuo, Meng-Jie Huang and Chih-Yu Hua. Their assistance and organized shifts during my XAS measurements

helped me in a great deal to measure many samples in a short time. I also appreciate very much their friendly work atmosphere and their kind and welcoming culture, in addition to their constant enthusiasm for help.

The accomplishment of many organizational and bureau issues during my project in the SOPRANO network could not have been achieved without the help and continuous work of Magali Kerdreux (former SOPRANO project manager), Lucía Lázaro Antón (colleague and department assistant at UCM), Christin Bahr (department secretary at MPI-CPfS) and Andrea Helldorfer (department secretary at the University of Cologne).

During my work in Madrid and Dresden, I was very lucky to share an office with highly motivated and hard-working colleagues. These were Qiang Liu in Dresden; Sourav Marik, Tedy Stoyanova, Jesus Prado, Paola Ramos Alvarez, Ivan Pirrotta and Subakti in Madrid. I also enjoyed the time with the other members of the research group at CPfS-MPI: Chun-Fu Chang, Stefano Agrestini, Daria Mikhailova, Simone Altendorf, Akfiny Hasdi Aimon, Katharina Höfer and Phillip Reichel.

I would like to show my gratitude to my professors at UCM: Susana Garcia Martin, L. Carlos Otero-Diaz, María J. Torralvo-Fernandez and Carmen Parada. Special thanks go to Prof Emilio Moran Miguelez for his support and continuous prompt help as the head of the inorganic chemistry department. His various advices and unique communication skills helped me to enjoy my stay in the department. Special thanks go also to Dr. Khalid Boulhaya for his intellectual support and continuous encouragement during my stay in Madrid. In such an atmosphere at UCM, I found it possible to carry out the scientific research in a friendly environment, where everyone feels as part of a one big family. I would like not to forget the beloved other (recent and previous) members of this family: Lucía Lázaro Antón, Javier Fernandez Sanjulian, Veronica Blanco, David Avila, Marta Perez, Achraf El Hadri, Andrea Peche, Pedro González García, José Jesús Espíndola Canuto, César Meza and many others. For all of them, I wish the best for their career and for their personal life.

It is my pleasure to add that I enjoyed very much the work and discussions in all SOPRANO meetings with the scientists in charge as well as all the promising early stage researchers (ESR) and experienced researchers (ER) in the network. I wish all of them the success and the best of luck for their career and personal life.

I would like to add my admiration and recognition of the fast and immediate action from both Dr. Angel Arevalo and Dr. Zhiwei to read and evaluate my thesis and send the referee reports as soon as possible in order for me to submit the thesis in the planned time. I appreciate their effort and their valuable help.

Finally, I would like to thank my family and my wife for supporting me during my Master and PhD studies in Europe; and for their prayers and best wishes for me the whole time. In particular, I would like to thank them for their understanding during the times I was devoting to my work. They let my understand that the beauty of life is not only about reaching certain accomplishments, but it is also about enjoying the company we have and the road we take to reach these short and beautiful moments. For their existence in my life, I am totally grateful.

Appendices

Appendix I

Available online at www.sciencedirect.com
ScienceDirect
JOURNAL OF RARE EARTHS, Vol. 28, No. 6, Dec. 2010, p. 936
JOURNAL OF RARE EARTHS
www.re-journal.com/en/

High-pressure scheelite-type polymorph of $SmCrO_4$: synthesis, structural characterization and magnetic properties

Regino Sáez-Puche, Mahmoud Gamal Rabie, Julio Romero de Paz, José-Manuel Gallardo-Amores, Esteban Climent Pascual

(Department of Inorganic Chemistry, Faculty of Chemical Sciences, Complutense University of Madrid, Ciudad Universitaria,E-28040 Madrid, Spain)

Received 31 August 2010; revised 9 November 2010

Abstract: The new scheelite form of $SmCrO_4$ oxide was obtained by heating the zircon-type $SmCrO_4$ oxide at 4 GPa and 803 K. X-ray diffraction revealed that this scheelite $SmCrO_4$ phase crystallized with tetragonal symmetry, S.G. $I4_1/a$ and lattice parameters: a=0.50776(3) nm and c=1.15606(2) nm. This structural phase transition from zircon to scheelite involved a decreasing of around 10% in the unit cell volume. Although the Cr–O and Sm–O distances did not change very much in both zircon and scheelite polymorphs, the changes occurred in the bond angles were remarkable that appear to support the proposed reconstructive model to explain this structural zircon-scheelite phase transition. Magnetic susceptibility and magnetization measurements revealed that the scheelite $SmCrO_4$ oxide behaved an antiferromagnetic material, where the Sm^{3+} and Cr^{5+} were simultaneously ordered. The estimated Néel temperature, T_N, was 16 K and the critical field at 12 K associated with the metamagnetic transition was 3.2 T.

Keywords: scheelite-type structure; zircon-type structure; high pressure synthesis; antiferromagnetic behaviour; metamagnetic transition; rare earths

RXO_4 oxides, where R=a rare earth element and X=P, As, V or Cr, constitute a large family of compounds which crystallize with two different structural types depending on the size of the rare earth element. In the case of the larger lanthanide trivalent cations R^{3+}, they crystallize with the so-called monazite-type structure, showing monoclinic symmetry, space group $P2_1/n$; however, the most of these oxides show the zircon-type structure, which crystallize with tetragonal symmetry, space group $I4_1/amd$. In some cases, the existence of dimorphism has also been reported, where the zircon or scheelite polymorph could be obtained using specific synthesis conditions. Stubican et al.[1] reported that several vanadates and arsenates which crystallize in the zircon or in the monazite structures transform to the scheelite-type structure at high temperature between 2.6 and 8.6 GPa, which are quenchable at ambient conditions. Recently, in the case of $YbVO_4$ and $LuPO_4$, using in-situ synchrotron radiation, a non-quenchable pressure-induced zircon to scheelite phase transition has been reported[2].

Regarding the high pressure phase transitions of $RCrO_4$, only few studies have been reported for $YCrO_4$[3], $HoCrO_4$[4], and more recently for $TbCrO_4$ derivative[4], which transform to a scheelite polymorph at 4 GPa and 813 K remaining stable after releasing the high pressure and temperature.

In this paper we reported the synthesis conditions used in the preparation of a new scheelite phase for $SmCrO_4$, its structural characterization and the study of the magnetic properties.

1 Experimental

$SmCrO_4$ scheelite phase were prepared from the zircon-type powder sample which were placed within a platinum crucible and treated in belt-type equipment at different high pressures, temperatures and reaction times. The selected conditions to obtain pure $SmCrO_4$-scheelite samples were 4 GPa and 823 K for 30 min. Further increasing of pressure and/or temperature yielded $SmCrO_3$ as a secondary phase.

The precursor zircon-$SmCrO_4$ was obtained following the preparation method described elsewhere[6].

X-ray powder diffraction data were collected on the Phillips Panalytical X'Pert MPD diffractometers using the monochromatic Cu Kα radiation (λ=0.154056 nn). The data were refined with the Rietveld method using the FullProf program[7].

Magnetic susceptibility measurements were obtained for powdered samples using a Squid Quantum Design XL-MPMS magnetometer in the 2–300 K temperature range in a magnetic field of 1000 Oe. Magnetization vs magnetic field were performed at different temperatures.

2 Results and discussion

2.1 Structural characterization

The obtained XRD patterns of the both polymorphs zircon and scheelite-type were refined by the Rietveld method, us-

---

Foundation item: Project supported by the Spanish MICINN and FEDER under Research Project No. MAT200763497, and SOPRANO Project Under Marie Curie Actions (FP7)

Corresponding author: Regino Sáez-Puche (**E-mail:** rsp92@quim.ucm.es; **Tel.:** +34-91-3944353)

DOI: 10.1016/S1002-0721(09)60218-0

ing the software FullProf based on the structural models proposed for both structural types. The XRD pattern corresponding to the SmCrO$_4$ zircon reveals that this compound used as precursor is a single phase and the data have been refined according to the zircon-type structure, S.G. *I*4$_1$/*amd*. Fig. 1 shows the refinement results of the XRD pattern corresponding to the new high pressure scheelite type of SmCrO$_4$. The structural parameters and some of the most relevant interatomic distances are given in Table 1. The data have been refined with the tetragonal *I*4$_1$/*a* space group. In this symmetry both Sm^{3+} and Cr^{5+} ions occupy special positions namely 4b (0, ¼, ⅝) and 4a (0, ¼, ⅛), respectively, while the oxygen atoms are located on 16f (*x*, *y, z*) position. Minor impurities of the distorted perovskite SmCrO$_3$ appear during the high-pressure synthesis and have also been included in the Rietveld refinement, see the second row of vertical marks in Fig. 1..

The structure-type corresponding to the scheelite is shown in Fig. 2. It can be observed that as in the case of zircon-type polymorph, Cr and Sm atoms are coordinated by four and eight oxygen atoms respectively, giving rise to tetrahedra and bisdisphenoids polyhedra for this scheelite polymorph. This structure can be described as being formed by corner sharing chains of alternating [CrO$_4$] tetrahedra and [SmO$_8$] bisdisphenoids units along the *a*-axis of the structure. Along the *c*-axis, the [SmO$_8$] polyhedra of two consecutive chains are sharing edges, giving rise to dimeric units of [Sm$_2$O$_{14}$] composition. Moreover, the [CrO$_4$] tetrahedral units are well isolated from each other as in the case of the zircon. As can be viewed in Table 1, there is around 10% of volume reduction during this zircon to scheelite phase transition, which is similar to that found in the case of the transition for analogous zircon-scheelite phase transitions reported for other RXO$_4$ compounds[1].

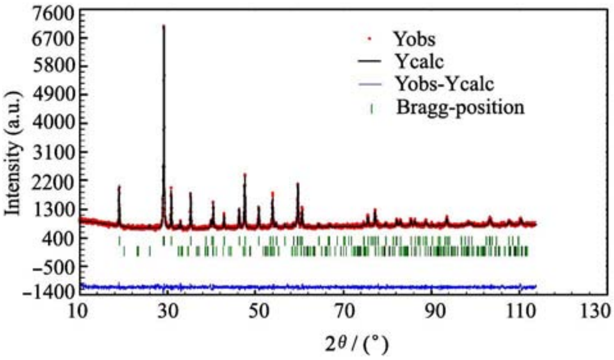

Fig. 1 Refined X-ray powder diffraction data for the scheelite-type SmCrO$_4$ oxide at ambient conditions (λ=0.154056 nm) (Vertical marks denote the Bragg positions for the SmCrO$_4$ scheelite polymorph (first line), and perovskite impurity SmCrO$_3$ (second line, 3 wt.%))

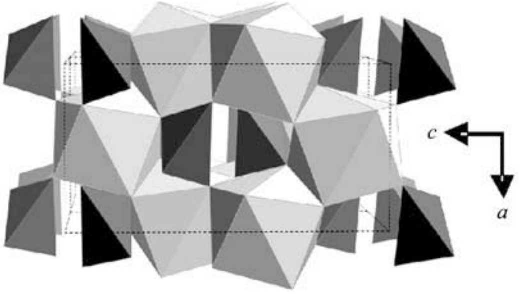

Fig. 2 Perspective view of the scheelite-type structure in the ac-plane showing the arrangement of the [CrO$_4$] tetrahedra (dark grey) and the [SmO$_8$] bisdisphenoids (light grey)

Table 1 Structural parameters and some of the most relevant interatomic distances and angles of SmCrO$_4$-scheelite and zircon

SmCrO$_4$				Zircon-type			Scheelite-type
Space group				*I* 4$_1$/*amd*			*I* 4$_1$/*a*
Cell parameters/nm	a			0.725104(11)			0.507704(20)
	c			0.635305(10)			1.15620(6)
Volume/nm^3				0.334028(9)			0.298026(23)
Rietvel *R*-factors	R_p			0.277			0.466
	R_{wp}			0.168			0.245
	χ^2			1.51			1.54
Bragg *R*-Factors	R_B			0.056			0.177
	R_f			0.047			0.207
Atoms, Wychoff positions, occupations, *x/a, y/b, z/c*	Sm	4a	1	0, ¾ , ⅛	4b	1	0, ¼ , ⅝
	Cr	4b	1	0, ¼ , ⅜	4a	1	0, ¼ , ⅛
	O	16h	1	0.0	16f	1	0.2524(20)
				0.4275(12)			0.6130(26)
				0.2108(11)			0.5520(10)
B_{iso}/nm^2				0.0020(3)			0.0050(3)
d(Cr–O)/nm				0.1657(8)×4			0.1667(14)×4
d(Sm–O)/nm				0.24011(16)×4			0.2398(12)×4
				0.2492(6)×4			0.2512(12)×4
Cr–O–Sm (°)				154.1(4)×1			123.0(6)×1
				97.9(3)×1			133.0 (6)×1

This decreasing in volume has been explained by Kusaba et al.[8] and recently by Wang et al.[9] who proposed a mechanism to describe the zircon-to-scheelite transition which involves a small displacement of oxygen atoms giving as result a more efficient packing in the scheelite polymorph compared with the zircon due to the cooperative displacements of the [CrO$_4$] tetrahedra. As can be observed in Table 1, the variation in the Sm-O distances for both polymorphs justifies the changes in the symmetry from D_{2d} to S_4 in going from SmCrO$_4$-zircon to the SmCrO$_4$-scheelite. However, it can be viewed remarkable changes in O-Sm-O and Cr-O-Sm bond angles between the zircon and scheelite phases that will be very important to explain the proposed reconstructive model to explain this first order structural zircon-scheelite phase transition[10].

2.2 Magnetic properties

The temperature dependence of the molar magnetic susceptibility for SmCrO$_4$-scheelite is shown in Fig. 3. The susceptibility does not follow Curie-Weiss behaviour as happened for most lanthanide cations, because of the particular behaviour of Sm^{3+}. The magnetic moment decreases with the decrease in temperature as was viewed in the χT vs. T plot (Fig. 1 inset). This behaviour can be explained as it is

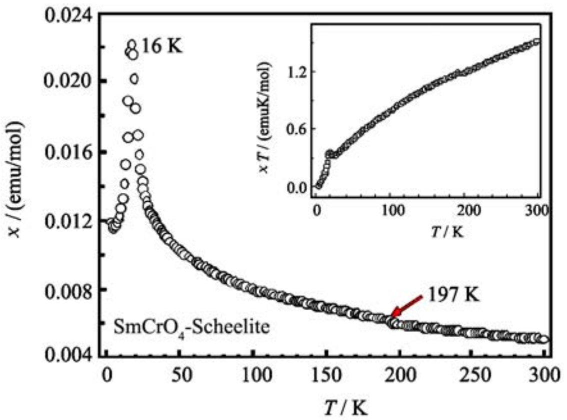

Fig. 3 Magnetic susceptibility vs temperature for SmCrO$_4$ scheelite. Inset is the χT vs T plot

well known that the spacing of the multiplets $^6H_{J/2}$ levels are not too large compared to the thermal energy *kT*. For this reason not all the Sm^{3+} ions will be in their $^6H_{5/2}$ ground state and the $^6H_{J/2}$ excited states should be taken in consideration to calculate the magnetic susceptibility[11]. The obtained magnetic moment at room temperature after discounting the Cr^{5+} contribution yields a value of 2.35μ$_B$ which fairly agrees with that previously determined for SmCrO$_4$-zircon[6].

The anomaly observed at 197 K in both χ vs T and χT vs T plots is due to the presence of small amount of the distorted perovskite SmCrO$_3$ which becomes canting antiferromagnetically ordered at 197 K[12]. The net maximum observed at 16 K indicates the presence of antiferromagnetic interaction in which Sm^{3+} and Cr^{5+} sublattices are involved. In the case of the zircon polymorph the Neél temperature is 14.9 K[6].

The analysis of the structure will be very important to explain the mechanism through this antiferromagnetic interaction taking place. In this sense, direct Sm^{3+}-Sm^{3+} interactions and/or superexchange of the type Sm^{3+}-O-Sm^{3+} [Sm$_2$O$_{14}$] bisdisphenoid units could be operative. However, this type of interactions should be neglected, since in the case of the isostructural RXO$_4$, where X= P, V and As, they are operative down to 4.2 K. This fact was explained by a consequence of well shielded 4f orbital by the outer 5s and 5p. However, a more realistic mechanism should involve the CrO$_4$ tetrahedra that interact with the [SmO$_8$] bisdesphenoid giving rise to superexchange pathways of the type Sm-O-Cr-O-Sm where the Cr^{5+} plays an important role as promoter of the interactions in the Sm sublattice.

Both the relative large Sm^{3+}–Sm^{3+} distances of 0.384723(11) nm and the superexchange angles, which are very different from 180°, yield a poor ovelap of the 4f orbitals which justifies the low value such as 16 K found for the Néel temperature for the scheelite form of this SmCrO$_4$ oxide. Magnetization measurements performed at different temperatures are shown in Figs. 4 and 5 for the new scheelite SmCrO$_4$ polymorph. As shown in Fig. 4, at temperatures higher than 16 K, which is the Néel temperature, the MvsH plots show a linear behaviour as it was expected in the paramagnetic regime for this compound. By contrast, below the Néel temperature, the μ vs H plot, Fig. 5, shows an S-shape feature characteristic for an antiferromagnetic compound showing a metamagnetic transition. This metamagnetic transition is clearly visualised when the derivative *d*(M/H) is plotted against *H* and a maximum can be observed around 3.2 T at 12 K. While at 2 K the maximum appears to be located above 5 T.

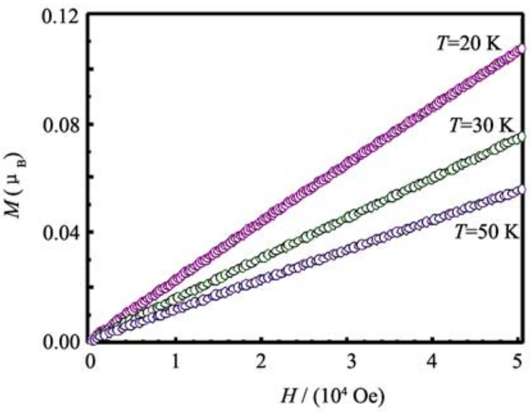

Fig. 4 Magnetization curve for the SmCrO$_4$ scheelite at temperatures above the Néel temperature

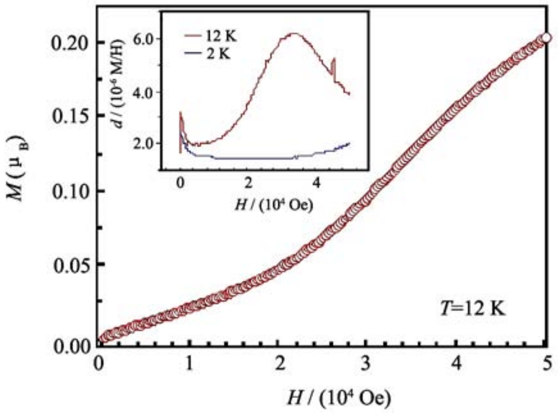

Fig. 5 Magnetization vs magnetic field at 12 K. The inset represents the *d*(M/H) vs *H* at 12 K (upper curve) and 2 K (lower curve)

3 Conclusions

The new scheelite-SmCrO$_4$ polymorph was obtained from zircon-type SmCrO$_4$ treated at 4 GPa and 803 K. This scheelite polymorph showed an antiferromagnetic behaviour with T_N=16 K. A metamagnetic transition was shown at 12 K with a critical field of 3.2 T.

Acknowledgement: The authors are grateful to Spanish MICINN and FEDER for financial support under research project No. MAT200763497, and also SOPRANO project under Marie Curie actions (FP7).

References:

[1] Stubican V S, Roy R. High-pressure scheelite-structure polymorphs of rare-earth vanadates and arsenates. *Z. Kristallogr.*, 1963, **119S**: 90.

[2] Zhang F X, Lang M, Ewing R C, Lian J, Wang Z W, Hu J, Boature L A. Pressure induced zircon-type to scheelite-type

phase transition in $YbPO_4$ and $LuPO_4$. *J. Solid State Chem.*, 2008, **181**: 2633.

[3] Long Y W, Yang L X, Yu Y, Li F Y, Yu R C, Jin C Q. Synthesis, structure, magnetism and specific heat of $YCrO_4$ and its zircon-to-scheelite phase transition. *Phys. Rev. B*, 2007, **75**: 104402.

[4] Climent-Pascual E, Romero de Paz J, Gallardo-Amores J M, Sáez-Puche R. Ferromagnetism vs. antiferromagnetism of the dimorphic $HoCrO_4$ oxide. *J. Solid State Chem.*, 2007, **9**: 574.

[5] Climent Pascual E, Gallardo Amores J M, Sáez Puche R, Castro M, Taira N, Romero de Paz J, Chapon L C. Zircon to scheelite phase transition induced by pressure and magnetism in $TbCrO_4$. *Phys. Rev. B*, 2010, **81**: 174419.

[6] Jiménez E, Isasi J, Sáez-Puche R. Synthesis, structural characterization and magnetic properties of $RCrO_4$ oxides, R=Nd, Sm, Eu and Lu. *J. Alloys Compd.*, 2000, **312**: 53.

[7] Rodriguez-Carvajal J. FULLPROF Program. ILL, Grenoble, France, 1990.

[8] Kusaba K, Yagi T, Kikuchi H, Syomo Y. Structural considerations on the mechanism of the shock-induced zircon-scheelite transition in $ZrSiO_4$. *J. Phys. Chem. Solids*, 1986, **47**: 675.

[9] Wang X, Loa I, Syassen K, Hanfland M, Ferrand B. Structural properties of the zircon- and scheelite-type phases of YVO_4 at high pressure. *Phys. Rev. B*, 2004, **70**: 064109.

[10] Smirnov M B, Mirgorodsky A P, Kazimirov V Yu, Guinebretière R. Bond-switching mechanism for the zircon-scheelite phase transition. *Phys. Rev. B*, 2008, **78**: 094109.

[11] Van Vleck J H. The Theory of Electric and Magnetic Susceptibilities. Oxford Univ. Press, 1965.

[12] De Combarieu A, Mareschal J, Michel J C, Sivardière J. Chaleurs specifiques entre 1,2° et 5 °K de quelques perovskites de terres rares. *Solid State Commun.*, 1968, **6**: 257.

Appendix II

Journal of Solid State Chemistry ▮ (▮▮▮▮) ▮▮▮–▮▮▮

Contents lists available at SciVerse ScienceDirect

Journal of Solid State Chemistry

journal homepage: www.elsevier.com/locate/jssc

Synthesis and magnetic properties of the high-pressure scheelite-type $GdCrO_4$ polymorph

A.J. Dos santos-García [a,*], E. Climent-Pascual [a], J.M. Gallardo-Amores [a], M.G. Rabie [a], Y. Doi [b], J. Romero de Paz [c], B. Beuneu [d], R. Sáez-Puche [a]

[a] Departamento de Química Inorgánica I, Facultad de Ciencias Químicas, Universidad Complutense de Madrid, 28040 Madrid, Spain
[b] Division of Chemistry, Graduate School of Science, Hokkaido University, Sapporo 060-0810, Japan
[c] CAI Técnicas Físicas, Facultad de Ciencias Físicas, Universidad Complutense de Madrid, E-28040 Madrid, Spain
[d] Laboratoire Léon Brillouin (CEA-CNRS), CEA/Saclay—91191 Gif-sur-Yvette cedex, France

ARTICLE INFO

Article history:
Received 20 February 2012
Received in revised form
24 April 2012
Accepted 24 April 2012

Keywords:
Scheelite-type structure
Zircon-type structure
Polymorphism
3*d*–4*f* interactions
High pressure synthesis
Metamagnetism

ABSTRACT

The scheelite-type polymorph of $GdCrO_4$ has been obtained from the corresponding zircon-type compound under high pressure and temperature conditions, namely 4 GPa and 803 K. The crystal structure has been determined by X-ray powder diffraction. This $GdCrO_4$ scheelite crystallizes in a tetragonal symmetry with space group $I4_1/a$ (No. 88, $Z=4$), $a=5.0501(1)$ Å, $c=11.4533(2)$ Å and $V=292.099(7)$ Å^3. The thermal decomposition leads to the formation of the zircon–polymorph as intermediate phase at 773 K to end in the corresponding $GdCrO_3$ distorted perovskite-structure at higher temperatures. Magnetic susceptibility and magnetization measurements suggest the existence of long-range antiferromagnetic interactions which have been also confirmed from specific heat measurements. Neutron powder diffraction data reveal the simultaneous antiferromagnetic Gd^{3+} and Cr^{5+} ordering in the scheelite-type $GdCrO_4$ with a $T_N \sim 20$ K. The magnetic propagation vector was found to be $k=(0\,0\,0)$. Combined with group theory analysis, the best neutron powder diffraction fit was obtained with a collinear antiferromagnetic coupling in which the $m_{Cr^{5+}}$ and $m_{Gd^{3+}}$ magnetic moments are confined in the tetragonal basal plane according to the mixed representation $\Gamma_6 \oplus \Gamma_8$.

© 2012 Elsevier Inc. All rights reserved.

1. Introduction

Among the crystal structures occurring for ABO_4 compounds, zircon-type $ZrSiO_4$ has been the most studied polymorph mainly due to its ubiquitous presence on the earth's crust. In order to emphasize its relevance, the mentioned zircon-type structure is adopted for a long range of radii ratios and A/B cation combinations; for instance, several minerals and synthetic silicates, phosphates, borates, vanadates, arsenates and chromates are isostructural with zircon [1]. Furthermore, a systematic series of high pressure–temperature phase transformations have been observed in the vast majority of the compounds crystallizing in this type-structure [2–5]. In fact, the more stable high-pressure polymorph of zircon crystallizes in the scheelite-type structure by reducing ~10% the unit cell volume across the transition. This is believed to occur via a martensitic-phase transformation, that is, there exist a subtle but rapid rearrangement of atomic positions nonetheless in a cooperative way since the coordination of the A and B cations, bisdisphenoids-$[AO_8]$ and tetrahedral-$[BO_4]$ respectively, do not change through the transition [6,7]. However, the microscopic mechanism, that is, displacive or reconstructive-model, remains highly controversial [6–8].

$RCrO_4$ oxides (R=rare earth) form a family of compounds with very interesting structural behavior and magnetic properties. At room pressure, these chromates crystallize in two different polymorphs: monazite-like-structure, space group (S. G.) $P2_1/n$, is found for the $LaCrO_4$ first member [9] and otherwise, zircon-like-structure with tetragonal symmetry, S. G. $I4_1/amd$, stems for the remaining rare earths [10]. The $PrCrO_4$ compound constitutes a special case since it is dimorphic; that is, is stable within both monazite and zircon structures at room pressure [11–13]. On the other hand, under pressure, these zircon-type structures exhibit a phase transition to a scheelite-type structure, S.G. $I4_1/a$ [14–16]. As it was previously stated, phase transitions induced by pressure from zircon- to scheelite-type structure have been studied in some detail for the vanadates and arsenates families RXO_4 (X=V and As) [17], however only few studies have been reported for the analogous $RCrO_4$ oxides. This fact and in general terms, the scarcity of Cr^{5+}-containing compounds seems to be due to the rather low stability of the Cr^{5+} oxidation state against the more stable Cr^{3+} and Cr^{6+} ones [18,19]. Recently, it has been reported the high pressure synthesis of the scheelite-type polymorph of

---

[*] Corresponding author. Fax: +34 91 394 4352.
E-mail address: adossant@quim.ucm.es (A.J. Dos santos-García).

0022-4596/$ - see front matter © 2012 Elsevier Inc. All rights reserved.
http://dx.doi.org/10.1016/j.jssc.2012.04.044

$RCrO_4$ (R=Nd, Sm, Tb–Tm and Y) oxides and the study of their magnetic properties [14–16,20–24]. It is important to notice that magnetic properties show dramatic changes, from zircon- to scheelite-type structure, in these polymorphs. In this sense, the variation of the R^{3+}–O–Cr^{5+} superexchange pathways resulting from this structural transition leads also to a change of the net magnetic interactions going from ferromagnetic to antiferromagnetic in the zircon-type to the scheelite-type polymorph respectively. Also, neutron diffraction studies have been carried out to shed light on the magnetic structure of these scheelite-type antiferromagnetic oxides $RCrO_4$ (R=Tb, Er and Tm) with Néel temperatures of 29, 22 and 27 K, respectively [21,24]. These analyses show collinear magnetic structures where both R^{3+} and Cr^{5+} sublattices become simultaneously ordered, with a propagation vector k=(0 0 0) for all these scheelite-type oxides. In the case of $TbCrO_4$-scheelite the magnetic structure is described by the antiferromagnetic coupling of terbium and chromium magnetic moments aligned along the c-axis. However, in $ErCrO_4$ and $TmCrO_4$-scheelite oxides, erbium (or thulium) and chromium magnetic moments lay in the ab-plane. The differences found in the magnetic structures seem to be due to the intrinsic rare earth R^{3+} anisotropy.

In the present work we report the synthesis conditions, thermal stability and the results of the neutron diffraction study on powder sample of the high pressure scheelite-type $GdCrO_4$ polymorph. Magnetic properties have been studied by means of magnetization and specific heat measurements, and the possible magnetic structure compatible with the symmetry and bulk magnetic properties has been obtained by following the group theory analysis.

2. Experimental

2.1. Sample preparation

$GdCrO_4$ scheelite-type polymorph has been prepared from a polycrystalline powder sample of zircon polymorph as precursor. The zircon $GdCrO_4$ polymorph was synthetized by heating the stoichiometric amount of the corresponding $Gd(NO_3)_3 \cdot 6H_2O$ and $Cr(NO_3)_3 \cdot 9H_2O$ nitrates in a continuous oxygen flow according with the experimental procedure described elsewhere [19,10]. After that, the already obtained $GdCrO_4$ zircon-type polymorph was loaded in air within a platinum crucible and treated in a Conac-type pressure module at 4 GPa and 803 K for 30 min. It is worth noting that modifications of these experimentally optima synthesis conditions, specially increasing the temperature, lead to the formation of the corresponding $GdCrO_3$ distorted perovskite-phase as secondary phase.

2.2. Structural analysis and thermal decomposition

The sample was characterized by X-ray powder diffraction (XRD) performed on a Philips X'Celerator diffractometer (Cu Kα_1-radiation). The XRD pattern was refined with the Rietveld method using the FullProf Suite program [25]. A study of the thermal stability of the scheelite-type $GdCrO_4$ has been carried out by in-situ XRD at different temperatures using a Philips X'Pert PRO MPD difractometer equipped with a high-temperature camera Anton Paar HTK1200. Diffractograms were recorded from room temperature up to 1173 K, with ΔT=100 K *per*-measurement. The heating rate was 10 K min^{-1}, with a dwelling time of 15 min for temperature stabilization before running the measurement.

Neutron powder diffraction experiments were carried out on the 7C2 two-axis diffractometer hot source at the Orphée reactor (Laboratoire Léon-Brillouin, Saclay-France). The incident wavelength of 0.581 Å was selected by the monochromator Ge (3 1 1). To minimize the absorption, the powder was loaded in a vanadium annular can. Since vanadium scattering is (almost) purely elastic, eventual residual background was also subtracted. Long scans were collected well above and below the Nèel temperature to determine the magnetic structure. On the other hand, shorter scans at 10, 17, 24 and 40 K were also recorded to follow the temperature dependence of the magnetic reflections. Lattice parameters, atomic positions, overall temperature factor and magnetic moments were refined by the Rietveld method using the FullProf Suite program. Diffraction peaks were fit with the Thompson–Cox–Hastings pseudo-Voigt. The background was determined by means of a linear interpolation. The symmetry analysis was performed by means of the program BasIreps [26].

2.3. Specific heat and magnetic measurements

Magnetic susceptibility measurements were performed at 0.1 T over the temperature range 1.9–300 K, using a SQUID Quantum Design XL-MPMS magnetometer in zero field cooling (ZFC) and field cooling (FC) conditions. Magnetic field dependence of the magnetization was analyzed 2, 8, 30 and 50 K up to 5 T.

Specific heat data were performed using Quantum Design PPMS equipment. A small portion of the sample was fixed to the sapphire platform of the sample holder by a small amount of Apiezon grease. The specific heat of the sample holder and the grease was measured separately in the same conditions and this addendum was subtracted from the experimental values in order to obtain the specific heat of the scheelite phase.

3. Results and discussion

3.1. Structural characterization

The Rietveld refinement of the powder XRD data is depicted in Fig. 1. The Bragg reflections has been indexed in the tetragonal space group $I4_1/a$ where the Gd, Cr occupy the special positions 4b (0 1/4 5/8) and 4a (0 1/4 1/8) respectively, while the oxygen occupies a general site. Table 1 shows lattice parameters, atomic positions, main atomic distances and bond angles; the agreement factors for both $GdCrO_4$ polymorphs are also included. These values are in good agreement with those obtained from other chromates crystallizing in the scheelite type structure. As often observed in high pressure samples of multi-cationic materials, $GdCrO_3$ (~3%), Gd_2O_3 (~5%) and Cr_2O_3 (~5%) impurities were

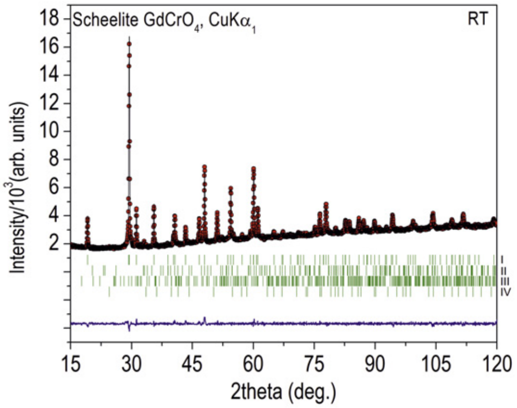

Fig. 1. Rietveld refinement of the X-ray powder diffraction data of $GdCrO_4$ (first row of ticks). Impurities taken into account are $GdCrO_3$ (second row), and small amounts of Gd_2O_3 (third row) and Cr_2O_3 (fourth row).

Please cite this article as: A.J. Dos santos-García, et al., J. Solid State Chem. (2012), http://dx.doi.org/10.1016/j.jssc.2012.04.044

Table 1
Atomic parameters, main interatomic distances and bond angles for both $GdCrO_4$ polymorphs, calculated from the Rietveld refinement of laboratory X-ray diffraction data. Agreement factors are also included.

	$GdCrO_4$			Zircon[a]		Scheelite
Space group				$I\ 4_1/amd$		$I\ 4_1/a$
Cell parameters (Å)	a			7.204		5.0501(1)
	c			6.315		11.4533(2)
	$V(Å^3)$			327.73		292.099(7)
Atoms, Wyckoff	Gd	4*a*	1	000	4*b*	0, 1/4, 5/8
positions,	Cr	4*b*	1	0, 0, 1/2	4*a*	0, 1/4, 1/8
occupations, *x*/*a*, *y*/*b*, *z*/*c*	O	16*h*	1	0.0, 0.182, 0.332	16*f*	0.2468(10), 0.6163(13), 0.5490(6)
U_{iso} (Å^2)						0.11(4)
Rietveld R-factors	$R_{p.}$					0.0181
	wR_p					0.0244
Bragg R-factor	R_B					0.0372
Main interatomic distances (Å) and bond angles (deg.) at room temperature						
	d(Cr–O)			1.687 × 4		1.688(6) × 4
	d(Gd–O)			2.349 × 4 2.473 × 4		2.394(6) × 4 2.446(6) × 4
∠(Cr–O–Gd)				153.76 × 2 96.96 × 2		121.06(28) × 2 134.1(3) × 2
∠(O–Cr–O)				102.04 × 1		105.4(3) × 4
				113.31 × 2		117.91(26) × 2
∠(O–Gd–O)				154.5 × 2		137.36(18) × 2
				92.8 × 4		97.6(20) × 4
				136.0 × 4		131.6(2) × 4
				64.0 × 2		70.8(2) × 2

[a] Data taken from Ref. [10].

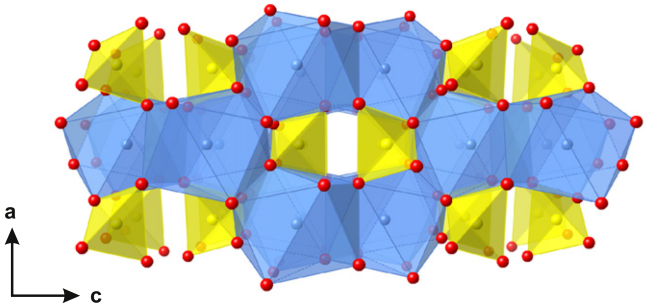

Fig. 2. Crystal structure of the $GdCrO_4$ scheelite polymorph. Cr sits at the tetrahedra while Gd resides in bisdisphenoids.

detected [27]. In both the structural refinement and the magnetic properties study these impurity contents were taken into account. From the distances one can see that, in zircon as well as in scheelite, chromium cations are placed in tetrahedra while gadolinium cations sit in bisdisphenoid or dodecahedra. It is interesting to notice that there is a small variation on the Cr–O distances between these polymorphs, that is, from 1.687(7) Å in zircon to 1.688(6) Å in scheelite. This is clearly indicative that the Cr–O distances are rather stiff and as consequence of that, when pressure is applied, the $[CrO_4]$ units remain essentially undistorted. Although, the 11% reduction in volume observed in the phase transition from zircon to scheelite could be associated to the decreasing in the size of the $[RO_8]$ bisdisphenoids, which are indeed highly deformed upon compression compared to $[CrO_4]$ tetrahedra, as one can see in Table 1, the Gd–O distances are rather similar in both compounds. It is also interesting to mention that the different high pressure behavior of the Gd–O distances (note that one is increasing and the other is decreasing when applying pressure!), 4 × (2.349) and 4 × (2.473) in zircon (taken from Ref. 10)and 4 × (2.394 (6)) and 4 × (2.446 (6)) in scheelite, can be explained from a geometrical approach [28]. $[GdO_8]$ bisdisphenoids can be understood as two interpenetrating tetrahedra, one is elongated, and the other is squat. Therefore, the bonds to the corners of the squashed tetrahedron are slightly shorter than those to the corners of the elongated one. Thus, the deformations operate in opposite senses being both tetragonal distortions parallel to the 4_1 screw-axis in both cases. This is in fact, related to the crystalline anisotropy and the c/a tetragonal ratio of the scheelite, which is more than twice that the zircon. Taking into account these considerations it appears that the decreasing of volume going from zircon to scheelite is mainly due to the more effective packing of the $[CrO_4]$ and $[GdO_8]$ polyhedra in the high pressure scheelite polymorph.

In light of these observations, the scheelite structure can be described as formed by corner sharing chains of alternating $[CrO_4]$ tetrahedra and $[GdO_8]$ bisdisphenoids units along the *a*-axis of the structure, see Fig. 2. Along the *c*-axis, the $[GdO_8]$ polyhedra of two consecutive chains are sharing edges giving rise to dimeric units of $[Gd_2O_{14}]$ composition. From this structural analysis, one can extract that the Gd^{3+}–O–Cr^{5+} superexchange pathway will govern the overall magnetic behavior of the $GdCrO_4$ scheelite-type polymorph since direct Gd^{3+}–Gd^{3+} or superexchange Gd^{3+}–O–Gd^{3+} interactions do not operate at temperatures higher than 4.2 K due to the poor overlap of the inner 4*f* orbitals and the $[CrO_4]$ tetrahedral units are well isolated from each other as in the case of the zircon [29].

Fig. 3 shows the thermal evolution of the X-ray diffraction patterns for $GdCrO_4$-scheelite. It can be observed that the scheelite-type structure remains up to 673 K, but further increase of the temperature up to 773 K result in a structural transition to the ambient $GdCrO_4$ zircon-type. At 873 K both the $GdCrO_4$-zircon and $GdCrO_3$ coexist and a further increase of the temperature up to 973 K produces the full decomposition of $GdCrO_4$ to the distorted $GdCrO_3$ perovskite phase with orthorhombic symmetry (S. G. *Pnma*). This is indeed a clear indication of the metastability of the high-pressure scheelite polymorph. This reversible phase transition back to the more stable zircon–polymorph at room pressure is kinetically activated by increasing the temperature. Finally, the Cr^{5+} oxidation state in the $GdCrO_4$-zircon phase reduces to the high stable Cr^{3+} one and concomitantly to this,

Please cite this article as: A.J. Dos santos-García, et al., J. Solid State Chem. (2012), http://dx.doi.org/10.1016/j.jssc.2012.04.044

there also exist an oxygen loss to stabilize the $GdCrO_3$ perovskite-structure.

3.2. Magnetic properties

Fig. 4 shows the temperature dependence of the magnetic susceptibility from 300 down to 2 K measured at zero field cooling (ZFC) mode at 100 Oe for the $GdCrO_4$-scheelite polymorph. As it has been pointed out in previous sections, there also exists a certain amount of $GdCrO_3$ perovskite (~3%). Taking into account that Cr ions order AFM at 170 K and Gd ions do it below 5 K [27], the reciprocal susceptibility data has been properly corrected by subtracting this magnetic contribution. Afterwards, it can be observed that the susceptibility follows a Curie–Weiss behavior over a wide temperature range (see Fig. 4(inset)), namely 300–50 K. The Weiss constant (θ) and the magnetic moment obtained are 12.69 (6) K and 8.080 (1) μ_B respectively, which agrees well with that expected for the Gd^{3+} ($S=7/2$) and Cr^{5+} contribution (8.12 μ_B) considering that for the latter, the tetrahedral coordination yields a value slightly lower than that expected for $S=1/2$ taking into account the spin–orbit contribution [30]. Although no maxima are observed in this plot, a careful examination of the data reveals the existence of sluggish changes in the slope at low temperatures. In fact, two maxima observed at 20 and 7 K, in the χT vs. T representation (depicted in Fig. 5) are indicative of long-range magnetic interactions. Furthermore, Fig. 5 inset shows a peak centered around 20 K in the $d(\chi T/dT)$ vs. T plot. This is indeed an evidence of the temperature where the magnetic entropy starts to drop as result of an AFM ordering. Furthermore, we are in the position to assert that this AFM ordering is due to the simultaneous ordering of Gd^{3+} and Cr^{5+} magnetic sublattices, which has been determined by neutron diffraction experiments at 2 K and, will be described Section 3.3. Nonetheless, there are still several issues that cannot be explained attributing the overall magnetic behavior of the $GdCrO_4$-scheelite only to cooperative antiferromagnetic interactions. In fact, at temperatures below T_N, there is a noticeable difference between FC and ZFC branches which constitutes a clear indication of a weak-ferromagnetic component, Fig. 5. It can be easily understood if a tiny canting angle is arising between the magnetic moments of the AFM sublattices. In light of this, we have performed further field dependent magnetization measurements at different temperatures (Fig. 6). An expected paramagnetic behavior is observed at temperatures well above the T_N; however, a slight bending of the plot measured at 30 K is clearly indicative of incipient magnetic interactions. Indeed, a non-linear M–H variation is observed in the plots obtained at 18 K, 8 K and 2 K. These results are in concordance with those observed in the susceptibility measurements and evince, as it has been previously reported for other isostructural chromates that, the $GdCrO_4$-scheelite also exhibits a field-induced metamagnetic transition [14,15,20,23], that takes place at a critical magnetic field as low as 0.1 T according to the isotropic character of the $^8S_{7/2}$ ground term of Gd^{3+} (see Fig. 6). This is also an evidence of the antiferromagnetic ordering in which both Cr^{5+} and Gd^{3+} sublattices appear to be involved since, as expected, the saturation moment at 2 K takes a value of 7.11 μ_B, which is close to the 8 μ_B considering both the $m_{Cr^{5+}}$ and $m_{Gd^{3+}}$ contribution. Moreover, the relatively high Neel temperature observed for the $RCrO_4$ zircon and scheelite polymorphs support that Cr^{5+} ions act as promoter of the magnetic interactions in the rare-earth sublattice. It is worth

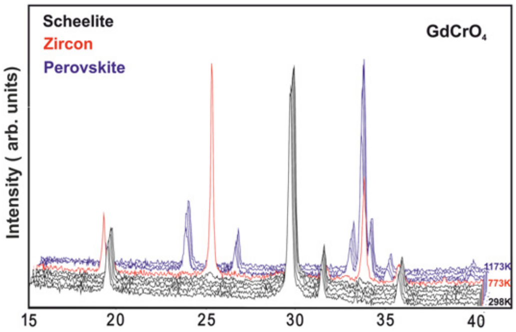

Fig. 3. Powder X-ray diffraction patterns for the $GdCrO_4$ scheelite polymorph measured at temperatures between 298 and 1173 K.

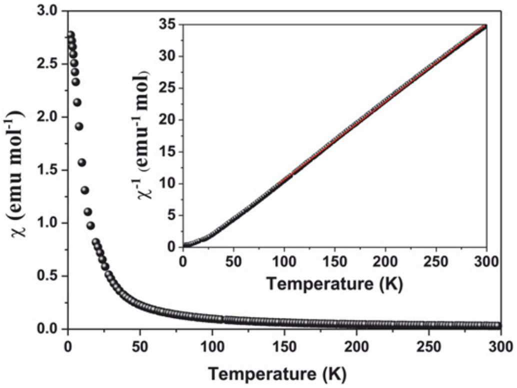

Fig. 4. Temperature dependence of the magnetic susceptibility under an external field of 100 Oe. At inset, reciprocal susceptibility plot and the corresponding Curie–Weiss fitting at high temperatures.

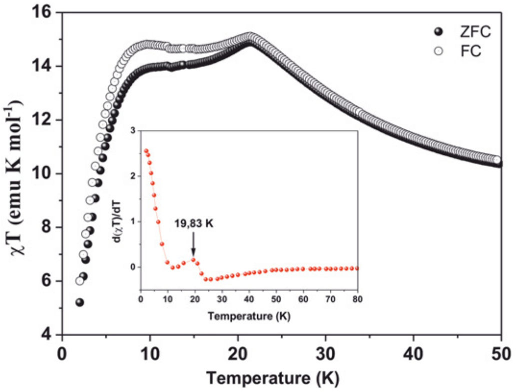

Fig. 5. χT vs. T plot at ZFC and FC conditions under an external field of 100 Oe. Inset shows the temperature where the magnetic entropy starts to drop.

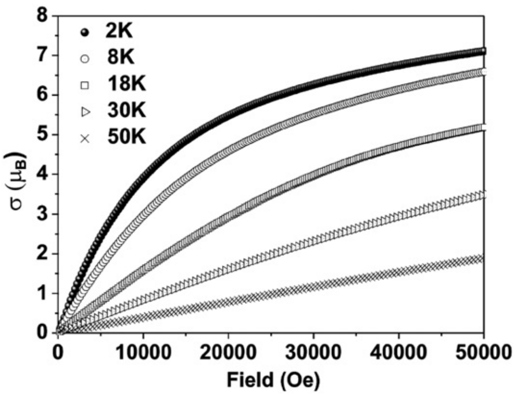

Fig. 6. Field dependent magnetization measurements at different temperatures. The crossing of the top curves at 1000 Oe is indicative of metamagnetism.

noting here that for isostructural RVO_4 and RPO_4 family of compounds, where V and P are non-magnetic ions, the ordering temperatures are very low indeed; that is, as low as 100 mK in $TmVO_4$ and 2.49 K in the analogous $GdVO_4$ zircon compound.

The origin of the AFM transition centered at 20 K can be fully explained according to the superexchange pathways occurring in this scheelite. From the structural analysis, Gd-bisdisphenoids and Cr-tetrahedra are only sharing corners. Furthermore, there is only one set of crystallographically equivalent Gd and Cr atoms respectively and, as consequence of that, there only exists one type of Gd^{3+}–O–Cr^{5+} superexchange interactions with two close bond angles as it is indicated in Table 1. Therefore, the second and unexpected maximum apparent in susceptibility at 7 K cannot be explained in terms of the presence of several superexchange interactions which operate at different temperatures. Furthermore, note that the $GdCrO_3$-perovskite which is present as secondary phase, orders AFM at 170 K; this could be the main reason of the increasing of the susceptibility below 5 K, because the Gd ordering temperature for the perovskite is as low as 4 K [27].

A similar susceptibility data has been recently reported in the isostructural $DyCrO_4$-scheelite [23], with 24 K and 18 K consecutive temperature transitions. The first maximum is attributed by the authors to an AFM transition, originated from the Cr–O–Dy interactions according to the Anderson–Goodenough–Kanemori (AGK) empirical rules [31–33]. However, in zircon and scheelite structures 3*d* and 4*f* electrons are involved, there also exist dramatic changes in the cation–polyhedra coordination (cations are not in corner-sharing octahedra!) and therefore Cr–O–R angles differ substantially from 180°. As consequence of that, the AGK empirical rules are not applicable in these polymorphs. On the other hand, the second maximum is explained in terms of a temperature dependence of molecular field, as reported in the isostructural $TbCrO_4$ scheelite compound [21]. In order to investigate these anomalies, we have performed specific heat measurements in the $GdCrO_4$-scheelite. The Cp vs. T plot depicted in Fig. 7 shows a λ-type anomaly at 21 K and a kink around 5 K, which are almost coincident with those determined from magnetic susceptibility measurements. These two magnetic transitions are more visible in magnetic specific heat plot, after subtracting the lattice contribution (Fig. 8a) obtained from a combination of the Debye and Einstein models. Then, the C_{lat} of $GdCrO_4$ scheelite was obtained from the sum of the Debye and Einstein models [34,35]:

$$C_{lat} = 9R\left(\frac{T}{\theta_D}\right)^3 \int_0^{\theta_D/T} \frac{(\theta_D/T)^4 e^{\theta_D/T}}{(e^{\theta_D/T}-1)^2} d(\theta_D/T) + R\sum_{i=1}^{3} \frac{(\theta_{E_i}/T)^2 e^{\theta_{E_i}/T}}{(e^{\theta_{E_i}/T}-1)^2}$$

where θ_D (224 K) is the Debye temperature, and θ_{E1}, θ_{E2} and θ_{E3} (372.11, 652,75 and 1082.11 K respectively) are the Einstein temperatures. The calculated C_{lat} values are shown as a solid line in Fig. 7. Then, the magnetic entropy was determined by using the equation $S_{mag} = \int_0^T C_{mag}/T dT$. The magnetic specific heat below 4 K was extrapolated by the relation $C_{lat} \propto T^3$ from spin-wave model proposed for an antiferromagnet [36]. The experimental magnetic entropy (Fig. 8b) takes the value of 17 J mol^{-1} K^{-1}, which slightly differs from the theoretical value, calculated from the contribution of Cr^{5+} ($S=1/2$) and Gd^{3+} ($S=7/2$) ions; that is, 5.76 and 17.29 J mol^{-1} K^{-1} respectively. The discrepancy between these two values could be due to covalent bond of the dx^2-y^2 empty orbital and Zeeman splitting of the $S=7/2$ ground state [30]. Such underestimation of spin entropy might be also due to an overestimation of the lattice contribution or the operability of short range order above the T_N. As consequence of this splitting only some of the Zeeman-split lower energy levels will be involved in these magnetic transitions and, consequently, the experimental entropy is reduced. It is interesting to point out here that, structural distortions to low-temperature orthorhombic symmetry seem to be common in the $RCrO_4$ family of compounds crystallizing in the zircon-like-structure [37]. In the case of the $DyCrO_4$-zircon compound, the λ-type anomaly observed at 23 K is also coincident with that observed

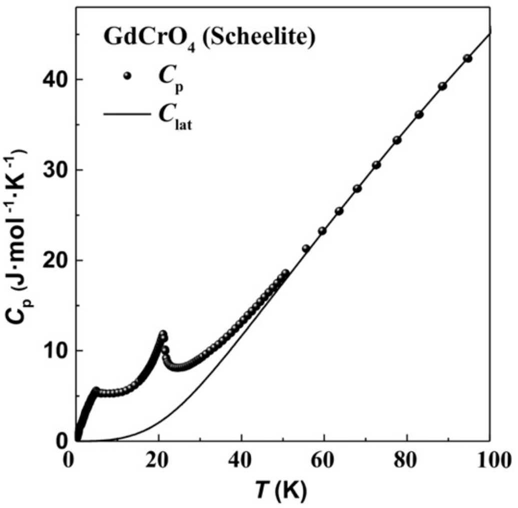

Fig. 7. Heat capacity as a function of temperature showing two transitions at ~20 K and 7 K.

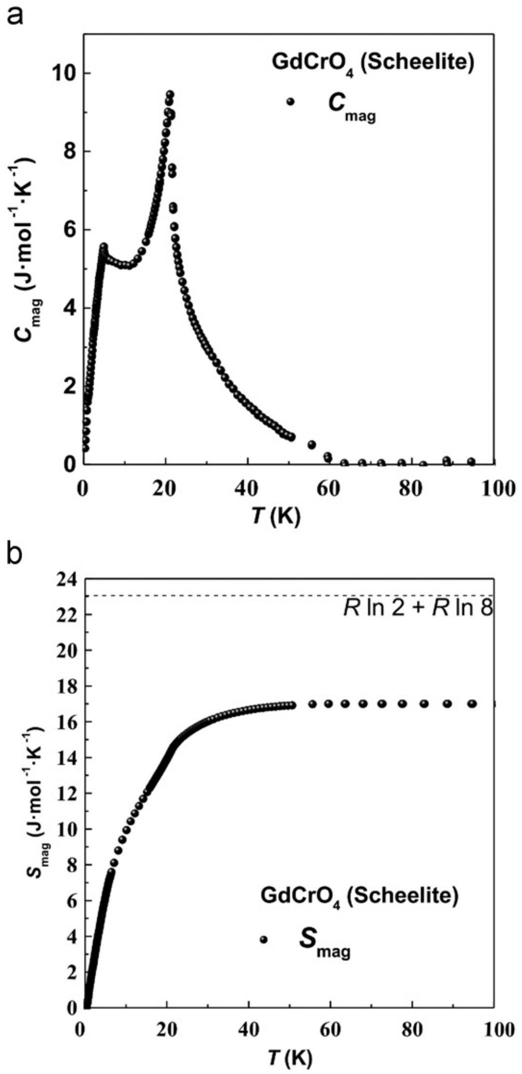

Fig. 8. (a) Temperature dependence of the magnetic specific heat for the $GdCrO_4$ scheelite polymorph and (b) magnetic entropy associated at the magnetic transitions.

in the susceptibility measurements and clearly indicative of a FM ordering. However, the appearance of another anomaly above T_C (32 K) is indicative of a structural phase transition from the tetragonal to orthorhombic symmetry as a consequence of the Jahn–Teller effect. Recent ^{155}Gd and ^{169}Tm Mössbauer spectroscopy results performed in these zircon-like-structure compounds reveal the existence of two sites for the rare earth element, which is clearly indicative of a tetragonal to orthorhombic transition [19]. The vast majority of these transitions can be understood in terms of a cooperative Jahn–Teller effect or spin–orbit coupling in the rare-earth site arising by a change from the tetragonal D_{2d} to orthorhombic D_2 local symmetries [38]. Otherwise, Gd is not a Jahn–Teller ion and there is no spin–orbit coupling.

A possible explanation of the origin of the tetragonal to orthorhombic transition in the $GdCrO_4$-zircon and, probably for the $GdCrO_4$-scheelite polymorph is that this change in symmetry has to arise from the Cr-site and no from the Gd-one. In fact, Cr^{5+} ion with d^1 electronic configuration, in a tetrahedral crystal field, is a Jahn–Teller ion. However, a Jahn–Teller transition is a purely structural transition, and the magnetic ordering occurs at some other (lower) temperature [38]. This Jahn–Teller transition is clearly operative in the $DyCrO_4$-zircon compound, as it was previously stated [37]. On the other hand, the transitions determined by the spin–orbit occur simultaneously with the magnetic ordering. This seems to be the situation in the $GdCrO_4$-scheelite since the transitions observed by specific heat are almost coincident with those determined from magnetic susceptibility measurements. Nonetheless, it is well known that the orbital angular momentum is completely frozen for e_g levels and, therefore, the spin–orbit coupling is inconsequential for them. In other words, the crystal field ground state of Cr^{5+} in tetrahedral coordination, that is ^2E, has not orbital momentum associated and hence spin–orbit coupling will not raise any of its degeneracy. Thus to a first-order approximation it has no effect on the magnetic properties. However, the ^2E term can be mixed with the higher lying ^2T excited state, in which the angular momentum is not frozen. In this case, via spin–orbit coupling, a magnetic anisotropy results; that is, the spins are parallel to the angular momentum which is directed along the deformation axis.

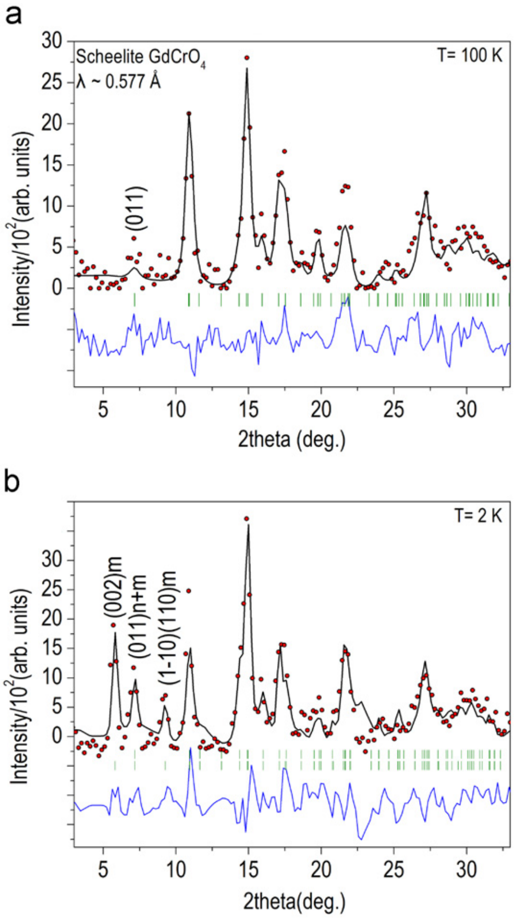

Fig. 9. (a) Rietveld refinement of the neutron diffraction pattern of the $GdCrO_4$ scheelite polymorph at 100 K and (b) at 2 K; first and second rows of vertical ticks correspond to the nuclear and magnetic reflections respectively.

3.3. Magnetic structure determination

Neutron powder diffraction patterns at 100 K and 2 K are shown in Fig. 9a and b respectively. The data have been refined in the $I4_1/a$ space group and the obtained lattice parameters together with the agreement factors are included in Table 2. These data agree with those previously reported from high resolution X-ray diffraction data. The small decreasing found in the lattice parameters observed in going from 100 K to 2 K can be understood by considering the thermal contraction.

From the thermal evolution of the neutron diffraction patterns, depicted in Fig. 10, and especially from that of the strongest (0 0 2) pure magnetic reflection, the estimated Neel temperature is about 20 K. The magnetic reflections appearing below this temperature can be indexed in a commensurate lattice related to the crystallographic one by a propagation vector $k=(0\,0\,0)$. This means no loss in translational symmetry coming from the spin arrangement and so the magnetic all dimensions will be

Table 2
Atomic parameters for the scheelite polymorph of $GdCrO_4$, calculated from the Rietveld refinement of neutron diffraction data obtained at 2 and 100 K. Agreement factors are also included.

Scheelite $GdCrO_4$					
Temperature (K)				100	2
Space group				$I4_1/a$	$I4_1/a$
Cell parameters (Å)	a			5.050(5)	5.047(8)
	c			11.401(23)	11.357(11)
Atoms, Wyckoff	Gd	$4b$	1	0 1/4 5/8	0 1/4 5/8
positions,	Cr	$4a$	1	0 1/4 1/8	0 1/4 1/8
occupations, x/a, y/b, z/c	O	$16f$	1	0.2468, 0.6163, 0.5490	0.2468, 0.6163, 0.5490
U_{iso} (Å^2)				0.033(9)	0.020(10)
Rietveld R-factors	R_p			0.36	0.35
	wR_p			0.44	0.39
Bragg R-factor	R_B			0.25	0.18
Magnetic R-factor					0.19

Please cite this article as: A.J. Dos santos-García, et al., J. Solid State Chem. (2012), http://dx.doi.org/10.1016/j.jssc.2012.04.044

coincident with those of the cell parameters of the crystallographic one. Below $T_N \sim 20$ K, the NPD patterns show only the appearance of additional magnetic peaks forbidden by the reflections conditions in the $I4_1/a$ symmetry as in Fig. 9b. For instance, the huge (0 0 2) and weak (1 1 0), initially surmised purely magnetic reflections [39], can be explained by an arrangement of the magnetic moments in the *ab* plane. Due to the tetragonal symmetry of the crystal structure, the orientation of the basal component of the ordered magnetic moments of the Gd^{3+} ions cannot be unequivocally determined within the *ab* plane and additional intensity below 7 K should not appear for (0 1 1) and (1 −1 0)(1 1 0) reflections. In fact, the notable differences observed in the intensities of the (0 *k l*) and (*h k* 0) group of reflections, before and after the magnetic transition at 7 K, could be attribute to a small lattice distortion from the tetragonal $I4_1/a$ to a pseudo-tetragonal symmetry. However, it is important to note here that the instrumental resolution of the 7C2 diffractometer coupled with the strong absorption inherent to the Gd element, seems to be not sufficient to detect this orthorhombic distortion. Therefore, following the method of the representations proposed by Bertaut [40], which gives the possible magnetic structures compatible with the crystal symmetry, all the possible arrangements of the ordering magnetic moment are determined through the base functions of the irreducible representations of the wave vector G_K, which contains only those symmetry operations of the high temperature space group, that is $I4_1/a$, which keep invariant the propagation vector or transform it in an equivalent vector.

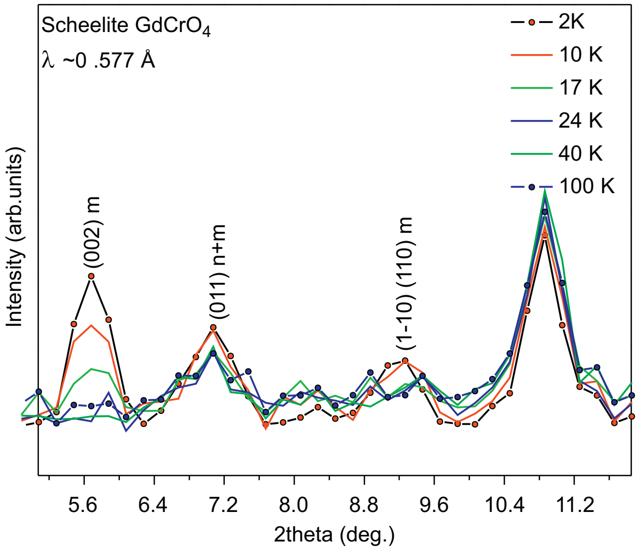

Fig. 10. Neutron diffraction patterns at temperatures ranging from 100 to 2 K for the $GdCrO_4$ scheelite polymorph between 5° and 12°.

In this sense, to generate all the spin configurations compatible with the crystal symmetry and the antiferromagnetic behavior of this oxide a group theory analysis has been carried out by using the program BasIreps [26]. It was found eight irreducible representations Γ_i (i=1–8) for the little group G_K (4/*m*) with k=(0 0 0). Among these, only the mixed representation $\Gamma_6 \otimes \Gamma_8$ allows for a simultaneous antiferromagnetic coupling of the gadolinium and chromium sublattices. The basis vectors of these representations are listed in Table 3. Hence, it is proposed a magnetic structure in which the Gd^{3+} and Cr^{5+} moments lying in the *ab* plane at 20 K. However, the collinear AFM coupling is observed between the magnetic moments lying in the (0 0 l) sheets as shown in Fig. 11. The best fit (magnetic R-factor=0.19), Fig. 9b, to the NPD pattern at 2 K corresponds to the magnetic moment values, $m_{Gd^{3+}} = 6.6(4)$ and $m_{Cr^{5+}} = 0.7(3)\ \mu_B$. The Néel temperature estimated from the temperature dependence of the strongest magnetic reflection (0 0 2) was found to be ~20 K which agrees with the magnetic susceptibility and specific heat measurements discussed previously.

4. Conclusions

$GdCrO_4$ scheelite polymorph has been prepared by heating at 803 K the $GdCrO_4$-zircon type compound at a pressure as high as 4 GPa during 30 min. This quenched $GdCrO_4$ scheelite gives in a reversible process the $GdCrO_4$ zircon polymorph when is heated at 773 K; further increasing of the temperature produce the reduction of the later yielding as result the $GdCrO_3$ distorted perovskite phase as final product of the thermal decomposition.

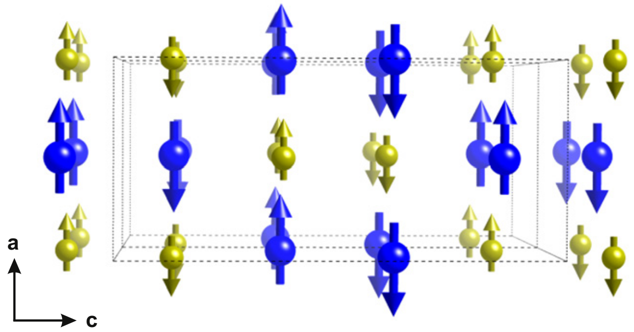

Fig. 11. Schematic representation of the magnetic structure of the $GdCrO_4$ scheelite at 2 K. Large blue and small yellow arrows correspond to Gd and Cr moments respectively. (For interpretation of the references to color in this figure legend, the reader is referred to the web version of this article.)

Table 3
Basis vectors of the irreducible representations for Cr^{5+} and Gd^{3+} sublattices in the space group $I\ 4_1/a$ with **k**=(000).

IR	Basis vectors											
	4*a*						4*b*					
	$Cr^{5+}(1)$			$Cr^{5+}(2)$			$Gd^{3+}(1)$			$Gd^{3+}(2)$		
	x	*y*	*z*	*x*	*y*	*z*	*x*	*y*	*z*	*x*	*y*	*z*
Γ_1	0	0	1	0	0	1	0	0	1	0	0	1
Γ_4	0	0	1	0	0	−1	0	0	1	0	0	−1
Γ_5	1	−*i*	0	1	−*i*	0	1	−*i*	0	1	−*i*	0
Γ_6	1	*i*	0	−1	−*i*	0	1	*i*	0	−1	−*i*	0
Γ_7	1	*i*	0	1	*i*	0	1	*i*	0	1	*i*	0
Γ_8	1	−*i*	0	−1	*i*	0	1	−*i*	0	−1	*i*	0

Please cite this article as: A.J. Dos santos-García, et al., J. Solid State Chem. (2012), http://dx.doi.org/10.1016/j.jssc.2012.04.044

Magnetic susceptibility and specific heat measurements reveal the existence of antiferromagnetic ordering with a $T_N \sim 20$ K. The magnetic structure has been solved from neutron diffraction studies and it can be described with a propagation vector $k=(0\ 0\ 0)$ where the $m_{Cr^{5+}}$ and $m_{Gd^{3+}}$ magnetic moments become ordered simultaneously within the *ab*-plane of the tetragonal scheelite-type structure. The mechanism of these magnetic interactions has been analyzed taking into account the Gd^{3+}–O–Cr^{5+} superexchange pathway through these interactions take place.

Acknowledgments

This work has been sponsored by Comunidad de Madrid under the research project S-2009/PPQ-1626 and MICINN through MAT2010-19460. A. J. Dos santos-García is also grateful to MICINN and UCM for a “Juan de la Cierva” contract (JCI-2010-08229). M. Rabie is grateful to financial support for a predoctoral grant under research SOPRANO-Marie Curie actions (Seventh Framework Programme FP7/2007–2013 under Grant Agreement no. 214040). For 7C2 beamtime allocation we are grateful to LLB, Saclay and the fund received by the NMI3 EU program. The PPMS measurements have been taken at Instituto de Ciencia de Materiales de Aragón, CSIC, and Universidad de Zaragoza, to whom we are grateful.

References

[1] J.M. Hanchar, P.W.O. Hoskin, Reviews in Mineralogy & Geochemistry: vol. 53 Zircon, The Mineralogical Society of America, Washington, 2003.
[2] D. Errandonea, F.J. Manjón, Prog. Mater. Sci. 53 (2008) 711–773.
[3] B.G. Hyde, S. Anderson, Inorganic Crystal Structures, John Wiley & Sons, New York, 1989.
[4] J.P. Bastide, J. Solid State Chem. 71 (1987) 115–120.
[5] O Fukunaga, S. Yamaoka, Phys. Chem. Miner. 5 (1979) 167–177.
[6] M.B. Smirnov, A.P. Mirgorodsky, V.Yu. Kazimirov, R. Guinebretière, Phys. Rev. B 78 (2008) 094109.
[7] K. Kusaba, T. Yagi, H. Kikuchi, Y. Syomo, J. Phys. Chem. Solids 47 (1986) 675–679.
[8] M. Marqués, J. Contreras-García, M. Flórez, J.M. Recio, J. Phys. Chem. Solids 69 (2008) 2277–2280.
[9] S.G. Manca, E.J. Baran, J. Appl. Cryst. 15 (1982) 102–103.
[10] G. Buisson, F. Bertaut, J. Mareschal, C. R. Acad Sci. Paris 259 (1964) 411.
[11] E. Jiménez Melero, J. Isasi, R. Sáez Puche, J. Alloys Compd. 115 (2001) 323–324.
[12] Von H. Schwarz, Z. Anorg. Allg. Chem. 323 (1963) 44–53.
[13] S.G. Manca, E.J. Baran, J. Phys. Chem. Solids 42 (1981) 923–925.
[14] E. Climent Pascual, J. Romero de Paz, J.M. Gallardo Amores, R. Sáez Puche, Solid State Sci. 9 (2007) 574–579.
[15] E. Climent Pascual, J.M. Gallardo Amores, J. Romero de Paz, N. Taira, R. Sáez Puche, J. Alloys Compd. 488 (2009) 524–527.
[16] Y.W. Long, L.X. Yang, Y. Yu, F.Y. Li, Y.X. Lu, R.C. Yu, Y.L. Liu, C.Q. Jin, J. Appl. Phys. 103 (2008) 093542.
[17] V.S. Stubican, R. Roy, Z. Kristallgr. 119 (1963) 90–97.
[18] R. Sáez-Puche, E. Jiménez, J. Isasi, M.T. Fernández-Díaz, J.L.García Muñoz, J. Solid State Chem. 171 (2003) 161–169.
[19] E. Jiménez-Melero, P.C.M. Gubbens, M.P. Steenvoorden, S. Sakarya, A. Goosens, P. Dalmas de Réotier, A. Yaouanc, J. Rodríguez-Carvajal, B. Beuneu, J. Isasi, R. Sáez-Puche, U. Zimmerman, J.L. Martínez, J. Phys. Condens. Matter 18 (2006) 7893–7904.
[20] R. Sáez-Puche, M.G. Rabie, J. Romero de Paz, J.M. Gallardo-Amores, E. Climent-Pascual, J. Rare Earths 28 (2010) 936–939.
[21] E. Climent-Pascual, J.M. Gallardo-Amores, R. Sáez-Puche, M. Castro, N. Taira, J. Romero de Paz, L.C. Chapon, Phys. Rev. B 81 (2010) 174419.
[22] Y.W. Long, L.X. Yang, Y. Yu, F.Y. Li, R.C. Yu, C.Q. Jin, Phys. Rev. B 75 (2007) 104402.
[23] Y. Long, Q. Liu, Y. Lv, R. Yu, C. Jin, Phys. Rev. B 83 (2011) 024416.
[24] R. Sáez Puche, E. Climent, M.G. Rabie, J. Romero, J.M. Gallardo, J. Phys. Conf. Ser. 325 (2011) 012012.
[25] J. Rodríguez-Carvajal, Physica B 192 (1993) 55.
[26] J. Rodríguez-Carvajal, T. Roisnel, FullProf WinPLOTR, and accompanying programs, 2008.
[27] J.B. Goodenough, W. Gräper, F. Holtzberg, D.L. Huber, R.A. Lefever, J.M. Longo, T.R. McGuire, S. Methfessel, Landoltz-Börnstein New Series III/4a,Magnetic and Other Properties Of Oxides and Related Compounds, Springer-Verlag, New York, 1970.
[28] H. Nyman, B.G. Hyde, S. Anderson, Acta Cryst. B40 (1984) 441–447.
[29] M.D. Guo, A.T. Albred, S.K. Chan, J. Phys. Chem. Solids 48 (1987) 229.
[30] F.E. Mabbs, D.J. Machin, Magnetism and Transition Metal Complexes, John Wiley and Sons, New York, 1973.
[31] P.W. Anderson, Phys. Rev. 79 (1950) 705.
[32] J.B. Goodenough, Phys. Rev. 100 (1955) 564.
[33] J. Kanemori, J. Phys. Chem. Solids 10 (1959) 87.
[34] G. Grimvall, Thermophysical Properties of Materials in Selected topics in Solid State Physics, Elsevier/North-Holland, New York, 1986.
[35] T. Endo, Y. Doi, M. Wakeshima, Y. Hinatsu, Inorg. Chem. 49 (2010) 10809–10814.
[36] S.J. Joshua, A.P. Cracknell, Phys. Rev. Lett. A28 (1969) 562.
[37] K. Tezuka, Y. Hinatsu, J. Solid State Chem. 160 (2001) 362367.
[38] K.I. Kugel, D.I. Khomskii, Sov. Phys. Usp 25 (1982) 231–256.
[39] G.E. Bacon, Neutron Diffraction, Oxford University Press, New York, 1975.
[40] E.F. Bertaut, Acta Crystallogr., Sect. A: Cryst. Phys., Diffr., Theor. Gen. Crystallogr 24 (1968) 217.

Please cite this article as: A.J. Dos santos-García, et al., J. Solid State Chem. (2012), http://dx.doi.org/10.1016/j.jssc.2012.04.044

Appendix III

Neutron diffraction characterization and magnetic properties of the scheelite-type $ErCrO_4$ polymorph

R. Sáez Puche, E. Climent, M. G. Rabie, J. Romero, and J. M. Gallardo

Departamento Química Inorgánica, Facultad de Ciencias Químicas, Universidad Complutense de Madrid, 28040-Madrid, Spain.

E-mail: rsp92@quim.ucm.es

Abstract. The new scheelite-type $ErCrO_4$ polymorph has been obtained from the zircon-type $ErCrO_4$ phase by a treatment at 4 GPa and 823 K. X-ray and neutron diffraction studies reveal that this scheelite-type polymorph crystallizes with tetragonal symmetry, space group $I4_1/a$ being the lattice parameters a= 4.9989(10) Å and c= 11.2332(23) Å. Although bisdisphenoids [ErO_8] and tetrahedra [CrO_4] polyhedra are present in both compounds, dramatic changes have been observed in the magnetic properties of both polymorphs of $ErCrO_4$. The zircon one is ferromagnetic with $T_C \approx$ 15 K; while the corresponding scheelite-type polymorph behaves as antiferromagnetic with $T_N \approx$ 21 K. The observed change of sign in these compounds could be explained by considering the differences found in the superexchange Er–O–Cr bond angles through which the magnetic interactions take place in both polymorphs.

1. Introduction

The RXO_4 oxides, where R= rare earth and X= P, As, Cr and V, crystallize in the zircon or monazite-type structures at ambient conditions and transform to scheelite-type at high pressures and moderate temperatures [1]. These phases are quenchable to ambient conditions [2] except for $YbPO_4$ and $LuPO_4$ where a non-quenchable pressure induced transition has been observed [3].

Regarding the zircon-$RCrO_4$, high pressure phase transitions have only been studied for $YCrO_4$ [4], $HoCrO_4$ [5] and $TbCrO_4$ [6]. This structural phase transition from zircon to scheelite produces important changes in the magnetic properties. In this sense, most of the zircon-type $RCrO_4$ oxides being ferromagnetic become antiferromagnetic for the corresponding scheelite-type polymorph [7].

In this paper, we report the synthesis conditions used in the preparation of the scheelite-type $ErCrO_4$ oxide and its structural characterization by means of X-ray and neutron powder diffraction data as well as the study of the magnetic properties.

2. Experimental

Zircon-type $ErCrO_4$ polymorph was prepared using stoichiometric amounts of $Er(NO_3)_3{\cdot}6H_2O$ and $Cr(NO_3)_3{\cdot}9H_2O$ according to the experimental procedure described elsewhere [7]. The obtained zircon-type $ErCrO_4$ oxide was placed in a gold container and treated in a belt-type press at different pressures and temperatures in order to optimize the synthesis conditions to yield the scheelite-$ErCrO_4$ phase. The optimized conditions were 4 GPa and 833 K for 40 min. The sample obtained from the high-pressure experiment was tested by means of X-ray diffraction measurements.

Published under licence by IOP Publishing Ltd

Neutron powder diffraction data were collected in the temperature range of 2-100 K using the medium resolution powder diffractometer D1B (λ= 2.5251 Å, $20 \leq 2\theta$(deg.) ≤ 90) at the Institut Laue Langevin (Grenoble, France). The data were analyzed by the Rietveld method using the program FullProf integrated in the software package WinPlotr [8].

Magnetic susceptibility and magnetization measurements were performed in a Quantum Design MPMS-XL magnetometer in the temperature range of 2-300 K at different applied magnetic fields.

3. Results and discussion

Figures 1(a) and (b) show the Rietveld refinement of the neutron diffraction data for the obtained scheelite-type $ErCrO_4$ oxide at 100 and 2 K, respectively. The data have been refined according to the scheelite-type structure, space group $I4_1/a$. The oxygen atoms are located in the general positions 16*f* (*x*,*y*,*z*), while the Er^{3+} and Cr^{5+} ions are placed in the special 4*b* (0,1/4,5/8) and 4*a* (0,1/4,1/8) sites, respectively. Note that the impurities Cr_2O_3 (4 wt %) and $ErCrO_3$ (10 wt %) have been also included in the refinement. The structural parameters obtained from the Rietveld refinement, main bond distances, angles and agreement factors are included in Table 1.

The temperature dependence of the magnetic susceptibility for $ErCrO_4$ is shown in figure 2. The onset of a net maximum found around 11 K is indicative of the appearance of antiferromagnetic interactions in which both Cr^{5+} and Er^{3+} sublattices appear to be involved. The small anomaly found around 133 K is due to the magnetic behavior of the detected $ErCrO_3$ impurity, a canted antiferromagnetism, but no further low temperature anomaly due to this impurity is observed [9]. Figure 3 shows the magnetization versus magnetic field curves obtained at different temperatures. Note that below the ordering temperature the plot shows the typical S-shape feature characteristic for an antiferromagnet that undergoes a metamagnetic transition, in this case with a critical field of 1.4 T.

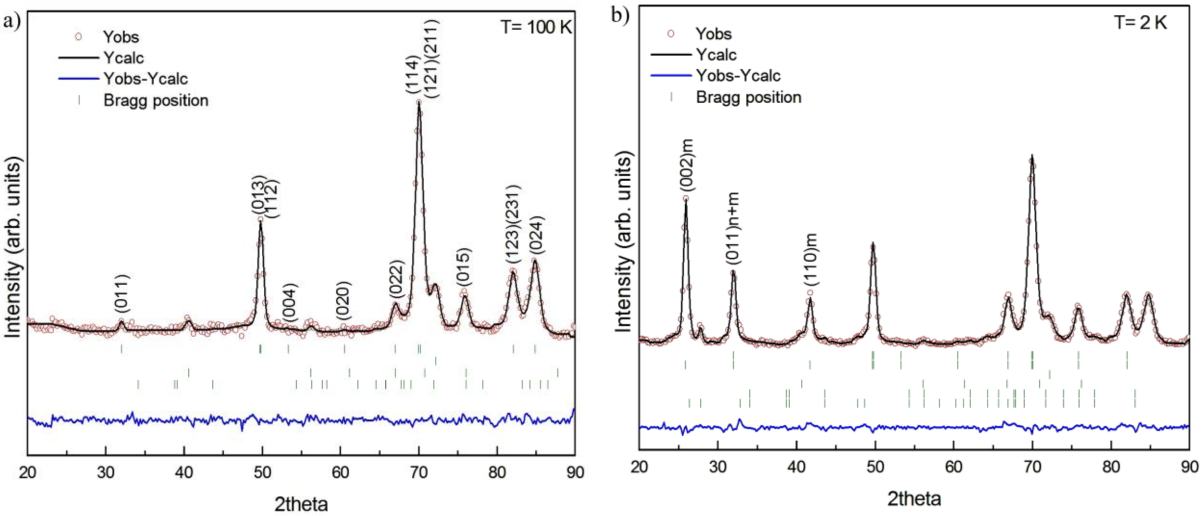

Figure 1. Rietveld refinement of neutron diffraction patterns obtained at (a) 100 K and (b) 2 K for scheelite-type $ErCrO_4$. Observed, calculated and difference profiles are denoted by circles, the upper solid line and the lower solid line, respectively. Vertical marks denote the position of (a) nuclear allowed reflections for the scheelite polymorph (first line), Cr_2O_3 (third line, 4 wt %) and $ErCrO_3$ (fourth line, 10 wt %); and (b) nuclear and magnetic reflections for the scheelite-type polymorph (first and second lines), Cr_2O_3 (fourth line), $ErCrO_3$ (fifth line) and magnetic reflections for $ErCrO_3$ (sixth line). Nevertheless, the second row of vertical marks in (a) and the third in (b) refer to the shoulder in the main reflection resulting from the sample environment equipment during the experiment.

TABLE 1. Atomic parameters, main interatomic distances and bond angles for the scheelite-type $ErCrO_4$ polymorph, calculated from the Rietveld refinement of neutron diffraction data obtained at 100 K. The corresponding reliability factors are also included

Space group				$I\,4_1/a$
Cell parameters (Å)	a			4.9989(10)
	c			11.2332(23)
Rietveld R-factors	$R_{p.}$			0.0115
	R_{wp}			0.0146
	χ^2			1.90
Bragg R-factors	R_B			0.0140
	R_F			0.0202
Atoms, wyckoff	Er	4*b*	1	0,1/4,5/8
Positions	Cr	4*a*	1	0,1/4,1/8
x/a, y/b, z/c	O	16*f*	1	0.2352(26), 0.6044(20), 0.5478(6)
B_{iso} (Å^2)				0.065(3)

Main interatomic distances (Å) and bond angles (deg.)

d (Cr-O)	1.744(10)×4	d (Er-O)	2.295(11)×4
			2.382(9)×4
∠ (O-Cr-O)	120.3(13)×2	∠ (O-Er-O)	135.5(9)×2
	104.4(10)×4		98.2(8)×4
			131.5(6)×4
			71.0(5)×2
∠ (Cr-O-Er)	121.5(5)×1		
	130.7(5)×1		

Neutron powder diffraction patterns show the onset of new reflections forbidden for the space group $I4_1/a$ along with a progressive increase of certain reflections below $T_N \approx 20$ K. These magnetic reflections, see Fig. 1(b), have been indexed on the basis of the coincidence between the crystal and magnetic cells, with the propagation vector **k**= (0,0,0). The thermal evolution of the integrated intensity of the (002) and (011) magnetic reflections reveals that these magnetic reflections disappear at 22 K, a higher ordering temperature than the observed one from the magnetic susceptibility measurements. The magnetic structure is defined in the primitive $P1$ space group and the best agreement (R_M= 0.032) between the experimental and calculated neutron diffraction profiles was obtained when Cr^{5+} and Er^{3+} magnetic moments are aligned parallel to the *ab*-plane [10]. The saturation moments obtained from the Rietveld refinement are 0.62(4) μ_B and 5.11(7) μ_B for the Cr^{5+} and Er^{3+}, respectively.

The different magnetic behavior observed between the zircon-type and the scheelite-type polymorphs of $ErCrO_4$ oxide could be explained by considering the changes in the Er-O-Cr superexchange pathways through which the magnetic interactions take place in both compounds. These changes are mostly due to the changes in the Er-O-Cr bond angles, since the bond distances remain almost constant in both polymorphs. Such bond angles take the values of 152.67(20)º and 96.27(15)º for the zircon-type phase, while in the case of the scheelite-type phase they are 121.5(5)º and 130.7(5)º.

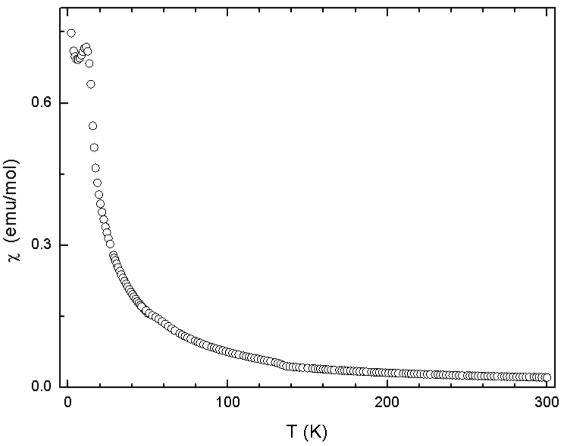

Figure 2. Thermal variation of the magnetic susceptibility for the scheelite- $ErCrO_4$ polymorph.

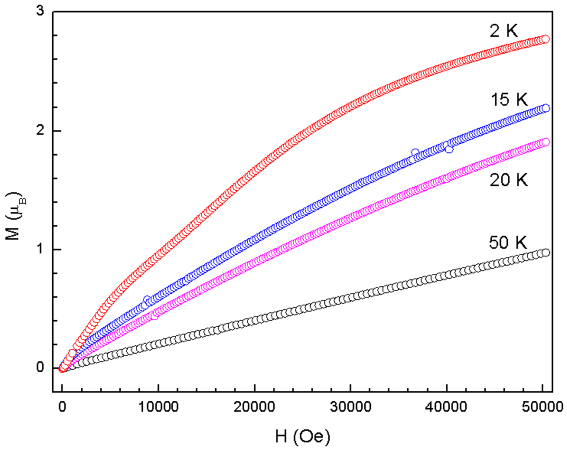

Figure 3. Magnetization versus magnetic field plot for the scheelite-type ErCrO4

Acknowledgments

The authors are grateful to Spanish MICINN for financial support under Research Projects No. MAT2007-63497 and ILL facilities where the neutron experiments were done.

References

[1] Stubican V S and Roy R 1963 *Z. Kristallogr.* **119 S** 90
[2] Errandonea D and Manjón F J 2008 *Prog. Mater. Sci.* **53** 711
[3] Zhang F X, Lang M, Ewing R C, Lian J, Wang Z W, Hu J and Boatmer L A 2008 *J. Solid State Chem.* **181** 2633
[4] Long Y W, Yang L X, Yu Y, Li Y, Yu R C and Lin C Q 2007 *Phys. Rev.* B **75** 104402
[5] Climent Pascual E, Romero de Paz J, Gallardo Amores J M and Sáez Puche R 2007 *Solid State Sci.* **9** 574
[6] Climent Pascual E, Gallardo Amores J M, Sáez Puche R, Castro M, Taira N, Romero de Paz J, and Chapon L C 2010 *Phys. Rev.* B **81** 174419
[7] Sáez-Puche R, Jiménez E, Isasi J, Fernández-Díaz M T and García Muñoz J L 2003 *J. Solid State Chem.* **171** 161
[8] Rodríguez-Carvajal J 1993 *Physica* B **192** 55
[9] Su Y,·Zhang J, Li L,·Li B, Zhou Y,·Deng D, Chen Z·and Cao S 2010 *Appl. Phys.* A DOI: 10.1007/s00339-010-5839-1
[10] Climent Pascual E, *et al*. (unpublished work)

Appendix IV

Determination of the crystal and magnetic structure of the $DyCrO_4$ -scheelite polymorph by neutron diffraction

A. J. Dos santos-García[1], E. Climent-Pascual[1], J. Romero de Paz[1], J. M. Gallardo Amores[1], M. G. Rabie[1], D. Khalyavin[2] and R. Sáez-Puche[1]

[1]Departamento de Química Inorgánica, Facultad de Químicas, Universidad Complutense de Madrid, 28040 Madrid, Spain.

[2]ISIS Facility, Rutherford Appleton LaboratoryCCLRC, Chilton, Didcot, Oxfordshire OX11 0QX, United Kingdom

E-mail: `rsp92@ucm.es`

Abstract. Neutron diffraction data of $DyCrO_4$ oxide, prepared at 4 GPa and 833 K from the ambient pressure zircon-type, reveal that crystallize with the scheelite-type structure, space group $I4_1$/a. Accompanying this structural phase transition induced by pressure the magnetic properties change dramatically from ferromagnetism in the case of zircon to antiferromagnetism for the scheelite polymorph with a $T_N = 19$ K. The analysis of the neutron diffraction data obtained at 2 K has been used to determine the magnetic structure of this $DyCrO_4$-scheelite oxide which can be described with a k = [0, 0, 0] as propagation vector, where the Dy and Cr moments are lying in the *ab*-plane of the scheelite structure. The ordered magnetic moments are 10 μ_B and 1μ_B for Dy^{+3} and Cr^{+5} respectively.

1. Introduction

Phase transitions induced by pressure have been studied for the zircon mineral $ZrSiO_4$ and the analogous zircon-types of RXO_4 (X= As and V) which transform the tetragonal space group $I4_1$/amd into a scheelite-type structure, space group $I4_1$/a. Recently for $YbPO_4$ and $LuPO_4$, it was revealed using in-situ synchrotron x-ray diffraction experiments that the pressure-induced zircon-to-scheelite transition is reversible and the scheelite high-pressure phase cannot be quenched to ambient conditions in these phosphates [1]. In the case of vanadates and arsenates, this phase transition from zircon to scheelite, with an increase in the density of 11%, takes place at 8 GPa and 773 K [2, 3]. Regarding the high pressure phase transformations in $RCrO_4$, in which we are interested, only few studies have been reported. This could be due to the high instability of Cr^{+5} and its tendency to be reduced to give the most stable distorted phase of perovskite $RCrO_3$. However, it has been recently reported by our research group that zircon-$RCrO_4$ phases transform to a scheelite polymorph at 4 GPa and 813 K for the $HoCrO_4$ and $TbCrO_4$ compounds, which are quenchable after releasing the pressure [4, 5]. Accompanying this structural phase transition from zircon to scheelite the magnetic properties change dramatically. In this sense, most of the zircon-type $RCrO_4$ oxides being ferromagnetic become antiferromagnetic for the corresponding known scheelite polymorph. Detailed structural analysis by x-ray diffraction

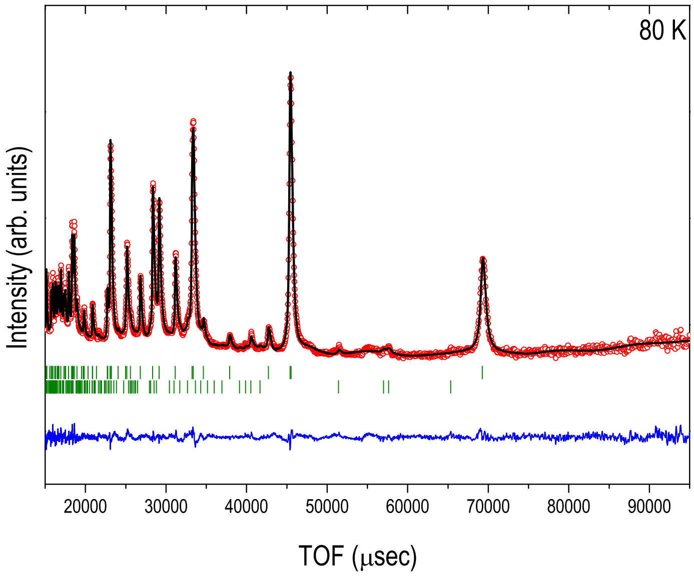

Figure 1. Rietveld refinement of the $DyCrO_4$ scheelite polymorph at 80 K for TOF neutron diffraction data. First raw of the vertical bars (i) corresponds to the $DyCrO_4$ scheelite. Second line (ii) is for $DyCrO_3$ distorted perovskite.

(XRD) and neutron diffraction (NPD) allow us to establish structure-magnetic properties relationships, which represents one of the main interests in the solid-state science. In this work, we aim to study the scheelite-$DyCrO_4$ oxide through investigating the structural and magnetic properties. Therefore, we focus first on the structural phase transition from the zircon-like to the scheelite-like structure under pressure and temperature. Second, we report the study of the magnetic properties of this $DyCrO_4$ from magnetization and neutron diffraction measurements.

2. Experimental

The $DyCrO_4$ zircon-phase sample, which was prepared by a precursor method described elsewhere, has been treated at 4 GPa and 833 K and 35-50 minutes in a CONAC-type press. $DyCrO_4$ scheelite oxide was first studied by X-ray powder diffraction using a Philips X'Celerator diffractometer with a primary beam monochromator consisting of a curved Ge (1 1 1) crystal aligned to obtain $CuK_{\alpha 1}$ radiation. A range of 2θ-angle between 10° and 90° was recorded with a step size of 0.0167° collected for 150s. Neutron diffraction experiments were done at the ISIS facility in the UK using the WISH cold-neutron time of flight (TOF) powder diffractometer. All obtained diffraction patterns were analyzed using the FullProf Suite Program. Magnetic susceptibility and magnetization measurements were performed in a Squid Quantum Design MPS XL from 300 K to 2 K temperature range in different magnetic fields up to 5T.

3. Results and discussion

3.1. Structural characterization

The structure of the $DyCrO_4$ compound obtained after treating the $DyCrO_4$-zircon polymorph at 4 GPa and 833 K has been refined from the X-ray and neutron diffraction data using the Rietveld method with the Fullprof program. As it is shown in Figure 1 the neutron diffraction data obtained at 80 K show the reflections conditions compatible with the space group $I4_1/a$ characteristic of the scheelite type structure.

The refined atomic positions are Dy at 4b (0, 1/4, 5/8), 4a (0, 1/4, 1/8) for Cr and the oxygen atoms are located at the 16f (x, y , z). The lattice parameters and main bond angles and interatomic distances are given in Table 1.

It is worth noting that small amount of impurities such as $DyCrO_3$ has also been include in the refinement. The zircon-type structure of $RCrO_4$ can be described as formed by chains of

Table 1. Control sequences to describe lines and symbols in figure captions.

T (K)	80	1.2
a (Å)	5.0170(2)	5.0148(2)
b (Å)	11.3079(6)	11.3037(5)
V ($Å^2$)	284.62(2)	284.27(2)
U_{Dy} ($Å^2$)	0.0003(8)	0.0002
U_{Cr} ($Å^2$)	0.019(3)	0.0002
x_o	0.2437(5)	0.2437
y_o	0.6091(4)	0.6091
z_o	0.5486(2)	0.5486
U_o ($Å^2$)	0.0105(14)	0.0002(8)
d_{Cr-O} (Å)	1.7020(22) x 4	1.7020 x 4
d_{Dy-O} (Å)	2.3413(22) x 4	2.3413 x 4
	2.4177(23) x 4	2.4177 x 4
Cr - O - Dy (deg.)	121.759 (114)	121.759
	132.242(82)	132.242
$\mu_{xy,Dy}$ (μ_B)	——	9.67(10)
$\mu_{xy,Cr}$ (μ_B)	——	0.99(12)
R_{Bragg} (%)	2.44	5.49
R_p (%)	3.81	4.02
R_wp (%)	2.10	5.18
χ^2	2.62	1.32
Magnetic R-factor (%)	——	6.82

CrO_4 and RO_8 polyhedra which are parallel to the c-axis and alternating by an edge sharing as seen in Figure 2a. Adjacent rods are connected along a and b-axis by zig-zag of edge sharing between RO_8 polyhedra. In case of the scheelite structure, CrO_4 distorted tetrahedra are aligned along the a-axis, while RO_8 bisdisphenoids are intercalated between the CrO_4 tetrahedra (Figure 2b).

The RO_8 polyhedra shares edges with adjacent RO_8 polyhedra and form along a-direction zig-zag chains, which are cross-linked by tetrahedra via corner-sharing (figure 2b). However, there is no edge-sharing between RO_8 and CrO_4 polyhedra. The difference in the tilting angle between different polyhedra, as well as in the packing after the transition provides an remarkable change in the Cr- O - R angles as it will be discussed later to explain the different magnetic behavior that presents this scheelite polymorph in comparison with the zircon one.

3.2. Magnetic properties

Figure 3 shows the evolution of the magnetic susceptibility with the temperature and it can observed that the susceptibility obeys a Curie- Weiss behavior, χ = C/T + θ in the temperature range 300 - 40 K, see Figure 3 inset.

It is also observed a small anomaly at 150 K due to the presence of the distorted perovskite $DyCrO_3$ that become antiferromagnetically ordered at this temperature with a small canting. However the presence of this phase doesn't affect to the magnetic properties of the scheelite-$DyCrO_4$ oxide. In this sense, the obtained magnetic moment takes the value of 11.2 μ_B which fairly agrees with the expected for this compound is 10.80 μ_B. The Weiss constant (θ) takes

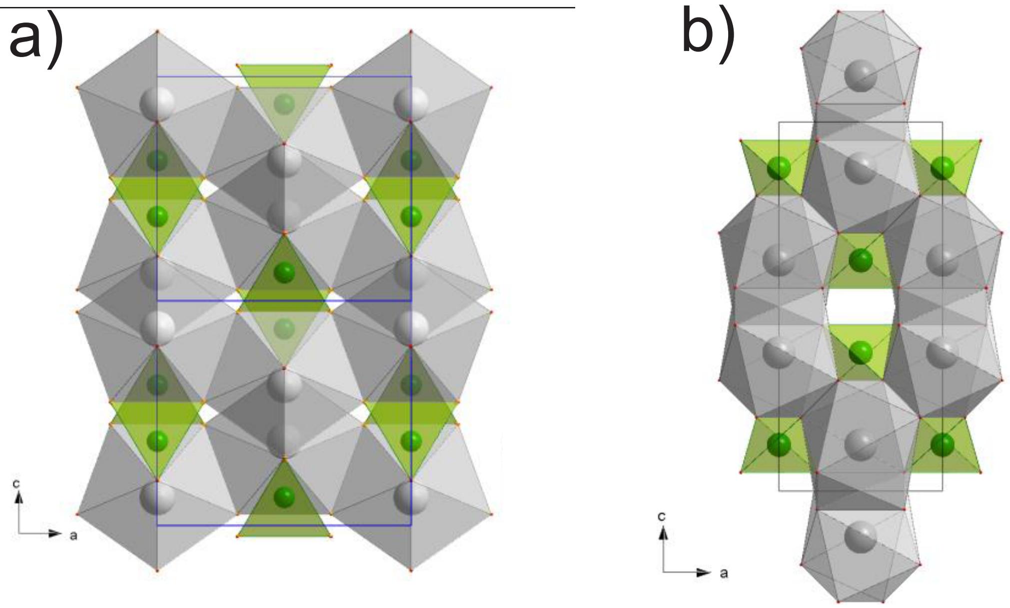

Figure 2. a) Crystal structure of the zircon-$DyCrO_4$ and b) scheelite-$DyCrO_4$ polymorph.

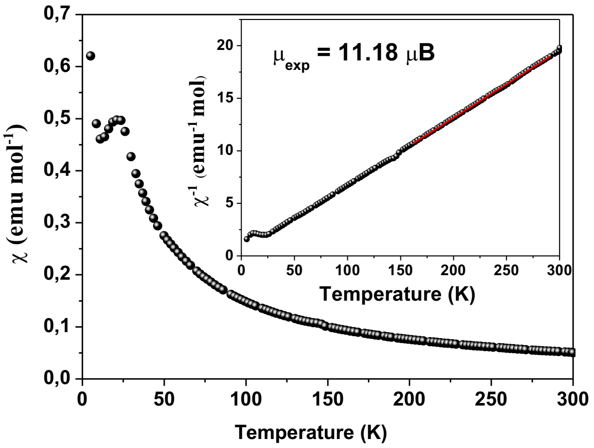

Figure 3. ZFC magnetization measurements for $DyCrO_4$ scheelite in a 0.05 T field. The inset shows the temperature dependence of the reciprocal susceptibility.

the value of -5.6 K which is indicative of the existence of antiferromagnetic interactions in this oxide. These interactions are fully confirmed the onset of a net maximum at 20 K in the χ vs T plot, see Figure 3. The increasing of the susceptibility below the T_N is due to presence of the small amount of impurities mentioned earlier. The different magnetic behavior that present both $DyCrO_4$ polymorphs, the scheelite form is antiferromagnetic, while the zircon-$DyCrO_4$ have been reported to be ferromagnetic [6] can be explained from the analysis of the structure of both polymorphs. As it was reported previously, these interactions take place through the superexchange Cr^{+5}-O-Dy^{+3} pathway in which both Cr and Dy are involved. Since the Cr-O and Dy-O interatomic distances remain almost constant for both polymorph, the change in the sign of the exchange integral going from the zircon to scheelite form is mainly due to remarkable differences found in the Cr^{+5}-O-Dy^{+3} bond angle found in both polymorphic phases. The magnetic structure of the $DyCrO_4$-scheelite polymorph has been determined from the analysis of the neutron diffraction data obtained at 2K. The neutron powder diffraction patterns show the

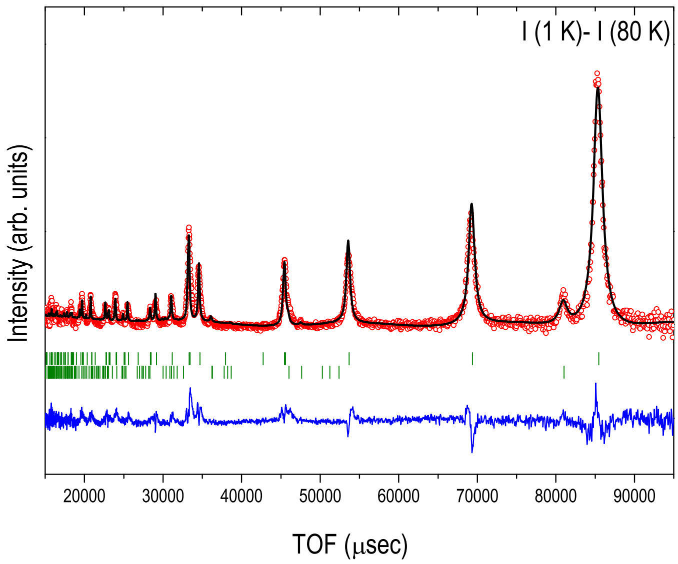

Figure 4. Magnetic structure fit from the difference between the 2 and 80 K neutron diffraction profiles of $DyCrO_4$. First ticks of vertical marks (i) corresponds to the magnetic contribution from the $DyCrO_4$ scheelite and second line (ii), magnetic contribution from the $DyCrO_3$ distorted perovskite.

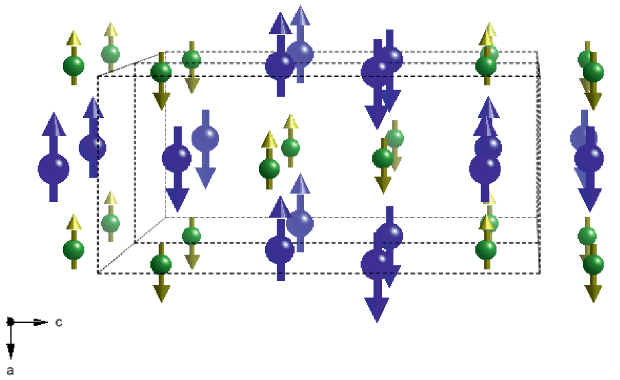

Figure 5. Magnetic structure of the $DyCrO_4$ scheelite. Blue and yellow arrows stem for the Dy and Cr magnetic moments respectively.

onset of new reflections forbidden for the space group $I4_1$/a along with a progressive increase of certain reflections below $T_N = 20$ K. These magnetic reflections, see Figure 4, have been indexed on the basis of the coincidence between the crystal and magnetic cells, with the propagation vector k = [0, 0, 0].

The thermal evolution of the integrated intensity of the (002) and (110) magnetic reflections reveals that these magnetic reflections disappear at 22 K, a higher ordering temperature than the observed one from the magnetic susceptibility measurements. The magnetic structure is defined in the primitive P1 space group and the best agreement (RM= 0.068) between the experimental and calculated neutron diffraction profiles was obtained when Cr^{+5} and Dy^{+3} magnetic moments are aligned parallel to the ab-plane in the same manner like for $GdCrO_4$ scheelite [7],see Figure 5.

The saturation magnetic moments obtained from the Rietveld refinement are 0.99(12) and 9.67(10) for the Cr^{+5} and Dy^{+3}, respectively. As it can be observed in Figure 5 the magnetic moments of Dy^{+3} are antiferromagnetically coupled between the (Dy_2O_{14}) dimers resulting from the two (DyO_8) bisdiphenoids sharing a edge in the ab-plane of the scheelite structure. The Cr^{+5} moments are also antiferomagnetically coupled in the ab-plane of the structure given as result the collinear magnetic structure depicted in Figure 5.

4. Acknowledgments

The authors acknowledge funding from Comunidad de Madrid under the research project S-2009/PPQ-1626 and MICINN through MAT2010-19460. AJD is grateful to MICINN and UCM for a Juan de la Cierva contract (JCI-2012-08229). M. Rabie is also grateful to financial support for a pre-doctoral grant under research SOPRANO-Marie Curie actions (FP7/20072013 under Grant Agreement no.214040). Authors are also indebted to ISIS-facility for beamtime allocation at WISH instrument and Dr. L. C. Chapon and Dr. P. Manuel for valuable comments.

5. References

[1] Zhang F, Lang M, Ewing R, Lian J, Wang Z, Hu J and Boatner L 2008 *Journal of Solid State Chemistry* **181** 2633 – 2638
[2] Duclos S J, Jayaraman A, Espinosa G, Cooper A and Sr R M 1989 *Journal of Physics and Chemistry of Solids* **50** 769 – 775
[3] Stubican V S and Roy R 1963 *Journal of Applied Physics* **34** 1888–1890
[4] Climent-Pascual E, de Paz J R, Gallardo-Amores J M and Sez-Puche R 2007 *Solid State Sciences* **9** 574 – 579
[5] Climent E, Gallardo J, de Paz J R, Taira N and Puche R S 2009 *Journal of Alloys and Compounds* **488** 524 – 527
[6] Long Y, Liu Q, Lv Y, Yu R and Jin C 2011 *Phys. Rev. B* **83**(2) 024416
[7] Dos Santos-García A J, Climent-Pascual E, Gallardo-Amores J M, Rabie M G, Doi Y, de Paz J R, Beuneu B and Saez-Puche R 2012 *Journal of Solid State Chemistry* **194** 119 – 126

Publication List

M.G. Rabie, Z. Hu, L. H. Tjeng, R. Sáez Puche “Electronic structure of $YCrO_4$ Zircon-like compound: a combined XPS and *ab initio* study” (under preparation)

A. J. Dos Santos Garcia, E. Climent Pascual, M. G. Rabie, J. Romero de Paz, J. M. Gallardo Amores and R. Sáez Puche “Determination of the crystal and magnetic structure of the $DyCrO_4$ -scheelite polymorph by neutron diffraction” *Journal of Physics, Conference Series* (Submitted)

A.J. Dos santos-García, E. Climent-Pascual, J.M. Gallardo-Amores, M.G. Rabie, Y. Doi, J. Romero de Paz, B. Beuneu, R. Sáez-Puche “Synthesis and magnetic properties of the high-pressure scheelite type $GdCrO_4$ polymorph” *Journal of Solid State Chemistry* **194**, 119 (2012)

D. Errandonea, R. Kumar, J. Lopez-Solano, P. Rodriguez-Hernandez, A. Muñoz, M.G. Rabie, R. Sáez Puche “Experimental and theoretical study of structural properties and phase transitions in $YAsO_4$ and $YCrO_4$” *Physical Review B* **83**, 134109 (2011)

R. Sáez Puche, E. Climent, M.G. Rabie, J. Romero, J.M. Gallardo “Neutron diffraction characterization and magnetic properties of the scheelite-type $ErCrO_4$ polymorph” *Journal of Physics: Conference Series* **325,** 012012 (2011)

R. Sáez Puche, M.G. Rabie, J. Romero, J.M. Gallardo, E. Climent “High-pressure scheelite-type polymorph of $SmCrO_4$: synthesis, structural characterization and magnetic properties” *Journal of Rare Earths,* **28** (6), 936 (2010)

Master’s Thesis: M.G. Rabie “Martensitic transformation of Ni-Mn-based magnetic shape-memory alloys upon cooling under magnetic field”, Ludwig-Maximilians-University Munich, (February 2009)

Bachelor’s Thesis: M.G. Rabie “Precipitation hardening of squeeze-cast Al-Cu-Mg alloys” Cairo University, (July 2003)

M.G. Rabie: “Research profile of the Egyptian Nobel Prize literate in chemistry 1999: A. H. Zewail (The story of Femtochemistry)”, Egyptian national competition for young researchers (2000)

Presentations and Posters at Conferences

22nd - 27th July 2012	Gordon Research Conference, Solid State Chemistry, NH, USA (Poster)
24th - 27th Feb. 2012	Solid State Chemistry Conference, Lanzarote, Spain (Presentation)
07th - 09th Sep. 2011	SFB 608 Tokyo-Cologne Workshop on Strongly Correlated Transition-Metal Compounds, Köln (Poster)
12th - 15th Sep. 2010	8th Scientific Meeting for solid-state chemistry, Cartagena, Spain (Presentation)
28th - 30th June 2010	5th Meeting for the Spanish Society for Neutron Techniques, Gijón, Spain (Presentation)
17th - 19th Mar. 2010	6th French-Spanish Meeting of Chemistry and Physics of the Solid State, Tarragona, Spain (Presentation)

Short Curriculum Vitae

Mahmoud Rabie

(born in Giza, Egypt)

Education:

02/2009	Double Master Degree in Geomaterials and Geochemistry (Master of Materials Science Exploiting European Large-Scale Facielities) from LMU Munich University, Crystallography Department (Germany) and Rennes1 University, Faculty of Chemistry (France)
07/2003	Bachelor Degree in Metallurgical Engineering (Physical Metallurgy) from Cairo University (Egypt). Bachelor thesis at TU-Berlin, Institute of Metallic Research (Germany)

Work:

7/2011 - 10/2012	Research fellow at Max Planck Institute for Chemical Physics of Solids (CPfS), Physics of Correlated Matter Department in Dresden, Germany (07/2011 - 07/2012: Financed by the University of Cologne as Marie-Curie ESR-fellow)
7/2009 - 6/2011	Research fellow at the Complutense University of Madrid, Inorganic Chemistry Department, Spain
03/2008 - 02/2009	Research associate at the Technical University of Munich, Physics Department, Germany
09/2005 - 10/2006	Teaching and research assistant at Modern Academy Institute for Engineering and Technology in Cairo, Egypt